Influence of a mechanical load on the ageing of Fe-Cr alloys

Alexander Dahlström

Normandie Université

THÈSE

Pour obtenir le diplôme de doctorat

Spécialité Physique

Préparée au sein de l'Université de Rouen Normandie

Inflence d'une contrainte mechanique sur le vieillissement d'alliages Fe-Cr

Présentée et soutenue par
Alexander DAHLSTRÖM

Thèse soutenue publiquement le 19 Septembre 2019 devant le jury composé de		
Mme. Suzana FRIES	Directeur de recherche / STKS, ICAMS, Ruhr-Universität Bochum.	Rapporteur
Mme. Krystyna STILLER	Professeur / Physics, Materials microstructure, Chalmers University.	Rapporteur
M. Philippe MAUGIS	Professeur / IM2NP, Aix-Marseille Université.	Examinateur
M. Peter HEDSTRÖM	Professeur / MSE, Structures, KTH.	Examinateur
M. Joakim ODQVIST	Professeur / MSE, Structures, KTH.	Examinateur
Mme. Helena ZAPOLSKY	Professeur / GPM, Université de Rouen Normandie.	Directeur de thèse
M. Frédéric DANOIX	Charge de recherche / GPM, Université de Rouen Normandie.	Co-directeur de thèse

Thèse dirigée par Pr. Helena ZAPOLSKY et M. Frédéric DANOIX
Groupe de Physique des Matériaux (GPM), UMR CNRS 6634
Université et INSA de ROUEN Normandie

UNIVERSITÉ DE ROUEN NORMANDIE

ED PSIME

GPM Groupe de Physique des Matériaux

Preface

The present doctoral thesis is based on the work I conducted as a PhD student at the University of Normandie, Rouen, France. The PhD position was initiated as a way of enhancing the scientific collaboration between the research lab Groupe de Physique des Matériaux (GPM), University of Rouen Normandie, France and the Unit of Structures, Department of Materials Science and Engineering, Royal Institute of Technology (KTH), Sweden. This project has in part been co-supervised through funding from Region Normandie and a research grant from Carl Tryggers Foundation.

The novel work in this thesis is foremost based on the experimental result, and in addition supported by atomistic modelling. Experimentally high purity model alloys bought in slabs from OCANO NV have been used throughout. Sample manufacturing and experimental work has been conducted at GPM and at Institut National des Sciences Appliquées (INSA) Rouen and INSA Lyon.

The modelling in this work has been performed at the supercomputer Myria at Centre Régional Informatique et d'Applications Numériques de Normandie (CRIANN). The main model itself is a phase field crystal model developed by technical staff and PhD students internally at GPM.

The structure of this monograph is based on chapters, Chapter 1 general introduction of the topic and research context, Chapter 2 a thorough review of the theory of phase separation, Chapter 3 experimental characterisation techniques, Chapter 4 thermal ageing of Fe-Cr alloys, phase separation and Cr-Cr clustering, Chapter 5 the influence of an external load on the ageing of Fe-Cr, Chapter 6 the atomistic modelling, quantitative results and comparison with experiment, Chapter 7 highlight of main results and connecting experiment with modelling, Chapter 8 conclusions and perspective.

Abstract

Stainless steel is an important alloy for the technical development of a modern society, they were discovered in the early 20th century. However, their base alloying system, Fe-Cr, is affected by a low temperature (<600°C) miscibility gap present in the phase diagram. Alloys with a miscibility gap in their phase diagram tend to decompose. This phenomenon is also known as the "475°C embrittlement", it is of technical importance as decomposition alters the mechanical properties of these alloys, in this specific case, by loss of ductility and impact toughness. The tendency to decompose increases with decreasing temperature, restricting the upper service temperature to around 300°C and limiting the service lifetime of these alloys. Because embrittlement can cause sudden failure of these alloys, this phenomenon is detrimental to their use as structural components in transportation and energy industry.

The decomposition of Fe-Cr alloys poses a challenge for traditional characterisation techniques, as composition variations occur at the nanoscale. Therefore, the state-of-the-art atom probe tomography have been utilised to study these composition variations at the atomic scale in 3D. Correlative atomistic modelling has been used to further enhance the understanding of the decomposition process in these alloys, this model was based on atomic density function theory. To emulate enhanced decomposition of the material, caused by temperature and/or an external load, decomposition in this work is stimulated by a higher than the normal service temperature. Hence, a need to know the exact limit of the miscibility gap. Thus, a need to evaluate the upper-temperature limit of this decomposition in the Fe-Cr system arose from inconclusive results in the literature. Hence, a high precision furnace in combination with atom probe was utilised to study decomposition and clustering in the Fe-Cr system more accurately than ever before. Furthermore, to explore in detail the location of the limit of the miscibility gap.

The decomposition of these alloys during ageing alter the mechanical properties. Thus, due to their use as structural components, the decomposition behaviour during ageing was investigated, as well as ageing during external stress. This last situation is also encountered in real applications during service, mimicked by stress-ageing using a simple tensile force. In order to in detail investigate the effect of the external stress, crystal orientation with respect to the tensile direction was considered during simple thermal ageing, and during the constantly applied tensile force. Thus, crystallographic orientation and load levels were considered for their effect on the decomposition process.

Résumé

L’acier inoxydable est un alliage important pour le développement technique d’une société moderne; cela a été découvert au début du 20ème siècle. Cependant, leur système d'alliage de base, Fe-Cr, est affecté par une lacune de miscibilité à basse température (<600°C) présent dans le diagramme de phases. Les alliages présentant une lacune de miscibilité dans leur diagramme de phase ont tendance à se décomposer. Ce phénomène également connu sous le nom de "fragilisation à 475°C", est d’une importance technique, car la décomposition modifie les propriétés mécaniques de ces alliages; dans ce cas présente, par la perte de ductilité et de résistance aux chocs. La tendance à la décomposition augmente avec la diminution de la température, ce qui limite la température de service supérieure à environ 300°C, limitant ainsi la durée de vie de ces alliages. Étant donné que la fragilisation peut provoquer une défaillance soudaine de ces alliages, cet aspect nuit à leur utilisation en tant que composants structurels dans les secteurs du transport et de l’énergie.

La décomposition des alliages Fe-Cr pose un défi aux techniques de caractérisation traditionnelles, car les variations de composition se produisent à l'échelle nanométrique. Par conséquent, la sonde atomique tomographique de pointe a été utilisée pour étudier ces variations de composition à l'échelle atomique en 3D. La modélisation atomistique corrélative a été utilisée pour améliorer davantage la compréhension du processus de décomposition dans ces alliages ; ce modèle était basé sur la théorie de la fonction de densité atomique. Pour émuler la décomposition améliorée du matériau, causée par la température et/ou une charge externe, la décomposition dans ce projet est stimulée par une température de service supérieure à la normale. Dont la nécessité de connaître la limite exacte de la lacune de miscibilité. Ainsi, la nécessité d'évaluer la limite supérieure de température de cette décomposition dans le système Fe-Cr est née de résultats non concluants des analyses de la littérature existant. Par conséquent, un four de haute précision en combinaison avec une sonde atomique tomographique a été utilisé pour étudier la décomposition et l’agglomération dans le système Fe-Cr d’une manière plus précise que jamais. En outre, d’explorer en détail l’emplacement de la limite de la lacune de miscibilité.

La décomposition de ces alliages au cours du vieillissement modifie les propriétés mécaniques. Ainsi, en raison de leur utilisation en tant que composants structurels, le comportement de décomposition dû au vieillissement a été étudié, ainsi que le vieillissement dû à la charge externe. Cette dernière situation se rencontre également dans des applications réelles pendant le service, émulées par le vieillissement dû à la pression en utilisant une simple

force de traction. Afin d'examiner en détail l'effet de la pression externe, l'orientation du grain par rapport à la direction de traction a été prise en compte lors d'un simple vieillissement thermique et lors de l'application d'une force de traction continue. Ainsi, l'orientation cristallographique et les niveaux de charge ont été pris en compte pour leur effet sur le processus de décomposition/dégradation.

Table of contents

List of tables

List of figures

Abbreviations

α'	Cr-rich ferrite
$\sigma_{ph.}$	Sigma phase
σ_y	Yield strength
AC	Allen-Cahn theory
ACF	Autocorrelation function
ADF	Atomic density function
ADT	Atomic density theory
AFT	Atomic fragment theory
AP	Atom probe
APT	Atom probe tomography
ASTM	American Society for Testing and Materials
bcc	Body centred cubic
bct	Body centred tetragonal
CALPHAD	Calculating Phase Diagram
CEF	Compound energy formalism
CH	Cahn-Hilliard theory
CHC	Cahn-Hilliard-Cook theory
CRIANN	Centre Régional Informatique et d'Applications Numériques de Normandie
CT	Computational Thermodynamics
DC	Direct current
DFT	Density functional theory
Duplex	Austenitic-Ferritic
EBSD	Electron backscatter diffraction
EDS	Energy dispersive spectroscopy
EDX	Energy-dispersive X-ray spectroscopy
EM	Electron microscopy
F	Free energy functional
fcc	Face centred cubic
FEM	Finite element method
FIB	Focused ion beam
FIM	Field ion microscopy
FM	Ferritic-Martensitic
FOV	Field of view
G	Gibbs free energy
GPM	Groupe de Physique des Matériaux
H	Enthalpy
hcp	Hexagonal close-packed
Hv	Vickers hardness
ICME	Integrated computational materials engineering
INSA	Institut National des Sciences Appliquées
IPF	Inverse pole figure
ISO	International Organization for Standardization
k	Position vector in reciprocal space
KMC	Kinetic Monte-Carlo
KTH	Royal Institute of Technology
LBM	Langer-BarOn-Miller theory
LEAP	Local electrode atom probe
LOM	Light optical microscope
LRO	Long-range ordering
LSW	Lifshitz-Sylozov-Wagner theory

MB	Mössbauer spectroscopy
MD	Molecular dynamics
MG	Miscibility gap
MOEM	Magnetic ordering energy of mixing
MRP	Mass resolution power
MTC	Mass to charge
NA	Not available
NG	Nucleation and growth
NN	Nearest neighbour
ODS	Oxide dispersed strengthen
PDE	Partial differential equation
PF	Phase field
PFC	Phase field crystal
Q	Activation energy kJ/mol
Qeff	Detection efficiency [%]
R	Universal gas constant, 8.314 J/kmol
RDF	Radial distribution function
RK	Redlich-Kister
S	Entropy
s(k)	Structure factor
SANS	Small-angle neutron scattering
SD	Spinodal decomposition
SEM	Scanning electron microscope
SOFC	Solid oxide fuel cell
SRO	Short-range ordering
SRO	Short-range ordering
T	Temperature
t	Time
TEM	Transmission electron microscopy
TEP	Thermo-electric power
TOF	Time of flight
x	Distance in direction x
X_i	Mole Fraction of element i
α	Fe-rich ferrite
σ	Statistical counting error

Chapter I

Introduction

1.1 Background

The development of a modern society in the 19th century can to a great extent be attributed to innovation in materials science. One important but often overlooked material during this time period is stainless steel. It is generally an Fe-Cr-Ni alloy with a vast variety of applications in both industry and consumer items. The development of steel to make them stainless is attributed to the addition of Cr, the addition of Ni increases ductility and toughness. The discovery of acid-resistant Cr-steel was first reported in 1821 by French mineralogist Berthier [1]. Thus, stainless steel is also known as inox steel, from the French inoxydable. However, the discovery of stainless steel was first recognized by scientist and industries from England, France and Germany around 1910. It was first in 1977 that stainless steel was clearly defined as an alloy with a minimum Cr content of 10.5 wt.% [2].

In relation to classic carbon steel stainless steels are known to be stronger, tougher and more durable. The spontaneous formation tightly adhered Cr-oxide layer provides a thin protective layer that inhibits further deterioration. This layer has great durability because of its self-repair mechanism. These are all attractive properties that make stainless steel a "sustainable" material with a low life-cycle cost. It is a material that can be recycled an infinite number of times without losing its properties. However, an underlying issue with the pricing of stainless steel is the volatility of the nickel (Ni) price. Forecasting steel prices is cumbersome yet important for corporations active in the diverse stainless-steel market. Thus, simpler steels with low Ni content, known as lean duplex stainless steel, has spiked new research interest in a wider market since they are generally cheaper and more price stable. However, the incentive of high Cr low Ni steel research is their application in automotive and energy industry. In part due to superior properties at elevated temperatures and ability to withstand corrosive environment.

These low Ni stainless steel grades are characteristically of ferritic microstructure and their main alloying element is Cr. Broadly speaking there are three important consumption areas of the ferritic stainless steels. The low alloyed Cr grades are greatly consumed by the automotive industry, intermediate Cr grades are common in household goods and higher Cr

grades are consumed by the nuclear energy industry. Even though the simpler ferritic grades historically have been considered a less premium product they have their obvious advantages.

In the automotive industry cutting fuel consumption is in part driving the technical development. The result over time is a better economy and lower emissions. Transportation industry in 2010 accounted for 14% of the global greenhouse gas emissions, 95% of those from petroleum-based fuel [3]. However, the industry is constantly evolving quickly adapting to new legislation. Thus, from a materials perspective the challenge is to reduce weight while maintaining structural integrity. The low Cr ferritic steels are often used in exhaust systems where there is a high demand for corrosion resistance and mechanical properties at high temperatures.

In the energy industry, ferritic stainless steel serves as a structural component in many of its applications. This is due to its great heat conductivity and ability to maintain mechanical properties and creep resistance at elevated temperatures. The ferritic grade can be found in e.g. cooling pipes and heat exchangers. Specific to the nuclear industry it is the resistance to irradiation-induced void swelling that is key. Therefore ferritic-martensitic (FM) Fe-Cr grades are frequently researched as materials for the next generation IV reactors by academia and industry. The potential applications of these materials are e.g. fuel assemblies and core support elements of primary system vessels. Thus, during service it is reasonable to assume different external loading, accompanied by intermediate operating temperatures in the range 300-600°C.

Thus, the understanding of the Fe-Cr base alloy system is important for the development of future stainless-steel grades. As an example, it is the main focus for oxide-dispersed-strengthen (ODS) FM grades which are not only interesting for gen IV reactors, but their potential in future fusion applications as well [4]. In addition solid oxide fuel cells (SOFC) [5], [6] is subjected to Fe-Cr research, which is essential for hydrogen-based automotive.

1.2 Materials design and phase transformations

Materials design is commonly used to describe materials science and engineering, i.e. the scientific discipline to engineer materials with specific properties. The approach to materials design has classically relied upon empirical evidence by trial and error, i.e. experimentation and analysis. However, nowadays this approach is often considered too time consuming and costly. Hence, computational materials design is an increasingly important genre within materials design. The purpose is to aid the experimental process and advance the development

of novel materials. In this spirit, strategic research initiatives are initiated inspired by e.g. the materials GENOME initiative [7].

The accumulated effect of alloying elements on material properties is the core of materials design. In stainless steel design, the influence of alloying elements can often be foreseen by the empiric Schaffer-DeLong diagram [8], [9]. It is in principle constructed by a Ni-equivalence that favours the formation of Austenite and a Cr-equivalence that favours the formation of ferrite. This allows for elemental design of the microstructure that have a great influence on the macroscopic properties.

Stainless steel grades are classified by their microstructure: Ferritic, Martensitic, Austenitic and Duplex (Austenitic-Ferritic). Metals are crystalline alloys, thus these names relate to their characteristic unit cells that describe the atomic regularity in its nearest neighbour form. The most common unit cells in steels are body centred cubic (bcc), body central tetragonal (bct), face centred cubic (fcc) and hexagonal close-packed (hcp) systems. These cells are situated in repeating or periodic arrays over multiple unit cells creating grains and grain boundaries, which construct their microstructure.

Within grains a periodic array over multiple unit cells may exhibit a periodicity or pattern, forming long-range ordering (LRO). Naturally, short-range ordering (SRO) is then limited to a finite number of unit cells/neighbours, in this context SRO is arbitrarily set to up to the 5^{th} nearest neighbour.

There are different methods of modelling material properties dependent on the time and length scale of the model. Indeed, there are corresponding experimental techniques suited for different purposes and length scales, since different phenomena become observable at different length scales. Hence, hierarchic engineering such as integrated computational materials engineering (ICME) is common practice within industry and research. In this thesis, the focus is on nanoscale connected to mesoscale through calculation of phase diagrams (CALPHAD).

Ab-initio or first principle calculations based on density function theory (DFT) is primarily used for the electronic structure with length scales ~1Å and time scale ~1psec. *Ab-initio* and molecular dynamics (MD) simulations are concerned with atomic processes. The kinetic Monte Carlo (KMC) simulation is a well-established method utilizing DFT input to bridge the gap between length scale of ~1Å to ≥10nm and diffusion time scale. At similar length scales as KMC we find the phase-field crystal (PFC) method and atomic density function (ADF) theory. With ADF and PFC, which has been used within this thesis, it is possible to

model nanostructure evolution at the diffusion timescale, i.e. from a fraction of a second to years. Classical modelling of the microstructure is made by phase-field (PF) methods often coupled with CALPHAD. Then at the macroscopic scale finite element methods (FEM) are used. The vision for ICME in this work would be to couple *ab-initio* – PFC (ADF) – PF – FEM to e.g. bridge the gap between the atomic structure and the macroscopic behaviour of a polycrystalline material.

Phase transformations in metallic materials are often diffusion dependent processes aimed to alter the mechanical properties. In this thesis, we are mainly concerned with diffusion transformation that involves changes in phase composition and precipitation of secondary phases. Recrystallization and grain growth are also diffusion transformations of interest where phases and their composition are considered as constants. Stress-induced twinning of ferrite in duplex steel is an example of a diffusionless transformation that might be seen in the fracture surface of a sample. However, martensite transformation is the more well-known diffusionless transformation in steels.

1.3 Research motive

For alloys with a miscibility gap in their phase diagram alloying elements tend to de-mix or decompose. The driving force for decomposition increases with decreasing temperature, ultimately this leads to phase separation. There are two mechanisms behind phase separation namely: spinodal decomposition and, nucleation and growth. This Fe-Cr miscibility gap is an issue for stainless steels that contain the ferrite phase. The result of decomposition is an increased hardness and loss of impact toughness, in the end this limit service lifetime and restrict the operating window. Even though this is a well-known phenomenon that has been studied for more than half a century [10], no real solution to prevent this issue has been presented. Today the approach is to try and avoid the phenomenon by restricting the service temperature of these alloys. This de-mixing phenomenon is also known as the "475°C embrittlement". Hence, the upper service temperatures of these alloys are generally restricted to around 300°C. The limited knowledge of this phenomenon is partially due to the fine-scaled nanostructure in these alloys, posing a challenge for traditional metallographic characterization techniques. The advent of atom probe tomography has opened up for atomic-scale characterization of the nanostructure, leading to new insight into the underlying mechanism [11], [12]. Thus, investigating the upper limits of the miscibility gap is key for the gradient energy term and driving force during modelling but also for the design of the initial structure to prolong material lifetime [13], [14]. Hence, the purpose of Chapter IV is to provide a more

accurate description of the miscibility gap and Cr-Cr clustering in its proximity than before. Since the target of this work is to investigate the effect of a mechanical load on phase separation, i.e. accelerated ageing in the upper part of the miscibility gap is a necessity. Because Fe-Cr based alloys are often found in structural applications or welded materials they are often subjected to a mechanical load in their real-life applications. This mechanical load is known to have an effect on phase separation [15], [16]. Hence, the purpose of Chapter V is to better understand the influence of a mechanical load on a binary Fe-35Cr alloy, considering different grain orientations. Thus, the research questions that are sought for are,

- How should the limits of the miscibility gap and its phase separation mechanisms be defined for Fe-Cr?
- How does grain orientation influence phase separation during ageing under mechanical load?

To further aid the understanding of the experimental investigation modelling is applied. A reason for the continuous development of the field is due to the complexity to accurately model phase separation in this system. Although it might seem straightforward at first the treatment of magnetism and the complex sigma phase cause large discrepancies in the description of the system. Thus, even though it is an easy system to model, the accuracy of the model connecting *ab-initio* to microscopic properties is still cumbersome. The early stages of phase separation will here be modelled using the phase field crystal (PFC) approach. PFC has emerged as an attractive way of tackling this class of problems where atomic and continuum scales are tightly coupled [17]. Later, the link to the decomposition at mesoscale, kinetics can be made through phase-field (PF) modelling. A further complicating issue which is the culmination of this work is that components manufactured from these steels are used in load-bearing applications, thus during service, these alloys will be exposed to thermal and mechanical load. Therefore, mechanical load level and crystallographic orientation dependency on spinodal decomposition is investigated by atom probe and PFC in this work. Moreover, in dual-phase systems such as duplex steels residual stress is a potential issue. Hence, the influence of compressive and shear stresses is modelled by PFC.

Chapter II

Phase separation in Fe-Cr alloys

2.1 Introduction to phase separation

Phase separation in stainless steel due to Fe-Cr de-mixing can cause significant degradation of mechanical properties [18]–[20]. This is an issue for all Fe-Cr based alloys with microstructures that contains the bcc (ferrite)/bct (martensite) phase. In spite of the vast possibilities to engineer mechanical properties, Fe-Cr is the base that gives stainless steel their characteristic properties [21]. Thus, phase separation is of importance for technical and theoretical understanding of many industrial materials. The high Cr steel grades are of particular interest as structural materials in the nuclear industry [22]–[25]. Hence, long-term experimental and thermodynamic understanding of Fe-Cr de-mixing is an important research topic. However, due to the limited amount of time in this work, the ageing conditions were focused on relatively short terms at high temperature. The Fe-Cr phase separation phenomenon has been studied since the 1950s, yet today the understanding is not conclusive.

The accumulated effect of alloying elements and thermal history defines the microstructure and thus the grades of stainless steel. The grades that may be subjected to phase separation are ferritic, duplex and martensitic as they all contain bcc/bct phases. These are grades with a vast variety of applications as microstructures define their innate mechanical properties. There are other secondary phases and precipitates that may form dependent on the microstructure, heat treatments and additions of minor alloying elements. These phases and precipitates also affect the mechanical properties of the materials. For example, sigma phase (σ) with its complex tetragonal unit cell comprised of 30 atoms [26], σ exist in a very narrow composition range $Fe_{1-x}Cr_x$ where $0.46 < x < 0.50$ and temperature range 523-727°C, its precipitates cause severe embrittlement of ferrite. The χ-phase is an intermetallic bcc phase composed of Fe, Cr and Mo, it exist in bcc/fcc stainless steel [27], while σ-phase is a binary phase, χ exists in the Fe-Cr-Mo, Fe-Cr-Ni-Mo and Fe-Cr-Ni-Ti systems. Since C can dissolve in χ it has also been considered a $M_{18}C$ carbide in the past [28], it has a negative effect on corrosion resistance in duplex steels. In addition, phases that may form in stainless steels are π-phase which is a form of nitrides in austenite and *G*-phase an intermetallic silicide that can be seen in martensite and ferrite.

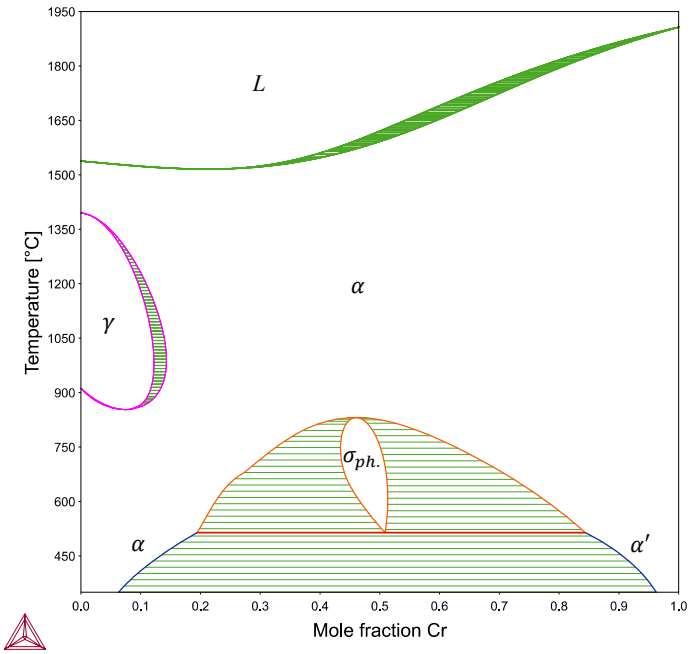

Figure 2-1. The Fe-Cr phase diagram calculated in ThermoCalc 2016a with the TCFE8 database.

The thermodynamic equilibrium phase diagram of Fe-Cr given in Figure 2-1, is calculated by the latest commercially available description of the Fe-Cr system by the ThermoCalc database TCFE8. The system includes the austenite (fcc) loop, at low Cr content (less than 14wt.%-Cr) in the range 850-1395°C.

The Fe-Cr miscibility gap consists of the ferrite (bcc) phase referred to α when it is Fe-rich and α' when it is on the Cr - rich side. In principle, the miscibility gap is a region within the phase diagram where Fe and Cr are not completely miscible. Thus, the ferritic structure consists of two phases with the only difference being the composition. The reason why it is favourable to study phase separation in the Fe-Cr system is apart from its width and convenient temperature range is the small lattice difference between α and α'. This small difference means that coherency strain caused by precipitation of α' can be neglected. In systems with larger lattice differences between its constituents, there is a distinction between the chemical and coherent miscibility gap. Therefore, the added strain between the phase boundaries shifts the limits of the miscibility gap. In the Fe-Cr phase diagram both miscibility gaps are considered equivalent due to the small difference.

The intermetallic sigma phase with a unit cell of 30 atoms in a complex tetragonal structure (space group $P4_2/mnm$) is also part of the miscibility gap (MG). Sigma phase is thermodynamically stable down to 515°C. However, the formation of sigma is very sluggish, in a recent review it was found that the incubation time to form at 570°C was 450h [26]. In

addition, the formation of sigma phase is highly dependent on experimental conditions and the purity of the alloy. However, it is possible to study the metastable miscibility gap in its early stages when σ-phase is suppressed.

2.2 Solid-state phase separation

In solid-state phase transformation, it is generally accepted that precipitation of a secondary phase can occur through either nucleation and growth (NG) or spinodal decomposition (SD). There is a classic distinction between homogeneous and heterogeneous NG in nucleation theory. Homogeneous NG appears at random in a homogenous solution and requires higher activation energy than heterogeneous precipitation. More commonly seen in the experiment is that heterogeneous nucleation occurs at grain boundaries, impurities, surfaces and dislocation lines. In heterogeneous precipitation, the process of nucleation benefits from the reduced surface energy.

The α' formation is a second-order phase transition that occurs within the miscibility gap that is highly interesting for alloys of the Fe-Cr system. It is a spontaneous compositional phase separation that results in two separate phases with the same crystal structure. This transition is often written as $\alpha \rightarrow \alpha + \alpha'$, and it is driven by minimization of the free energy of the system. NG and SD are both mechanisms present in the miscibility gap, the inherent difference is that SD is often described to proceed without an activation energy barrier.

This secondary phase separation is not unique to the Fe-Cr system similarly phase separation through SD/NG can be found in other alloys with miscibility gaps in their phase diagram e.g. Al-Zn [29], Al-Ag [30], Au-Pt [31], Cu-Sn [32] and Au-Ni [33]. The origin of the theory of phase separation comes from Gibbs theory of unstable phases which Hillert developed in his thesis [34], [35]. This theory was later further developed and generalized into 3D by Cahn and Hillert and then Cahn again [36]–[38]. Later on, his theory was again refined to take into account fluctuations and non-linear effects of the thermodynamic factor [39].

The theory of phase separation, namely spinodal decomposition and nucleation and growth will be reviewed more in detail in the following section 2.3 and 2.4. The review is generally formulated as a binary A-B system but restricted first-order terms with the Fe-Cr system kept in mind. Thus, neglected terms and assumptions made regarding the Fe-Cr system will be highlighted.

2.3 Nucleation and growth

Homogeneous nucleation and growth, in a solid metallic solution, is essentially phase transformations by redistribution of atoms. In essence, it is a diffusion-controlled phenomenon that facilitates secondary phase precipitation in a supersaturated matrix. In a physical system, thermal fluctuation is always present even at equilibrium. However, if large enough, these fluctuations enable nucleation. In statistical thermodynamics, the probability (p) of a thermal fluctuation is given by the Boltzmann relation,

$$p = N_0 \exp\left(-\frac{\Delta G}{k_B T}\right) \tag{2.1}$$

Where k_B is Boltzmann's constant, N_0 is a normalizing constant and ΔG is the free energy increase of the whole system due to this fluctuation. Thus, ΔG of a stable system increases with the size of the fluctuation, and according to equation (2.1) there is a greater probability of finding smaller fluctuations. If fluctuation sizes in a metastable system increase, ΔG will grow and reach a maximum at a certain point. Then, if this ΔG maximum is exceeded, the free energy of the system tends to decrease with increasing fluctuations, which at this point will be regarded as precipitates rather than fluctuations. This is how the critical energy of nucleation is defined.

As an example, consider the generic A-B system containing a miscibility gap, as in Figure 2-2 a). If an alloy with composition C_0 is quenched and isothermally aged within the metastable part of the MG, solute diffusion will proceed. Eventually micro-clusters of solute atoms of element i are formed. There are two parts to the contribution of energy change of the system, one dynamic and one static part. The static part is given by the change of Helmholtz free energy due to the size and distribution of clusters. The dynamic part is given by the kinetics of the decomposition of the solid solution that now is represented by a distribution of non-interactive micro-clusters. Thus, the dynamic part can be viewed as the nucleation rate. These clusters or solute fluctuations can be treated as droplets of equilibrium phase's α/β if their interface is sharp. As a consequence of the minimization of surface energy, these macroscopic droplets can be described by spheres of radius (r), so that $(4\pi/3)r^3 = i\Omega_\beta$ where Ω_β is the atomic volume of the crystal. So that, in a bcc matrix with 8 nearest neighbours $\Omega_\beta = V_{at}/8$ where V_{at} is the atomic volume of the unit cell.

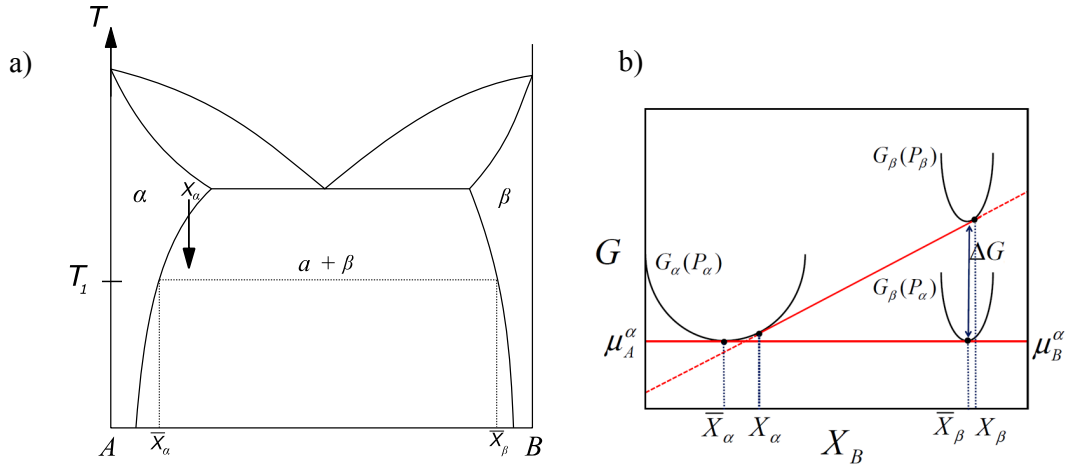

Figure 2-2. a) Precipitation reaction in a supersaturated matrix in a fictive A-B system, b) the free energy change of the system in response to the precipitation [40].

Thus, the precipitation reaction: $\alpha' \rightarrow \alpha + \beta$ is how to approach equilibrium, where α' is the B supersaturated phase after quenching at temperature T_1. Thermal diffusion facilitates formation of the β - phase nucleus, then the β - precipitate grows by depleting the α'- matrix of B atoms. The ΔG due to nucleation is as illustrated in Figure 2-2 b) a function of composition X and pressure P (mechanical equilibrium), thus the local equilibrium is defined by $\mu_i^\alpha\left(\overline{X}_j^\alpha, P^\alpha\right) = \mu_i^\beta\left(\overline{X}_j^\beta, P^\beta\right)$ [40]. The free energy change of the system as a result of the precipitation of a spherical precipitate with radius r is then given by,

$$\Delta G(r) = \left(\Delta g_{chem} + \Delta g_{el}\right)\frac{4\pi}{3}r^3 + 4\pi r^2\gamma_{\alpha\alpha'} \qquad (2.2)$$

Where Δg_{chem} is the chemical energy, Δg_{el} is the elastic coherency energy due to lattice mismatch and A-B atom size differences. $\gamma_{\alpha\alpha'}$ is the surface energy of the precipitate, which here is assumed to be a sphere in accordance with the minimization of free energy. There are two fundamental contributions to the energy in this expression. The first term is a volumetric term with a negative contribution to $\Delta G(r)$ that minimize the energy of the system, in favour of nucleation. The second term, the surface energy contribution is positive. Thus, the creation of an interface retards the nucleation process.

Through the derivative of equation (2.2) with respect to the radius ($\partial\Delta G(r)/\partial r = 0$) it is possible to derive the critical radius (r^*) of a nucleus and its corresponding free energy (ΔG^*) accordingly,

$$r^* = \frac{-2\gamma_{\alpha\alpha'}}{\left(\Delta f_{chem} + \Delta f_{el}\right)} \tag{2.3}$$

$$\Delta G^* = \frac{16\pi}{3} \frac{\gamma_{\alpha\alpha'}^3}{\left(\Delta f_{chem} + \Delta f_{el}\right)^2} \tag{2.4}$$

As there are thermal fluctuations present in all A-B alloy (also at equilibrium), AA and BB atoms tend to form small clusters. This is of concern, especially in the Fe-Cr case as above 10at.%-Cr, Cr has a positive short-range order factor. Hence, Cr is known to cluster even outside of the MG. This may lead to experimental difficulties to discriminate between a large cluster and a nucleus. However, by utilizing the relationship between the precipitate of radius r and atoms i in that volume it is possible to calculate the critical number of atoms in a cluster i^*.

In our case, it is convenient to consider homogeneous nucleation through the classical nucleation theory [41], [42]. Since we are dealing with a single-phase, high purity alloy with very large grain size. Thus, nucleation is a stochastic process which's rate again is treated as a diffusion phenomenon. The free energy of the α' equilibrium reaction, normalized by the molar volume of the precipitate $\Delta G_m^{\alpha\to\alpha'} / V_m^{\alpha'}$, is used instead of the chemical and elastic energy in equation (2.3) and (2.4) to calculate the critical radius and energy. In this way, it is possible to utilize the CALPHAD method to estimate the critical number of atoms in an equilibrium nucleus, as in Table 2-1, where γ is the surface energy taken from *ab-initio* calculations [43].

Table 2-1. Critical number of atoms in a nucleus for the α/α' equilibrium by CALPHAD methods.

Temp. [°C]	**Pressure [atm]**	X_0^{Cr}	X_0^{Fe}	$V_m^{\alpha'}$ **[m³/mole]**	$\Delta G_m^{\alpha\to\alpha'}$ **[J/mole]**	$f_{V_m^{\alpha'}}$	γ [43] **[J/m²]**	r^* **[m]**	**Crit. Nr. of atoms**
500	1	0.35	0.65	7.306e-6	-3.70e4	0.25	2.48	3.93e-9	88
525	1	0.35	0.65	7.274e-6	-2.65e4	0.235	2.48	3.64e-9	70

During growth, it is assumed that just after nucleation the matrix phase is still supersaturated while the nucleus has close to equilibrium composition. This creates a concentration gradient, the difference in chemical potential gives rise to a driving force for solute diffusion. This diffusion depletes the surrounding matrix, hence at the matrix/nucleus interface, local equilibrium is generally assumed to hold, see Figure 2-3.

Thus, the growth of α' is limited by either one of the two following mechanisms: diffusion of solute to the interface or diffusion of solutes through the interface. The slower of the two would control the rate of growth. In the case of α' growth in Fe-Cr the interface is mobile due to good α/α' coherency, however, interfacial reactions are fast in comparison [44],

[45], thus it can be assumed that bulk diffusion is the rate-controlling mechanism. Thus, the concentration at the interface $C(r)$ is then given by the Gibbs-Thomson equation,

$$C(r) = C_e \exp\left(\frac{2\gamma_{\alpha'\alpha} V_{at}}{k_B R_B T}\right) \tag{2.5}$$

Where C_e is the local equilibrium concentration, R_B is the gas constant and k_B is the Boltzmann constant, an illustration of this growth phenomenon is given in Figure 2-3.

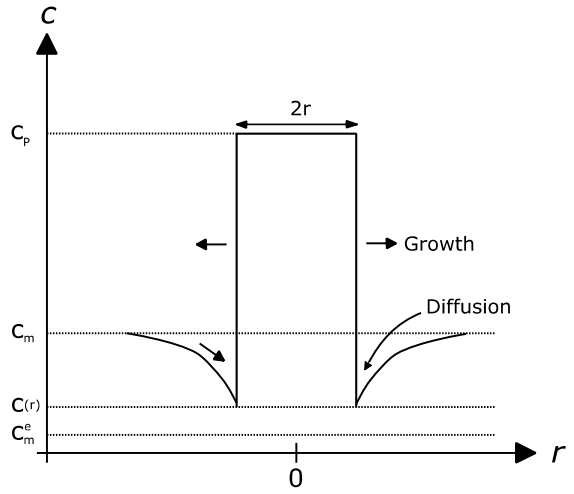

Figure 2-3. Schematics of nucleus growth from a supersaturated matrix, C_p: composition of precipitate, C_m: composition of matrix, $C(r)$ composition at radius r and C_m^e matrix composition at equilibrium.

The flux of solute atoms between matrix and the precipitate is given by Fick's first law,

$$\bar{J} = -D\left(\frac{\partial C(r)}{\partial r}\right)\bar{u}_r \tag{2.6}$$

Where D is the diffusion coefficient, $C(r)$ is concentration expressed by the radial variable r and $\bar{u}_r$ is the radial unit vector.

To obtain the expression for infinitesimal volume variations of the sphere one must introduce the mass balance condition at the surface of the precipitate which gives,

$$\frac{\partial}{\partial r}\left(\frac{4\pi}{3}R^3\right) = -\bar{J}\cdot\bar{u}_r 4\pi R^2 \quad \rightarrow \quad \frac{\partial R}{\partial t} = D\left(\frac{\partial C(r)}{\partial r}\right) \tag{2.7}$$

To obtain the time dependency it is necessary to solve Fick's second law, for the concentration $C(r)$ from R to $+\infty$. In the supersaturated matrix where $(C_m - C_m^e)$ is very small, it is possible

to assume that $C(r)$ is time-independent. Assuming quasi-stationary state, it is sufficient to solve $\Delta C(r) = 0$, where Δ is the Laplacian. So that the concentration gradient in the vicinity of the surface of the precipitate is equal to,

$$\frac{\partial R}{\partial t} = \frac{1}{R}\frac{(C_m - C(R))}{(C_p - C(R))} \tag{2.8}$$

Where C_m is the matrix composition which can be approximated as the initial composition C_0. C_p is the equilibrium concentration of the precipitate and $C(R)$ the concentration in the depleted zone, which can be approximated as the matrix composition at the end of the growth stage C_m^e. Thus, the integration of the time derivative of this expression gives,

$$R = \left(2\frac{C_0 - C_m^e}{C_p - C_m^e} Dt \right)^{\frac{1}{2}} \tag{2.9}$$

This expression assumes growth of spherical precipitates, however, in reality, precipitates may grow in different shapes and sizes. It is also assumed that the diffusion coefficient is independent of the concentration and that the precipitates has a single size distribution. In addition, it is assumed that the particles grow without the influence of surrounding particles, diffusion fields do not overlap, and hence the concentration far away from precipitate is equal to the initial concentration (i.e. C_0). The NG process is near its completion when the equilibrium volume fraction is reached, then larger particles start to grow at the expense of smaller ones, this is characteristic of the next coarsening stage.

The simple expression of the growth of the mean radius, equation (2.9), provides a time dependency of $t^{1/2}$. This time exponent, is, as we shall see later different from the one obtained in the case of spinodal decomposition, which will make it possible to distinguish the kinetic rate between both mechanisms from an experimental point of view.

2.3.1 Coarsening: Lifshitz-Sylozov-Wagner theory

At the later stages of phase transformation (i.e. when equilibrium volume fraction is reached) the evolution of the system is characterized by Oswald rippling or coarsening [46]. It is a spontaneous process driven by the reduction of surface energy. It is because the surface energy of a precipitate is higher than its internal energy. Thus, small precipitates tend to dissolve and redeposit into larger particles that coarsen the structure to decrease the surface area in the system. It is the elastic energy that ultimately limits of coarsening if it could proceed to a single

spherical particle the lattice mismatch between precipitate and matrix would be too large so that it would cause the sphere to split into smaller precipitates again.

Key improvements to the theory of later stages of coarsening was made by Lifshitz, Sylozov and Wagner [40], [41], hence LSW theory. LSW theory is a way of treating an ensemble of dilute coarsening particles and make quantitative long-term predictions without resulting to numerical solutions. In a dispersed system of particles with various sizes, competitive growth will take place. Some particles grow at the expense of others, this is an effect of the contribution of ΔG to the system by the individual precipitates. Since ΔG of the precipitation reaction differ due to composition and pressure, as a result, precipitates nucleate with different sizes in the matrix.

The radial growth of a precipitate originates from the concentration gradient at its surface. This concentration at the surface can thus be predicted by the Gibbs-Thomson effect. In general, the concentration at the interface of a large particle is lower than that of a small particle. A disperse particle system with a certain particle solubility will be thermodynamically unstable due to a large interface area. Thus the equilibrium concentration at the surface (C_r) of a spherical precipitate vary dependent on size, as given by the Gibbs-Thomson equation [47], [48],

$$C_r = C_e \exp\left(\frac{2\gamma_{\alpha\alpha'}\Omega_\beta}{R_B T}\cdot\frac{1}{r}\right) \tag{2.10}$$

Where C_e is the solute concentration of the matrix in equilibrium (i.e. when $r = \infty$) and R_B is the universal gas constant. The concentration difference between C_r and C_e induces a diffuse flux from smaller particles to larger ones. Over time, the mean radius of the particles in the system will increase as the number of particle decreases, again driven by minimization of free energy of the whole system. This distinctiveness is known as coalescence.

Diffusion is then rate-controlling in the growth of coherent stable precipitation. An analytical solution of the diffusion flux across the interface: $j = D\nabla^2 c(\mathrm{r,t})$ gives a parabolic growth law for both spherical and plate-like precipitates [49]. For small supersaturations, i.e. $C - C_e = \Delta,\ \Delta << 1$, the interactions between precipitates may be ignored since their dimensions are small in comparison to the distance between them. Thus, an isolated spherical particle with radius r will grow at a rate given by,

$$\frac{\partial r}{\partial t} = \frac{D}{r}\left(\Delta - \frac{\alpha}{r}\right) \tag{2.11}$$

Where $\alpha = (2\gamma_{\alpha\alpha'}/kT)V_{at}C_e$ is a parameter that includes the atomic volume of the solute. Analysis of equation (2.11) reveals that for every supersaturation Δ, there is a critical radius $r_e = \alpha/\Delta$ that is in equilibrium with the surroundings. Thus, if $r > r_e$ the precipitate will continue to grow if $r < r_e$ the precipitate will dissolve.

Coalescence starts during the growth period of the precipitation and in some cases during nucleation, then known as transient coalescence. However, it is during its later stages that coalescence becomes the predominant mechanism for the morphological evolution of the system.

The coarsening of dispersed secondary phase particles is a classic yet complex multi-precipitate diffusion problem. LSW theory is a simplified approach to the problem based on the classic coalescence theory, i.e. Ostwald ripening. The main assumption made in LSW is that the distance between particles is infinitely large in comparison with their radius, the volume fraction of the dispersed phase is infinitesimally small and solute atoms diffuse to the particles under steady-state conditions, i.e. no interaction between particles and an infinitely dilute system. Thus, the morphology of the dispersed system is characterized in terms of particle radius distribution $f(r,t)$, thus the rate change of f is given by a continuity equation on the form,

$$\frac{\partial f}{\partial t} + \frac{\partial\left(f \cdot \dot{r}\right)}{\partial r} = j \tag{2.12}$$

Where $j = 0$ in LSW which means that processes such as nucleation and particle coalescence that introduce particles are negligible. The flux of particles in LSW is determined by $\dot{r}(r)$, i.e. the examination of the dissolution of growth of a particle. Thus, based on equation (2.12) in combination with (2.11) the time evolution of the mean particle radius $\overline{r}(t)$ and the particle number density $N_v(t)$ are derived, the solution is based on the following assumptions

- The volume fraction of the precipitate is close to zero, $f_p = (4\pi/3)\overline{R}^3 N_v$, i.e. particle-particle diffusion is neglected only particle-matrix interaction is considered in a dilute system.
- $f_p = const.$, means that the process is close to completion, $\Delta C \approx 0$. This inherently defines the LSW theory in the later stages of coalescence.

- The radii of the particle is insufficiently large to use the linearized version of the Gibbs-Thomson equation, hence equation (2.10) is used when $2\gamma_{\alpha\alpha'}V_{at}/R_BkT << 1$.
- The particles are always superimposed as spheres.

With these assumptions, asymptotic analysis of the temporal evolution of the system undergoing Ostwald ripening reveals the following power laws,

$$\overline{r}^3 - \overline{r}_0^3 = \frac{8DV_{\alpha'}\gamma_{\alpha\alpha'}C_\alpha^e}{9\left(C_{\alpha'}^e - C_\alpha^e\right)R_BT}t \equiv K^{LSW}t \tag{2.13}$$

$$N_v^{-1} - N_{v0}^{-1} = \frac{4\pi}{3f_p}K^{LSW}t \tag{2.14}$$

Thus, these equations are the so-called modified LSW equation showing the average radius $\overline{r}$ and number particles N_v following a power-law behaviour with time exponent $t^{1/3}$.

2.3.2 Non-classical nucleation and growth

In classical nucleation theory, it is assumed that the nucleus is formed with close to equilibrium composition and that the precipitate can be approximated by a constant composition with a sharp interface. In the late 1950s, Cahn and Hilliard developed the theory of isotropic systems with non-uniform composition or densities, also known here as the non-classical nucleation theory [37], [50], [51]. In non-classical nucleation theory, it is assumed that the solution is heterogeneous in that sense that it contains concentration fluctuations with diffuse interfaces and the composition of the precipitates has distinct deviations from the equilibrium composition. Thus, the critical nucleus/precipitate is classified in terms of its spatial extension, i.e. the composition fluctuation and size e.g. radius. In addition, the composition of the precipitate and its interfacial energy can no longer be treated as independent variables.

To formulate the free energy of the system non-uniform composition one discretizes the system into small volumetric elements ∂V. The free energy of the homogenous reference alloy (G_0) with composition X_0 is thus given by volume integration: $G_0 = \int_V f(X_0)dV$, where $f(X_0)$ is the free energy per unit volume. The heterogeneous alloy contains diffuse composition gradients of non-equilibrium compositions, the gradient energy term is proportional to $(\nabla X)^2$. Hence the free energy of a heterogeneous alloy with volume V can be written as,

$$G = N_V\int_V\left[f(X) + \kappa(\nabla X)^2\right]\partial V \tag{2.15}$$

Where N_v is the number of molecules/precipitates per unit volume. X is the average composition of volume segment ∂V, κ is the proportionality coefficient associated with the local composition variation ∇X of the gradient.

The treatment of the free energy of a precipitate as in equation (2.15) has many similarities with the treatment of spinodal decomposition. When there is a significant difference in lattice parameter (η) of the precipitate and matrix it is necessary to include the elastic energy contribution due to coherency strain. It is written as: $f_{el}(X) = \eta^2 E'(X - X_0)^2$, where $E' = E/(1-\upsilon)$, E is the Young's modulus and υ is the Poisson's ratio. Thus, the free energy change of a homogeneous solid due to a critical composition fluctuation is written as,

$$\Delta G = \int_V \left[f(X) - f(X_0) + \kappa(\nabla X)^2 + f_{el}(X) \right] dV \tag{2.16}$$

The significance of this expression is the gradient energy term, which as the surface energy in the classical nucleation theory imposes the formation of a critical fluctuation. However, when the difference in composition between the fluctuation and matrix is large enough the change of free energy is dominated by the volumetric contribution.

The activation energy of the nucleation process is defined by the functional dependency, equation (2.15), of composition on position that yields extreme values, i.e. the shape of the fluctuation. The work done by such a system to form a critical nucleus is given by the change of free energy ΔG from the formation of a critical nucleus. It can be assumed that for an isotropic system with cubic symmetry the critical nucleus will be of spherical shape. If $f(X)$ is known, it is possible to evaluate the critical radius of a nuclei at an extremal of equation (2.16) that minimizes the free energy of the system. Thus given of alloy X it is possible to calculate the spatial composition variation of the critical nucleus by integrating,

$$2\kappa \frac{d^2X}{dr^2} + \frac{4\kappa}{r}\frac{dX}{dr} + \frac{d\kappa}{dX}\left(\frac{dX}{dr}\right)^2 = \frac{d\Delta f}{dX} \tag{2.17}$$

Equation (2.17) can be used to provide some general properties of the nucleus. The equation is used to solve for the composition variation $C(r)$ that is necessary to cause a critical ΔG in order to activate nucleation. To be able to obtain physically acceptable answers the following boundary conditions must be satisfied,

$$\begin{gathered} dX/dr = 0, \quad \text{at} \quad r = 0 \quad \text{and} \quad r = \infty \\ \mathrm{X} = X_0 \quad \text{at} \quad r = \infty \end{gathered} \tag{2.18}$$

Thus, with these conditions Δf of the material in the centre of the nucleus (X_n) not only has to be negative but it must be stable with respect to the matrix phase, i.e. $\Delta f(r=0)<0$. The specific energy associated with the interface (σ) can be expressed in terms of the composition variation across that interface $\kappa(\nabla X)^2 = \Delta f$. The expression of the mean radius ($\bar{r}$) for the precipitate can be used in combination with the free energy change of the material in the precipitate and its interfacial energy to form the expression,

$$\bar{r} = -2\gamma / \Delta f(r=0) \tag{2.19}$$

From this expression, it is evident that as a metastable alloy X approaches the stable matrix phase composition (X_0) if Δf approaches 0, thus given by the boundary condition the mean radius goes towards infinity [52].

2.4 Spinodal decomposition

Spinodal decomposition (SD) is an isothermal spontaneous phase transformation that occurs through diffusion that give rise to composition differences, in contrast to structural phase transformation which are highly temperature-dependent in steels (i.e. diffusion less changes in lattice structure). This SD phenomenon can be observed in liquid as well as solid-state phase transformations when the components in the system are not completely miscible. Characteristically this phase transformation proceeds without activation energy, thus it is a continuous temporal evolution. SD is enabled by an unstable regime in the centre of the miscibility gap (MG), viz. higher concentration regions is thermodynamically favoured. Thus, within the MG a phenomenon referred to as uphill diffusion occur where composition differences grow from an initially homogeneous state.

A miscibility gap, as sketched in Figure 2-4 a), contains two phase separation regions, namely nucleation and growth and the SD regime. These are mechanisms by which phase separation occur, and they are dependent on the relative free energy change of the system. Figure 2-4 b) illustrates the isothermal molar Gibbs free energy curve plotted through the MG. It is defined by a positive heat of mixing between the equilibrium phases, at the energy minima, which limits the MG. There are two inflexion points at which $\partial^2 G/\partial X^2 = 0$ that discriminates between the phase separation mechanisms, these are called the spinodal nodes. Within the metastable part of the MG when $\partial^2 G/\partial X^2 > 0$ phase separation occurs through NG. The system is unstable when $\partial^2 G/\partial X^2 < 0$, thus the phase separation occurs through SD. A feature of MG's is that the driving force for phase separation increases with the quench depth for any

given alloy within the MG. Hence, following the temperature dependence of the free energy curves in Figure 2-4 the thermodynamic net benefit of acquiring the equilibrium configuration decrease. Naturally, kinetic mobility benefits from an increased temperature, thus the rate of phase transformation generally benefit from increased temperature.

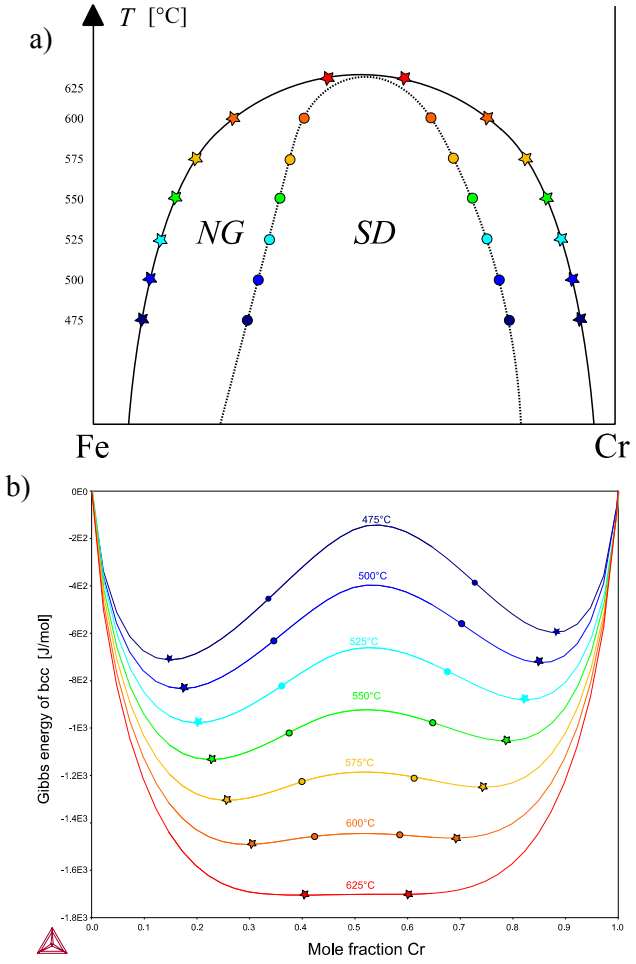

Figure 2-4. a) An illustration of the metastable miscibility gap with the metastable NG region and unstable SD region highlighted, b) isothermal Gibbs molar free energy curves of the binary Fe-Cr system calculated by ThermoCalc with the common tangent ✦ (i.e. MG) and spinodal node ● indicated.

Figure 2-5 a) illustrates the free energy curves at a fixed temperature in a binary system with an MG. It is a classic illustration of how the energy curve looks in e.g. the Fe-Cr system among others. It has already been established that the equilibrium configuration of this system is defined by the minimization of free energy, and therefore the equilibrium composition of the phases α and α' is X_α and $X'_{\alpha'}$ respectively.

Given an alloy with an initial concentration X_0 as in Figure 2-5 b) one can see that the G_m curve is concave at this point between X_α and X'_α . Thus, it would imply that any composition fluctuation here would increase the free energy of the system. Hence, the alloy remains in a metastable state, unless the composition fluctuations are great enough (i.e. close to the equilibrium X_α and $X'_{\alpha'}$) to decrease the energy of the system. This is how the metastable NG regime is classically defined.

For the X_0 alloy Figure 2-5 c) the G_m curve is convex between X'_α and the peak point indicated by ★. Thus, any composition fluctuations would decrease the energy of the system. Hence, it is an unstable regime that favours the growth of composition fluctuations and therefore will push the system towards phase separation. The amplitudes of the composition fluctuations grow continuously until the equilibrium compositions are reached. This is the unstable spinodal regime.

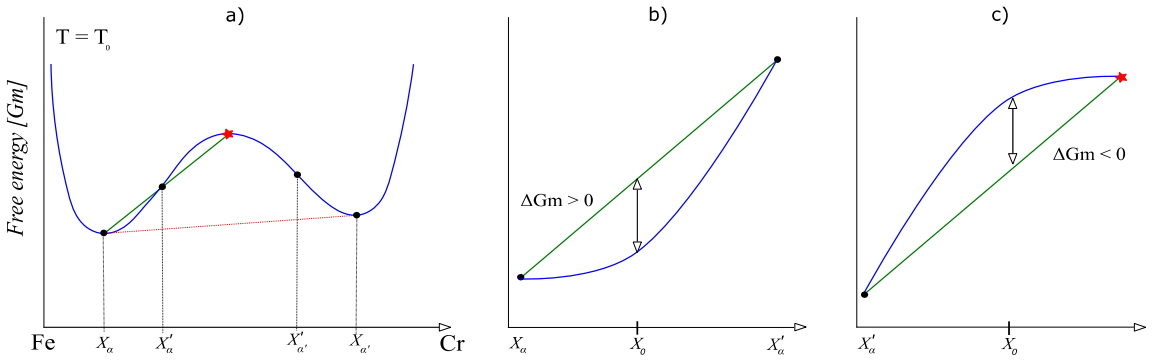

Figure 2-5. a) Discriminating between SD/NG by the contribution of free energy to the system, b) $\Delta G_m > 0$ for phase transformation to proceed in the metastable NG regime, c) $\Delta G_m < 0$ for any phase transformation in the unstable SD regime.

The limit of phase separation or equilibrium configuration is defined by the common tangent between α and α' where the chemical potential gradient will be zero and de-mixing is suppressed.

Consider a homogenous A - B alloy with the composition X_0, the Gibbs free energy of that alloy is then given by G_0 . A composition fluctuation (ΔX) that forces alloy X_0 to decompose into two parts can be expressed as: $X_0 \pm \Delta X$. The effect of the compositional difference on the free energy of the system is then given by,

$$\Delta G_C = \frac{1}{2}\frac{\partial^2 G}{\partial X^2}\left(\Delta X^2\right) \tag{2.20}$$

However, if the phases are highly dispersed and coherent there will be a surface energy contribution ($\Delta G\gamma$) between the two phases. This contribution exists even though the interface between α/β is very diffuse during the initial stages of phase separation. Thus, it is not a sharp interface between the two phases, but the energy contribution comes from the composition gradient over the interface. Hence it is more commonly known as a gradient energy term rather than an interface energy therm. In solid solutions which energetically favours the clustering of atom-like (AA, BB) pairs rather than unlike (AB) pairs. Thus, the energy contribution of the gradient energy term originates from the fact that a solution with sinusoidal composition fluctuations will contain more AB like nearest neighbours than a homogeneous solution. The fluctuations can be described by a wavelength (λ) with an amplitude ΔX , the maximum composition gradient is then proportional to $(\Delta X/\lambda)$. The gradient energy contribution is given by,

$$\Delta G\gamma = K\left(\frac{\Delta X}{\lambda}\right)^2 \tag{2.21}$$

Where *K* is a proportionality constant dependent on the difference in bond energies between like and unlike pairs.

If there is a size difference between the atoms in the solution, the composition gradients will give rise to coherency strain energies (ΔG_s). The misfit δ between A-rich and B-rich regions will give rise to an energy contribution $\propto E\delta^2$ where *E* is the Young's modulus. Thus, for a composition difference ΔX the, misfit δ will be given by $(\partial a/\partial X)/(\Delta X/a_0)$, where a is the lattice parameter of the Fe-Cr mixture and a_0 is the lattice parameter of the element in question. Hence the gradient energy term is given by [53],

$$\Delta G_s = \eta^2\left(\Delta X\right)^2\frac{E}{1-\upsilon}V_m \tag{2.22}$$

Where $\eta = {}^{1}/_{a_0}\left(\partial a_0/\partial X\right)$ i.e. the fractural change of lattice parameter per unit composition change ($\eta^{FeCr} = 0.005$), *E* is the Young's modulus, υ is the Poisson's ratio and V_m is the molar volume. Worth noticing is that the strain energy contribution is independent of the wavelength of the composition fluctuations.

Thus the combined expression of the free energy change given by equations (2.20), (2.21) and (2.22) as follows,

$$\Delta G = \left(\frac{\partial^2 G}{\partial X^2} + \frac{2K}{\lambda^2} + 2\eta^2 E' V_m \right) \frac{(\Delta X)^2}{2} \tag{2.23}$$

As it is an unstable system, driven by the minimization of free energy, with time the wavelength and compositional amplitude will grow. In addition, the system is only unstable with respect to infinitesimal fluctuations that decrease the energy of the system, i.e. if $\Delta G < 0$.

From this expression, it is easy to derive the instability condition of spinodal decomposition of a homogeneous solid solution as,

$$\frac{\partial^2 G}{\partial X^2} + \frac{2K}{\lambda^2} + 2\eta^2 E' V_m < 0 \tag{2.24}$$

The actual composition and temperature range within which SD occurs is defined by the limit $\lambda = \infty$. Hence, $\partial^2 G / \partial X^2 = -2\eta^2 E' V_m$ represents the coherent spinodal which lies within the chemical spinodal nodes. The coherency strains are considered when they are very high. The more the coherency strain is important the smaller the coherency spinodal domain will be, it is evident that the stress contribution will suppress both the MG and spinodal. Because of these energies constraints, there is a critical wavelength (λ_C) that defines the minimum wavelength of the fluctuations that can grow within the spinodal regime,

$$\lambda_C = \left(\frac{2K}{-\frac{\partial^2 G}{\partial X^2} - 2\eta^2 E' V} \right)^{1/2} \tag{2.25}$$

Thus, LRO will exhibit periodic composition fluctuations, of wavelengths that exceeds λ_C . Cahn developed an expression to obtain the dominant wavelength given by a maximum rate of developing fluctuations at $\lambda_m = \sqrt{2}\lambda_c$ [38].

The effect of composition gradients on the top of the MG due to strain energy contributions from η can be calculated accordingly,

$$\Delta T = \frac{4\eta^2 E'}{k_B N \upsilon} \tag{2.26}$$

Since the radial difference and lattice parameter between Fe and Cr is small the coherency stress effect on the critical temperature of the MG is often neglected. However, it is possible to calculate the difference by equation (2.26), the result is a difference in temperature of ~5°C

[36], [54]. Due to the experimental difficulty to measure the consolute temperature of the MG this temperature difference would often fall within the accuracy of the measurements.

2.4.1 Linear Cahn-Hilliard theory

One of the earliest theories of the temporal evolution of spinodal decomposition was made by Hillert (1956) [28], based on Gibbs theory of unstable phases [34]. Hillert's theory included the thermodynamic description of a system within the kinetic equation. The complexity of the formulation restricted the solution to an analytic expression in one dimension.

By limiting the theory to the early stages of decomposition it is possible to obtain a new analytical expression for the rate and form of the fluctuations [37]. It is described by the Cahn-Hilliard (CH) equation,

$$\frac{\partial C}{\partial t} = \left\{ M \left(\frac{\partial^2 f'}{\partial C^2} + \frac{2\eta^2 E}{1-\nu} \right) \nabla^2 C - 2Mx\nabla^4 C \right\} \tag{2.27}$$

Where $M[(\partial^2 f'/\partial^2 C) + (2\eta^2 E/1-\upsilon)]$ is identified as the interdiffusion coefficient, M is the mobility. Note how the second term, i.e. the coherency strain, contribution alters the thermodynamics and kinetics. The thermodynamic correction factor for incipient surfaces is given by $-Mx$. The general solution to equation (2.27) has the form: $C - C_0 = A(\beta,t)\cos(\beta \cdot r)$ where $A(\beta,t)$ obeys the differential equation, where t is time and β is the wavenumber as defined by Cahn [36]. Thus, solving equation (2.27) with the general solution one obtains: $A(\beta,t) = A(\beta,0)\exp[R(\beta)^t]$, where $R(\beta)$ is the kinetic amplification factor given by,

$$R(\beta) = -M\beta^2 \left(\frac{\partial^2 f'}{\partial C^2} + 2\beta^2 x + \frac{2\eta^2 E}{1-\upsilon} \right) \tag{2.28}$$

One serious issue with equation (2.27) is that it is not able to describe small fluctuations, and therefore it is not able to describe spontaneous initiation. It is most suitable to describe a system whose energy decreases monotonically by a diffusion process.

However, equation (2.28) can give us information about which infinitesimal concentration fluctuations will grow. If $R(\beta)$ is negative, then the system is stable with respect to that fluctuation and if it is positive, then that fluctuation will grow with the unstable system. Hence, at the $R(\beta)$ is equal to zero, we find the critical value or wavelength of the fluctuations in the system. It is possible to obtain the maximum of the amplification factor at exact $\sqrt{2}$

times the critical wavelength. This will be the dominating wavelength of the structure, as explained earlier by equation (2.25).

The CH equation gives a rigorous description of the interplay between the bulk free energy, gradient energy and strain energy effect on kinetics and morphology. It is a linear theory suitable for the early stages of decomposition. Thus, CH is used extensively in the modelling of two-phase problems in multicomponent system. CH coupled with Navier-Stokes equations makes it possible to model spinodal decomposition and, nucleation and growth.

As previously explained, CH does not allow to describe spontaneous initiation of SD. In order to overcome this issue, in 1970 Cook [55] further developed the CH theory to include thermal fluctuations in the early stages. The limitations of the theory were well-known, i.e. that initial conditions with large deviations from randomness would break down the theory. Thus, the CH difficulties to handle thermal fluctuations motivated the addition of fluctuation. Brownian motions by Cook, leading to the Cahn-Hilliard-Cook (CHC) equation.

The Allen-Cahn (AC) equation similar to CH is used in phase-field methods to describe phase transformations. However, AC utilizes an order parameter field variable to determine the phase, φ. Thus φ is not a conserved parameter and therefore it doesn't follow Fick's law. The kinetic Onsager type equation is driven by the minimization of free energy where the free energy of φ is generally given by a double-well potential. Consequently, AC/CH differ in the way they minimize entropy. The AC equation is mostly applied in simulations of solid-liquid transformations, crystal growth and complex structures by e.g. atomistic modelling [56].

2.4.2 Non-linear Langer-BarOn-Miller theory

The origin of the Langer-BarOn-Miller (LBM) stems from Cahn's theory of the later stages of spinodal decomposition and the beginning of coarsening [57], where the essential nature of non-linear effects on decomposition was pointed out and a nonlinear fourth-order differential equation was constructed to describe the fluctuations. The LBM theory is a statistical formulation of the nonlinear equations along with a treatment of the later stages of coarsening. Thus, LBM is a quantitative method used e.g. to obtain the amplitude of phase separation.

An order parameter $C(\vec{r})$, thought of as the average concentration of the binary system is used to form the coarse-grained Helmholtz free energy [58]. One crucial assumption is that $C(\vec{r})$ is a smooth function on the scale of the equilibrium correlation length, at any temperature. This allows for the description of large-scale phase separation. The kinetics of the system is

given by a continuity equation ($\partial C / \partial t = -\vec{\nabla} \cdot \vec{j}$) where the current density $\vec{j}$ describes the inter-diffusion of the atomic species. Then it is possible to derive the master equation for the distribution functional $\rho\{C\}$ defined on the space function $C(\vec{r})$. It is given by,

$$\frac{\partial \rho\{C\}}{\partial t} = -\int d\vec{r} \frac{\partial J(\vec{r})}{\partial C(\vec{r})} \tag{2.29}$$

Where the probability current is given by,

$$J(\vec{r}) = M\nabla^2 \left(\frac{\partial F}{\partial C(\vec{r})} \rho + k_B T \frac{\partial \rho}{\partial C(\vec{r})} \right) \tag{2.30}$$

Together with the free energy formalism equation (2.29) and (2.30), it constitutes the basis of the LBM theory. The primary use of the LBM theory is the calculation of the structure factor $s(k)$, which is the Fourier transform of the pair correlation function and directly proportional to the X-ray scattering intensity to be directly compared with SANS data. Thus, the evolution of $s(k)$ might be obtained through the LBM method. The solution of equation (2.29) is based on the correlation function [19]. The addition of the nonlinear term in LBM assumes that the solution $\rho(x)$ takes an exponential function of some quadratic form. Part of the idea behind the LBM method is that the initial distribution of atom deconvoluted into two Gaussian distributions, providing the solution of the general form,

$$\rho(x) = \frac{1}{\left(2\pi \cdot \sigma^2\right)^{1/2}} \left\{ \frac{p_2}{p_1 + p_2} \exp\left[-\frac{\left(x - p_1\right)^2}{2\sigma^2} \right] + \frac{p_1}{p_1 + p_2} \exp\left[-\frac{\left(x - p_2\right)^2}{2\sigma^2} \right] \right\} \tag{2.31}$$

Where p_1 and p_2 are the peak and trough compositions respectively, σ is the variance of the Gauss distribution. Thus, it would be possible to extract an amplitude from the difference between p_1 and p_2. The time exponent for the evolution of the spinodal structure well within the spinodal regime is ~0.20 [58].

2.5 The CALPHAD approach to binary systems

Calculating phase diagram (CALPHAD) is a thermodynamic method developed in 1970s with widespread use in metallurgy and materials science. Based on the minimization of Gibbs free energy of a system, it is possible to calculate the equilibrium state, given fixed temperature, composition and pressure. The CALPHAD approach is based on the regular solution and multi-

sub-lattice models that assume random mixtures within each sub-lattice. A drawback of this method is that SRO is neglected [59]. The atomic state of the bcc Fe-Cr system is defined by the unit cells that can be repeated indefinitely. Thus, the bcc Fe-Cr system can be described as a substitutional solution, i.e. Fe and Cr have the same probability of occupying any site in the unit cell. The Gibbs free energy of the regular substitutional solution model is given by,

$$G_m = \sum_{i=1}^{n} x_i {}^{o}G_i + RT\sum_{i=1}^{n} x_i \ln\left(x_i\right) + {}^{E}G_m \tag{2.32}$$

Where ${}^{o}G_i$ the Gibbs free energy of a given constituent is, ${}^{E}G_m$ is the excess Gibbs free energy. In this case, the original CALPHAD approach, the compound-energy formalism (CEF), is based on a two sublattice model. The reason for not including an explicit SRO term in the CEF model is that the numerical treatment in a multicomponent system would be too cumbersome. In addition, an explicit SRO term is often neglected for steels and aluminium alloys due to the small excess energy contribution. It can be approximated in the excess energy term without being stated explicitly.

The basic form to express the excess Gibbs energy of this system is as a multicomponent substitutional solution,

$${}^{binE}G_m = \sum_{i=1}^{n-1}\sum_{j=i+1}^{n} x_i x_j L_{ij} \tag{2.33}$$

This expression only gives a single interaction parameter for the phase in the *i-j* system which is often not enough to accurately describe experimental data. Hence, through the binary Redlich-Kister (RK) excess model one may extend the regular-solution term by using the difference between the fractions of *i* and *j* accordingly,

$$L_{ij} = \sum_{v=0}^{k}\left(x_i - x_j\right)^{v} * {}^{v}L_{ij} \tag{2.34}$$

This form is also known as an RK power series is the recommended excess Gibbs energy term since it preserves the shape of the binary case also in multicomponent systems.

2.6 The effect of elastic energy on phase separation

In this section, the total elastic energy, derived from the elastic properties, is considered for its effect on the change in free energy of the system. Thus, including external (applied force), internal (composition fluctuations) and configurational strain (crystal structure and dislocation

density), by imposing mechanical equilibrium the elastic energy is obtained through the elastic constants and strain in reciprocal space.

It is well-known that phase separation in the Fe-Cr alloys is dependent on temperature, composition, solution treatments and prior elastic-plastic deformation [60]. Thus an imposed elastic strain field and prior dislocation generation will influence the thermodynamic stability and the kinetics of morphological evolution [60], [61]. As the material is often found in structural application external loading within the elastic domain during service conditions is expected. Thus, the external elastic strain energy effect on the decomposition process is one of the areas of interest in this work. The contribution of the elastic energy in the system thus originates from two sources: the internal coherency strain effects due to lattice mismatch by the composition fluctuations and externally applied loading that train the dimensions of our system. Although coherency strain between α/α' is often neglected due to the small lattice mismatch in the Fe-Cr system, this effect is proportional to $\propto \eta^2 \Delta X^2$ as seen from equation (2.22). Hence, coherency stresses in this work have also been discarded, however the elastic properties of the Fe-Cr system are highly composition dependent. From a thermodynamic point of view, the change in free energy due to SD is as previously stated contributed to the molar energy of mixing, composition gradient energy and elastic energy contributions. When an external elastic load is applied to the system the total elastic energy of that system is mainly generated from internal eigenstrain, thus orientation dependent, as a response to the applied strain. This effect modifies the driving force of SD phase separation through its free energy contribution, i.e. elastic stresses influence the thermodynamic stability. Thus Cahn's expression of the free energy [38] can be modified to include the total elastic energy (E_{el}) [61], [62] accordingly,

$$F = \int_V \left\{ \frac{1}{V_m} \left[G_m + \kappa (\nabla c)^2 \right] + F_{el} \right\} \partial V \tag{2.35}$$

Where E_{el} is be given by,

$$F_{el} = \frac{1}{2} \int_V \sigma_{ij} \varepsilon_{ij}^{el} dV \tag{2.36}$$

The applied stress is given by σ_{ij} , the total elastic strain can be written as: $\varepsilon_{ij}^{el} = \varepsilon_{ij}^{a} + \varepsilon_{ij} - \varepsilon_{ij}^{0}$, where ε_{ij}^{a} is the applied strain, ε_{ij} is the internal strain due to compositional variations and ε_{ij}^{0} is the local eigenstrain sensitive to composition and position. Thus, the eigenstrain ε_{ij}^{0} is then dependent on initial dislocation configuration, obtained through: $\varepsilon_{ij}^{0} = b \otimes n = (b_i n_j + b_j n_i)/2d$

where *b* is Burgers vector, *n* is the normal vector and *d* is the interplanar distance of the considered slip planes.

Thus, E_{el} as by equation (2.36) is the elastic strain energy density per unit volume. As we are dealing with a modulated structure the local elastic property does vary. Thus, the local elastic compositional inhomogeneity tensor is described by [63],

$$\lambda_{ijkl}\left(r,\ \mathrm{t}\right) = \lambda_{ijkl}^{m}\frac{\left(X_{eq}^{p} - X(r)\right)}{X_{eq}^{p} - X_{eq}^{m}} + \lambda_{ijkl}^{p}\frac{\left(X(r) - X_{eq}^{m}\right)}{X_{eq}^{p} - X_{eq}^{m}} \tag{2.37}$$

An assumption regarding the effect of compositional changes is that Vegard's law holds, i.e. that the lattice parameter a_0 is directly dependent on the alloy composition. Therefore, for small deformations, the local material strain can be linearly approximated in the elastic region by the modified Hooke's law.

$$\sigma_{ij}^{el}(r) = \left[\lambda_{ijlk}^{0} + \lambda_{ijkl}^{'}\delta X(r)\right]\left[\varepsilon_{kl}(r) - \varepsilon_{kl}^{0}(r)\right] \tag{2.38}$$

One additional assumption is then that mechanical equilibrium holds at any given moment during the process. It means that elastic displacement is established much faster than any occurring diffusion process. Hence the mechanical equilibrium condition, $\left(\partial\sigma_{ij}^{el}/\partial r_j\right) = 0$, holds. The total strain is in turn related to the kinematic displacement equation: $\varepsilon_{ij}(r) = \frac{1}{2}\left[\frac{\partial u_i}{\partial x_j} + \frac{\partial u_j}{\partial x_i}\right]$ where *u* and *x* are displacement and position vectors [62]. Thus, using the mechanical equilibrium condition, one obtains the following expression,

$$\left[\lambda_{ijkl}^{0}\frac{\partial^2}{\partial r_j \partial r_i} + \lambda_{ijkl}^{'}\frac{\partial}{\partial r_j}\left(\delta X\left(r\right)\frac{\partial}{\partial r_i}\right)\right]u_k(r) = \left(\lambda_{ijkl}^{0}\varepsilon_{kl}^{0} - \lambda_{ijkl}^{'}\overline{\varepsilon}_{kl}\right)\frac{\partial\left(\delta X(r)\right)}{\partial r_j} + \lambda_{ijkl}^{'}\varepsilon_{kl}^{0}\frac{\partial(\delta X(r))^2}{\partial r_j} \tag{2.39}$$

To solve this equilibrium equation with appropriate boundary conditions is to determine the equilibrium elastic field for an elastically inhomogeneous system. This is the case for the spinodal decomposed structure in Fe-Cr but the same approach also holds for strained thin films [64]. Composition fluctuations induce elasticity differences due to inherent differences between Fe and Cr. Noticeably local elastic properties do change which is a concern as micro-plasticity may appear in some locations but should be avoided since it would significantly enhance dislocation generation and thus locally advanced decomposition.

It is possible to obtain displacement and internal energy by solving equation (2.39) in Fourier space. Then the solution for elastic strain energy density per unit volume can be calculated by,

$$F_{el} = \frac{1}{2}\int_{V} C_{ijkl}\varepsilon_{ij}^{el}\varepsilon_{kl}^{el}dV = \frac{1}{2}C_{ijkl}\left(\varepsilon_{ij}^{a} + \varepsilon_{ij} - \varepsilon_{ij}^{0}\right)\left(\varepsilon_{kl}^{a} + \varepsilon_{kl} + \varepsilon_{kl}^{0}\right) \tag{2.40}$$

It is well known that spinodal decomposition is lowered by the contribution of elastic energy in many systems. That is the case in Au-Ft, Au-Ni, Al-Zn, semiconductors doped with transition metals, Ci-Ni (Fe) nano-laminates. However, self-assembled quantum dots and wires in epitaxial grown thin films are produced through spinodal decomposition. The effect of strain on spinodal instability is asymmetric, e.g. compressive stress might promote phase separation while tensile stress suppresses it [65]. In the case of the Fe-Cr system the strain energy effect is estimated to lowers the top of the miscibility gap by approximately ~4.5°C [54], thus the difference between tensile and compression is however yet unknown. Thus the elastic energy change ΔE_{el} associated with an arbitrary deformation given by small strain can also be calculated by the matrix of elastic constants and corresponding strain tensor, this is made later on by equation (6.41), this approach has also been executed by Grimvall et al. [66] previously. The elastic energy associated with an externally applied force is then associated with Hooke's law ($\sigma_{ij} = C_{ijkl}\varepsilon_{kl}$), by linear elastic behaviour.

Orientation dependent elastic energy contribution is dependent on the specific elastic properties of the orientation in question. Hence, the use of elastic tensors by Voigt notation it is possible to include the orientation relation of elasticity, which was done by ADF modelling. Strain energy then becomes an issue of static displacement of atoms from sites of a perfect crystal lattice, which has been treated by Varsilyev and Udovsky [67] including the orientation dependency.

2.6.1 Diffusion in elastic stress field and stress-ageing

For the temporal evolution of the system under stress the purpose of this section is to connect the atomic jump frequency, activation energy and diffusion of atoms in the presence of a continuum displacement field.

In the case of random walk diffusion, the presence of an applied or internal stress field changes the activation energy barrier due to two reasons. The first is the drift effect associated with the changes in equilibrium point-defect energy due to the interaction with the stress field in the lattice created by the point defect. The second one is the barrier effect which is a result

of the stress field, altering the height of the activation energy barrier [68]. It has been shown by Monte-Carlo simulations that external stress fields can induce an anisotropy of the diffusion of defects. In such fields, the jump direction become in-equivalent even for cubic defects like vacancies. Investigating the change in diffusion coefficient dependent on the crystallographic orientation with rather high applied force reviled changes to the diffusion coefficient at room temperature by only a few percent, unfortunately, this was in the range of the accuracy of the measurement of the diffusion coefficient thus the effect was inconclusive [69].

Thus, in substitution solutions, e.g. Fe-Cr, rate of phase transformation is controlled by the flux of vacancy diffusion. Hence, at low-temperature solute diffusion is slow in relation to interstitial elements. In the past, the description of diffusion flows under elastic stress fields has been known to be complex hence atomic configuration is often neglected [70]. Thus, a simple approach considering vacancy diffusion in cubic crystals on which the stress field is applied have been made by Nazarv et al. [71]. The atomic energy depends on the jumping atom s and its neighbouring atoms $E_s = E(r_1 - r_s,....,r_k - r_s), k \in \{1,...,n\}$ where n is the number of atoms in the system and the position of an atom is characterized by the position vector: $r_k, k \in (1,....,n)$. The notion is that if there is a continuous displacement field present, then the equilibrium positions of atoms are shifted, and their potential energy is changed. This is true both in the case when the moving atom is in a saddle point configuration as well as in the equilibrium configuration. Thus the exchange probability of an atom and a vacancy position is given by an Arrhenius law [71]. Where the activation energy barrier is then $Q = E_i^W - E^0$, E_i^W, E^0 is the potential energy of system atoms in saddle point configuration and equilibrium configuration respectively, this expression is true also in the presence of a displacement field. The displacement field $u_k \equiv u(r_k)$, displacement of atom k given by the position vector r_k, alter the distance between the jumping atom and its neighbours. Thus, if affected by a displacement field the potential energy of such an atom can be put as: $E_s = E(r_k + u_k - r_s - u_s)$. The change of the activation energy barrier due to the displacement field is then $\Delta Q_S = \Delta E_i^W - E^0$. This method enables one to calculate the balance of jumps rates in different directions, by the probability of vacancies exchanging positions [72]. The vacancy flux is then the sum of the density of vacancy sites and the probability of vacancies exchanging positions. Vacancy diffusion flux in bcc is given by Fick's law $J = -V_m^{-1}\tilde{D}_i \nabla C$, where is a strain-dependent hyperbolic diffusion coefficient. In a single component bcc there are only two coefficients K_1 and K_1 in $\tilde{D}_i$ that determines the influence of the deformation. These coefficients are linearly dependent on the displacement and atomic specific potential energy E_i^W, E^0 [72].

Ageing itself is confined by several parameters such as time, initial concentration of solute atoms, temperature and dislocation number density, which is generally given by a Friedel type relation from previous plastic deformation or the quench [73]. The dislocation number density is directly linked to the plastic deformation before ageing. The static ageing is defined as ageing which occurs at zero rate of plastic deformation. Dynamic ageing is where ageing occurs at a given speed of plastic deformation. Ageing do occur during e.g. micro-plastic deformation. The process is often associated with Portevin le Chatelier effect [74], [75]. The enhanced mobility of interstitial solutes during stress ageing of interstitials has been observed by Van den Beukel [76]. The local strain hardening due to dislocation interaction was treated by Kubin and Estrin [77].

Solution hardening that occurs as an effect of ageing is due to interaction between dislocations and solute in solid solution. The strain ageing is characterized by a strong interaction between dislocations and interstitial atoms (e.g. C, N) that allows for low-temperature interstitial atom diffusion. Thus, after strain room temperature diffusion of C and N occur towards dislocation and stops them. An effect of stress ageing is that the elastic limit, i.e. dislocation mobility, is higher than before ageing and the plastic heterogeneous deformation is characterized by Lüders strip. Stress ageing cause increase of the elastic limit lowering the strain capacity that leads to a reduction in ductility. Thus, the embrittlement is more severe than the embrittlement only caused by strain hardening. The effect of the added ageing increase the ductile-to-brittle transition temperature and the hardening is more severe than the strain hardening itself [78], [79].

The issue of strain ageing is also a problem for C-Mn steels and their welds as they are sensitive to dynamic strain ageing. Whereat low-temperature C and N diffusion is high enough to inhibit dislocation, motion reducing strain capacity. N is the main contributor to this effect because of faster diffusion The solution, in this case, is Mn addition to create Mn-N pairs, but also Al additions with strong affinity to form AlN [80] to allow dislocation movement.

2.7 Final remarks

It is the MG that facilitates phase separation by the mechanisms SD or NG. They are both second-order phase transformations that occur within a single phase, their temporal evolution of composition differences gives rise to the difference in nano-morphology and properties. SD is an unstable phase transformation, i.e. spontaneous. Phase separation trough NG is a meta-stable transformation.

Thus, the characteristic distinction between the two is their kinetic evolution, as illustrated by Figure 2-6. Uphill diffusion is often used to describe SD when solute atoms diffuse towards higher concentrations of itself. An interconnected structure develops continuously and so does its effect on mechanical properties early on. The only energy requirement is the activation of Cr diffusion as it is a diffusion-controlled process. NG requires an activation energy barrier for nucleation and thus has generally a longer incubation time. NG form precipitates with close to equilibrium composition. The majority of the detrimental effect of NG on mechanical properties occurs during nucleation of precipitates, so the evolution of mechanical properties after nucleation in the early stages is small.

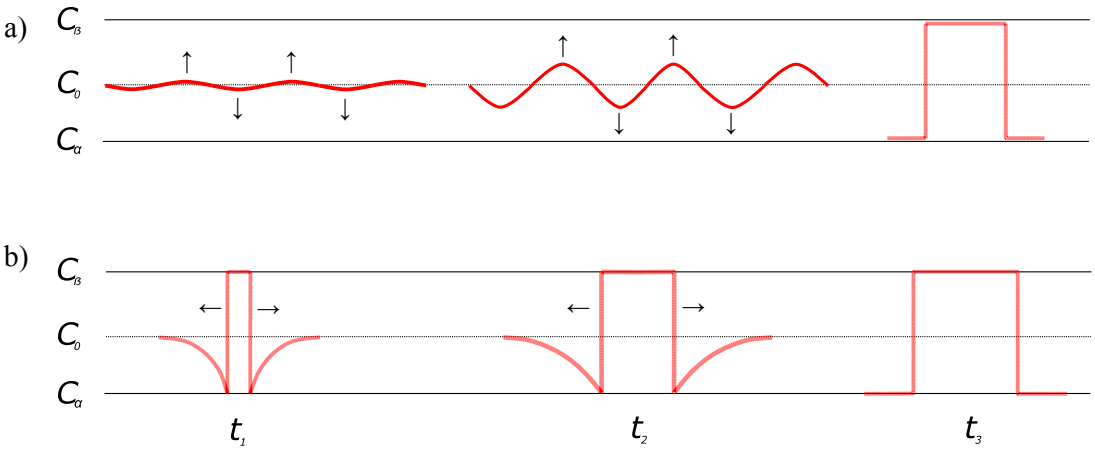

Figure 2-6. Kinetic evolution of a) continuous SD versus b) NG at initial (t_1), intermediate (t_2) and final time step (t_3).

One of the major differences between NG and SD is how the kinetic evolution of the composition fluctuations differs. In Figure 2-6 is three arbitrary time steps illustrated: t_1) SD in the very early stages small periodic composition fluctuations form in the matrix, NG dispersed nuclei is formed with close to equilibrium composition depleting the immediate surrounding matrix. t_2) SD stable spinodal waves defines the structure with a characteristic wavelength and amplitude obeying CH and LBM theory, NG the radius of the precipitate grows by depleting the surrounding matrix following LSW theory. t_3) final ageing time the matrix phase is depleted, and equilibrium composition has been reached with a specific volume fraction.

Chapter III

Characterization methods of phase separation in Fe-Cr

The choice of an analysis technique obviously depends on the compromise one is willing to make to obtain the sought-for information. Phase separation in Fe-Cr are often perused by state-of-the-art two-dimensional diffracting techniques such as small-angle neutron scattering (SANS) and transmission electron microscopy (TEM), in addition, Mössbauer spectroscopy (MB) is a widely held technique. TEM investigation of α and α' at the nanoscale in Fe-Cr is limited by the similarity of the diffraction X-rays from Fe and Cr. The combination of high coherence between α and α' is why TEM is seldom used [11]. MB probes infinitesimal changes in the energy levels of an atomic nucleus, the nuclear interaction that occurs in the Fe-Cr system when α and α' regions develop an induced modification of the mean hyper field [81], thus MB can provide information of the 1st and 2nd nearest neighbour configuration however no information about the characteristic wavelength. Through the Ferro- to paramagnetic transition temperature MB can provide composition information of α' and as a consequence information about the decomposition mechanism through the kinetic evolution of α' [11], [82]. SANS is a diffraction technique that can provide information of the characteristic distance between α and α' [83]. Hence it is used to validate various theories of SD such as CH and LBM through the evolution of the characteristic wavelength [84], [85]. However, no direct comparison in real space between SANS and modelling can be made which limits this technique.

Since the 1990s atom probe tomography (APT) has arisen as one of the most important analytical microscopy techniques. It allows for a unique combination of chemical sensitivity down to a few ppm, with a near atomic-scale spatial resolution. Along with its 3D capabilities, it may reveal novel information about the nanostructure in real space.

Phase separation in Fe-Cr is known to affect the macroscopic properties of the material. Thus, nano- and microstructural investigation is key in the analysis and understanding of Fe-Cr phase separation. The objective of this work is to characterize nanostructure through APT and in extension its effect on mechanical properties. Auxiliary experimental techniques to aid APT analysis in the understanding of phase separation and its kinetics are also used.

3.1 Hardness measurements

Vickers micro-hardness is an efficient way of monitoring the thermal ageing of Fe-Cr alloys. Here samples are prepared by SiC polishing paper after ageing with a final grit size of 5µm, to ensure a mirror-smooth surface finish. Twelve measurements were made on each sample with a load of 200g (Fe-20Cr and Fe-35Cr), 300g (Fe-50Cr) and a 10sec dwell time. The higher load was selected for the stiffer alloy so that the indentation size was kept large enough to assure a reproducible measurement accuracy of ±0.2µm. The reported micro-hardness is the average of the middle eight values. The two largest and smallest extreme values were removed. The standard deviation was calculated and presented as the uncertainty. Furthermore, the indentation measurements themselves in terms of depth and position were performed in accordance with the ISO 6507-1 standard. The schematics of the measurement technique is presented in Figure 3-1.

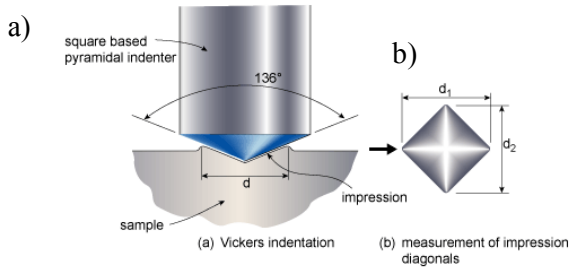

Figure 3-1. a) Vickers microhardness schematics, b) illustration of indent measurement [86].

The average indentation diameter $d=(d_1+d_2)/2$, see Figure 3-1 b), is used to calculate the Vickers Hv number through the equation [87],

$$\mathrm{Hv} = \frac{2F\sin\frac{136^\circ}{2}}{d^2} \tag{3.1}$$

Where F is the force to achieve the specified load. The evolution of all measurements is presented in reference to its initial solution treated state. Thus, the relative micro-hardness change ($\Delta\mathrm{Hv} = \mathrm{Hv}_{\mathrm{aged}} - \mathrm{Hv}_{\mathrm{init.}}$) is important for the kinetic measurements. A rule of thumb is that the thickness of the sample should be at least 3 times the penetration depth of the indent. As we analyse a 2D cross-section of the sample the influence of grains underneath the surface as well as the risk of making indents over multiple is not controlled. Thus, to make indents close to the sample surface at the nanometre scale ensures that the analysis is restricted to a single grain. For this purpose, a nanoindenter is used.

In principle, nanoindentation is when the penetration depth of the indent is measured in nanometres rather than microns. Thus, it requires a more sophisticated indenture. In this work, the Hysitron TI 950 has been used to make quasistatic nanoindentation. The nanoindentation has been made with a triangular pyramidal Berkovich indenter. This shape is routinely used for nanoindentation. Its design with the sharp tip allows for a more precise control of the indentation process.

A quasi-continuous symmetric load function is introduced to control the experiment, see Figure 3-2 a). It contains a linear loading curve that reaches its peak force of 8500μN (i.e. a 0.87g load) after 20sec. Then a 2 sec dwell time is added to the peak force to avoid unstable drift. The stiffness (S) of a material is defined as the slope of the unloading curve, i.e. $S = \partial F/\partial h$.

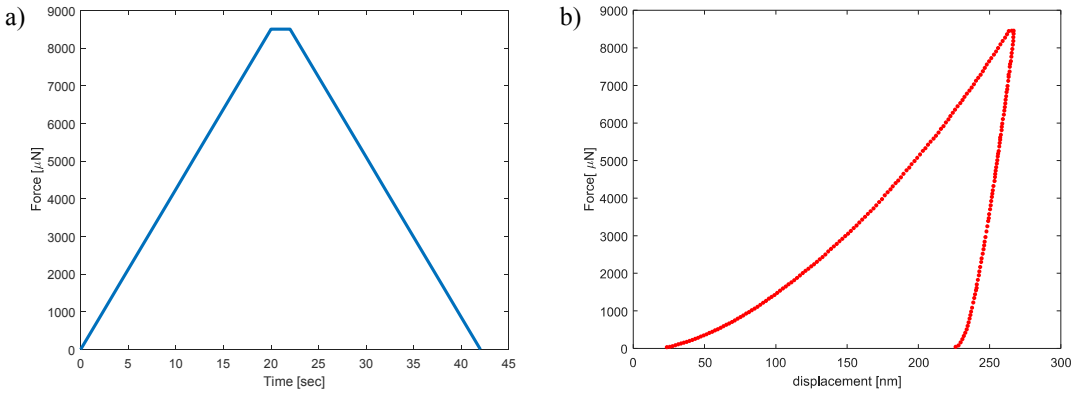

Figure 3-2. a) Load curve from nanoindentation, b) displacement curve.

The reduced Young's modulus of elasticity (E_r) is: $E_r^{-1} = E^{-1} \cdot (1-\nu^2) + E_i^{-1} \cdot (1-\nu_i^2)$, where the elasticity of the indenter is E_i = 1140GPa and Poisson's ratio ν_i is 0.07 [87]. The Poisson's ratio varies between 0 and 0.5 for most materials [88]. The harness has the normal definition: $H = F_{\max} \cdot A^{-1}$, where $F_{\max}$ is the maximum indentation force and A is the resultant projected contact area. It is customary to use the "plastic depth" (h_p) to represent the mean contact pressure. Thus A is given by the analytical expression [89],

$$A = 3\sqrt{3} h_p^2 \tan^2 \theta \tag{3.2}$$

Where θ = 65.27° for the Berkovich indenter. However, when calculating elastic properties (e.g. E_r) the TriboScan software utilize a sixth-order polynomial to fit the area function A versus h_C curve, where h_C is the contact depth. Note that the samples used in these indentations were

baked in a polyfast resin. Thus, the influence of the resin on the absolute values has not been considered, i.e. the absolute values should not be taken as the true elastic modulus of the alloy.

3.2 Thermoelectric Power (TEP)

Thermoelectric power (TEP) is a technique to measure the electric potential difference in an A/B/A circuit, induced in the B thermocouple due to a temperature difference between the two A/B junctions. This thermo-electric effect is a way of measuring the relative Seebeck coefficient (S_{AB}).

$$S_{AB} = \Delta V / \Delta T \tag{3.3}$$

The two Cu reference blocks (A) are separated by a thermal gradient (ΔT).Where T_1 = 15°C and T_1 = 25°C, thus an average TEP value is measured at 20°C. Mechanical pressure ensures good contact in the A/B junction [90]. The relative TEP between pure Cu and Fe is previously known, thus S_{AB} can be defined as TEP with respect to pure Fe. The value of S_{AB} is affected by lattice defects present in the Fe matrix, it is a sum of various contribution: $S_{AB} = \Delta S_{sol.} + \Delta S_{dis.} + \Delta S_{pre.}$, where the contributions are from solute atoms, dislocations and precipitates respectively. The contribution due to the elements in solid solution on the diffusional component of TEP is given by the Gorter-Nordheim law[91],

$$\rho S = \rho\left(S^* - S_0^*\right) = \sum_i \rho_i S_i = \sum_i \alpha_i C_i S_i \tag{3.4}$$

Where $\rho = \rho_0 + \sum \rho_i$ is the resistivity of the steel by the Matthiessen's rule [92], ρ_0 is the resistivity of the pure metal, $\rho_i = \alpha_i * C_i$ is the increase in resistivity due to solute atoms *i* given in wt.% (i.e. C_i) [93]. Thus, α_i is the specific resistivity and S_i is the specific TEP of the alloy.

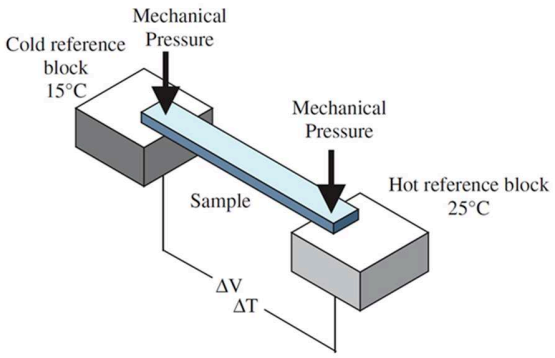

Figure 3-3. Schematic illustration of the TEP technique [93].

The assumption made when utilizing the Matthiessen rule is that the solid solution is fully disordered. This is not the case during phase separation which can be categorized as clustering in its early stages. If the clusters are small enough to generate isotropic electron scattering, the residual resistivity can be directly integrated into the classic Matthiessen rule.

Clusters have an excess of resistivity with respect to the solid solution, thus a global resistivity increase in a clustering system is expected. The integrated cluster resistivity term in the Matthiessen rule is then given by [94],

$$\rho_N = C\int_0^{2k_F} V(q)^2 \left\langle \mathrm{s}(q)^2 \right\rangle q^3 dq \tag{3.5}$$

Where C is a material-specific electrochemical constant, $V(q)$ is the Fourier transform of the solute atom potential and $\mathrm{s}(q)$ is the structure factor of the scattered clusters, often from SAXS or SANS [95]. The wave vector q is of magnitude $|q| = 4\pi \sin\theta / \lambda$, while wave vector k is of magnitude $|k| = 2\pi / \lambda$, hence the structure factor s(k).

3.3 Electron Microscopy

Electron microscopy (EM) is used when light optical microscopes (LOM) are restricted by their optical diffraction limit of the light source. In the case of green light with wavelength 550nm, the lowest resolvable size by LOM is at most ~200nm. Thus, in EM an electron source is used to illuminate the sample with shorter wavelength ($\lambda=h/mv$). So that images with sub-nanometre spatial resolution can be achieved. However, another advantage of EM is the different signals generated when the electron beam interacts with the sample. As matter

interacts with the electron beam, different site-specific information can be acquired from the generated signals.

3.3.1 Scanning electron microscopy (SEM)

In scanning electron microscopy (SEM) an image is generated by the electron beam that scans the surface in a raster pattern. The beam interacts with matter below the sample surface; hence it is a near-surface analysis technique (see Figure 3-4 b for the generated signals by the incident beam). The interaction volume of the electron beam is determined by the acceleration voltage, spot size and electron density of the sample [96]. A higher acceleration voltage results in a deeper penetration depth and thus a larger interaction volume. A lower acceleration voltage is then more surface sensitive. In normal operating conditions the voltage can range between 2 to 30 kV depending on sample and application. The SEM uses a series of electromagnetic focusing lenses to scan the sample surface, a typical SEM configuration is illustrated in Figure 3-4 a).

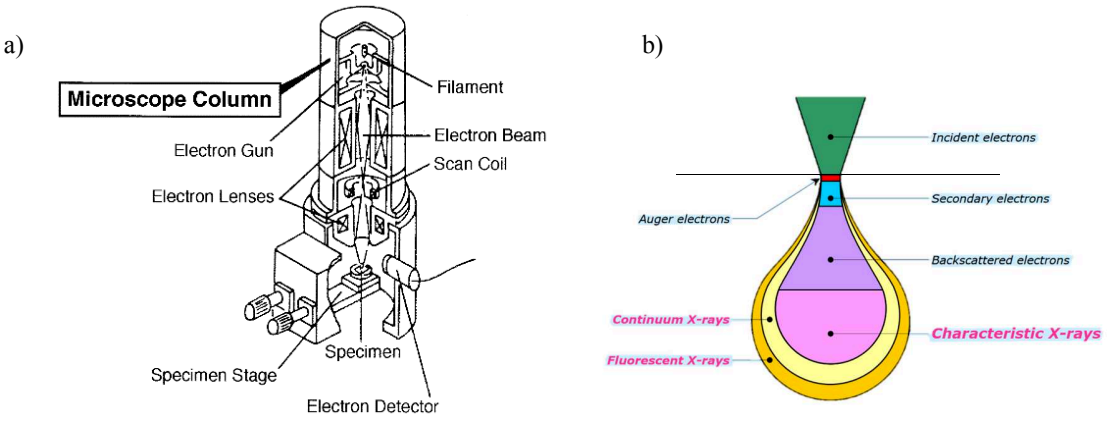

Figure 3-4. a) Schematics of a scanning electron microscope [97], and b) beam - matter interaction [98].

Secondary electrons (SE) and backscatter electrons (BE) are primarily used for imaging. SE is the standard imaging mode as it requires a lower imaging voltage. The BE mode can be used to see the contrast difference in and between phases and precipitates. Matter with low electron density has low BE intensity and therefore appear to be dark in the BE image. This feature can be used to investigate e.g. nitrides in ferrite or crystallographic orientation in a single phase. In certain crystallographic orientations with low atomic densities, channels are formed so that incident electrons penetrate the sample deeper. This influences the yield of BE at the detector so that grains appear different depending on their orientation.

An important signal generated from the interacting volume is the characteristic X-rays. These emitted X-rays are specific to the elements in the interactive volume. Thus, the local elemental composition can be obtained by energy dispersive spectroscopy (EDS). In the EDS spectrum elements can be identified and their intensities are used to quantify elemental concentrations [99]. Quantification is made through numerical algorithms in reference to standard elemental values, thus correcting for absorption and atomic interaction. When regions of interests (ROI) are small in comparison to the interactive volume, SEM-EDS yields a poor quantitative result. Since the main X-rays will come from the surrounding matrix and not from the ROI. It is possible to estimate the penetration depth/scattering of electrons in the material through Monte Carlo simulations, as done by the CASINO simulation software developed at the University of Sherbrooke for electron implantation depth [100], see Figure 3-5 .

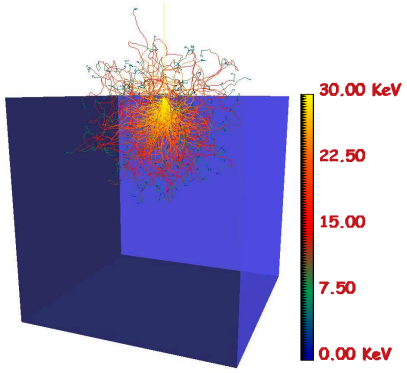

Figure 3-5. CASINO simulation of 30keV implantation depth in Fe-50Cr material, volume 5x5x5µm.

The figure displays the trajectory of 200 backscattered electrons, the alloy is a Fe-50Cr material. Electron energy 30keV beam diameter 1nm, simulated 1000 electrons in total.

3.3.2 Focused ion beam (FIB)

A focused ion beam (FIB) is most often an auxiliary technique to SEM and therefore often referred to a FIB-SEM instrument. The FIB itself is primarily used for micro/nanofabrication of samples by sputtering and deposition of material (e.g. by Pt or W gas injection systems) at a submicron level. In this work, FIB has been used to fabricate APT samples. Two Ga^+ systems have been used mainly Zeiss Nvision 40 equipped with a Kleindiek micromanipulator, and also a Zeiss XB 1530. In addition, an FEI-Helios Xe plasma FIB has been used to a limited extent.

There are a few advantages to Ga as an ion source. First, it has a low melting point (29.8°C) which means that it is a liquid, ion source and suitable to use at room temperature. It is a stable source with long service life and low surface energy, which gives it better viscosity. It also has great electrical and mechanical strength.

These FIB-SEM systems are configured in such a way that the SEM column is placed directly above the sample stage and the FIB is placed on the side at a given angle. In the Nvision 40 the FIB angle is 54°, and the FIB-SEM crossbeam at a working distance (WD) ~5.1mm. Thus, in the crossbeam, position, the sample can be imaged through either SEM or FIB, it is in this position that one manipulates the samples. Various currents and accelerating voltages are available for APT sample preparation, these parameters will be presented later. Higher currents ablate the sample quicker, but also damage the material more easily due to Ga^+ implantation. The Ga^+ penetration depth depends on material, accelerating voltage, beam current and the angle of the incident beam.

3.3.3 Electron backscatter diffraction (EBSD)

Electron backscatter diffraction (EBSD) is a microstructural analysis technique for crystalline solids based on SEM. EBSD utilizes backscattered electrons that exit the material in Bragg condition, i.e. electrons that satisfy Bragg's law. The sample is tilted 70° relative to the incident beam to further increase electron scattering yield during analysis. The scattered electrons form a Kikuchi pattern on the phosphor screen of the EBSD camera. The bands that form correspond to different diffracting planes, thus the Kikuchi pattern can be used to give the crystal structure and its orientation. SEM allows for the mapping of an area of interest which may contain several grains or particles. Thus, EBSD can provide statistic crystallographic information such as phase distribution, crystal orientation and crystalline defects of the material. The primary use of EBSD in this work is to index grain orientation and provide the pole figure of the individual grains.

The EBSD technique is based on the detection of Kikuchi lines, hence the electron backscatter diffraction pattern (EBSP). The EBSP is created by the specimen – high-energy-electron interaction in this work the accelerating voltage of the electron beam was 20kV. These patterns are specific to crystal structure, depending on orientation and composition. The spatial resolution of EBSD is typically dependent on the shortest pixel step size in which different Kikuchi patterns can be detected. It can be extended down to ~20nm for TKD and closer to 50nm in EBSD.

The experimental parameters used in this work have been presented in Table 3-1. The WD is adjusted depending on the configuration of the SEM-EBSD detector so that a clear EBSP with low noise is generated. Here the EBSD binning mode is collecting and averaging the readings in 4x4 adjacent cells, to get a better signal. Averaging of three frames is made to improve the EBSP and enhance the image resolution. Frame averaging slows down the

acquisition speed, but the signal to noise ratio can be significantly reduced. The exposure time ~21µs is used to adjust the image signal saturation level, while the beam dwell time was 10µs. An overexposed image has a bright spot in the centre of the EBSP image making it impossible to detect the Kikuchi lines while an underexposed image is too dark to generate a good contrast.

Table 3-1. EBSD experimental parameters for acquisition.

WD	Binning	Exposure time	Frame averaging	Acquisition speed
14.5	4x4	21µs	3	9.95Hz

The Oxford instruments AZtecHKL software was used to detect the EBSPs. Thus, the phases that were scanned for were bcc, fcc and sigma. The inverse pole figure (IPF) Z was the orientation map of interest. I.e. giving the Müller indexes of the crystallographic direction parallel to the normal of the sample surface. A schematic representation of grain orientation in a polycrystalline material can be seen in Figure 3-6. The obtained data during the scan was further post-processed in the CHANNEL 5 software. Due to the large scanned area (~1mm^2) some poor EBSPs are unavoidable, so noise appears as unidentified pixels. By extrapolating these zero solutions unidentified pixels are filled with information from their neighbours.

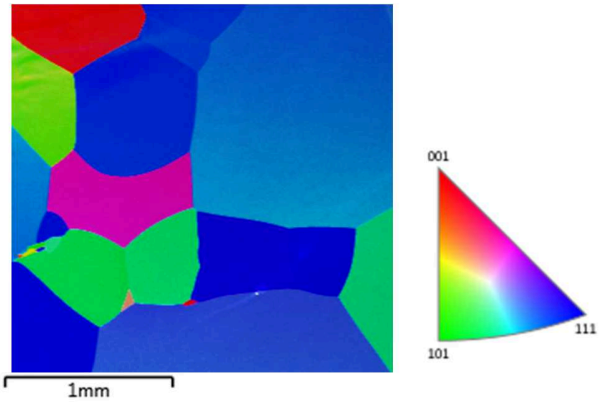

Figure 3-6. The IPF Z colouring of grain orientations in a Fe-35Cr alloy aged 100h at 525°C.

The EBSD technique is useful for obtaining statistic information of polycrystalline materials but unable to obtain atomic distributions. For this purpose, we use atom probe tomography.

3.4 Atom probe tomography

Atom probe tomography (APT) is a collective term referring to tomographic atom probe microscopy. It is a state-of-the-art 3D imaging technique at the atomic scale with mass resolution sufficient to discriminate the different species. This means visualization of atomic

distributions, clustering of atoms, segregation and grain boundary segregation in 3D for example. The technique itself is based on field ionization, field emission and field evaporation. In APT, a needle-shaped specimen with an apex radius < 50nm is evaporated atom by atom by high voltage pulses in ultra-high vacuum (UHV) at cryogenic temperatures, 20-80K. The result is a 3D data sets with up towards 50 million ions at most in this thesis.

3.4.1 Field ion microscopy (FIM)

The origin of APT dates back to 1935 and the pioneering work of E. Müller, who built the first field electron emission microscope (FEM) [101]. The FEM used a positively biased needle to create a field electron emission source, the emission pattern being projected onto a fluorescent screen. In the 1940s FEM research was focused on improving spatial resolution. It was observed that reversing the polarity of the needle could remove H from the apex. In addition, when a gas is introduced into the analysis chamber, this caused a steadily emitting streams of positive ions to form. Thus, a field ion emission pattern was formed on the fluorescent screen, hence the name field ion microscopy (FIM). FIM required higher electric fields and thus sharper needles than for FEM to work. In 1955 atomic resolution was achieved with FIM by Müller and Bahadur [102].

To image a sample by FIM requires the usage of an imaging gas. Commonly used gases are H/He/Ne depending on material and operating temperature. The parameters used to alter an FIM image during experimentation is gas, temperature and voltage.

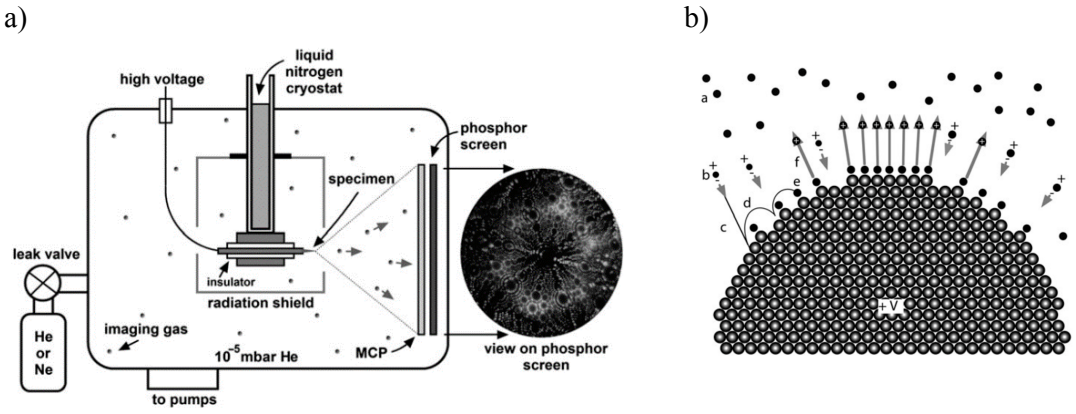

Figure 3-7. a) Field Ion Microscope schematics and illustration of sample evaporation b) imaging gas, b, is attracted to the ionized tip where they migrate along the apex, c-e, acclimated and then radially repelled, f [103].

The configurations of the analysis chamber in FIM and APT share many similarities, see Figure 3-7 a). In principle, high voltage is applied to the sample to create an electric field between the

sample and the imaging screen/detector. In FIM the imaging gas is used to produce the image on the phosphorus screen amplified by the microchannel plates (MCP). The schematics of FIM imaging are explained by Figure 3-7 b) as follow: the imaging gas atoms, a, approach the positively charged sample where they become polarized, b, and adhere to the sample, c. They migrate along the sample surface (d-e) allowing the temperature of the imaging gas to acclimate to the samples one. At some point the gas atoms are ionized, and then are repelled radially, f, from the tip towards the screen.

To create a stable FIM image the imaging field must be lower than that of the evaporation field, to avoid evaporation of ions. In addition to the voltage required for evaporation is usually lower in the presence of an imaging gas. In FIM individual atoms can be seen, but their chemical nature is unknown.

The magnification of a FIM is given by the radius of curvature of the sample and the distance, *L,* between the sample and the display screen. The value of the magnification, η' is given by,

$$\eta' = \frac{L}{(1+m)R} \tag{3.6}$$

Where *m* characterizes the position of the projection-point (where ion trajectories seem to be issued from), *R* is the radius of the tip and the distance *L* from the apex to the phosphorus screen is typically 10cm. Thus, the magnification is generally in the range of ~10^6.

3.4.2 Atom probe tomography (APT)

The discovery of surface-atom evaporation by the application of high base voltage enables the identification of the chemical nature of ions by their time-of-flight (TOF). Surface-atom evaporation can be stimulated by simultaneously applying voltage pulses to the base voltage or adding laser pulses. This technique is called field desorption microscopy (FDM), in combination with TOF mass spectrometry, it allows for the identification of individual elements resulting in the tomographic AP or APT [104]. The time-of-flight (TOF) mass spectrometry is essential to APT in order to not lose evaporated ions. Basically, each electronic pulse triggers a timer, upon arrival at the detector the timer is stopped, see Figure 3-8. Later, Cerezo et al. [105] combined this technique with a position-sensitive detector to detect the projections XY-position. The third intrinsic dimension coming from the evaporation sequence is added to complete the 3D capabilities of the AP.

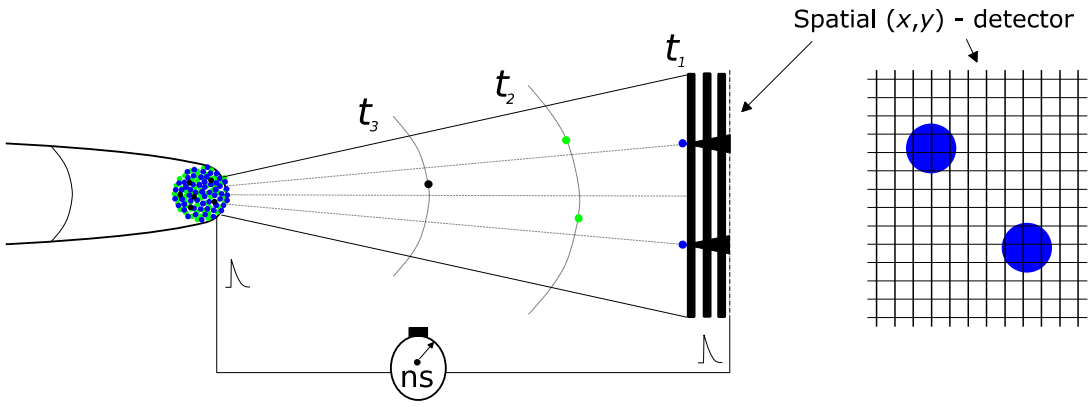

Figure 3-8. Principal sketch of 3D atom probe tomography field evaporation "frozen" during one pulse, elements of different masses $m_1 > m_2 > m_3$ will reach the detector with different kinetic energy/ "times" t_1, t_2, t_3 illustrating a straight flight path.

The main difference between FIM and APT is that the ion evaporation is stimulated by pulses, in an environment without any imaging gas, and the nature of the detection system, which allows for time of flight mass spectrometry. Also, the voltage for field evaporation is higher than the one used for FIM. This is due partly to the absence of imaging gas and because the field for evaporation is higher than the one for ionization of imaging gas atoms.

One of the main assumptions in APT is that the potential energy of the ions is transferred into kinetic energy instantaneously, i.e. terminal velocity is achieved at the moment of evaporation. Thus, the kinetic energy of the ion upon arrival at the detector is equal to its charge multiplied by the potential difference between the sample and the detector. Given by,

$$n \cdot e \cdot V = \frac{m \cdot v^2}{2} \tag{3.7}$$

Where m is the mass of the detected ion, n is its state of charge. V is the potential applied at the tip at the time of ion evaporation. If the detector is placed at a known distance L from the ion position at evaporation it is possible to determine the mass-to-charge state ratio of each detected ion as a function of flight time given by the following equation,

$$\frac{m}{n} = 2 \cdot e \cdot V \cdot \frac{t_v^2}{L^2} \tag{3.8}$$

All ions detected can be displayed in the same mass spectrum, see Figure 3-9. This makes APT unique in that it is an extremely accurate chemical composition tool that requires virtually no calibration when investigating new materials. The composition obtained at the detector can be

displayed as a function of the evaporation depth, equivalent to the intrinsic third dimension also known as 1D atom probe since its invention by Müller and Panitz [106].

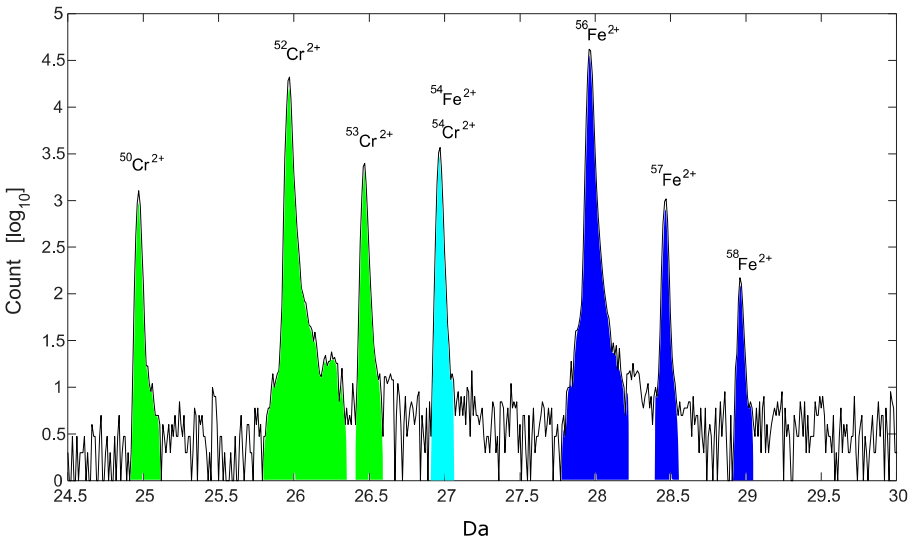

Figure 3-9. Mass spectrum of a Fe-35Cr alloy with the position of Fe and Cr peaks, total ion count 294123.

In the mass spectrum, the number of detected ions is presented as a function of their mass-to-charge ratio, in the official unit Dalton (Da). The number of ions associated with each peak makes it possible to measure the concentration of each of the elements in the whole volume analysed provided all individual peaks are identified (according to a process called "ranging"). The uncertainty (ΔC) of the local measured concentration (C) is, in its simplest form, attributed to the statistical sampling uncertainty. It is dependent upon the size of the sample, i.e. the number of collected ions (N). Thus, it is given by,

$$\Delta C = 2\sqrt{\frac{C(1-C)\cdot(1-Q_{effi.})}{N}} \tag{3.9}$$

Where $Q_{effi.}$ is the detection efficiency, which is necessary to consider when estimating the local composition error. When the global statistical counting error is considered the $Q_{effi.}$ is discarded [107], [108].

3.4.2.1 The tomographic atom probe

In the 3D atom probes, one utilizes a position-sensitive 2D detector to detect the ion impacts. Knowing the position of the ion impact it is possible to recalculate the position of the ion on the tip by inverse projection, see Figure 3-8. The third dimension which is the depth is

calculated by the number of detected ions, the atomic volume of the material and the detection efficiency of the detector.

Thus, with position-sensitive detectors, it is possible to reconstruct a 3D volume very high spatial resolution, especially in the analysis direction. For the instrument used in this work a CAMECA® LEAP 4000 HR the spatial resolution is approximately 0.4nm laterally and <0.2nm in-depth, of course, dependent on the material and sample. In many cases, it is possible to separate the atomic planes in the analysis direction if a low index crystallographic direction is close to the specimen axis. This property will be explored later. One of the most important properties of the detector is for it to be able to separate multiple hits [109]. Since, when an evaporation pulse is applied, several atoms are subjected to the very high electric field. Ionic micrographs which is an image of the electric field show that the atoms of the same terrace have the same brilliant contrast and are thus subjected to very high electric fields [110]. Thus, at one electric pulse, it is very likely that several ions are evaporated.

Atoms that are evaporated simultaneously are situated in regions of the sample where the electric field is similar. When the surface is at its equilibrium there are several atom positions at the surface where the electric field is completely equivalent. Thus, considering the evaporation process, the evaporation of one atom can trigger rapid evaporation of its neighbours. This is because the local roughness of the surface is modified, surrounding atoms are subjected to higher electric field and evaporated quickly. Hence, multiple evaporation events are often situated in close proximity of one another.

The detector must therefore for each of them be able to determine the mass and position. For example, if a detector can't detect two ions of the same mass arriving at the detector at the same time, it will induce preferential loss of the major species, and then APT tend to underestimate the concentration of the major elements (the solvent in solid solution). This has been and is still the driving force for detector development since the 1990's. The spatial and temporal separating powers of the APT system are therefore key points guaranteeing the quantitative nature of the measurements, it is still today driving the technical development of APT detectors, e.g. the advanced delay-line position-sensitive detector developed by Da Costa et al. [109]. Within this thesis, we have solely relied upon the local electrode atom probe (LEAP) 4000HR by CAMECA ® for our analysis.

3.4.2.2 Local magnification

Local magnification is a specimen artefact that arises from e.g. a precipitated phase whose evaporation field differs significantly from the matrix, so that projection errors appear. This is an experimental effect in multiphase materials, degrading the lateral accuracy. The difference in local evaporation field causes variations in the local radius of curvature, which may affect the trajectory of the ions during their initial flight path from the tip to the detector.

This local effect may then modify the characteristic dimension and composition of the precipitate alter reconstruction. The recovery of the ion path may also appear as well as bias of the chemical composition of the phase.

The phenomenon is indeed an issue for Fe-Cr alloys [111], [112]. The difficulty to obtain accurate composition measurements of Cr amplitude in α' was investigated using variance method and LBM by Miller et al. [113], where LBM was deemed advantageous. Even for long-term ageing in precipitates with more than 70at.%-Cr in α', composition measurements are non-trivial, e.g. Novy et al. [114]. It was seen that the precipitates were compressed in the (*x, y*) - plane and they are elongated in the analysis direction, indicating that they are low evaporation field regions.

The de-focusing depends on high field regions A versus low-filed regions B illustrated in Figure 3-10.

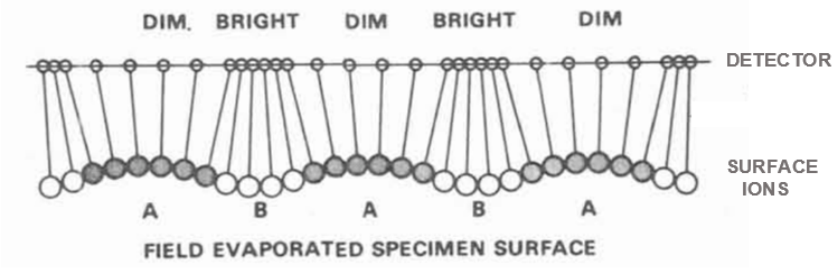

Figure 3-10. Local magnification effect (modified image [115]), low field regions B results in focusing and the creation of bright fields at the detector, and high field regions A results in defocusing at the detector.

When the field required to evaporate a precipitate is lower than that required to evaporate the matrix, it is referred to as a low field precipitate. The opposite is true for a high field precipitate. What happens in the case of a low-field precipitate is the flattening of the surface which deflects the ion trajectories inwards (compared to a truly hemispherical specimen apex). This creates a local increase of ion hits on the detector. A high-field precipitate creates locally a higher evaporation field, which repels the ions causing an apparent decrease in ion density of hits.

Local magnification effects partially control the spatial resolution and are often suspected of giving rise to apparent solute content lower than expected, particularly for particles smaller than 5nm [114]. A field evaporation model to study local magnification effects and ion trajectory overlaps was proposed by Vurpillot et al. [116]. It was found that spherical low field particles with a diameter > 2nm did not suffer much from compositional bias at their core. However, uncertainties at the interface remain. Note that the local magnification effect varies with the size of the precipitate, smaller precipitates are subjected to stronger focusing or defocusing from the same electric field. This low/high field-effect of local magnification has recently been reproduced using molecular dynamics simulations in Cu-Fe with potential to model other metallic systems by Parviainen et al. [117].

3.4.3 The local electrode atom probe (LEAP)

The fundamental limitation of the 3DAP's in the early 2000's was a (relatively) narrow field of view (FOV), and slow acquisition rate of the existing instruments. A breakthrough was made by T. Kelly based on the use of a local electrode and field electron emitter arrays, where a major electric field enhancement could be achieved by proximal electrodes [118]. In combination with a wide-angle reflectron [119]. The result for 3DAP was that a local electrode could be used to reduce the voltage and improve data collection. A relative reduction in energy spread made it possible to achieve high mass resolution over the entire FOV. Thus, the local electrode eased three of the major concerns of the APT today, namely: sample shape, data collection rate and mass resolution over a large FOV. Hence the name of this new APT version became "local electrode atom probe", also known as LEAP instruments by CAMECA®.

As mentioned, the main issue with the first 3DAP was the slow acquisition rate and narrow FOV. However, it was possible to obtain a larger FOV at the expense of mass resolution power (MRP). Thus, the remaining challenge was to obtain high acquisition rated at high MRP in large FOVs. There are currently two solutions to this problem made by the configuration of the LEAP system. There is the straight-flightpath and the reflectron compensated configuration which is used in the CAMECA® LEAP 4000 HR^{TM} system, used for analysis throughout this work.

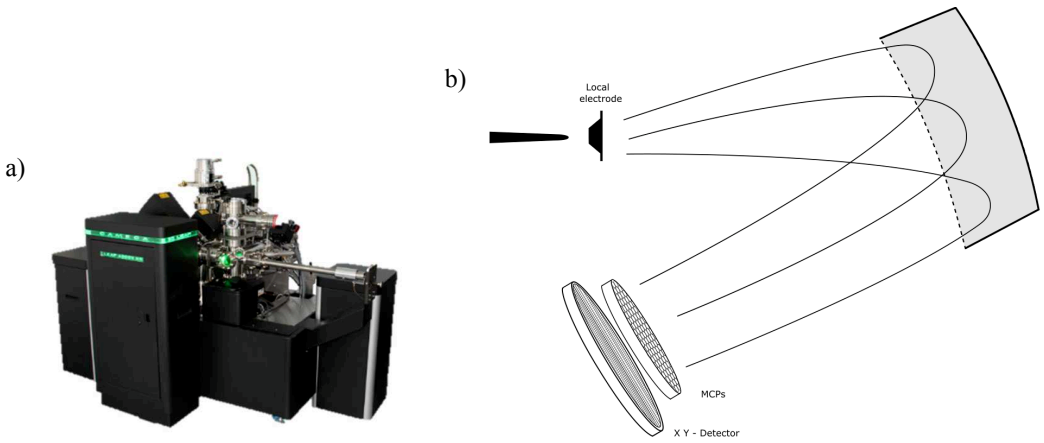

Figure 3-11. a) Conventional Pb-glass MCPs cross-section detected and missed ions hence 37% detection efficiency, b) illustrated configuration of the curved reflectron-configuration of a CAMECA® LEAP 4000 HR™.

The reflectron-compensated configuration, illustrated in Figure 3-11, is a misleadingly called form of energy-compensating technique, truly a where it's a "time-compensating". It is a way of compensating for the elemental masses of ions. The reflectron concept is because when the evaporated ions at the sample tip are directed into the electrostatic field, the ions with lower energy will be deflected first and high energy ions will travel further into the electric field. The result is that ions evaporated with the same mass-to-charge ratio (MTC) will arrive at the detector at similar time-of-flight (TOF). The reflectron refers to the design of the "electrostatic mirror" that completely returns the ions with successively higher electrostatic fields, deeper within the reflectron for ions with higher energies. The benefit of reflectron-compensating is the reduction of the tail of the mass peaks, major improvements to the mass resolution and minor improvement of the signal-to-background noise ratio.

What sets reflectron configured LEAP apart from other AP's is yet again performance parameters such as FOV, MRP and data collection rate. The LEAP reflectron design has limitations as well, e.g. flight path length has an inherent trade-off in terms of MRP versus data collection rate. LEAP systems with straight flight paths are designed to work with laser modes and higher detection efficiency ~55-60%, while reflectron configuration has superior MRP in voltage pulsing mode. A reflectron configured LEAP also has a degraded detection efficiency of ~37% similar number of ions is lost at the detector as for the straight flight path configuration, but the additional reduction in detection efficiency is due to a ~80% transparency of the grids used in the reflectron.

The advantage of a large FOV is better statistics, ideally without loss of spatial fidelity. In a straight flight path configuration, this would be achieved by a larger detector and short

flight path. However, spatial focusing provided by the reflectron enables longer flight paths without loss of FOV (which is an advantage for mass resolution).

The specimen-electrode positioning and aperture diameter of the electrode has a major influence on the potential difference required for field evaporation. Under normal operating conditions, this distance is 30-40μm. In comparison with FIM and 3DAP, a LEAP with a sample positioned 25μm away from a 25μm aperture electrode will require half the standing voltage.

3.4.3.1 Point projection reconstruction and intrinsic dimension

The spatial reconstruction is in its simple form point projection from the specimen apex to the detector. The *x* and *y* position on the tip are being estimated by the X_d and Y_d impact position at the detector through the image magnification η', as by equation (3.6). Thus, it is possible to obtain the position of the *x* and *y* position of the ion in the sample for an analysis along the specimen axis given by,

$$x = \frac{X_d}{\eta'} = \frac{X_d}{L} \times \xi \mathrm{R} \quad , \quad y = \frac{Y_d}{\eta'} = \frac{Y_d}{L} \times \xi R \tag{3.10}$$

Where *L* is the distance between the tip apex and the detector and *R* is the radius of the tip. The third-dimension *z* corresponding to the depth coordinate is a function of the total number of evaporated ions. The depth increment (Δz) of each detected ion is given by,

$$\Delta z = \frac{\eta^2 V_{at}}{Q_{eff.} \cdot S} \tag{3.11}$$

Where $Q_{eff.}$ is the detection efficiency, *S* is the surface of the detector. Typically, the detection efficiency for the LEAP used in this study is ~37%. Thus, the volume can be reconstructed atom by atom and thus atomic layer by atomic layer.

3.5 Theory of field evaporation

Field evaporation is the physical phenomenon which atom probe tomography (APT) is based upon. It describes field-induced removal of surface atoms from a needle-shaped specimen with single or multiple charge state. The atoms at the specimen surface are subjected to high-intensity electric fields, ~10-60 V/nm.

The electric field at the surface of the tip apex depends upon the applied voltage (V_0) and the radius (R) of the tip. The relation between the electric field (F) and radius is,

$$F = \frac{V_0}{k_f R} \tag{3.12}$$

Where k_f is the field factor, which is linked to the shape and electrostatic environment around the tip. k_f is a variable due to the elongated tip shape and it would be 1 for an isolated sphere. However, k_f is most often considered a constant that may range between 2 to 8 depending on instrument and specimen holder geometries[104]. The radius of the tip is the key in producing a high electric field, as a very small radius can produce a high field from just a few kV.

Field evaporation is a thermally activated process, with ions leave the surface of the specimen due to the lowered activation energy barrier because of the imposed electric field. The evaporation rate is given by an Arrhenius law,

$$K_{evap.} = \vartheta_{atom} \exp\left(\frac{-Q(F)}{kT}\right) \tag{3.13}$$

Where ϑ_{atom} is the surface atom vibrational energy, $Q(F)$ is the "height" of the energy barrier. Similarly, to equation (3.13) it is possible to obtain the detection rate if ϑ_{atom} is replaced by ηN_{atom} where η is the detection rate and N_{atom} is the number of imaged surface atoms facing a detector.

The evaporation energy barrier varies linearly with the electric field in close proximity to the evaporation field (F_{evap}),

$$Q(F) = Q_0\left(1 - \sqrt{\frac{F}{F_{evap}}}\right) \approx Q_0\left(1 - \frac{F}{F_{evap}}\right) \tag{3.14}$$

Where Q_0 is the barrier without the application of the electric field. Thus, from equation (3.13) and (3.14) it is evident that high temperature and high electric field increase field evaporation rate.

It is therefore important to optimize the experimental parameters such as temperature and specimen geometry to get reliable results. Otherwise, it may lead to preferential evaporation of an element, illustrated in Figure 3-12 for an A-B alloy. It occurs when one of the elements has a lower evaporation field than the other one.

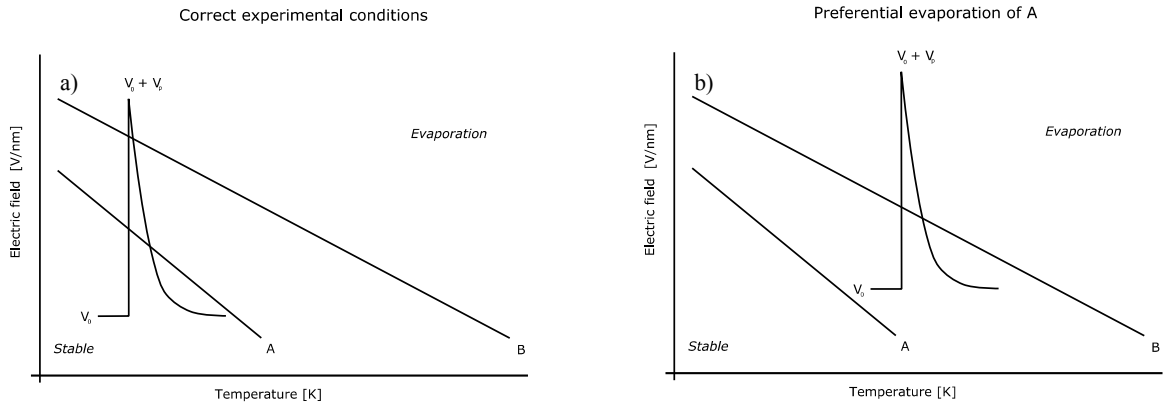

Figure 3-12. Illustrations of the evaporation of the two elements A and B, a) during correct experimental conditions and b) during preferential evaporation of A.

Considering a binary A-B alloy where one component e.g. A has a significantly lower evaporation field, so that $F_B > F_A$ (see Figure 3-12 for the temperature dependency of these fields). In the case of correct experimental conditions, the evaporation field of both F_A and F_B is reached by the addition of the standing voltage and the pulsating voltage. Ideally, both elements are then systematically evaporated by the pulsating voltage and are therefore detected, i.e. there is no preferential evaporation. In the case with preferential evaporation, the field of element A is lower than the base field of the specimen. This means that A can evaporate at the constant field. Ions that are evaporated in-between pulses no start time of the evaporation will be recorded and therefore the mass of the ion will be lost. Preferential evaporation contributes to the background noise. If this evaporation error is not corrected for, it will introduce a bias in the composition measurements. To avoid this preferential evaporation, it might be tempting to increase the pulse fraction that is to lower the DC bias voltage for the same total potential. However, there is a limitation of this approach. That is if the DC bias potential is too low impurities from the residual vacuum of the instrument, mainly hydrogen, will adsorb to the surface of the tip between the pulses, and then field evaporated the next pulse, modifying the evaporation conditions.

The phenomenon can be further limited by the cooling of the sample, the general tendency is then that the field evaporation gap between the various elements is reduced. The potentially negative effect is that the evaporation field of the specimens is enhanced so that it is necessary to increase the field applied to the tip. The material is then subjected to higher stresses, i.e. cyclic electrostatic pressures which increase the risk of premature rupture by fracture of the sample.

In this work with binary ferritic Fe-Cr model alloys the temperature 50K and pulse fraction, 20% was used in order to limit the possible artefacts. These are the classical values of this intensively studied system, leading to quantitative analysis [12], [15], [120]–[123].

The evaporation rate is chosen experimentally to limit the number of multiple hits on the detector. However, the nature of the evaporation process is such that it is not always possible to avoid that more than one atom is detected during one pulse.

For preferential evaporation of a material, the number of atoms evaporated in-between pulses may be evaluated with respect to the atoms evaporated at pulses. In voltage AP atoms evaporated on electric pulses naturally has a higher kinetic energy and are identified in the mass spectrum. Atoms that are evaporated in-between pulses are detected without any correlation to the pulses and thus identified as "background noise" events. Analysing alloys composed of several elements with different evaporation field is more complex. Atoms with high cohesive energy also have a strong evaporation field constant (C_F). These atoms may be more difficult to evaporate at the top of the voltage curve than other elements. Thus, a non-steady evaporation state may arise, atoms with low C_F are preferentially evaporated in-between pulses. These atoms have lower kinetic energy and thus contribute to background noise. Since the evaporation rate is the rate by which the tip evaporates continuously on average elements with low C_F may evaporate at the standing DC voltage. Thus, in such a case the composition detected at the detector does not represent the bulk composition of the material. Because we evaluate the composition of the alloys by the peaks in the mass spectra, i.e. elements evaporated on pulses. Experimentally the ways to limit preferential evaporation is by increasing the pulse repetition rate, increasing the pulse fraction or decrease the base temperature of the specimen.

In models used to explain AP composition bias events that may occur before field evaporation are often neglected. This refers in particular to the movement of atoms at the sample surface before field evaporation, i.e. surface diffusion. This phenomenon troubles both spatial performance and composition measurement. The motion of lattice atoms can be observed in FIM [124], [125]. In voltage mode the probability of surface diffusion is very small in relation to field evaporation, however, in laser pulsing mode this might overthrow the evaporation process. As an example, Gault et al. [126] reported that compositional inconsistencies of C and N in steels that might arise from this phenomenon. Elemental segregation follows crystallographic features; thus, the impact of directional diffusion needs to be considered to understand these artefacts. This phenomenon primarily affects interstitial elements. However, deviations from randomness for substitutional Si in stainless steel could

be seen in laser pulsing mode. It was concluded that solutes are migrating towards high-electric field regions over the specimen surface and the spatial resolving power of the technique is lowered.

3.6 Samples, reconstruction and data mining

Tomography is the key feature of the 3D atom probe, the word itself means superposition of layers or slices. Most analytic 3D microscopes produce their 3D map composed of a pile-up 2D map of intensities used to deduct structure and elemental distributions. However, in APT an atom occupies a single position. The atomic positions of the APT dataset are deduced from an ordered list of impact coordinates from the FE of the sample. Thus, the reconstruction algorithm entails producing the 3D spatial coordinate of the raw data before useful nanostructure information can be acquired.

3.6.1 Sample preparation

There are two preparation methods of the needle-shaped specimens used in this work. Electropolishing and FIB-SEM preparation. Electropolishing is more of a manual craft based on experience of working with the specific material, while FIB allows more careful selection of the sample and control of its manufacturing.

3.6.1.1 Electropolishing preparation

Electropolishing of needle-shaped specimen are classically made by a solution of in a two-step process [127]. First, blanks of the sample are cut with a precision saw to approximate dimensions ~0.3x0.3x15mm. After we have used a micro-loop to do the polishing of our samples, which means placing a droplet of electrolyte in a metal loop, then applying a small voltage to the loop while moving the blanks back and forth in the droplet creating a neck on the blanks. For further illustration, see e.g. Gault et al. [127].

The two steps of polishing refer to the usage of two different solutions, here the first step being Ethanol/Perchloric acid in 75/25-vol.%, and the second step is nono butoxyethanol / Perchloric acid in 98/2-vol.%.

The second step of electropolishing requires some experience, it is crucial to get a good shape and size of the tip. The parameters used for the Fe-Cr samples in this work are given in Table 3-2. The rate at which the material is removed is naturally dependent on the electrochemical properties of that material. Thus, what is the most important is to find the

polishing plateau in the V-I curve, see interval B-C in Figure 3-13. This will allow a controllable material removal rate while avoiding pitting, as optically a smooth, clean surface with metallic glance is desired. The issue with a too low current (A) is etching, which will weaken the grain boundaries and increase the risk of sample fracture during APT analysis. At the final stage, one will no longer be able to see the neck in LOM, however, polishing continues until the neck fractures hoping that the apex radius is good enough. However, when the neck has fractured it is possible to do some cleaning by pulsating low voltage in the etching region for 1-2sec. This usually helps remove potential damages from the neck fracture or oxide layer, but this is not necessary for Fe-Cr alloys.

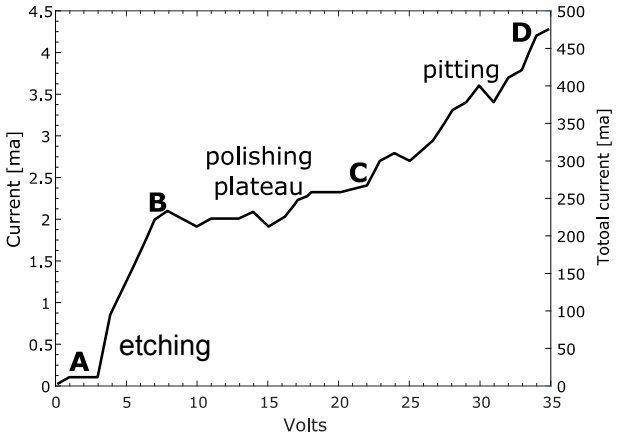

Figure 3-13. Selection of the electropolishing condition [103], in the case of the $Fe - xCr_{(x=20,35,50)}$ alloys final cleaning was made with 3mA and 5V.

After electropolishing, the needles are cleaned with ethanol, and carefully dried by compressed air, to remove liquid from the needle/holder. Most electropolished tips tend to outgas when they are introduced to the load lock of the APT. Hence it may take up to ~12h to achieve UHV, thus it is advantageous to check the needles in a TEM before they are introduced to the APT. However, it requires some careful manipulation that may damage the tip.

Table 3-2. Parameters used for the second step of electropolishing of bcc Fe-35Cr.

Step	Voltage [μV]	Current [mA]	Optical mag.
2. 1	18	10	4x
2. 2	14	7	6x
2. 3	7	3	10x

These parameters presented in Table 3-2 has proven suitable for the ferritic Fe-Cr alloys, used in this work.

3.6.1.2 Focused ion beam preparation

This in-situ FIB-SEM sample preparation allows for very precise sample preparation, however, it is somewhat time-consuming and FIB sessions are not easy to get. There are essentially two ways of extracting samples and preparing the needles for APT, either by placing samples on W pre-tips, or on a manufactured coupon with Si tips. The benefit of using a coupon is that you can make several tips out of a single lift-out, in case of fracture or problems with annular milling. Pre-tips are better when preparing a small number of tips. The lift-out process is presented in Figure 3-14.

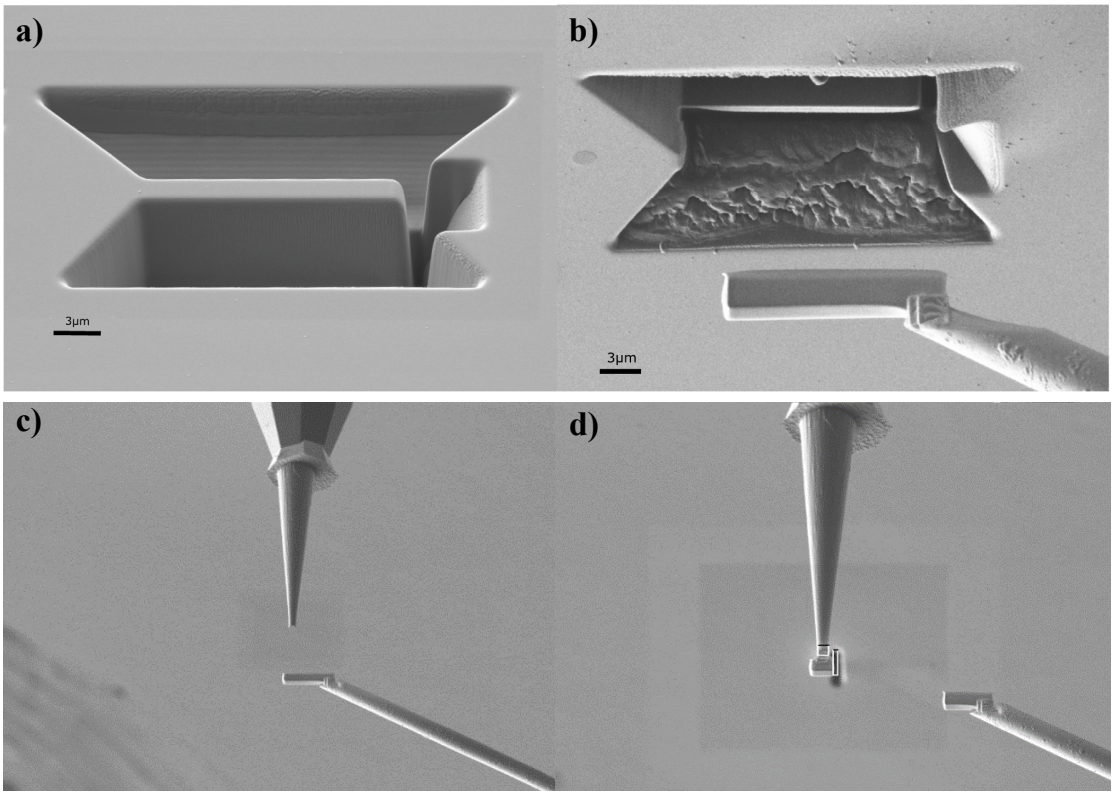

Figure 3-14. Lift-out procedure. a) SEM view at 0° tilt of a chunk, b) FIB view of a chunk being lifted out with the µ-manipulator welded to the chunk, c) approaching the Si µ-tip with the chunk, d) annular milling when the tip is ~1µm in diameter.

The lift-out technique, onto Si tips on a coupon, is performed in the following way,

1) In the crossbeam position at 54° tilt, the sample surface is perpendicular to the FIB gun. This position is used to mill the sample chunk. Two ~17µm wide and 9µm high trapezoids are placed facing each other 2.5µm apart, milling with a current from 30kV;6.5 to 3nA. This can be seen in SEM view in Figure 3-14 a). The micro-manipulator will enter from the bottom left in FIB view, see Figure 3-14 b) tilt 0° at this position. So, it is important to make sure it is possible to access the chunk and lift

it out, a rectangle is therefore placed on the left side of the wall to make sure of this. Then at 0° tilt, the wall is cut free from underneath with a 0.75µm wide rectangle, with current 30kV:300pA.

2) The micromanipulator is welded to the wall using Pt-gas, a 2x2µm area is used for the deposition welding with a current of 30kV:80pA and pixel fill factor of 50.9%. The wall is cut free from the sample using a 0.75µm rectangle with 30kV:300pA current from the left side. A rectangular blank can now be lifted out from the surface of the sample, see Figure 3-14 b).
3) The sample is placed on the top of the Si pre-tip using the same deposition parameters as in step 2 and the same width and current of the rectangle to cut it free from the micromanipulator, see Figure 3-14 c) - e).

The procedure is repeated until the chunk is fully consumed. The other method that is slightly more cumbersome, however efficient for a lower number of analysis conditions is the usage of a W pre-tips prepared by electro-polishing. In this case, the tip is prepared by micro-loop using a single polishing step with 10%NaOH. In this case, a slightly shorter neck than when preparing samples for atom probe is desired. Since a flat apex of the tip with a ~2µm diameter section is to be made in FIB. It is important to obtain a smooth surface of the pre-tip for good contact ease of welding the sample to the tip. Hence, a stepwise decrease of the milling current was used accordingly: step 1) 30kV:6.5nA, step 2) 30kV:700pA, step 3) 30kV:300pA and final cleaning with a reduced window in FIB view with high imaging speed and an imaging current of 30kV:80pA.

Once a sample has successfully been lifted out and adhered onto its support tip (Si in the case of micro-tips or W for the electro polished pre-tip), it is time to create the needle shape through annular milling (see Figure 3-15).

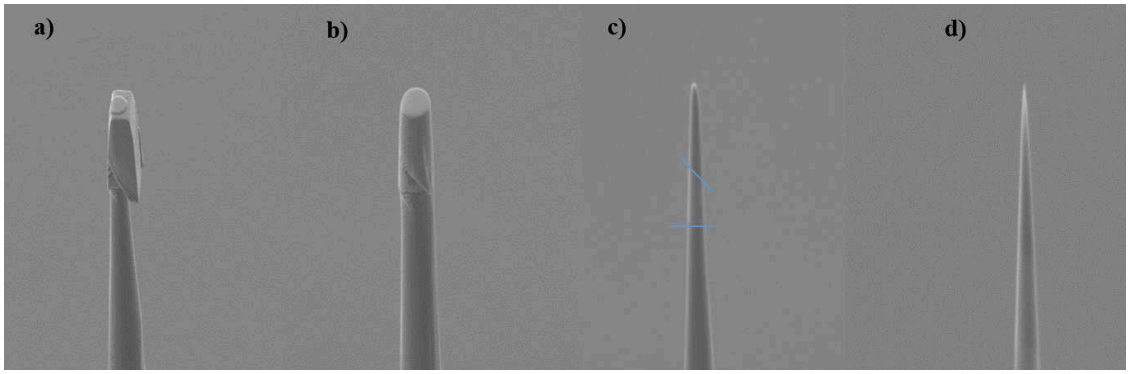

Figure 3-15. a) Chunk of <001> stress-aged sample, b) milled sample with some OP-S on the surface, c) milled sample diameter ~300nm, d) milled sample diameter ~80nm.

The first step of annular milling is aimed to form the chunk that is welded to the tip into a circular shape. Thus, in the feature mill application of the FIB, a circle with an inner diameter of ~1.8µm and an outer diameter of ~3-4µm was created at the centre. At this point, it is important to align the centre of the chunk with the vertical axis of the pre-tip. Milling with a milling current of 30kV:300pA for 2min at the time until an inner diameter of the tip reached ~600nm. See Figure 3-15 a) - b).

For the second step of milling, FIB magnification was increased to lower the outer diameter of the circle to ~2.0-2.5µm. Milling was made for at most 2min at the time to maintain high control of the sputtering yield with a current ranging from 30kV:150pA to 40pA with a final diameter of ~100nm. See Figure 3-15 c). The third step, milling with a current of 30kV:10pA to a final diameter of ~80nm. See Figure 3-15 d). Lastly is cleaning the tip 30sec by FIB imaging at 2kV:30pA with low scanning speed. This last step removes most of the Ga^+ contaminated layer.

3.6.2 Reconstruction optimization

After out gazing for about 12h in UHV conditions the sample can be run with the previously specified conditions. To the first-order, the m/n ratio of the incoming ions is calculated by equating the kinetic and potential energies. The n/m calculation is based on two assumptions: the potential energy of the ion is completely converted into kinetic energy upon FEV, the acceleration of the ion up to its terminal velocity is instantaneous. The TOF raw data needs to be corrected before converting into n/m. The correction based on the voltage and the flight path ("bowl"), without these corrections' n/m does not represent a narrow TOF range, but rather a distribution of TOF dependent on ionization voltage and detector impact location. Thus, first voltage correction is made by selecting a mass peak to maximize MRP. The peak

should include ions that are distributed over the entire FOV. Then voltage corrections are applied, i.e. oversimplified electrostatic assumptions, linear detector response, detector bias etc. Then the bowl correction is applied, it considers the flight path difference as a function of detector hit location. An appropriately curved detector would not require this type of correction, hence the name "bowl" correction. The bowl correction is also parameterized to fit the 2D TOF distribution originating from a single ion peak. TOF corrections are iterated until MRP stops improving by a predefined value, i.e. improvement of the full width half maximum (FWHM) of the MRP.

Then a mass calibration procedure is applied, using a linearization method. Well defined mass peaks identified by the user are placed in the correct position in the mass spectra and all other counts are shifted by linear interpolation. It is better to choose peaks far apart to get better accuracy in the linear interpolation.

For reconstruction issues, it is important to estimate the electric field to fit the Fe-Cr alloy at the cryogenic analysis temperature. The Fe temperature dependency of the evaporation field has prior been investigated by Wada [128], using FIM with an evaporation rate of 0.1 layer/s in 10^{-2} Pa Ne atmosphere. The resulting evaporation field (F) normalized by the extrapolated field (F_0) at 0K shows a linear dependency between 20-100K for the Fe <011> plane, with $y = -0.0021x + 0.9855$ and R^2=0.9899. This linear assumption yields the following relation between temperature and Fe <011> evaporation field,

$$F = F_0 - \theta T \tag{3.15}$$

Where $\theta = -(\partial F/\partial T)$, therefore F increases with decreasing temperature.

For the investigated Fe-Cr alloys the assumption is that, there is a linear relation of the evaporation field between pure Fe and pure Cr. Thus, in addition to temperature, it is necessary to adjust for composition due to the high amount of alloying element. The field for Fe is 33 V/nm and for Cr it is 27 V/nm at 77K. The approximated experiential evaporation field of various Fe-Cr alloys is thus given by,

$$F = \left(F_0^{Fe_{<011>}} - X_{Cr} * F_0^{Cr}\right) - \left(-\tfrac{dF}{dT}\left(T_{ref} - T_{\exp}\right) * \left(F_0^{Fe_{<011>}} - X_{Cr} * F_0^{Cr}\right)\right) \tag{3.16}$$

Where simply put the field is corrected by composition in the first term because of the high Cr solute content. The second term is a temperature correction because of the analysis conditions is at a lower temperature than the tabulated field values. The calculated values for the alloys are given in Table 3-3.

Table 3-3. Calculated experimental evaporation fields at 50K.

Alloy	Temperature [K]	Field [F]
Fe-20Cr	50	33.60
Fe-35Cr	50	32.65
Fe-50Cr	50	31.70

Experimental parameters of the APT analysis were evaluated to find an acceptable compromise between specimen yield and data quality. Thus, the voltage pulse fraction was set to 20%, evaporation rate 0.20%, while specimen temperature was varied. As Cr has a lower evaporation field, it is plausible that ions would evaporate in-between pulses. Data evaporated at a lower than combined ~2kV was discarded due to the small pulse fraction. The evaporation of the analysis was conducted at 80, 40 and 20K, to see the change of Cr content in the tip as previously explained. Thus 50K is a good compromise, for quantitatively accurate elemental composition measurements [111].

Table 3-4. Composition temperature dependency of a single Fe-35Cr sample 560°C 120h.

Alloy	Conc. [at.%-Cr]	Temp. [K]	Ion count [million]	Voltage range [kV]
Fe-35Cr	34.15 ± 0.02	80	26.41	2.0 - 6.0
Fe-35Cr	35.30 ± 0.03	40	10.00	6.4 - 6.6
Fe-35Cr	35.11 ± 0.04	20	8.41	7.0 - 7.3

For some alloys, to discriminate between ions in the mass spectra is non-trivial. One or more isotopes of different elements may overlap at the same *m/n* value. Thus, it can be impossible to distinguish the individual ions in the spectra. In alloys containing Fe and Cr, there is an issue with $54Cr^{2+}$ and $54Fe^{2+}$ because they correspond to the same mass (they are called isobars) and to the same mass over charge ratio, 27 Da. The natural abundance of these isotopes is 2.36% of total Cr for 54 Cr and 5.8% of total Fe for 54 Fe. Thus, the fraction of Cr atoms within the 27 Da peak is given by,

$$U_{27Da}^{Cr} = \frac{X_{Cr} \cdot 0.0236}{X_{Fe} \cdot 0.058} \tag{3.17}$$

Depending on the global composition of the alloy, X_{Cr} and X_{Fe}, the error introduced by this attribution can systematically be corrected. Thus, for the Fe-35Cr alloy, approximately 22% of the 27 Da peak consists of Cr, which is lost from the global composition if this peak is assigned to Fe in its entirety. Hence, deconvolution of this peak is systematically being applied to composition measurements. However, for distribution analysis, the entire 27 Da peak is assigned to Fe for 3D reconstructions, where deconvolution cannot apply.

The trajectory of ions leaving the specimen apex is not dependent on the mass of the ion or the voltage, but the distribution of the electric field lines. This is true for far-fields, the complexity in APT reconstructions arises from the first few nm of flight. Numerical calculation of ion trajectories has shown that they were close to radial, thus ions leave the needle apex almost radially [129], [130]. However, trajectories are progressively compressed after a distance corresponding to a few times the radius of curvature of the apex. This is equivalent of considering that their trajectories are straight but originate from a point that is not at the centre of the hemispherical cap, but further down on the specimen axis. As it is too difficult to compute the exact ion trajectory without knowing the exact electric field distribution, extensive research by FIM researchers has been made on the topic of a simple projection law to reproduce the observed pattern on the phosphorus screen. The simplest model assumes that the ions follow straight trajectories, this forms the basis of the point-projection reconstruction algorithms, which are used in FIM and APT [131]. Ions from HV-pulsating APTs experience a field that varies with time. Calculations have been made for DC and pulsating FEV assuming a hyperbolical field distribution. Extending these assumptions to a modern wide FOV APT would induce up to 6% inaccuracy, however, these types of estimates are difficult to make accurately [132], [133].

Thus, there is a discrepancy between the straight point projection and what is seen on the detector. The image in the detector has been compressed. Hence, the image compression factor (ξ or $(m+1)$) and field factor (k_f) needs to be corrected for a more accurate reconstruction. The image compression factor (ξ) is calculated, based the discrepancy between the calculated angle between the crystallographic poles (ϕ_{cryst}) and the observed angle on the detector (ϕ_{obs}), see Figure 3-16. In IVAS we use point-projection where it is assumed that the ion is launched in the normal direction of the apex sphere, or bent plane projection is used to account for the hemispherical sample apex shape [103], [134]. The reconstruction algorithm used in IVAS is described more in detail by Larson et al. p.267, when calculating the analysed volume with a fixed shank angle and image compression the volume consists of three geometric elements the radius of the tip apex, the cone section of the tip and the hemispherical cap at the bottom defined by the final tip radius.

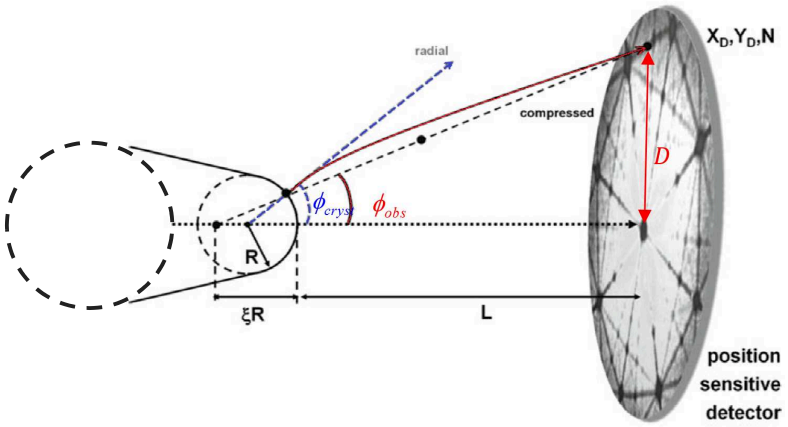

Figure 3-16. Projection of the ion trajectory [127], the image has been modified to highlight the parameters used for the reconstructions in this work.

The ion impact density at the detector is affected by the crystallographic nature of the sample, thus a non-uniform pattern may appear at the detector that can reflect crystallinity and orientation of the sample. These patterns are revealed by the desorption maps that are essentially cumulative 2D histogram of the specified ion impacts/evaporation sequence, revealing the crystallographic features [135]. To be able to measure the angle between e.g. two poles, they obviously need to be within the FOV on the detector. In the other case, it is possible to identify several poles by the symmetry lines in the detector, if the orientation of the grain is not known a priori. There are different evaporation behaviours between the poles as well, hence by singling out either the single or multiple events it is possible to identify different information as in Figure 3-17. Multiple events are when multiple impacts are detected originating from the same pulse, also known as ion pile up. These ion impacts are more likely to come from regions of higher evaporation field (or high ionization field). As a result retention at the specimen surface may appear stimulating the occurrence of multiple events, this is an issue, especially for carbon [136], [137], the effect of multiple event creates a reduction of the concentration of the element in question and subsequently an increase of all other elements.

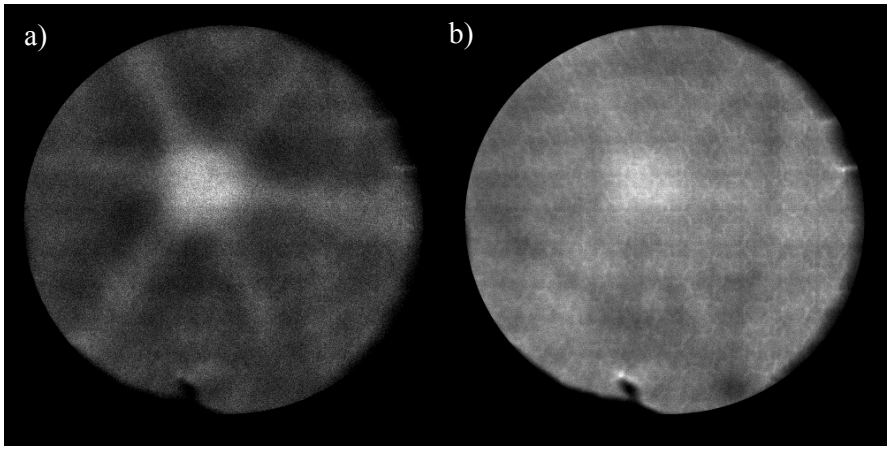

Figure 3-17. Desorption map from APT of the Fe-35Cr, 235MPa, <111>-grain, a) from multiple event map, b) <111> pole in the single event map.

As we have a simple 2D image in the detector the (*x, y*) coordinates for the centre of the pole is used to calculate distance. The observed angle between the two poles can be calculated by,

$$\phi_{obs} = \arctan\left(\frac{D}{L}\right) \tag{3.18}$$

Where D is the distance between the two poles and L is the distance between the sample and the detector. In this work the distance L = 49.4mm has been used for the reconstructions, based on internal work at the GPM laboratory.

The cosine of the angle between two crystallographic poles in the bcc structure of our Fe-Cr alloys can be calculated by,

$$\cos\phi_{cryst} = \frac{h_1h_2 + k_1k_2 + l_1l_2}{\sqrt{\left(h_1^2 + k_1^2 + l_1^2\right)\left(h_2^2 + k_2^2 + l_2^2\right)}} \tag{3.19}$$

Then the image compression factor is fixed as $\xi = \phi_{cryst}/\phi_{obs}$. The second step is to decide the field factor k_f which is adjusted to correct the interatomic plane distance at the poles as measured on 3D reconstructions. Calculating the interatomic planar distance (d) for a cubic (bcc) crystal is done by the equation,

$$d^2 = \frac{a^2}{h^2 + k^2 + l^2} \tag{3.20}$$

Where a is the lattice parameter and *h,k,l* are the Miller indexes of the pole. The interatomic plan distance for the most common orientations in this work is given in Table 3-5.

Table 3-5, interatomic plane distances in nm.

<h, k, l>	**bcc-Fe**	**bcc-Cr**
a_0 (nm)	0.287	0.289
<011>	0.203	0.204
<002>	0.1435	0.1445
<112>	0.1172	0.118
<111>	0.1657	0.1669

An interesting feature arises at the <011> pole in the Fe-Cr alloys, observed in the APT reconstructions is a low Fe density thus it is enriched in Cr. Hence, in atomic distribution analysis, this pole needs to be excluded to avoid polarity bias in the result. The interatomic plane distance can then easily be adjusted to the bcc Cr crystal by $d^{Cr}_{<011>} = 0.204\,\text{nm}$. This is a strong feature thus this is the pole that most often appear in an electro-polished sampled, in part due to the large FOV.

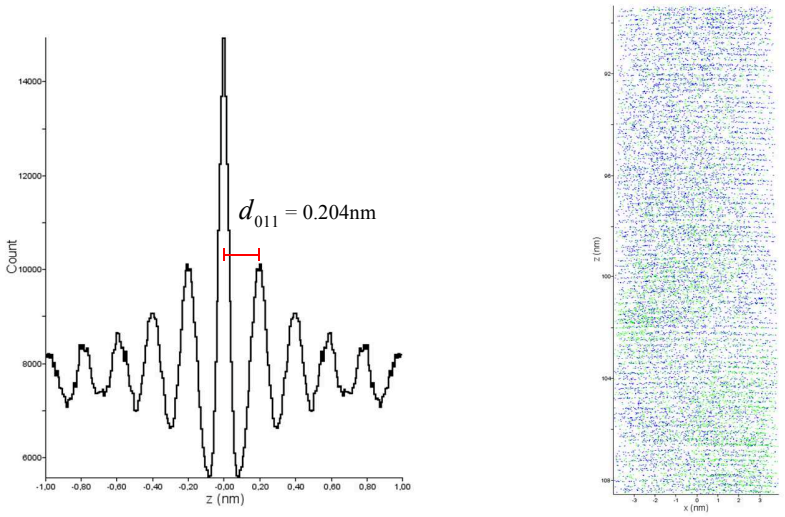

Figure 3-18. Reconstruction of a Fe-35Cr 1000h at a <011> -pole the interatomic plan distance in the analysis direction *z* is adjusted to 0.204nm with Fe as the base alloy.

Thus, for electropolished samples, the standard value of the field factor k_f used in this work is 4.1, when no obvious pole can be identified the corresponding image compression was 1.6 based on the relation: $k_f \propto \xi^3$ presented by Vurpillot et al. [138]. When the <011> -pole present itself the k_f can be updated to adjust Δz according to the spatial distribution map (SDM) Moody et al. [139]. The observed interatomic plane distance $d_{observed}$ is obtained from the SDM in IVAS, as seen in Figure 3-18 a). Ideally, the distance between atomic planes in the analysis direction can be corrected to the theoretical values presented in Table 3-5 the result of which is seen in Figure 3-18 b) for the <011> pole.

When the FIB lift-out method is applied when several poles are present in the reconstruction the ξ is fixed, and then k_f is corrected to obtain the correct interatomic distance. This resulted in a k_f closer to 4.25, more details presented in section 5.3.1, this higher field factor is because of the coupon that shields the environment surrounding the tip and therefore alters the electric field.

3.6.3 Morphology and composition measurements of phase separation

A challenge in nanostructure analysis of APT data is how to discriminate the various phases formed in the matrix from the matrix. Without careful consideration, this can lead to critical errors in the interpretation of the result. The simplest "phase separation" visualization method is here based on the bulk average composition (C_0) where the composition gradient with the matrix (C_m) and precipitate (C_p) is evaluated by proximity histograms over the *iso*-surface at C_0. A proximity histogram is essentially a 1D concentration profile constructed as distance from an interface, here 0.3nm fixed binning is used and the maximum length is 30nm to ensure to encapsulate the α/α' distance [140]. The *iso*-surface is a surface drawn within the 3D data set corresponding to a fixed Cr threshold, the accuracy of the surface depends on voxel size and delocalization [118], [141]. In this work voxel size 0.5nm and the default IVAS delocalization 3nm laterally (the same as O'Neill et al. [141]) was used, it has been seen that the relative error increases exponentially with decreasing voxel size below 0.4nm [142]. For disperses particles with an internal structure priori requirement on high spatial resolution has been assumed to key in the analysis of these features, binning of fine voxel size (0.5nm) will improve the signal to noise ratio while revealing segregation features that otherwise will be lost in larger voxels [143]. Increasing the voxel size averages out the density variations and reduces noise, in a Ni-Al-Cr super alloy the voxel size 1.6nm minimized the mean square error of the measured and estimated density in the voxels [144].

The average composition of an element in a volume, C_0, can be thought of as a homogeneous distribution of the element in that volume. Hence, any deviation from homogeneity or the average would indicate a local enrichment/depletion of that element. Therefore, the C_0 composition is used to evaluate the presence of α/α' regions based on Cr composition. Once a clear α/α'-interface with error-function behaviour has been established a threshold is given by the half distance between α/α' to more accurately depict α', by the following equation,

$$iso^{th.} = C_m + \tfrac{1}{2}\left(C_p - C_m\right) \tag{3.21}$$

This is a variable threshold that best encapsulates the morphology of the precipitates, based on their composition difference. Proximity-histograms or concentration profiles are not always able to measure the composition of precipitates, then cluster analysis can be used to obtain the composition. As the threshold is based on the composition, the lever rule can be used to compare the composition and phase fraction with the phase diagram. Alternatively, for direct comparison of the kinetic evolution of morphology between different samples, a fixed concentration threshold is more suited. This approach is more suitable for comparison of precipitates in the transient growth stage for example.

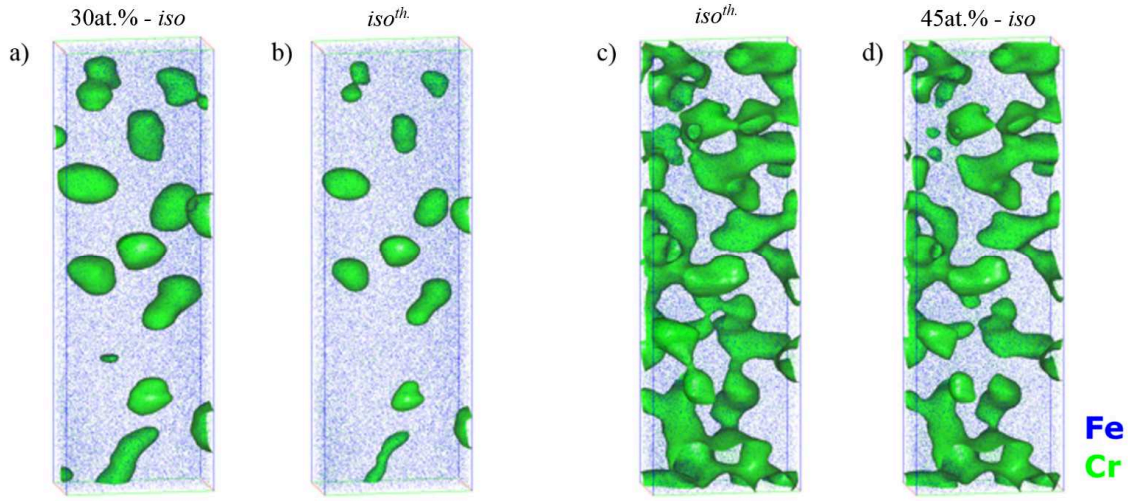

Figure 3-19. Visualization of α' with *iso* - surface of confidence 0.10, NG and SD in a 10x20x60nm volume, a) NG after 23days with interface at 30at.%-Cr, b) Fe-20Cr NG after 23days 525°C, $iso^{th.}$ at 39.8at.%-Cr, c) Fe-35Cr SD after 120h 525°C $iso^{th.}$ at 40.7at.%-Cr and d) Fe-35Cr SD after 120h 525°C interface at 45at.%-Cr.

The effect on the visualization of NG and SD by a variable threshold, $iso^{th.}$ i.e. equation (3.21), versus an arbitrary fixed value (here ~10at.% above C_0). The issue that arises in the case of NG is that smaller fluctuations in the matrix can be detected as precipitates and artificial agglomeration. In addition, a threshold closer to the matrix will include more of the interface between α/α' and therefore lower the average composition of the precipitates and surface roughness increase. In the case of SD, the difficulty to select the threshold is further increased by the continuous diffusion-controlled growth of periodicity and amplitude of the Cr fluctuations. Hence, a too high threshold as in Figure 3-19 results in isolated precipitates where only the peak value of the amplitude is encapsulated. A too low will make it very difficult to distinguish the interconnected structure because the volume fraction is so high.

Consider an analysed volume V, in which the total number of atoms N_V^{tot} is a distribution of different species *i*. Thus, N_i is the number of atoms of species *i*, this species has

an average atomic density $\rho_i = N_i / N_V^{tot}$. Thus, similarly the volume fraction α' can be calculated based on the number of Cr atoms encapsulated by an *iso* surface in relation to the total number of Cr atom in that volume. Classically the number density of precipitates is used to describe the NG structure in a similar fashion.

The cluster analysis method as by e.g. Stephenson et al. [145] and Moody et al. [146] is at present an accurate method to calculate the average composition of the precipitates. It entails that 5th-order Cr-Cr nearest neighbour (NN), ions that are placed closer together than the random distribution are assumed to belong to a cluster. Thus, a maximum Cr-Cr separation distance is decided. The minimum number of ions in the cluster needs to be decided. In our case, it is done through the CALPHAD phase diagram and calculation of the critical radius of nucleation. Thus, at 525°C with an analysis, detection efficiency of 37% the number of Cr ions in a cluster to qualify as α' phase is set to 64. The diffuse interface would jeopardize the composition of the precipitates thus the cluster interface is eroded. The result of cluster extraction of SD α' is visualized in Figure 3-20, to make sure of a good extraction the α matrix is analyzed by the 5th - *NN* to make sure that the resulting Cr distribution is random.

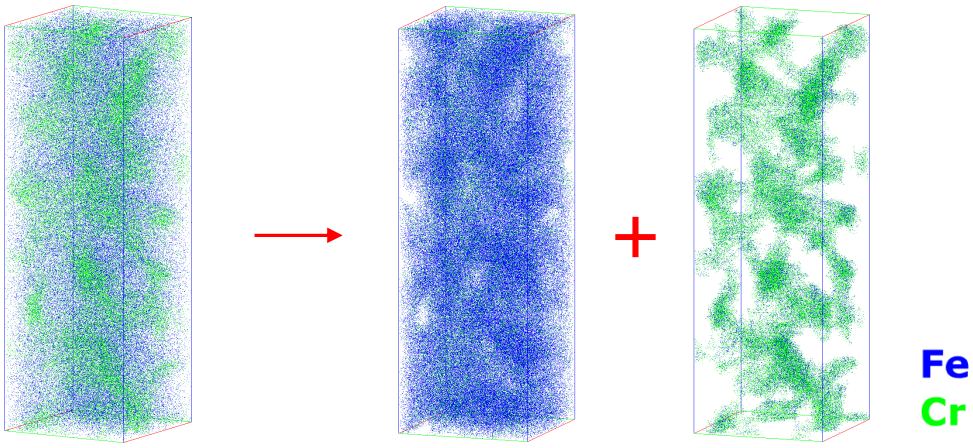

Figure 3-20. Cluster extraction analysis of α', the initial volume is separated into matrix and precipitate based on Cr nearest neighbour distribution.

The calculation of volume fraction (f_V) based on Cr composition can be made by the lever rule [147]. Hence, no assumption of the interface needs to be made the uncertainty comes from the accuracy of the composition measurement. Spatial overlaps due to local magnification can be corrected by geometrical models, e.g. Blavette et al. [148], however, no such assumptions have been made in this work.

$$C_0^{Cr} = (1 - f_V^{\alpha'})C_\alpha^{Cr} + f_V^{\alpha'} C_{\alpha'}^{Cr} \quad \rightarrow \quad f_V^{\alpha'} = \frac{C_0^{Cr} - C_\alpha^{Cr}}{C_{\alpha'}^{Cr} - C_\alpha^{Cr}} \tag{3.22}$$

Assuming conservation of mass the global Cr concentration (C_0^{Cr}) is constant, i.e. the bulk composition of the alloy. Thus, during ageing Cr diffusion may form or dissolve α'. The mass balance between the precipitate and the matrix gives the relation of the composition fluctuations: $\Delta Cr = C_{\alpha'}^{Cr} - C_\alpha^{Cr} = C_0^{Cr} - C_\alpha^{Cr} \big/ f_V^{\alpha'}$. Thus equation (3.22) reviles that the composition measurement of C_α^{Cr} matrix is crucial. Naturally, a simple way of measuring it would be to select an area, that is large and away from any noticeable precipitates or artefacts and calculated the average. Another approach is to use proximity histograms at the global average composition. However, in this work, the matrix has been calculated as the average composition after extracting the α' by the cluster method as in Figure 3-20.

The characteristic distance or wavelength of the decomposed structure is one of the key characteristics in phase separation. It can be measured by either autocorrelation or radial distribution functions. The autocorrelation function (ACF) is calculated based on concentration profiles. A 120nm cylinder is placed in *z*-direction of the reconstruction and the composition profile is calculated with a fixed bin width of 0.6nm. The radius of the cylinder is ~5nm, but it can be adapted (reduced) to improve the signal in the ACF. Ideally, one would have one wave encapsulate in the cylinder so the radius should be approximately equal to the half the wavelength in an isotropic structure. Then the raw concentration profile is processed by the autocorrelation function [149], according to:

$$R_k = \frac{\sum_{i=1}^{N-k} \left(C_i - \bar{C}\right)\left(C_{i+k} - \bar{C}\right)}{\sum_{i=1}^{N} \left(C_i - \bar{C}\right)^2} \tag{3.23}$$

Where R_k is the correlation factor at rank *k*, in our case evaluated every 0.6nm. In conjunction with concentration profiles, this method has been used to quantify the characteristic wavelength of the modulated structure in the case of the spinodal decomposed sample. In the case of precipitates, the characteristic distance is usually the mean distance between precipitates. But in practice, only volume fraction and number density of precipitates are used to describe the microstructure.

The analysed volumes by APT has increased several orders of magnitude since its early days of 1DAP, for which ACF was much adopted. Nowadays, the 3D capabilities of APT make

it possible to calculate the radial distribution function or pair correlation function of different species.

The radial distribution function $G(r)$ can be defined as the probability of finding an atom *j* at a distance *r*. It is necessary to calculate the number of atoms in the spherical crown of inner radius r and outer radius $r+dr$. This is equal to the volume of the crown multiplied by the corrected average density by a factor $g(r)_{ij}$ taking into account the difference in random distribution of the atoms of *j* as a function of the atoms of *i* is: $G(r)_{ij} = g(r)_{ij}\rho_j 4\pi r^2 dr$. The correction factor $g(r)_{ij}$ is often the desired quantity. It is therefore deducted from the radial distribution function by the following relation [150],

$$g(r)_{ij} = \frac{G(r)_{ij}}{\rho_j 4\pi r^2 dr} \tag{3.24}$$

This normalized radial distribution function takes the value 1 when the distribution is random. The value is positive when there is a tendency for the species to cluster, and less than 1 indicates a depletion of the matrix. Thus $g(r)_{ij}$ or more specifically the pair correlation function $h(r)_{ij} = g(r)_{ij} - 1$, can be used to obtain the structure factor s(*k*) by its the Fourier transform [151]. The s(*k*) is a desirable quantity as it can be used to make comparative studies between APT and diffraction techniques like SANS [152] or SAXS. It is also thermodynamically useful in modelling to define interaction potentials [153] and subsequently e.g. the periodicity of a SD structure [154].

An efficient way of quantifying phase separation by atomic distributions is the variance parameter (V) originally defined by Blavette et al. [155] as,

$$V = \sum_{n=0}^{N} \left| P^*(n) - B(n) \right| \tag{3.25}$$

This is a measurement of the integrated area difference between the observed frequency distribution histogram $P^*(n)$ and binomial distribution $B(n)$ cantered on the nominal composition of the alloy. The distributions in this work were obtained from 20x20x60nm volumes with a 50ion binning volume in IVAS. The sample count blocks are 1 by 1 nm in *z/y* to maintain spatial coherence and varied in *x*-direction to minimize bias, the details of the statistical treatment has been presented by Moody et al. [146]. The visual representation of this statistical analysis is presented in Figure 3-21.

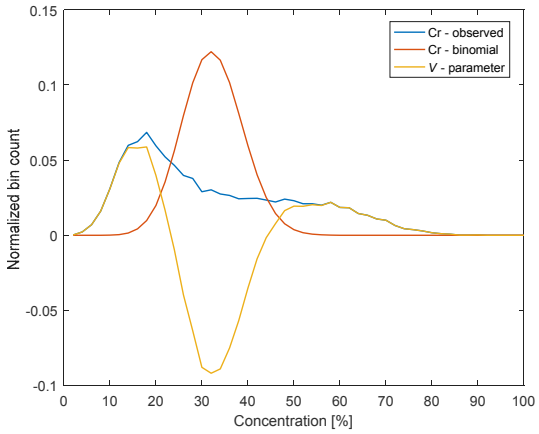

Figure 3-21. Visualization of the *V*-parameter in Fe-35Cr 100h 525°C, frequency distribution analysis 50ion binning in a 20x20x60nm volume.

The supplementing χ^2 test is a way to check for the frequency distribution whether the distribution of atoms is random. The acceptance for the random distribution hypothesis to be valid is here 5%, the test is given by [146],

$$\chi^2 = \sum_{i=0}^{N} \frac{\left(N \cdot B(i) - P(i)\right)^2}{P(i)} \tag{3.26}$$

Where N is the fixed number of B ions in the sampling volume, $B(i)$ is the binomial distribution. The null hypothesis of this test is that B atoms are randomly distributed across the investigated volume. Thus, if this value is larger than the mean than the hypothesis is rejected with the probability of error equal to P. Too low values of N would be detrimental to the quality of the result. Hence, it is very unlikely that small clusters would be unlikely by this method.

Chapter IV

Results: thermal ageing of Fe-Cr alloys

This chapter is dedicated to phase separations that occur during isothermal heat treatment of binary Fe-Cr alloys. First, the alloys used in this study are presented along with their reference state. After which direct investigation of nucleation and growth (NG) and spinodal decomposition (SD) by APT is presented. Then the limit of the miscibility gap (MG) is explored by APT supported by the auxiliary experimental technique thermo-electric power (TEP), which is used to investigate the spinodal line within the MG. A CALPHAD re-optimization of the metastable Fe-Cr MG was made, and Cr-Cr clustering outside the MG is explored. Finally, this is all supported by the evolution of mechanical properties as a result of phase separation investigated by ΔHv.

4.1 Alloy fabrication and isothermal heat treatments

The investigated samples were fully ferritic binary Fe-Cr alloys, bought from OCAS NV. Three 33kg ingots were cast in a vacuum induction furnace. A 125x125x70mm block was cut, reheated to 1200°C and then hot-rolled to 15mm thickness. The realized chemical composition by ICP-OES, combustion and XRF upon delivery is provided in Table 4-1. Before thermal ageing samples were cold rolled to a thickness of 0.3mm with 2 intermediate 15min 1100°C stress relaxation treatments followed by a water quench. In addition, 10x15x50mm bars were cut. All samples were solution-treated in a Thermo Scientific Thermolyne FB1410M furnace at 1100°C for 2h in air, followed by a water quenching to room temperature. Thermal ageing was performed in a Jofra 601 dry-block calibrator, thus all heat treatments were performed in air. The temperature accuracy of the furnace during heat treatment was ± 0.9°C verified by a K-type thermocouple. Two types of samples were prepared, comb-shaped samples for atom probe analysis (illustrated in Figure 4-1) and 1mm thick rectangles for micro-hardness measurements. The TEP samples were cut to 2x5x70mm directly from the ingot, then also solution treated at 1100°C 2h.

Table 4-1. Chemical composition of as received alloys [at.%].

Alloy	Cr	Ni	Al	C	Fe
Fe-20Cr	19.53	0.0093	0.0456	0.0011	Bal.
Fe-35Cr	34.61	0.0077	0.0407	0.0016	Bal.
Fe-50Cr	49.63	-	0.0428	0.0033	Bal.

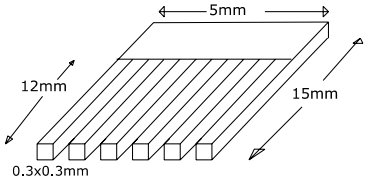

Figure 4-1. Samples for thermal ageing.

After isothermal ageing, all samples were quenched in water to room temperature. As an example, the thermal history of a 25h heat treatment is provided in Figure 4-2. Even if there is some delay in the homogenization of the temperature of the sample upon heating and quenching, in reference to the time scale of the heat treatment, this effect can be neglected in particular for the 300µm thick specimens. The quench from solution treatment to room temperature is very important in providing a homogeneous reference state, particularly for TEP. Hence, one sample at the time is quenched in a large water bath of ~5l to be sure of this.

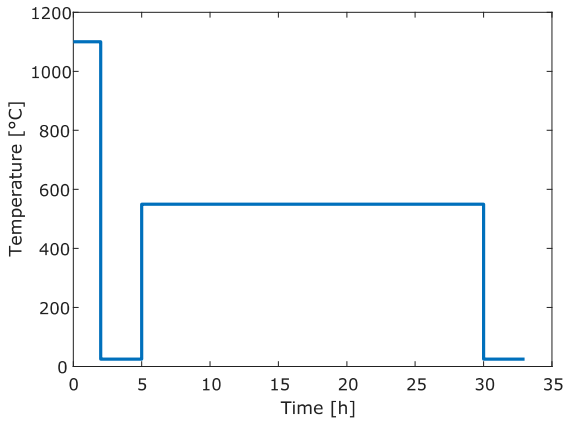

Figure 4-2. Thermal history of 25h ageing at 550°C, solution treatment at 1100°C for 2h. Thin sheets are quenched very efficiently to room tempered in water.

4.1.1 The reference states

First, the solution treatment was investigated to ensure a homogenous Cr distribution. Energy Dispersive Spectroscopy (EDS) in an electron microscope (Zeiss XB 540) and APT in a LEAP 4000HR was used for this purpose. The EDS analysis consisted of three, 3mm line scans with a 1µm resolution. The result did not show any inhomogeneity. Thus, six quantitative spot analysis was made on the surface of the Fe-35Cr alloy, the result gave variations of ±0.046at. %-Cr with a measurement error of 0.53at.%-Cr. Six quantitative spot analyses were also made in the thickness direction, they gave a variation of ±0.062at.%Cr with error 0.52at.%-Cr. Because no Cr concentration variation could be measured larger than the margin of error of the

measurements themselves, in terms of the EDS analysis the sample was deemed homogeneous at the EDS scale (≈ cubic micron).

Three additional EDS line scans on the edge of the 1mm thick samples were made, i.e. in the thickness direction to investigate the effect of the formation of the passivation oxide layer. It consistently gave a 0.2wt.%-Cr deficit at the surface. Thus, this Cr depletion at the surface is most likely due to the passive oxide layer formation which was ~60µm deep into the sample of the Fe-35Cr alloy.

The solution treated condition of the Fe-35Cr alloy is given as an example of the APT analysis in Figure 4-3, where a) is the reconstructed Fe and Cr distribution from APT and b) is the corresponding *V*-parameter based on frequency distribution analysis.

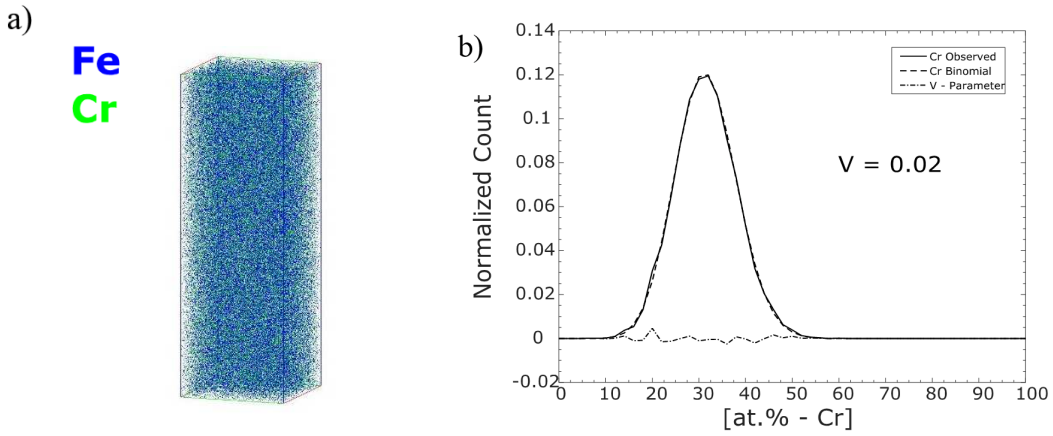

Figure 4-3. a) The solution treated Fe-35Cr alloy, reference state before ageing, reconstructed APT volume 20x20x60nm and b) corresponding Cr frequency distribution analysis.

Ocular examination might be biased since it is only a fraction of the collected ions that is represented, here by 8%. Accurate reconstruction parameters and deconvolution of the $^{54}Fe^{2+}/^{54}Cr^{2+}$ overlap is crucial for the quantification of Cr distribution so that the analysed volume is not artificially compromised. The *V*-parameters can provide us with more information than its absolute value (given in Figure 4-3 $V = 0.02$). The line representation can indicate the preferred Cr frequency distributions similar to an LBM fitting. But here some evenly distributed statistical fluctuations without a preferred frequency, which is unavoidable in a sample that is globally considered to be homogeneous, see *V*-parameter Figure 4-3 b). As a result, *V* is highly sensitive, to the degree that it is possible to detect Cr-Cr clusters in a solution treated sample. The homogeneity of our solution treated samples are in this work quantified by $V = 0.02$, it is in agreement with what has previously been reported to be as-quenched samples [11], [15].

4.2 Phase separation through spinodal decomposition and nucleation and growth

Phase separation in the Fe-Cr system has been studied by atom probe since the early 1980's [156], where it has been proven a very efficient analytical instrument to study phase separation at the nanometre scale. Its 3D capabilities make it very well adapted to study NG through size evolution, volume fraction and number density for example. The theory of phase separation in the Fe-Cr system has already been reviewed in chapter 2. Due to the presence of an MG in the phase diagram, the mechanism by which Cr segregation occurs is either unstable (SD) or metastable (NG). The discrimination between the two mechanisms is based on the free energy variation across the MG at a given temperature. Based on the second derivative of free energy gives us two regions within the MG: if $\partial^2 G / \partial C^2 > 0 \rightarrow \Delta G > 0$ the system is metastable and we are within the NG regime, if $\partial^2 G / \partial C^2 < 0 \rightarrow \Delta G < 0$ the system is unstable and we are within the SD regime.

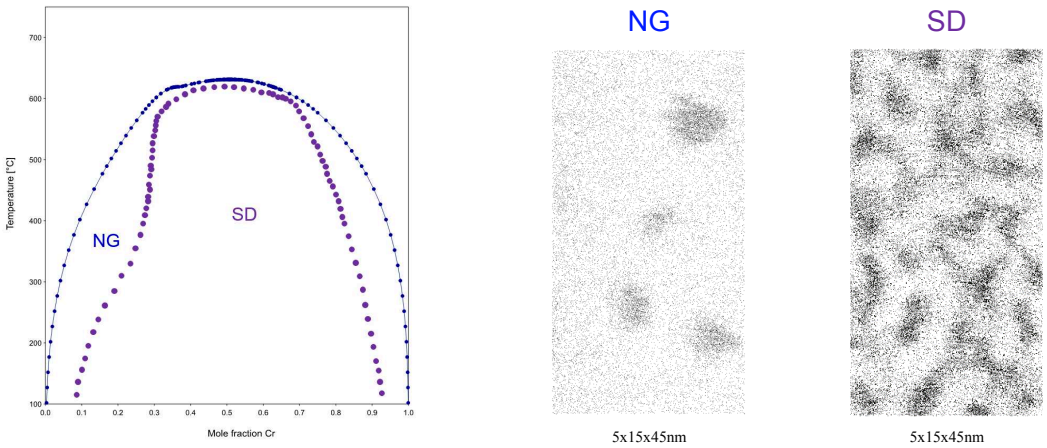

Figure 4-4. The metastable Fe-Cr MG calculated by ThermoCalc TCFE8, spinodal regime indicated by spinodal nodes, Cr spot map from a Fe-20Cr alloy at 537°C (NG) and Fe-35Cr alloy at 550°C (SD), both after 120h ageing.

The characteristic trait of phase separation kinetics in the MG is uphill diffusion, schematically presented in section 2.6. The essential part to empathize there is a difference in ageing behaviour between the NG and SD region within the MG. The continuous process by which the alloy decomposes in the SD region makes it possible to follow the evolution of mechanical properties by e.g. a continuous ΔHv evolution. The NG process is on the other hand dependent on an energy barrier that needs to be exceeded before the decomposition process can proceed. Hence, a distinction can be made between the two processes in the initial stages through the incubation time of the NG process. This distinction between the two mechanisms is an important part of the MG as it is defined by $\partial^2 G / \partial C^2 = 0$ and therefore can be used to support

the thermodynamic description of the MG. However, the determination of this line is not always non-trivial and highly dependent on the experimental technique, as seen before [12], [157]. Therefore, in this work, TEP has been tentatively used as a new simple approach to distinguish between these two mechanisms.

4.2.1 The kinetics of nucleation and growth by APT

In addition to the binary alloys presented earlier in this chapter an Nb-stabilized Fe-20Cr alloy was studied in the framework of a collaboration with INSA Lyon, to thoroughly study the kinetics of the NG process, the composition of this alloy is given in Table 4-2. It is used in this report to illustrate how an NG process is revealed by APT.

Table 4-2. Chemical composition of the Nb-stabilized Fe-20Cr alloy [at.%], determined by fluorescence and combustion, residuals <0.01wt. % were discarded.

Element	**Cr**	**Mo**	**Nb**	**Mn**	**Si**	**Ni**	**V**	**N**	**C**
[at. %]	20.2	1.08	0.34	0.30	0.52	0.16	0.14	0.08	0.04

Even if it is not relevant for our present study, the reason for introducing Nb to ferritic steel is to improve mechanical properties at intermediate temperature, to refine as-cast grain size and prevent chromium carbide formation. The solution treatment was performed at 1050°C and thermal ageing was made at 500°C.

The CALPHAD description of the MG suggest that Fe-20Cr at 500°C is well within the NG regime [12], [158], which has also been experimentally established by FIM, APT and Mössbauer spectroscopy [114], [159], [160]. Thus, in Figure 4-5 it is clear we are investigating the kinetic evolution of an NG process, the *iso*-surface is fixed at 25 at.%-Cr to highlight the temporal evolution of the morphology of Cr-rich regions.

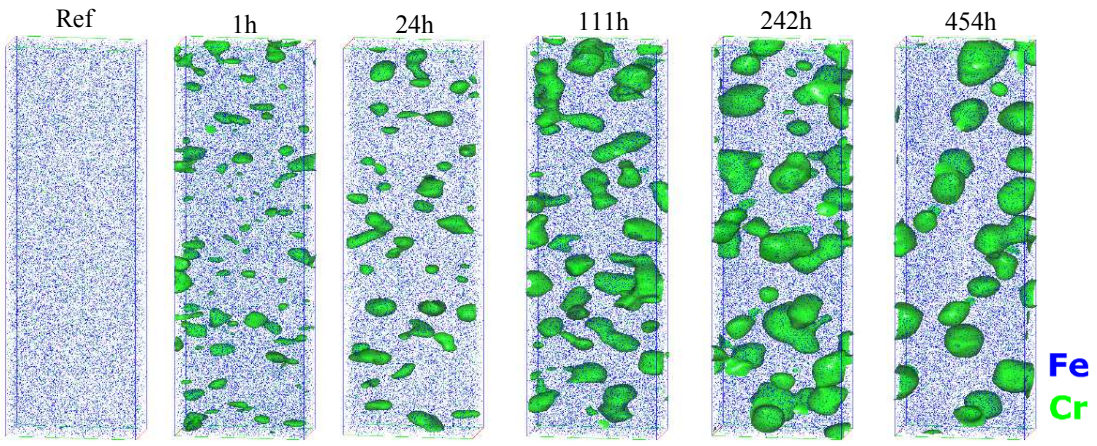

Figure 4-5. Kinetic evolution of the Nb-stabilized Fe-20Cr alloy at 500°C, the extracted volumes are 10x20x60nm and *iso*-surface threshold was set to 25at. %Cr.

Not surprising, the number density of precipitates ($Nr.\rho_{\alpha'}$) is higher in the beginning and then precipitates start to grow in size at the expense of smaller ones, decreasing the overall number of precipitates. The details of this analysis are provided in Table 4-3, where volume fraction, matrix and precipitate composition are also presented.

The 5th -*NN* cluster analysis method is employed to analyse the evolution of volume fraction, α and α' compositions. In this case, the threshold is set to a minimum of 25 ions in a single Cr cluster. Not surprisingly, in the first hour of ageing, a lot of nuclei are formed with a high Cr content. The volume fraction of nuclei is low regardless of analysed volume, due to their size. Hence Cr in the α matrix phase remains close to the nominal composition. What happens after 24h is interesting because at.%-Cr in α'decreases significantly after what seems like a marginal increase in volume fraction, see Table 4-3. This is due to the effect of the size of the α' precipitates. A precipitate after 1h is closer to the equilibrium composition as it more resembles a nucleus, but a 24h precipitate has a lower average composition because of their larger size. A second point to notice towards the end of the graph in Figure 4-6 is that the rate of f_V^{α} has stabilized, this is an indication the transformation is in the coarsening stage. The evolution of f_V^{α} follow the classic behaviour of the Avrami law [161].

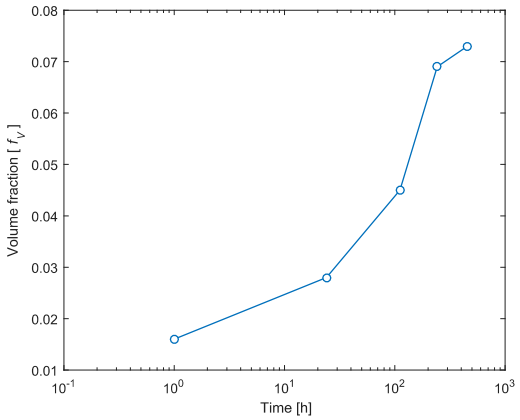

Figure 4-6. Graphical representation of the Nb-stabilized alloy, data collected in Table 4-3. The measurements are global compositions based on 5th-*NN* analysis followed by cluster erosion, the α/α' interface was left in the matrix. The first data point is at 1h.

In Figure 4-6 it should be noted that the time scale is logarithmic and that the line is only connecting the dots. Looking at the results compiled in Table 4-3 the composition of α', at the final stage after 454h has reached just back to the same value as the nucleus after 1h within the margin of error. The decreased rate of f_V^{α} evolution towards the end is in part because the precipitates become spherical. This is an effect of minimization of the surface free energy that contributes to the free energy of the system because spheres has the lowest volume to surface area ratio of any shape [162]. Hence, precipitation in steel is often treated as precipitation of spherical particles [163], it is also possible to see that the number density of precipitates decreases with increasing time in Table 4-3, which is the sign that the coarsening has already started.

Table 4-3. Kinetic evolution of the Fe-20Cr alloy at 500°C, extracted sub-volumes of 10x20x60nm.

Time [h]	**Variance [*V*]**	***Nr.*$\rho_{\alpha'}$**	$\mathbf{f_v^{\alpha'}}$	***C*$_0$ [at.%-Cr]**	**α [at.%-Cr]**	**α' [at.%-Cr]**
0	0.07	0	-	19.17 ± 0.13	0.00 ± 2.17	0.00 ± 2.17
1	0.16	79	0.016	20.04 ± 0.15	19.33 ± 0.14	64.22 ± 1.18
24	0.19	44	0.028	19.72 ± 0.14	18.62 ± 0.14	58.26 ± 0.92
111	0.25	38	0.045	20.48 ± 0.16	18.71 ± 0.15	57.53 ± 0.67
242	0.47	34	0.069	20.56 ± 0.14	17.48 ± 0.15	61.76 ± 0.60
454	0.57	28	0.073	18.72 ± 0.15	15.12 ± 0.13	64.47 ± 0.58

Even though the matrix composition of the 5th-*NN* method is sensitive to the extraction of clusters, its reproducibility is much higher and the correlation with the concentration amplitudes measured by RDF is high, as see in Table 4-7. It is, of course, possible to use a fixed *iso*-surface threshold and calculate the number density of Cr ions encapsulated by that surface ($f_v^{Nr.\rho}$ in Table 4-7). However, this would introduce a level of uncertainty regarding the software treatment which, depending on the properties of the 3D grid in the reconstruction

[140]. Including the arbitrary assumption that must be made to select that interface. To measure the difference between f_V^{α} and $f_v^{Nr.\rho}$ the alloy aged for 23 days in Figure 4-14 is used. The same composition measurements presented in Table 4-7 is used to select the interface as by equation (3.21). It is not that surprising that the spherical precipitates are overestimated and the more complex structure with more interface surface area is underestimated when comparing the measurements: $f_v^{Nr.\rho}(\text{Fe-20Cr}) = 0.165$, $f_V^{\alpha}(\text{Fe-20Cr}) = 0.10$ to $f_v^{Nr.\rho}(\text{Fe-50Cr}) = 0.302$, $f_V^{\alpha}(\text{Fe-50Cr}) = 0.372$. In essence, excluding the arbitrary selection of *iso*-surface makes for a more rigid volume fraction measurement as presented in Figure 4-6.

4.2.2 Investigation of spinodal decomposition by APT

There are three parameters that heavily influence the rate of SD in Fe-Cr namely: time, temperature and composition. Therefore, an essential part of SD investigation is to find an ideal structure that makes it easy to investigate small changes during ageing while favouring the rate of transformation by an increased temperature. The temperature selected to study SD phase transformation for both the binary alloys Fe-Cr alloys in this work was 525°C.

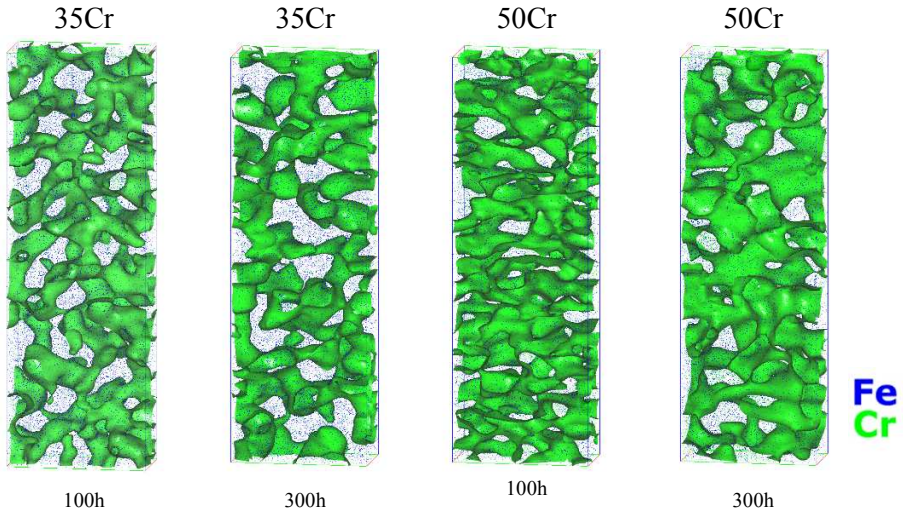

Figure 4-7. Time and composition dependency of SD Fe-35Cr and Fe-50Cr at 525°C, reconstructed volumes 10x20x60nm, the $iso^{th.}$, equation (3.21) threshold.

In Figure 4-7 we have an illustration of the time and composition dependence of the morphology highlighted by the $iso^{th.}$, equation (3.21) threshold. The target with the selection of this temperature is to be able to easily follow the early stages of SD as the coarsening stage of SD has just been entered after 100h, i.e. a state where the evolution of the structure can easily be predicted. It has been shown by Hyde et al. [164] that precipitation in Fe-Cr alloys with 24-45at.%-Cr at 500°C is in good agreement with LSW theory [49], [165]. Thus the mean

characteristic wavelength has a time dependency $\lambda(t)$ during coarsening that follows a power law: $\lambda(t) = t^m$, where the time exponent m during coarsening of λ during SD in the Fe-Cr system previously has been reported in the range ~0.2-0.3 [85], [157], [164].

Thus, favouring the SD to obtain extensive phase separation with a time restriction of ~100h is a balance between favouring the kinetics and obeying thermodynamic restrictions. The preferred alloy of choice for further investigation is Fe-35Cr, later on, is then Fe-35Cr at 525°C. Because it exhibits a clearly spinodal structure with $\lambda \sim 6.5$nm, which is relatively stable in time according to Table 4-4. Later on the λ time exponent evaluated from the time step 100h to 1000h, Table 5-4, gives m = 0.215 in agreement with LBM theory [164], [166]. The difference in λ between Fe-35Cr and Fe-50Cr is attributed to the number of solute atoms available to form α'. If there is less Cr available to form α' the volume fraction will also be less, resulting in a longer λ. The values of the morphological investigation of SD have been compiled in Table 4-4.

Table 4-4. The evolution of wavelength and decomposition dependency.

Alloy	Temperature [°C]	Time [h]	Wavelength [nm]	*V*- parameter
Fe-35Cr	525	100	6.57	0. 72
Fe-35Cr	525	300	6.71	0. 94
Fe-50Cr	525	100	6.00	0.64
Fe-50Cr	525	300	6.62	0.81

The result of SD and the corresponding evolution of λ in Figure 4-7 can be attributed to the kinetics of the decomposition (which later on will be explored by TEP in Figure 4-13). Because temperature is the same the kinetics of Cr diffusion should be favoured similarly, however, Cr diffusion distances in the Fe-50Cr matrix is shorter due to a larger amount or α'. Hence, even though the driving force for phase separation is greater in the case of the Fe-50Cr alloy the amount of Cr atoms in the matrix phase is higher as evaluated by a lower V value and a shorter wavelength.

4.3 Exploring the limit of the miscibility gap

The APT technique provides unique insight by direct investigation of α' in close proximity to the limit of the MG. As shown in Figure 4-8. It highlights a severe change of nano-morphology of the Fe-20Cr alloy after 120h when ageing temperature is increased from 537°C to 540°C. This discovery was facilitated by the combination of high precision thermal heat treatments and APT. Prior to APT experiments changes of the mechanical properties were investigated by

ΔHv, which will be presented later on in section 4.7, where also no indications of hardness evolution was observed at 540°C. This can be interpreted as the alloy been aged outside the MG, even if it cannot be ruled out that incubation time is longer than the allocated ageing time. However, as incubation time is shorter than 120h at 537°C, then it is very unlikely that it would be that much longer at 540°C, and thus this possibility is rejected here.

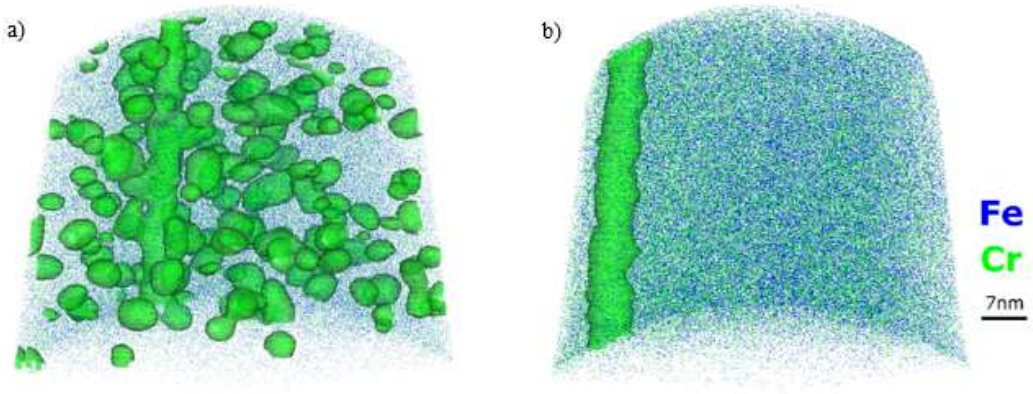

Figure 4-8. The Fe-20Cr samples at a) 537°C and b) 540°C, the *iso*$^{th.}$-surface threshold set as by the proximity histogram method. At 540°C a low-density Fe pole is visible, which is a characteristic trait of the α-Fe <110> pole.

Figure 4-8 b) exhibits a relatively homogenous sample without the presence of α'. Present is in addition a low-density region, associated with a crystallographic pole, it is a characteristic of the α-Fe <110> pole. It's an experimental artefact that would induce an orientation biased distribution of atoms. Hence, a representative sub-volume, excluding such poles are used for quantitative analyses, revealing that the 540°C sample is less homogeneous than the solution treated state. This quantification of Cr frequency distribution analysis made through the V and χ^2 parameters are collected in Table 4-5.

In Figure 4-8 a) the morphology consists of quasi-spherical Cr enriched precipitates. At this point, the selection of threshold is crucial to highlight the morphology. Therefore, the proximity histogram approach as in equation (3.21) was selected. The proximity histogram across the Cr_0 interface exhibits an error function "like" behaviour, and a representative value for the precipitate and bulk composition can easily be extracted. In essence, the *iso*-surface is put in the middle of the diffuse interface between α and α' based on at.%-Cr.

The morphology in Figure 4-8 a) is an example of decomposition through NG, even though α' precipitates have an average composition of 59.54±2.15 at.%-Cr which is not the expected CALPHAD equilibrium composition of ~80at.%-Cr. Equilibrium conditions are very seldom met for numerous reasons. Mainly due to the fact that Fe and Cr motilities are highly composition dependent. It spans approximately eight orders of magnitude at 500°C [13], with

significantly slower Cr mobility in high concentrations. In addition, measurement inaccuracies from the APT may affect the composition measurements. Meaning errors induced by e.g. the detection efficiency, ion multiplicity and the local magnification effects due to α/α' composition differences. However, the fact that nuclei do not reach their equilibrium compositions in APT measurements has been attributed to their size and the contribution of the surface energy in the early stages [167], also known as non-classical NG.

In the Fe-35Cr alloy, characterization of α' phase morphology has a higher sensitivity to the selected *iso*-surfaces thresholds. The main difficulty is due to the interconnected structure that develops continuously during SD. Therefore, by nature, SD results in a longer even more diffuse α/α' interface in relation to NG and non-classical NG. This is true particularly in the early stages of transformation, even with significant undercooling and great rate of transformation. Even though equilibrium conditions are yet not met it is still possible to follow the evolution of SD through composition measurements, see Figure 4-9 a) - c), where *iso*-surfaces over the bulk composition is used to evaluate α' morphology evolves across the MG, based on composition fluctuations as in equation (3.21). From Figure 4-9 a) a fully interconnected morphology is developed at 560°C (in the MG), over the top of the MG where α' is barely or not formed (or dissolved) by increasing temperature b) to c). Hence the top of the MG clearly lies in-between 568°C and 570°C in the Fe-35Cr alloy.

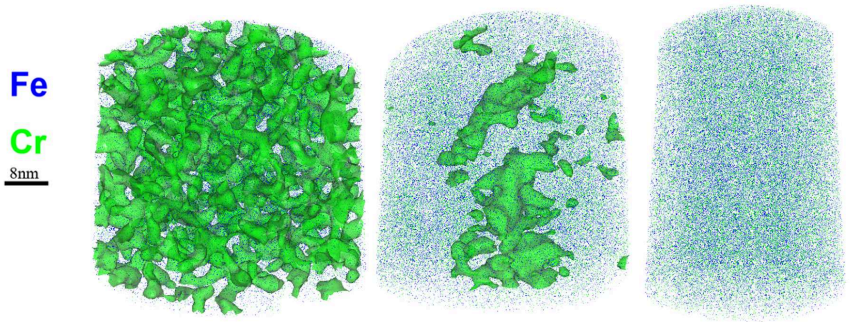

Figure 4-9. Reconstructions of decomposed Fe-35Cr alloys with $iso^{th.}$-surfaces, i.e. equation (3.21), a) 560°C, b) 568°C and c) 570°C, all aged for 120h.

In the Fe-50Cr alloy, to discriminate α' is made harder due to the high content of solute atoms in combination with a low driving force. Thus, the transition over the top of the MG might be interpreted as an extended transition region, where small Cr fluctuations close to the MG limit can be easily missed or misinterpreted. Hence, due to the high Cr content in the matrix, greater undercooling is required to clearly distinguish α' formation in the Fe-50Cr alloy. Thus, the consolute temperature might present itself within a greater temperature span of ±10°C. The

morphological evolution over the top of the MG in this temperature span is presented in Figure 4-10.

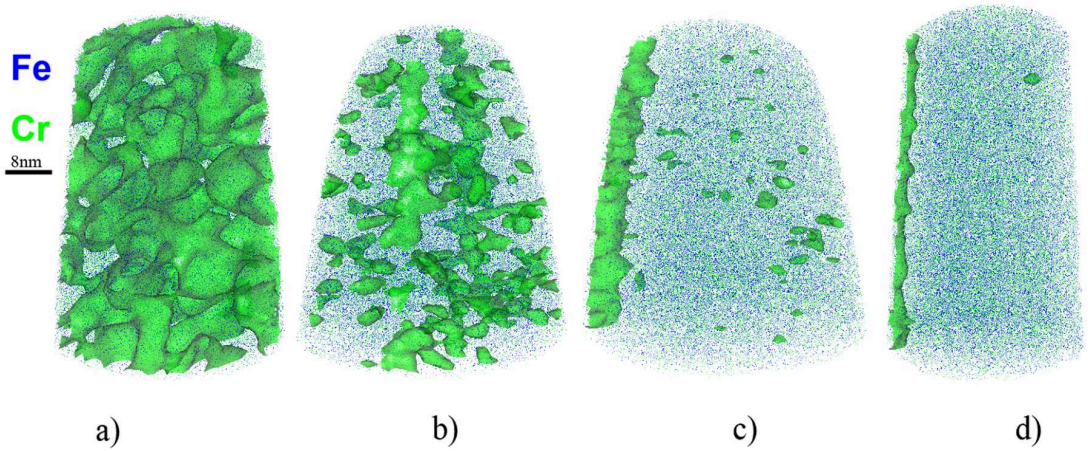

Figure 4-10. APT results of the Fe-50Cr alloys aged 120h, *iso* surface threshold is set at 60at.%-Cr. Displaying: a) an interconnected structure (SD) at 565°C, b) high-density Cr fluctuations at 570°C, c) dispersed Cr fluctuations at 578°C and d) stochastic Cr fluctuations at 580°C.

Figure 4-10 a) - d) shows the evolution of α' phase as temperature increases, the threshold is here fixed at 60at.%-Cr, since the $iso^{th..}$ approach fails to distinguish between Cr rich regions and clustering in a 50/50-alloy when the amplitude of those fluctuations is too small. It may result in a threshold below the bulk average (Cr_0) composition, which is clearly not representative of α' precipitation. In Figure 4-10 a) there is a clear "spinodal" structure. In b) there is early stages of SD where the threshold only captures Cr peaks of a developing interconnected structure, cluster analysis of 25nm^3 reveal an average α' composition of 71.36±0.18 at.%-Cr. Thus, at 570°C the morphology of α' is characterized by isolated precipitates when *iso*-surfaces are used. However, we know from the phase diagram the consolute temperature of the MG coexist with the consolute temperature of the spinodal at 50at.%-Cr. Therefore, this is only a representation artefact and the decomposition process is still SD at 570°C. Following the trend of the *V*-parameter presented in Table 4-5 it shows similar behaviour as when the limit of the MG was approached in the Fe-35Cr alloy. However, at 575°C the rate of SD is significantly reduced up until 580°C, at which temperature *V* is rather stable in time. This can be seen in Table 4-5 where $V = 0.17$ after 24h and $V = 0.18$ after 120h. Even though Cr-Cr clustering is present at 580°C the ΔCr from the Cr_0 proximity histogram is not able to detect anything else than random fluctuations. Increasing the temperature to 595°C the *V*-value reaches 0.09 which suggest that there is a temperature dependency of Cr-Cr clustering. In addition, the presence of Cr clustering without α' phase formation has been seen above the MG before [12], [82]. Therefore, the limit of α' formation is regarded as the limit of

the MG. Temperature dependent Cr-Cr clustering may appear outside the MG. This suggestion is supported by the fact that Cr fluctuations are not large enough to generate a significant hardness change. The short-range clustering is regarded as a different temperature-dependent phenomenon, which will be investigated later.

The bulk normalized RDF calculated according to equation (3.24) provides a means to indicate the favoured Cr-Cr separation distance, related to the strength of Cr self-affinity. In a periodic structure, the distance between the two first maxima would then correspond to the characteristic wavelength of that structure [120]. Thus, during α' formation the height of the first peak indicates the radial "strength" of Cr-Cr correlation in α' relative the nominal composition, and the width the size of α' region. Thus, the integrated RDF curve (RDF_{Area}) is obtained by: $RDF_{Area} = \sum_0^r g(r)dr$, gives a mean to make quantitative Cr probability in α' relative the nominal Cr composition of the specimen. This approach (similar to the integrated coordination number [168]) is applied to the Fe-50Cr alloys in the transition over the top of the MG. The maximum radial length of α' is arbitrarily set to 3nm, mostly because we are interested in the α' core but also to ease computational power. The values of RDF_{Area} are compiled in Table 4-5, the investigated volume was 20nm^3 and dr = 0.3nm, as a reference in this case when there is no deviation from the nominal composition in the sample RDF_{Area} = 3. As expected, there is quite a significant difference between alloys with a clearly spinodal α' morphology and alloys with much smaller Cr rich regions, i.e. <570°C versus higher temperatures. For higher temperatures no significant difference in the amount of Cr-Cr affinity was detected, however interestingly the 580°C value is slightly higher than 578°C. Thus, looking at the Cr distribution distances on the RDF curve itself revealed a reduced height at 0 radial distance but a higher average value. Meaning that Cr-Cr affinity at the α' core is lower, but spread out over a larger distance, this could be an indication of dissolution of small Cr rich regions.

Thus 580°C is the temperature that is clearly out of the MG for 50at.%-Cr. Due to the fact that the alloy is not prone to form Cr rich regions, the detected cluster size is stagnant, the V-parameter does not evolve with time and it is not possible to detect any ΔHv. The statistical characteristics of the samples included in this study have been compiled in Table 4-5.

Table 4-5. Collected AP analysis of the limits of the MG at Fe-xCr$_{x=20,35,50}$.

Alloy	Temp. [°C]	Time [h]	*V*	χ^2/freedom	λ [nm]	RDF_{Area} [nm^2]
Fe-50Cr	565	120	0.88	385.9 / 36	10	3.386
Fe-50Cr	570	120	0.45	127.6 / 31	12.5	3.137
Fe-50Cr	575	24 / 120	0.21 / 0.39	271.0 / 29	-	3.039
Fe-50Cr	578	24 / 120	0.18 / 0.22	85.3 / 28	-	3.035
Fe-50Cr	580	24 / 120	0.17 / 0.18	67.3 / 28	-	3.036
Fe-50Cr	595	145	0.09	53.4 / 28	-	3.017
Fe-35Cr	550	120	1.05	375.2 / 36	10.8	-
Fe-35Cr	560	120	1.00	394.8 / 35	11.0	-
Fe-35Cr	563	120	0.49	437.6 / 35	13.2	-
Fe-35Cr	568	120	0.43	522.2 / 36	20.4	-
Fe-35Cr	570	120	0.19	56.3 / 29	-	-
Fe-35Cr	1100	2	0.02	41.0 / 29	-	-
Fe-20Cr	537	120	0.36	419.9 / 31	-	-
Fe-20Cr	540	168	0.08	69.1 / 24	-	-
Fe-20Cr	550	120	0.03	40.8 / 23	-	-

Significant changes to the *V*, e.g. the Fe-35Cr alloys transition from 568°C to 570°C, is attributed to a change of Cr segregation mechanism. Comparing the *V* in the Fe-50Cr alloy between 580°C and 595°C, we see the temperature-dependent trend decrease of *V* that appears to be stable in time. The transition between 537°C and 540°C in the Fe-20Cr alloy is the sharpest transition from NG to very little clustering. This is due to the nature of the Cr-segregation mechanism (i.e. NG) where an activation energy is needed, the lower temperature (i.e. less thermal fluctuations) and the lower Cr solute content (a lower probability to form randomly Cr rich regions in the volume).

4.3.1.1 Fe-35Cr: Wavelength evolution in proximity to the limit of the miscibility gap

When modelling phase separation, the initial structure, (such as initial fluctuations) definition of the free energy function, kinetic, motilities etc. is key for the evolution of the modulated structure [14]. In relation to the NG process where the three stages are: nucleation, growth and coarsening, is clearly defined, SD is more complex as the transitions are generally "softer".

Still, to evaluate the thermal effect on characteristic wavelength λ of the structure, a time exponent of its growth rate can be used [169]. Naturally, at higher temperature, kinetics favours the growth rate of λ periodicity, given that ageing occurs within the limits of the MG. The result is faster formation of a coarser SD structure. As seen by Yan et al. [169] through a

lower volume fraction of α' at higher temperature in the steady-state, at the same time a larger α' average "radius" and lower number density of α'.

The instability to compositional fluctuations in Fe-Cr is often described in phase field modelling by the Cahn-Hilliard (CH) equations, see section 2.4.1, where, in essence, the general solution of a sinusoidal expression for the composition fluctuations by which wavelength develop within the structure is obtained as,

$$\lambda > \lambda_C = 2\pi \left(\Big/ -\frac{\partial^2 G}{\partial C^2} \right)^{1/2} \tag{4.1}$$

Where λ_c is the critical wavelength below which concentration fluctuations are unstable. A maximum of the development rate is found at $\sqrt{2}\lambda_c$ which naturally would be the favoured characteristic wavelength. As the wavelength is dependent on the second derivative of the free energy term in equation (4.1) it means it is dependent on thermodynamic parameters, i.e. the temperature and composition. Naturally, when the spinodal curve is approached, defined by $\partial^2 G/\partial C^2 = 0$, the wavelength goes towards infinity.

By this reasoning, it is possible to investigate the approach towards the spinodal through incremental temperature increases for a single alloy within a fixed time interval. Thus, isothermal heat treatments of 120h were investigated in the Fe-35Cr alloy. Starting from within the MG where the alloy decomposes through SD and then increasing the temperature until the limit of the miscibility gap is reached (i.e. $\partial^2 G/\partial C^2$ tends to 0). The result is shown in Figure 4-11.

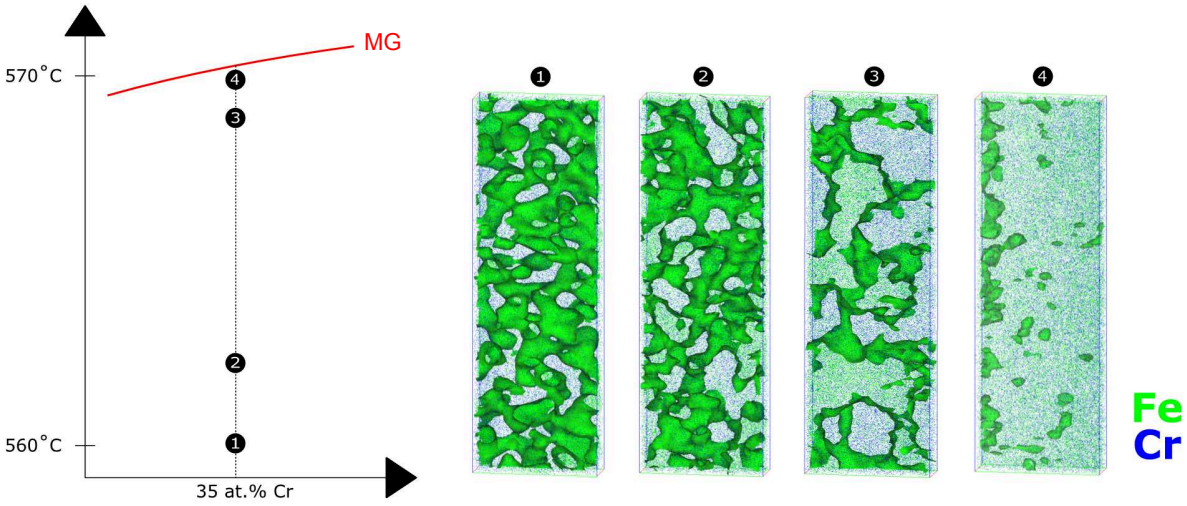

Figure 4-11. Evolution of the nanostructure approaching the top of the estimated metastable miscibility gap (MG), volumes 10x20x60nm the *iso*$^{th.}$ have been used to illustrate α'.

The variable *iso*$^{th.}$ surface is evaluated by the proximity histogram, and only 8% of the Fe and Cr ions are displayed in the reconstruction for clarity. What can be seen is the evolution of the characteristic wavelength as the top of the MG is approached. Within the top 10°C of the MG, there is an evolution of λ that follows an exponentially increasing trend. This occurs as the free energy derivative in equation (4.1) goes towards zero and thus λ_c to infinity. The temperature dependence of the wavelength evaluated by ACF is presented in Figure 4-12 along with the corresponding V values.

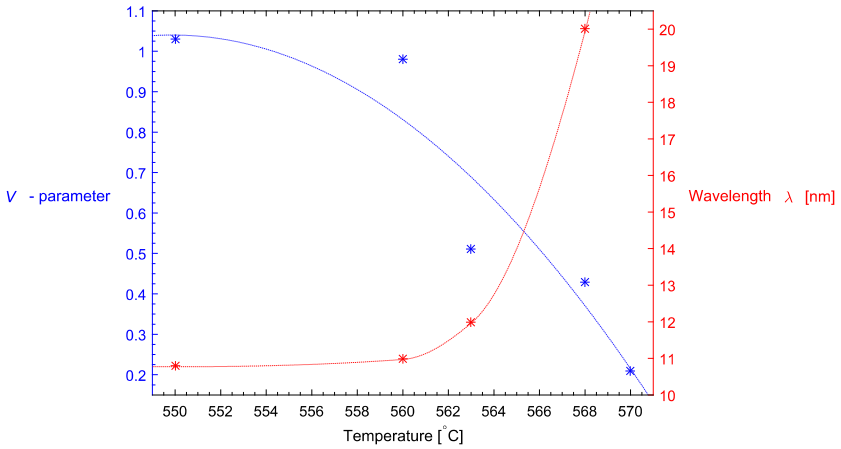

Figure 4-12. Evolution of wavelength and V-parameter with temperature of the Fe-35Cr alloy ageing time 120h. The curves are fitted with a cubic trend for V and shape-preserving spline interpolant for λ [170].

What is seen in Figure 4-12 is a clearly more homogenous alloy forming as the periodicity of the Cr fluctuations increases. Given the small temperature range, this is clearly not an effect of temperature-dependent Cr diffusion or surface energy, but rather a decreased undercooling

from the critical limit of the spinodal line. The reason why no wavelength is presented in Figure 4-12 although there are clearly some Cr rich regions in Figure 4-11 is because they appear irregularly. Meaning it is possible to measure some Cr-rich regions by a wavelength of approximately 90nm, but it is not repeatable over several wavelengths as the investigated volumes covers only a few wavelengths in-depth or representative of the structure.

4.4 Thermoelectric Power: finding the spinodal line in binary Fe-Cr alloys

Thermoelectric power (TEP) is a unique and simple way of investigating the kinetic evolution of phase separation with very high precision and efficiency, in a large interactive volume. An additional benefit is that it is a non-destructive method and has a high accuracy of the reproducibility of the measurements, and do not require sophisticated experimental devices. The utilization of simpler techniques is a more efficient way to explore different aspects of the MG, for example, the detailed kinetic evolution at different alloy compositions and temperatures. This is now possible as we know with high precision the limits of the MG.

The binary alloys have all been aged at a fixed temperature within the miscibility gap. The selected temperature was 525°C so that the Fe-20Cr alloy should be within the NG regime of the MG, where a ΔHv response due to phase separation was clearly measured after ~24h. Based on CALPHAD calculations and our exploration of the limits of the MG Fe-35Cr and Fe-50Cr is well within the SD regime of the MG [158], [171], [172]. High temperature within the MG favours the kinetics so that a transient growth stage would be reached within the first 120h.

TEP is highly sensitive to redistribution of solute atoms, therefore the number of solute atoms and the nature of the decomposition process would influence the absolute TEP values. The result of the kinetic TEP investigation is presented in Figure 4-13. In this figure the evolution of the ΔTEP is represented, i.e. its change relative to the solution treated reference state.

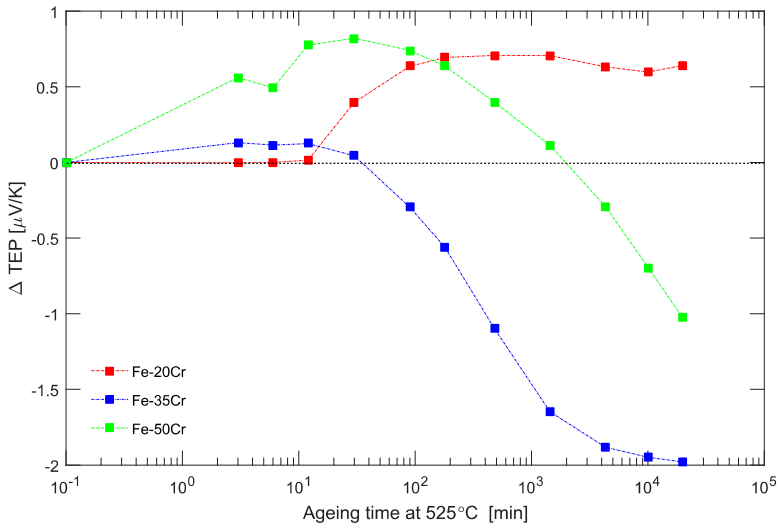

Figure 4-13. The diffusion path of NG and SD in Fe-Cr alloys according to ΔTEP at 525°C.

An interesting point is to notice the potential difference in response to the kinetics of alloys with different Cr content, i.e. supposedly the difference in kinetic evolution NG versus SD. Cr should have a positive effect on TEP, so when Cr is leaving the solid solution to form α', the TEP value is expected to decrease [93]. TEP is more sensitive to the effect of solute atoms on the matrix phase rather than the number density or volume fraction of the precipitating α' phase. It has been seen that coherent precipitates may have positive or negative effect on the absolute value of the TEP [173]. Thus, the effect of α' formation on ΔTEP is more complex than what one might expect for Fe-Cr alloys.

TEP of magnetic Fe/Cr multilayers has previously been investigated [174]. Where, assuming free electrons, the sign of the TEP was attributed to the so-called spin-mixing resistivity, $\rho\uparrow\downarrow$: where ρ is the resistivity, ↑ are positive electron spins and ↓ are negative spins. By considering the electron-magnon scattering contribution to the TEP the point to notice is that there is an essential difference between the scattering of ↑ and ↓ electrons. A spin ↑ electron with wave vector $\boldsymbol{k}$ can be scattered into a spin ↓ state given by the wave vector: $\boldsymbol{k'} = \boldsymbol{k} + \boldsymbol{q}$, through the annihilation of a magnon ($\boldsymbol{q}$). So that the energy of the magnon (E_q) is transferred to the electron: $\varepsilon'_k\downarrow = \varepsilon_k\uparrow + E_q$. For the opposite, scattering of a spin ↓ electron involves the creation of a magnon $\boldsymbol{q}$ and thus a decrease of the electron energy: $\varepsilon'_k\uparrow = \varepsilon_k\downarrow + E_q$. Through this reasoning, it was the sign of the magnetic - TEP is dependent on whether the ratio between the resistivities for the two spin directions is greater or less than unity. Thus, ΔTEP is negative for $\rho\downarrow > \rho\uparrow$ and positive for $\rho\downarrow < \rho\uparrow$. Hence, if the majority of the spins would be in one ↓ direction in a ferromagnetic state, and the contribution to ΔTEP would be negative. In an anti-

ferromagnetic state, there is a mix of positive and negative spins so that their net contribution ΔTEP ≈ 0.

The magnetic transition zone was investigated in homogenous Fe-Cr alloys by Loegel [175], through room-temperature resistivity measurements of high Cr alloys. They were solution treated at 1100°C for 3days. It was found that alloys with less than 71%-Cr were ferromagnetic and if they contained more than 80at.%-Cr they were antiferromagnetic. Between 80-71 at.%-Cr a superparamagnetic state was found. The magnetic mixing contribution can be determined by the heat capacity of the system, i.e. as a function of the Curie temperature. Thus, the Ferro- to paramagnetic transition has an SRO magnetic energy effect on the heat of mixing [176].

Because ΔTEP is very sensitive to the deformation of the Fe matrix lattice, and Vegard's law: $a_{Fe_{1-x}Cr_x} = (1-x)a_{Fe} + xa_{Cr}$ holds for Fe/Cr mixing in the Fe-Cr system, a lattice difference can be expected between the Fe-35Cr and Fe-50Cr due to the amount of Cr. In addition, the fractional change in lattice parameter per unit composition change (η) is $\eta_{Fe-Cr} = 0.005$. It is possible that this may affect TEP evolution between Fe-35Cr and Fe-50Cr displayed in Figure 4-13 since time temperature and decomposition process are the same. Thus, the removal of Cr atom from the Fe based matrix may still largely influence on the changes of ΔTEP. To further understand the change one may need to consider clustering effects on resistivity, local lattice defects due to composition changes and SRO magnetic effects [94], [176].

The Fe-20Cr alloy and the Fe-50Cr alloy presented in Figure 4-14 were further aged up to 23 days to solidify their ΔTEP evolution before APT analysis. The APT results revealed that the Fe-20Cr alloy had been affected by nitrogen (N), presumably from the air atmosphere. The N content in the Fe-20Cr alloy (see Table 4-6) is close to the solubility of N in the Fe-Cr-N system at 1100°C [177], which indicates that contaminations may have occurred during homogenization. No such contamination was observed for the Fe-50Cr alloy. Cr has a high affinity towards O and N thus solution treatment in air of ferritic stainless steel could possibly result in nitride formation 1050-1200°C and retain fcc/bct [178], [179]. Although the Fe-50Cr alloy has a higher N solubility in α at this point, but it is still the Fe-20Cr alloy that contains the most N from the APT analysis. One might argue that it is an effect of APT being a local measurement but still, the result in Figure 4-14 is based on one large tip of 32 million ions for Fe-20Cr and another even large 50 million ions for Fe-50Cr.

To be sure that we measure SD with our ΔTEP measurements prior to this kinetic analysis presented here, the setup of the test had been tested. Samples in capsuled in Ar atmosphere versus air were aged up to 3.5days outside and inside of the miscibility gap. Samples aged at ~600°C, i.e. outside the miscibility gap remained homogenous with an average ΔTEP ≈ 0.01 μV/K. The samples aged in Ar atmosphere had a standard deviation of ~21%, while those in air had a standard deviation of only ~3%. This was attributed to the much smaller and more accurate calibration furnace possible to use for the in-air aged samples. Ageing within the MG in Ar atmosphere was also made for Fe-50Cr at 570°C, which gave an initial increase of ΔTEP = 0.24 μV/K after 3min before the ΔTEP = -0.17 μV/K was reached after 3.5days, ensuring that encapsulation of the samples in Ar atmosphere was not necessary to follow the evolution of ΔTEP. Thus, it is unlikely that this ΔTEP evolution in the Fe-50Cr alloy is attributed to anything else than phase separation.

In addition, it has been reported that N has a negative effect on ΔTEP and that incoherent precipitates do not change the ΔTEP [180]. Thus, from the reported ~0.14at. %N in Fe-20Cr one would expect a decrease of the ΔTEP if N pickup occurred during ageing. Since the absolute value of the ΔTEP in its initial state was positive. A possibility is that N pickup occurred during solution treatment and that during ageing N leaves the matrix to form Cr_2N and thus lowering the ΔTEP. But ΔHv measurements shall, later on, support the fact that we have α' precipitation after approximately 24h at 525°C (see Figure 4-24). We can be sure that this is in fact incubation time for NG and not Cr_2N that affect the surface mechanical properties [181], by variation of ΔHv response to temperature and time variations. Since N is an interstitial element in the Fe matrix, thus its diffusion should be much faster than for Cr [179]. The following table is the bulk composition of the samples that had been aged for 23days.

Table 4-6. Mass-spectrum analysis of the Fe-20Cr and Fe-50Cr alloys aged for 552h.

Alloy	**Al**	**Fe**	**Cr**	**V**	**Si**	**P**	**S**	**Ni**	**FeN**	**CrN**	**N**
Fe-20Cr	0.044	79.47	20.25	0.0035	0.022	0.0016	0.0024	0.0044	0.0069	0.026	0.138
Fe-50Cr	0.056	49.78	50.06	0.012	0.062	0.0027	0.0014	-	0.011	-	-

What is peculiar with the estimation of Si and N in the APT mass spectra is that they "share" a similar mass-over-charge state. Thus, discrimination between Si and N in the mass spectra is cumbersome, 96.23% of Si^{2+} sits at 13.99 Da. while 99.63% of N^{+} is at 14 Da. The way to discriminate between them is through the minor isotopes of Si^{2+} and then estimate the composition of the common 14 Da. peak through their natural abundance. This is made in combination with mass peak deconvolution when FeN and CrN nitrides are clearly visible in the mass spectra. If an exceptionally high-quality mass spectra is experimentally produced

without the obvious presence of nitrides in the reconstruction, then the full 13.99 Da. peak is assigned to Si^{2+}, but only if it is accurately cantered (i.e. not drifting towards 14 Da.), and if the minor Si^{2+} peaks are clearly present.

The morphological difference after ageing the samples for 23days is displayed in Figure 4-14. The proximity histogram threshold, $iso^{th.}$ equation (3.21), has been used in both cases since 23days was proven to be sufficiently long to create significant Cr depletion of α matrix for Fe-50Cr.

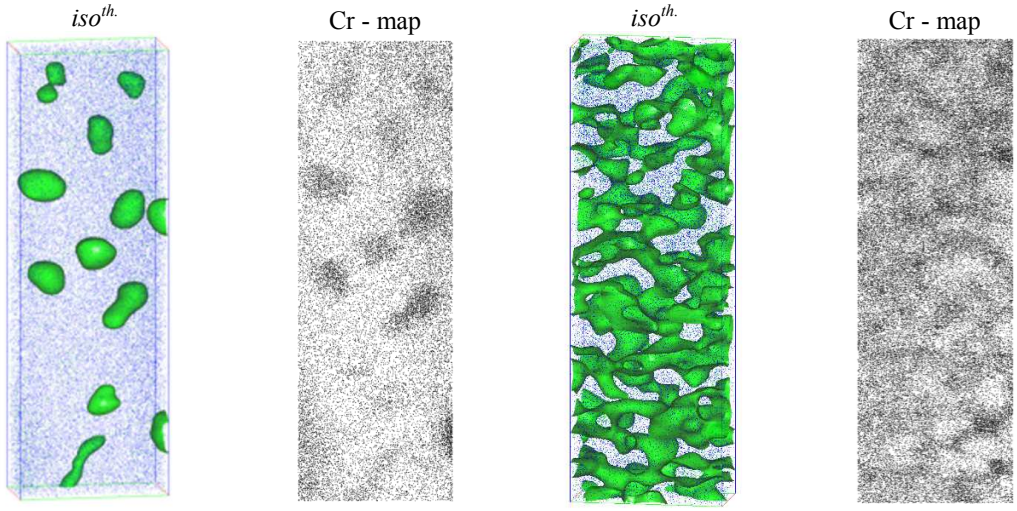

Figure 4-14. Final morphology Fe-20Cr versus Fe-50Cr, volume: 10x20x60nm, temperature: 525˚C, time: 23days. The threshold is variable (equation (3.21)) and Cr atoms displayed are 10%.

From Figure 4-14 it is evident that the $iso^{th.}$ threshold is a good way of highlighting the morphology of the Cr enriched zones, the comparison with the Cr dot maps are added to confirm that.

In Table 4-7 is the quantitative analysis of the nanostructure compiled. The variance V and cluster analysis (5^{th}-*NN*) were conducted in a 20x20x60nm volume similar to the displayed volume in Figure 4-14.

The reason for selecting such a volume is that it is easy to visualize, easy to avoid artefacts in a relatively large volume and the resolution is better in-depth (due to the presence of the low index pole). The RDF uses Cartesian coordinates and periodic boundary conditions, thus it works better in a square volume, 20x20x20nm so that any dependency on e.g. analysis direction is avoided. The radial increment, *dr*, was fixed to approximately the length of one lattice parameter.

Table 4-7. Analysis of the binary Fe-Cr alloys, volume 20x20x60nm for *V*, 5th - *NN* and 20^3nm for RDF.

Alloy	V	$f_v^{Nr.\rho}$	5th – *NN*			RDF- analysis	
			$f_v^{5^{th}\text{-}NN}$	α	α'	*Amplitude* [at.%-Cr]	*Wavelenght* [nm]
Fe-20Cr	0.99	0.165	0.100	14.93	68.01	54.33	9.70
Fe-50Cr	0.95	0.302	0.372	37.55	70.38	56.63	6.47

The value of the RDF at the "zero distance", i.e. RDF(0), is related to the amplitude of the periodic structure. Because RDF gives the average composition of our first dr = 0.3nm shell at r = 0.3nm, backwards extrapolation of the RDF curvature is used to obtain the composition at the very core of the Cr enriched zone at r = 0nm. This approach was proposed by Zhou et al. [120], based on the theory of Cahn [36]. The RDF curve is a sinusoidal distribution of a periodic function *f*. Thus, integrating *f* over one period of the sinusoid, normalized by the volume of this period is how to solve for the general periodic function: $f(r) = C_0 + A\sin((2\pi/\lambda)\cdot r)$, similar to Cahn's general solution. The amplitude ($2A$ at $f(r=0)$) from the RDF function is then calculated as: $2A = 2C_0\sqrt{2(\mathrm{RDF}(0)-1)}$. These values are reported in Table 4-7, as RDF-Amplitude. Note that the fluctuation amplitude of SD by RDF is greater than the difference in composition between α and α' evaluated by 5th-*NN* cluster method. This is because the reported concentration of the clusters is an average of all extracted clusters. While the amplitude provides the extreme values, at the very core of the α' zones. The RDF analysis at 525°C after 23days is given by the graph in

Figure 4-15. What signifies the difference is that the Fe-20Cr exhibits stronger short-range affinity and the Fe-50Cr alloy have a shorter preferred long-range separation difference, i.e. λ.

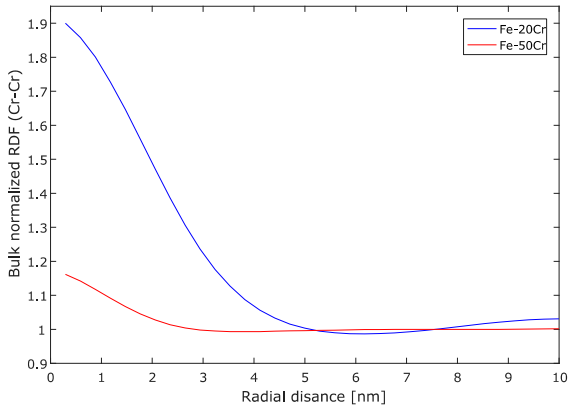

Figure 4-15. RDF of Fe-20Cr and Fe-50C at 525°C for 23days. The strength of Cr-Cr affinity is associated to the width and height of the RDF. Thus $(Cr-Cr)_{max}^{20Cr} = 1.90$, the distance to the 2nd RDF maxima $R_2^{20Cr} = 9.70nm$, $(Cr-Cr)_{max}^{50Cr} = 1.16$ and $R_2^{20Cr} = 6.47nm$.

In the frequency distribution analysis, *V*, the alloys are similar far along in terms of global Cr redistribution even if the morphology of Cr rich phases are clearly different. This measurement becomes less sensitive in the later stages during coarsening, because of diffuse interfaces, dissolution and annihilation of precipitates. Of course, sampling size matters and here 50ion binning was used.

Worth noticing from Table 4-7 is the matrix composition of the Fe-20Cr alloy, where Cr content is significantly less than current CALPHAD estimates for α' precipitation, meaning that the precipitate is not yet at equilibrium.

4.4.1 TEP verification of NG by the Nb-stabilized Fe-20Cr alloy

As a result of the uncertainty introduced by the N effect on the ΔTEP of the binary Fe-20Cr a lot the Nb-stabilized Fe-20Cr alloy presented in section 4.2.1 was used to verify our results, i.e. to be sure that NG provokes in an increased ΔTEP.

In the case of this Nb-stabilized Fe-20Cr alloy it is clearly established that it is the nucleation and growth process that has been studied, see Figure 4-5 and Figure 4-6. Mass spectrum analysis from APT did not indicate any pickup of N nor did any of the reconstructions show any visible nitrides. No niobium (Nb) precipitates were found in the reconstructions either, even if Fe_3Nb_3X precipitation in the same alloy has been studied earlier [180], with volume fraction was deemed very small. But Fe_3Nb_3X present in the initial state after annealing at 1050°C was, in that case, analysed in APT by FIB sample preparation, a lever rule estimation based on their composition would give a volume fraction of 0.53% [180]. In addition, ageing

at 650°C and below did not give any ΔTEP response from Nb precipitation. Thus α' precipitation in this alloy is considered as the only process investigated by TEP at 525°C, the results of which are shown in

Figure 4-16. Relating the NG precipitation process to ΔTEP in Fe-Cr alloys is made through the Avrami equation [22], where the transformed fraction $f(t)$ is given as a function of time t,

$$f(t)/(1-f(t)) = K(T)t^n \tag{4.2}$$

Where K and n are material constants specific to the nucleation process, the fraction of precipitated can be related to ΔTEP by the relation,

$$Y = \frac{\Delta TEP_t - \Delta TEP_i}{\Delta TEP_f - \Delta TEP_i} \tag{4.3}$$

Y is given in Figure 4-16, where ΔTEP_t is the relative TEP measurement at time t, ΔTEP_i and ΔTEP_f are the relative measurements at initial and full transformation respectively.

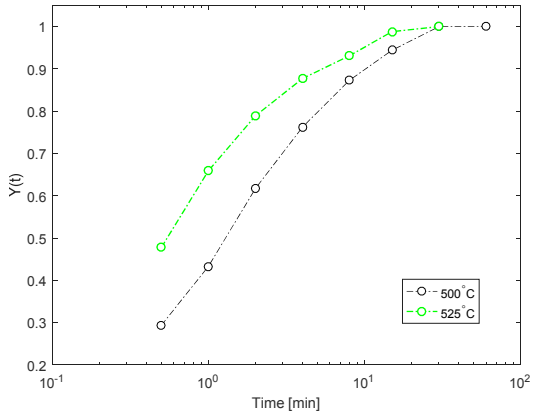

Figure 4-16. Normalized TEP graphs at various temperatures for kinetic comparison of the Nb-stabilized ferritic steel.

The function Y is the normalized ΔTEP evolution, note the positive kinetic evolution in the same way as for the Fe–20Cr alloy in Figure 4-13. To solve for the material-specific constants in equation (4.2) in our case we plot the graph ln(Y/(1-Y)) versus ln($t/\Delta TEP_i$) to obtain ln$K(T)$ and n from the linear approximation for both temperatures. We then plot ln$K(T)$ versus 1/RT to obtain the apparent activation energy (Q) from the TEP variation. The value we obtain is Q=232.12kJ/mole, close to the activation energy of Cr self-diffusion in α-Fe which is Q=248kJ/mole [182]. Therefore, given the relation of the increase in volume fraction, Figure 4-6, and the correlation with ΔTEP, it is certain that this variation comes from the apparent

activation of Cr diffusion in the matrix. Therefore, the increase in ΔTEP is associated with the NG process consequently the decrease in ΔTEP is then associated with the SD process.

4.5 Literature review: Experimental phase separation in the Fe-Cr system

Fe-Cr alloys are a well-researched topic yet there is still interest from academics and industry, as the experimental techniques evolve the understanding of the system do too.

A comprehensive review of the Fe-Cr system, including the metastable MG, has been compiled by Xiong et. al. [171]. It was shown that the determination of the limit of the metastable MG has in the past been inconsistent and the experimental results of the consolute temperature varied ~120K. A new magnetic model based on the work by Chen and Sundman [183] was since implemented [12]. In addition, *ab-initio* data for the enthalpy of mixing (H_{mix}) and magnetic ordering energy of mixing (MOEM) was considered to extend the thermodynamic model down to 0K. The possibility of Cr solubility in α-Fe at 0K was ruled out based on deviating effect of experimental H_{mix} measured at 1256°C and its effect of a much higher consolute temperature than in experiment [172]. The new thermodynamic model by Xiong et al. matches their APT results for the spinodal and Kuwano's Mossbauer experiments of the MG consolute temperature [184]. However, some differences between the thermodynamic model and the ab initio calculations at 0K remained, they were attributed to the simplistic ferromagnetic *ab-initio* treatment.

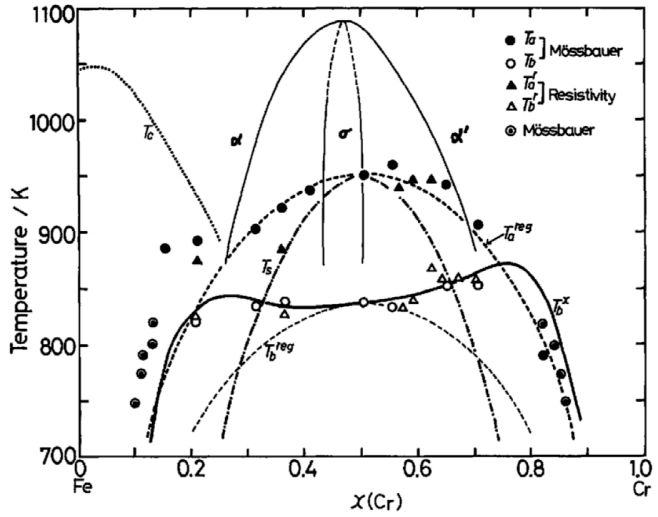

Figure 4-17. The Fe-Cr miscibility gap evaluated by Mössbauer spectroscopy [82].

Kuwano [184] found two demarcations, defined by the temperatures T_a and T_b, that describes the transition over the top of the MG. The T_b dataset corresponds to the lower temperature in the MG below which α' forms. A region T_b to T_a was found where de-mixing occurs in the presence of a competing σ phase formation. In the end, the critical limit of the MG was represented by T_a. However, the two representations (i.e. T_a^{reg} and T_b^{x}) of the MG limit was still presented. The T_a data points were fitted with a model T_a^{reg} in good agreement with the regular solution behaviour. The T_b data were fitted by T_b^{x}, but it was discarded as the limit of the MG, because it deviated largely from behaviour of a regular solution, without any physical explanation for this behaviour. As an example, a regular solution fit to the T_b data would give approximately 30at.%-Cr solubility in α-Fe at 500°C, which is unreasonable. Hence, Kuwano concluded that T_a should represent the limit of the MG, however, it was also stated for the region T_b - T_a : "*the attending concentration change is not so large in amplitude to yield the Cr-rich phase and/or the Fe-rich phase. The temperatures, Tb's are the limiting temperatures above which these phases cannot exist stably*".

The thermodynamic description by Xiong et al. is, however, still less frequently used than the description by Andersson and Sundman [158]. Because the Andersson and Sundman [158] description (in good agreement with Vilar's thermal gravimetric results [185]) is a "popular" description considering that it is the description is currently implemented in ThermoCalc TCFE9. In experimental work on α' formation the evolution of mechanical properties is generally explored at temperatures of ~500°C. The upper limit of the MG has also been investigated frequently and several reports suggest that it should be lower than the thermodynamic descriptions in [158], [183], see e.g. [159], [186], [184], [187]. However, the

result in literature is still ambiguous and one of the reasons for this could be the complicated transition between mechanisms of Cr nano-segregation, i.e. clustering due to short-range order (SRO) as well as stable growth of α' by either NG or SD.

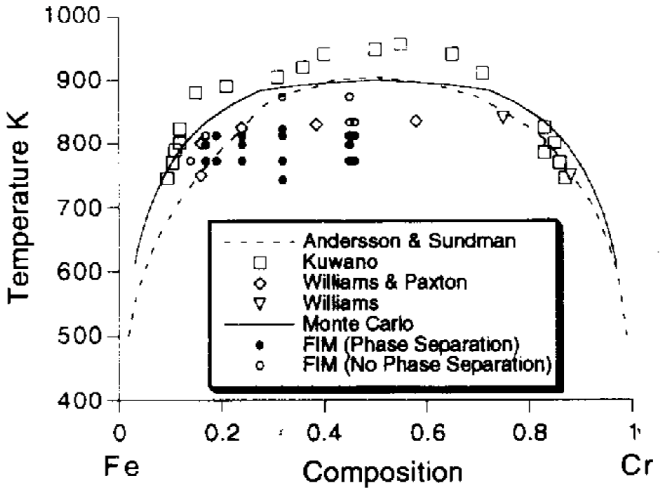

Figure 4-18. Compilation of experimental and theoretical description of the metastable Fe-Cr MG [159].

It is evident that a regular solution model cannot accurately capture the complexity of the Fe-Cr system. For example, at temperatures 1200-1400°C, well above the MG, α' is still not fully homogeneous and high-temperature Cr-Cr clustering can be observed [187]. Therefore, stating that Kuwano's T_a experiments represent the true MG limit based on its nearly ideal behaviour seems to be too simplistic. The limit of the MG must be further investigated, especially against the SRO clustering in the vicinity to the MG limit and MOEM effect on Cr-Cr interaction above the MG. Since SRO is both temperature and composition-dependent, therefore it increases the difficulty to indirect investigate the limit of the MG [159], [172], [184]–[187]. The Cr-Cr clustering is distinctive in the atomistic modelling of thermodynamic properties for the Fe-Cr system [188]. One of the characteristics of the Fe-Cr MG is that it is asymmetric. This can be explained by the contribution of the negative enthalpy of mixing. The enthalpy of mixing is also known to have an effect on the height of the miscibility gap [12], [172].

The solubility of Cr in α and α' is determined by the limits of the MG. Thus, at $\alpha+\alpha'$equilibrium their compositions define the boundaries of the MG. Therefore, in many experiments, long-term heat treatments are performed and at.%-Cr in α' is asymptotical extrapolation in order to estimate the equilibrium compositions [189], [190], [114] [191], [192]. This is because the MG in Fe-Cr is a low-temperature MG, and therefore (when possible) very

long time is required to reach close to equilibrium. However, even after very long heat treatments as by Hedin [193], 100,000h at 350°C equilibrium condition is not reached.

The spinodal curve can give important information regarding the shape and position of the MG. In theory, the spinodal is delimited by the line calculated using the second derivative of the Gibbs free energy (G), at $\partial^2 G/\partial X^2 = 0$, which should not be misinterpreted as a sharp transition between NG and SD. It has been observed that there is a large transition region where both decomposition mechanisms are present simultaneously [12], [82]. A percolated nanostructure with high density of α' precipitates can make it hard to distinguish between these two mechanisms, even with direct 3D measurements such as APT. However, indirect measurements to determine the dominant mechanisms based on the kinetics of phase separation have been made. For example, the kinetic development of the paramagnetic peak which corresponds to the Cr-rich α' has been studied using the Mössbauer spectroscopy (MB) technique, by Kuwano [82]. Determining the decomposition mechanism in close proximity to the NG/SD transition is not exact [18], [84]. During the thermodynamic modelling by Xiong et al. [12], one of the key points was to accurately pinpoint the spinodal line using APT, although in a 10at.% composition range at 500°C.

In spite the fact that Xiong et al. [171] through an extensive review of the experimental data showed that the limit and the understanding of the MG is not fully conclusive, they presented a model in reasonable agreement with the experimental T_a data obtained by Kuwano [184]. However, this description is questionable [152] and one of the purposes of the present work is to define the limit of the MG and to provide a better understanding of the transition between mechanisms of nano-segregation in Fe-Cr, i.e. NG, SD and SRO.

4.5.1 Comparison with CALPHAD

To conclude this section on α' precipitation should be noted that the limit of the miscibility gap found in this work differs significantly from the current CALPHAD description, seen in Figure 4-19. Hence, in combination with a new unary description and in light of these experimental data a re-optimization was performed based on the result presented here and the literature review (section 4.5.2).

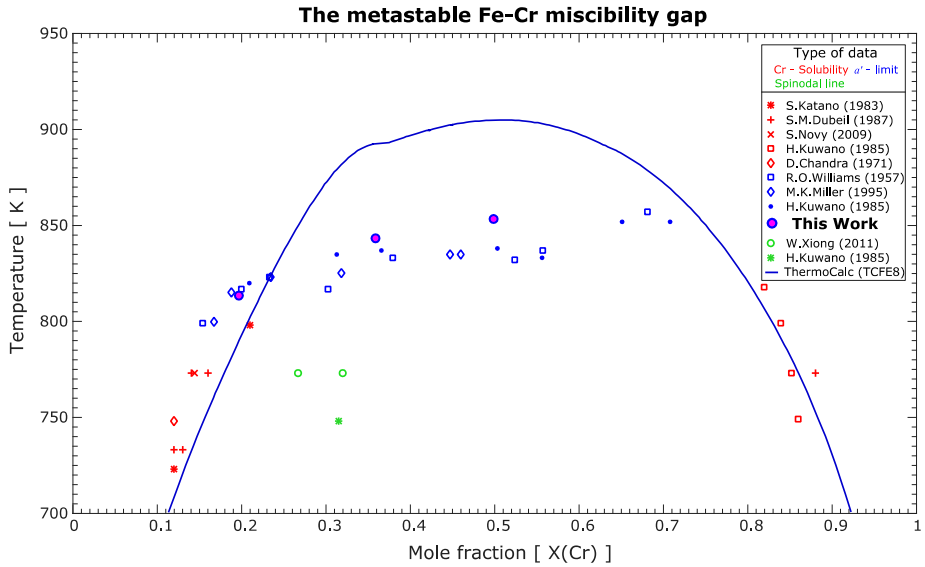

Figure 4-19. A comparison between the metastable MG according to CALPHAD, i.e. ThermoCalc TCFE8 database, this work and literature data. Not that the temperature is given in Kelvin as it is the standardized unit when working with CALPHAD.

In Figure 4-19 focus is on binary alloys that defines the limit of α' formation. What is obvious is that the CALPHAD description (given by the solid line) overestimates significantly the consolute temperature and the Cr solubility in α. The transition from ferro- to paramagnetic state defined by the Curie temperature contributes to the heat of mixing (ΔH), producing the asymmetric shape of the MG. Previously, there has been reported a hump at approximately X(Cr)=0.7 which has been linked to the antiferromagnetic transition to the Cr based alloy [186]. Supporting the fact that the top of the MG is approached in Fe-35Cr alloy is that λ increase as V decrease, as explored in section 4.3.1.1, what is reveals increased randomization and wavelength in-between Cr fluctuations.

To conclude, the experimental work conducted here has provided us with novel results in reasonable agreement with selected previous works. The high precision heat treatments in combination with APT allow for the determination of the MG limit in a very narrow temperature range, by direct investigation of the α' phase. This has not been made before by direct methods, which is why we now can determine the limit of the MG with such high precision. For example, the investigation by Miller et al. [159] did not focus on finding the MG limit they merely indicated the presence of α' at high temperatures.

4.5.2 Optimization of the Fe-Cr CALPHAD description

The physical limits of Fe-Cr phase separation are determined by the thermodynamic descriptions of the system, this also affects the kinetics which is highly temperature-dependent. Based on the review in section 4.5 the thermodynamic description of the MG has been re-optimized using the PARROT moduli in the ThermoCalc software. Thus utilizing a third-order RK polynomial in conjunction with the new unary descriptions of Fe and Cr, and the new magnetic model [12] the shape of the MG has been optimized by experimental data. The PARROT module works by minimizing the sum of squared errors, where the error is the difference between the calculated and experimental value. It is possible to assign weights to the experimental values so that the importance of certain data can be empathized. The result is a new regular solution parameter that better describes the experimental in literature and data presented later in this work all compiled in Table 4-8.

Table 4-8. Compiled data from literature.

Reference	Material	Time [h]	Technique
Inden & Dubiel [192]	Fe-0.15Cr	10^5	MB
	Fe-0.706Cr	35500	MB
	Fe-0.208Cr	35500	MB
Katano & Iizumi [191]	Fe-0.40Cr	20	SANS
Novy et al. [114]	Fe-0.20Cr	1067	APT
Chandra [189]	Fe-0.24Cr	1738	MB
Bergner* [190]	Fe-0.09Cr	NA	SANS
Gou et al. [149]	Fe-0.24Cr-1Ni	10 000	APT
	Fe-26Cr-4Ni	10 000	APT
Miller et al. [159]	Fe-0.17,0.19,0.32, 0.45Cr	500	FIM-APT
Kuwano [82]	Fe-xCr	50	MB
Williams & Paxton [186]	Fe-xCr	1000	HV / RES
This Work	**Fe-20,35,50Cr**	**120**	**APT**

MB: Mössbauer, SANS: Small-angle neutron scattering, APT: Atom probe tomography, HV: Vickers hardness, RES: Resistivity measurements, *Irradiated samples 0.6 and 1.5dPa.

The optimization requires classification of the experimental data here focused on phase diagram data, i.e. solubility, temperature ranges of phases, etc. The selection of literature data is restricted to peer-reviewed primary sources. In the evaluation of the MG selection of published data has been mainly based on work with binary bcc Fe-Cr alloys. In addition, the aim of the publication should have been to either determine the presence of α' close to the limit of the MG or the solubility limit of Cr in α or α'. The resulting CALPHAD description is seen in Figure 4-20.

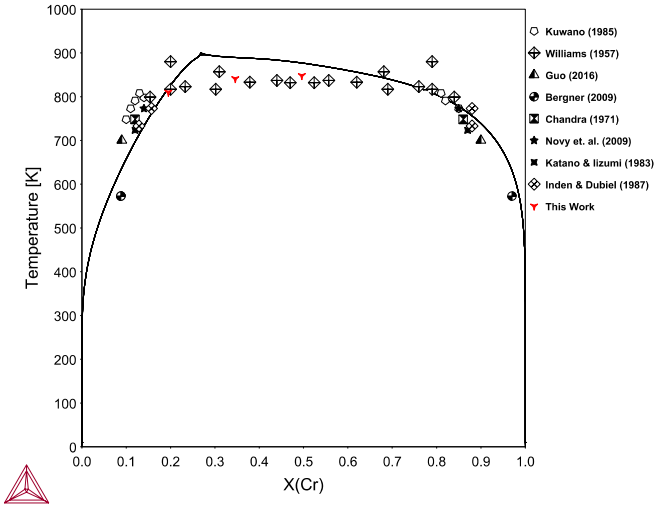

Figure 4-20. CALPHAD description of the Fe-Cr miscibility gap, where temperature (T) is given in Kelvin, this work is highlighted by red markers.

The re-optimization of the Fe-Cr miscibility gap results in a new interaction parameter evaluated by a 3rd-order RK polynomial to be: $L_0^{FeCr} = 28990 - 22.082T$.

The notion that the top of the miscibility gap in Fe-Cr should be flat is simply not achievable with a realistic CALPHAD approach due to anti- to para-magnetic transition. However, it is known than the α phase is not fully homogeneous even well above the MG [187]. The clustering is due to positive Cr-Cr short-range atomic interaction above ~10 at.%-Cr, i.e. a positive Warren-Cowley parameter [194]. Clustering is strong close limit of the miscibility gap and decreases with increasing temperature, so rather than include it within the MG (as Kuwano did [82]) an effort to describe this phenomenon with a quasi-chemical model has been made [195],

$$\frac{p_{AB}}{\sqrt{p_{AA}p_{BB}}} = \exp\left(-\frac{2L}{zRT}\right) \tag{4.4}$$

Where p is the probability to find AA, BB, AB pairs respectively, L is the A-B interaction parameter and z is the number of nearest neighbours. By is this approach it is possible to describe temperature-dependent configurational heat of mixing, through the quasi-chemical equilibrium constant. Where the equilibrium is similarly as defined by Hillert [35].

The calculated metastable miscibility gap is asymmetric due to the magnetic influence on the enthalpy of mixing. Therefore, it is more important to capture the solubility data and have the exact top freer rather than forcing the ultimate temperature down at 50at. %-Cr.

Because forcing down the top results in unreasonable solubility limits and neglect of the magnetism. Thus, a weight between 1-10 is assigned to the experimental data-based reliability, then an error of that measurement is estimated before optimization proceeds.

4.6 Fe-50Cr: Cr-Cr clustering outside of the miscibility gap

As mentioned earlier the initial microstructure is key in predicting the evolution of decomposition through modelling and sensitive kinetic measurements such as ΔTEP. The instability towards infinitesimal fluctuations and thus the kinetics is naturally dependent upon the initial level of fluctuations [14], [152]. Hence, solution treatment and subsequent quench is very important for a homogeneous reference state.

A second-order phase transition that occurs on a level of change in electronic structure has previously been observed by Ustinovshikov and Pushkarev [187]. It is described as the "ordering-separation" regime present from 900±50°C to 570±10°C. Below 570°C is where the first-order phase transition occurs, i.e. the nano-structural transformation described previously also by Kuwano [184].

In the APT reconstruction of α it is obvious that Cr clusters exist in the microstructure that based on the CALPHAD phase diagram is expected to be homogeneous, see Figure 2-1. Cluster analysis methods based on 5th *NN* distribution reveal a high number density of very small clusters with approximately 50ions in them. However, to determine maximum separation distance in a small cluster is non-trivial thus one might question the existence of the clusters. To determine the existence of positive Cr-Cr affinity in a sample is, therefore, better analysed by RDF, see Figure 4-21.

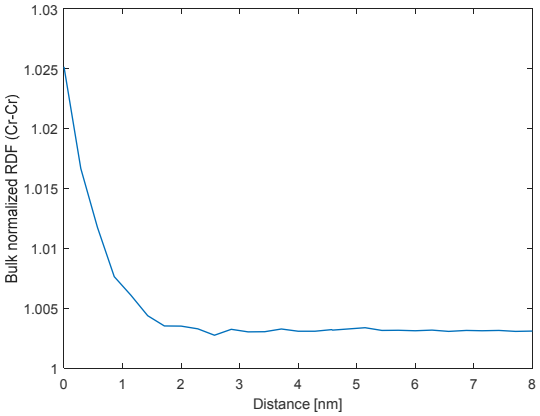

Figure 4-21. Cr-Cr correlation, i.e. clustering affinity in Fe-50Cr alloy at 650°C after 250h analysed by RDF.

What is seen in Figure 4-21 is positive Cr-Cr affinity at distances below 2nm there is no anti-correlation of the Cr-Cr affinity from the bulk composition. Hence, these Cr-Cr clusters are defined as SRO. To quantify the extent of SRO the *V*-parameter is used to obtain the deviation from the binomial distribution.

Short-range ordering (SRO) in terms of Cr-Cr clustering in the Fe–Cr system might the reason why there are so large discrepancies in the definition of the MG by indirect experimental techniques. This SRO was suspected to be temperature-dependent. Hence, knowing the importance of SRO acting as nucleation sites for α' and excitation of the growth of periodic waves it was deemed interesting to pursue this point by APT.

The evolution of the *V*-parameter of samples aged above the miscibility gap as a function of temperature is presented in Figure 4-22 a). It exhibits an exponential decrease as temperature is increased. The analysis is made on a 20x20x60nm volume binning the frequency distribution with a 50ion binning volume. The *V* - parameter is able to detect small deviations from randomness, even in solution-treated alloys it is possible to quantify small Cr fluctuations. In the solution treated Fe-35Cr alloy we obtain $V = 0.02$ and in Fe–50Cr $V = 0.032$. A kinetic investigation of clustering well outside the MG was made, comparing *V* at 650° after 50, 100 and 250h. The result revealed that the quantitative amount of clustering was stable in time with $V = 0.072 \pm 0.003$. To rule out an effect of the MG we come back to the evaluation in section 4.3 and particularly in the Fe-50Cr alloy deemed to be outside of the miscibility gap, at 580°C, where the difference in *V* was 0.01 between 24 and 120h. If the evolution of *V* was greater than the variations in the reference state, then the alloy was deemed to have been affected by the decomposition and therefore aged within the MG. Thus, at 580°C there is clearly a detectable

difference, however, in relation to the solution treated state evolution of fluctuations were insignificant.

As V is based on the deviation from randomness in that specific alloy it is possible to compare the value relative alloys of different compositions. Which gives us further indication that the limit of α' formation from SD is obtained around $V = 0.18 \pm$ the value obtained in the reference state, supported by the Fe-35Cr alloy. Increasing the temperature just 10°C above this α' limit we obtain a kinetically stable value of $V \approx 0.1$ with kinetic variation much smaller than in the reference state. Thus, from this point, temperature-dependent clustering of the α phase exist outside the MG and the results of the investigation are compiled in Table 4-9.

Table 4-9. Cr-Cr clustering analysis through frequency distribution, V.

Alloy	**Time [h]**	**Temperature [°C]**	V	χ^2/ *freedom*
Fe–50Cr	250h	850	0.053	93.3 / 24
Fe–50Cr	250h	750	0.059	60.5 / 25
Fe–50Cr	250h	650	0.072	43.4 /27
Fe–50Cr	100h	650	0.072	50.2 / 28
Fe–50Cr	50h	650	0.072	45.4 / 26
Fe–50Cr	145h	595	0.092	54.3 / 28
Fe–50Cr	2h	100	0.032	59.8 / 23

The V from 595°C is added as a kinetically stable reference point just above the MG to highlight the decreasing trend of clustering, even though the consolute temperature was set 10°C lower in the evaluation of the α' MG limit. The reference point is set 15°C above the α'-limit, because the transition over the top of the MG at 50 at.%-Cr is not abrupt as for the lower Cr alloys. Hence there is a possibility that the significance of the Cr-Cr clustering in the immediate proximity to the MG limit is an effect of the MG. We have also seen a spinodal α' structure up to 565°C, α' precipitates present up to 578°C and significant SRO at 580°C, but very little SRO at 595°C.

The variation of the V-parameter as a function of temperature is presented in Figure 4-22 a). Prior to ageing, the alloys were solution treated at 1100°C before they were quenched through the MG to room temperature. There is a possibility that this might influence the homogeneity of the solution treatment, due to the fact that we find slightly more composition fluctuations in the solution treatment of the Fe-50Cr alloy in comparison to the Fe-35Cr alloy. However, the hypothesis that this would cause the composition variations observed after ageing above the MG is ruled out in our case. Because the quench is made with high efficiency and all samples come from the same 10x15x50mm bar which means they have the same solution treatment, quench and preparation of the APT samples (see Figure 4-1). After ageing the

quench of the 0.3mm thin APT samples is even more efficient, thus the quench to room temperature occurs within a matter of a couple seconds, not enough time to cause this temperature-dependent variation of *V*.

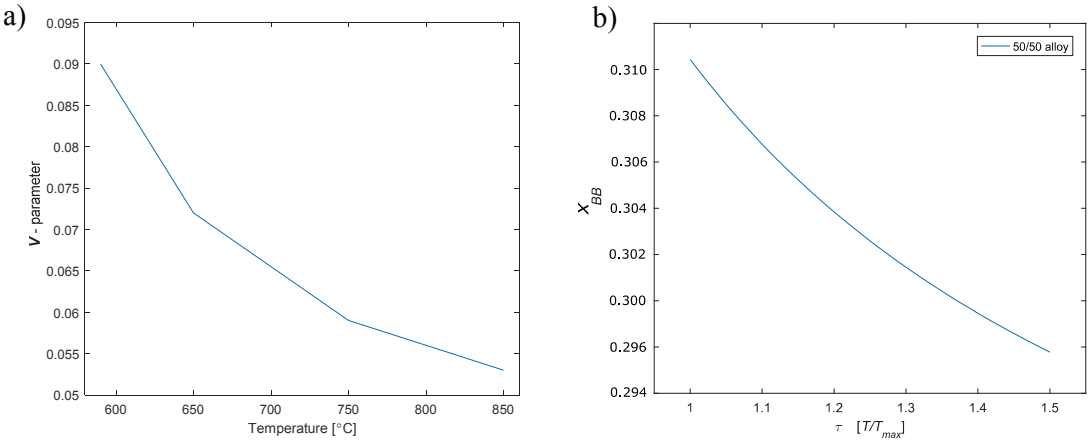

Figure 4-22. a) *V*-parameter as a function of temperature, b) the analytical quasi chemical clustering model.

In Figure 4-22 b) we have the analytical quasi-chemical model introduced in section 4.5.2. It is merely used to illustrate the point that it is possible to treat the clustering phenomenon separate from the MG itself. In a binary alloy the number of AA, BB and AB bonds are given by their pair fraction p_{ij}, thus $p_{AA} = Y_A^2, p_{BB} = Y_B^2, p_{AB} = 2Y_AY_B$ holds for ideal solution [196]. Where Y_i is the coordination equivalent fraction, i.e. the number of *i* pairs per mole dependent on crystallography. The quasi-chemical equilibrium distribution of BB bonds is then investigated by the "equilibrium" equation presented in section 4.5.2. The graph in Figure 4-22 b) illustrates the probability of finding a BB pair in a bcc A-50B alloy above the consolute temperature of the miscibility gap (T_{max}). By using the relation: $x_A = 1 - 2x_B = p_{AB} + p_{AA}$ and $x_B = p_{AB} + p_{BB}$ for the 50-50 alloy we obtain the probability function: $p_{BB} = 0.5(1 + \exp(-4 / z\tau))$. Where z is the coordination number which is 8 for bcc, the value for a random solution is 0.25, there is thus an obvious tendency to form cluster according to this model.

4.7 Hardness measurements

It is well-known that Vickers hardness (Hv) of a Fe-Cr alloy depends on the Cr fluctuations present in the material, for example during embrittlement [11]. The general understanding of the α' effect on these alloys is that α' restrict dislocation mobility. Thus α' will also cause a loss of impact toughness and ductility. Through the relative hardness between the initial

solution treated state (Hv_o) and isothermal ageing (Hv_{iso}) it is possible to detect phase separation and relate it to the kinetics of NG/SD.

The experimental results of the Hv measurements can be seen in Figure 4-23 a) and b). When significant hardening develops it indicates that phase separation is present, as in a). On the other hand, if the Hv values stay close to Hv_0, it indicates that the alloy remains close to the solution treated state. Some relaxation of residual stress after the solution treatment quench can be expected from samples aged outside of the miscibility gap, resulting in a drop of hardness

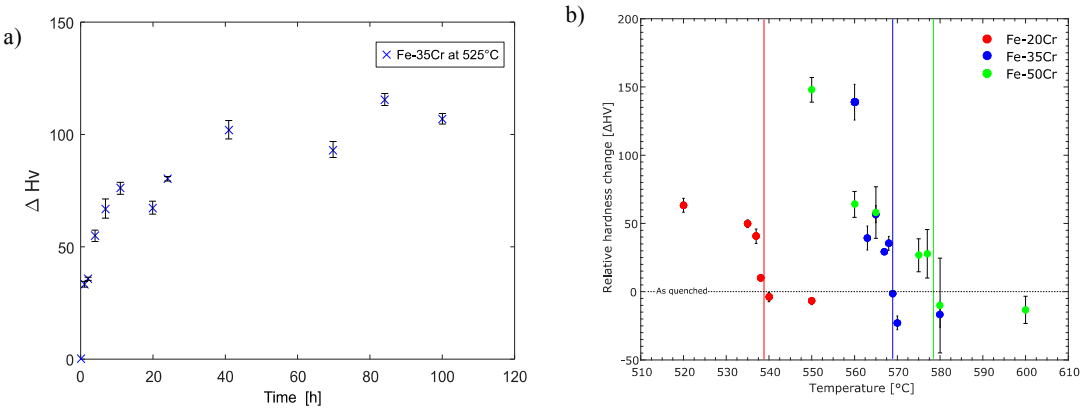

Figure 4-23. a) Relative hardness, ΔHv, of the first 100h of ageing Fe-35Cr at 525°C, error bars represent the standard deviation of the measurements. b) lines highlight the indicated limit of α' formation after 120h of ageing for each alloy.

The differences in kinetic ageing behaviour of these alloys that can be attributed to the nature of the decomposition processes and its respective thermodynamic properties. We know this based on the phase diagram, see Figure 2-1. In this case, the difference is that the Fe-20Cr alloy decomposes through NG at the intermediate temperature we are investigating. Thus, there is a small (ΔHv) incubation time dependent on the driving force to exceed the α' nucleation barrier, i.e. undercooling from the top of the MG. This can be seen in the evolution of ΔHv with different ageing times as a function of temperature in Figure 4-24. Fe-35Cr and Fe-50Cr both decomposes through SD, characteristically without an activation energy barrier for α' formation. Therefore, a more gradual increase of ΔHv is expected, as seen in Figure 4-23 a). Where the Fe-35Cr alloy has reached a transient ageing stage after ~24 at 525°C.

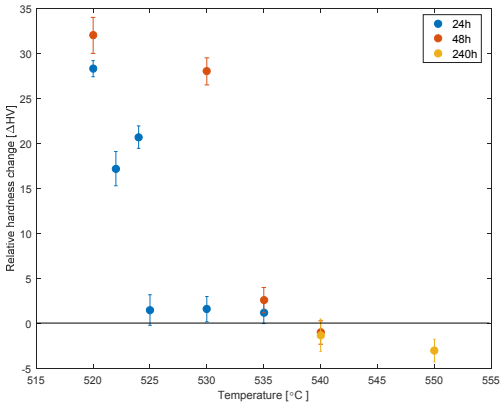

Figure 4-24. Evolution of hardness at different times and temperature Fe-20Cr.

Naturally, when the undercooling from the top of the MG is reduced the rate of α' formation is reduced. Hence, by ΔHv one could see an extended incubation time when increasing the temperature from approximately 24h at 525°C to below 48h at 530°C. At 540°C the incubation time for ΔHv is much greater than the standard 120h, even beyond 240h, therefore 540°C is deemed to be just outside of the MG. The decreased rate of α' transformation exhibits the behaviour classic of the time, temperature and transition diagram (TTT) [197], as the limit of α' formation is reached the undercooling from the MG consolute temperature is rate controlling therefore the transformation require longer times[198], [199]. However, the much-increased incubation time between 537°C and 540°C is the reason we can define the limit of the MG as in-between these two temperatures.

4.8 Final remarks

Phase separation in binary Fe-Cr alloys during isothermal ageing has been studied at intermediate temperatures. The purpose of the investigation was to determine the upper limits of α' formation in the miscibility gap as the extensive Fe-Cr review by Xiong et al. [12] resulted in such inconsistent information in regards to the upper limit. This was done because of the limited amount of time in this work requires us to favour the kinetics of phase separation through increased temperatures.

A combination of atom probe and Vickers microhardness was used to determine the limits of α' formation in the Fe-Cr system. The three binary alloys: Fe-20Cr, Fe-35Cr and Fe-50Cr were first solution treated and then isothermally aged up to 120h (5days). The evolution of the microhardness was monitored as phase separation is known to cause embrittlement of the Fe-Cr alloy. The temperatures of the isothermal heat treatments were gradually increased

until hardness changes could no longer be detected, this was an indication that the limit of α' formation had been reached. Subsequently, atom probe was used to confirm a temperature range in between which α' dissolved. For the Fe-20Cr alloy, this temperature was found between 537-540°C, in the Fe-35Cr alloy this limit was found between 568-570°C and for Fe-50Cr alloys this limit was found 575-580°C.

The kinetic evolution of the decomposition process was investigated by thermo-electric power. A simple yet effective technique is very sensitive to Cr redistribution in the matrix phase. All alloys were isothermally aged at 525°C and changed in thermo-electric power was monitored. A difference kinetic behaviour between the Fe-20Cr alloy and the other alloys were observed. Most likely due to a difference in magnetic behaviour between the alloys as Cr-rich phase is expected to exhibit paramagnetic properties [82]. Thus, a non-destructive way to potentially distinguish between spinodal decomposition and nucleation and growth was presented. To confirm the thermo-electric power effect in the Fe-20Cr alloy came from nucleation and growth in an additional correlative thermoelectric power atom probe study was conducted in collaboration with INSA Lyon. Where volume fraction evolution versus thermo-electric power evolution indeed correlated with the activation of Cr self-diffusion.

It was discovered that the α was not fully homogeneous, but indeed Cr-Cr clusters were present at temperatures well above the miscibility gap. A kinetic investigation of the evolution of these clusters revealed that they were stable in time but decreased with increasing temperature. Quantifying this deviation from a random distribution with increasing temperature revealed a trend similar to what is expected from a quasi-chemical model of bond probability distributions above the miscibility gap [195].

Chapter V

The effect of external stress on Fe-Cr phase separation

The innovative objective of this work has been to investigate the effect of an external load on the ageing behaviour of Fe-Cr alloys. Thus, for this purpose, an evaluation of the mechanical properties of the system is required in order to understand the effect of the external load. Prior to this work what has been further progressed is a more accurate understanding of the thermodynamics and kinetics of the system. In this chapter, experimental investigation is restricted to uniform axial loading in the tensile direction. This choice is made because e.g. compression would potentially induce a more complex stress state with shear at the contact surface and possibly bending. Since the alloy subjected to analysis is polycrystalline, some important experimental parameters need to be considered. First, the difference in crystallographic orientation and interaction between grains, thus the exact stress state in an individual grain is complex. Second, as will be seen later on by modelling in chapter 6, the effect of strain on the microstructural evolution differs with respect to orientation of the applied load, thus note that experimental strain of individual grains cannot be exactly determined. Consequently, it is important to make assumptions/simplifications and yet be aware of these parameters. A principal sketch of the experimental investigation is provided in Figure 5-1.

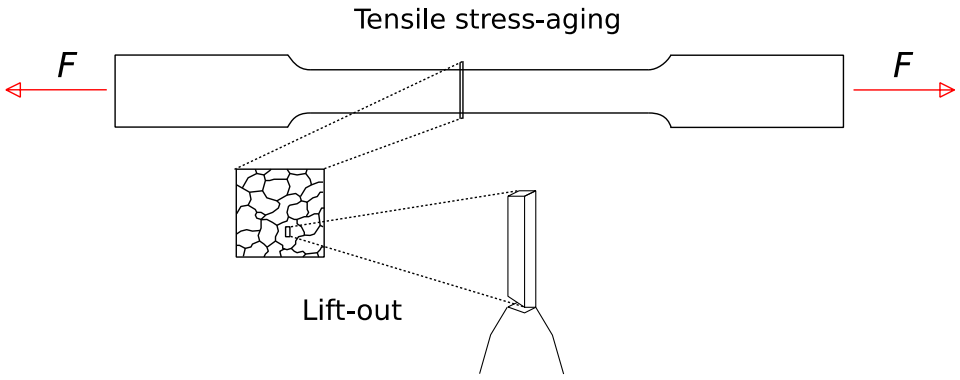

Figure 5-1. Schematic illustration of project execution, extraction of specific grains, not to scale.

In order to perform stress-ageing under an applied load, the methodology involves the use of a hydraulic tensile rig at intermediate temperature. The experiment is controlled by a constant applied tensile force with high accuracy, which is a key experimental parameter. After ageing,

a cross-section is cut so that the applied load is parallel to the normal direction of the sample surface and subsequently parallel to the APT tip axis. Prior EBSD is used to map the orientation of the grains, then the lift-out technique is deployed to make needle samples for APT. Thus, from here on, the analysis direction in APT needles is parallel to the direction of the applied force and EBSD maps index the normal direction of the sample surface, i.e. the stress axis.

5.1 Evaluation of tensile properties in Fe-Cr alloys

The general trend of the mechanical properties in Fe-Cr alloys is that ductility and formability decline with increasing Cr content. Hence, for commercial purposes, Cr content seldom exceeds 30at.%-Cr the maximum is often found around ~25at.%Cr [200].

Mechanical properties of high purity Fe-50Cr and Fe-60Cr alloys have been investigated after ageing at intermediate temperature by Kanou et al. [201]. It was found that the Fe-60Cr alloy experienced a constant, but a minor decline of tensile strength with increasing temperature in the range 200-550°C. It was also shown that ductility can be maintained through a finer grain size while increasing Cr content. However, at room temperature Fe-50Cr and Fe-60Cr alloys exhibited brittle behaviour with yield strengths of 580MPa and 800MPa respectively, fracture occurred after ~24% elongation for round specimen with 8mm in diameter.

Moreover, the deformation behaviour of a single crystal <001> Fe-30Cr was investigated by Miura and Koushima [78], where activation volumes for Lüder's band yielding were obtained, thus yield strength at room temperature was found to be ~200MPa.

Mechanical properties of the entire range from 28 - 68at.%-Cr in 10at.%-Cr increments were investigated by Matsui et al. [202]. The alloys were synthesized by mechanical alloying of powders using a planetary ball mill (360ks under 1.33kPa) followed by 0.3ks annealing at 900°C. Their tensile strength ranged from 800MPa with ~10% elongation to 1500MPa with ~0.2% elongation for 28at.%-Cr and 68at.%-Cr respectively. In terms of elongation versus strength the 48at.%-Cr alloy was deemed the best compromise. SEM/EDX images revealed clustering of Fe and Cr for the two highest Cr alloys, so these alloys are not considered homogeneous.

Experimental investigations of mechanical and diffusion properties of high Cr binary Fe-Cr alloys are rare to come across [203]. Especially for alloys that have been aged within the miscibility gap for an extensive period of time.

Thus, for our case in addition to evaluate the homogeneous reference state of the alloy a pair of tensile specimens has been aged at 500°C for 49h in the high precision furnace. The time 49h is selected due to practical reasons so that an estimated mean value of the mechanical properties during SD can be obtained. As Fick's first law applies to the steady-state diffusion flux in this case, the mean self-diffusion distance ($\propto t^{1/2}$) can easily be calculated. Thus, after 49h we have simply reached 70% of the diffusion distance reached after 100h. At 500°C after 49h this distance is ~18μm [61].

For the tensile test of aged and reference samples, an MTS Criterion 43 machine with 30kN wedge grips was used. The results are presented in Table 5-1. Strain rate control was used to control the test at constant strain rate of 0.25mm/min, similarly to the strain rate used by Chen et al. [204] (0.2mm/min) to comply with the ASTM E 21-92 (1997) standard. The slightly higher strain rate in our case is used to comply with the standard requirement of the gauge length elongation of 0.005 ± 0.002/min. Beam displacement and an extensometer were used to monitor the elongation. ASTM - E8 tensile specimen was first manufactured from the Fe-50Cr alloy, as this alloy should present the best compromise in terms of strength and ductility. The time to manufacture these specimens was 4 months. Five samples were solution treated at 1100°C and quenched in water, tensile test revealed extremely brittle behaviour. Samples did not only brake by brittle fracture along the gauge length, but they also fractured close to the facet to the grip. For this reason, the clip-on extensometer was removed to avoid added momentum and only beam displacement was used to calculate the elongation at 75Hz acquisition rate. Closing the wedge grips was done very carefully for not allowing more than 100N (σ =8.5MPa) axial force on the specimen. The best result was 2% elongation with a peak force of 2.5kN (σ =213MPa). Slow cooling at 3°C/min down to 600°C before the quench did not improve ductility either. Three samples were aged at 500°C for 1h, 4h, and 9h each. After 1h the yield point was found ~185MPa and 0.45% strain. After 4h and 9h these values were ~150MPa and 0.35% strain. These results are compiled in appendix 10.2. Due to this very small elastic region, with metallic squealing noise from internal fractures (seen as hacks in the $\partial\sigma/\partial\varepsilon$ curve) long before rupture, these alloys were deemed too difficult to work with during elastic stress ageing.

Thus, another set of Fe-35Cr tensile specimen was ordered, this alloy was selected so that SD would still be the decomposition process, but in (hopefully) a more ductile material. The width of the sample was also increased to allow for a higher peak force. When these tensile specimens were ready, the more extensive APT-TEP kinetic study had been conducted at 525°C. Thus, two samples were tested in the reference state and two samples were tested after 49h of ageing at 525°C, 49h due to the fact that SD is diffusion-controlled and Cr self-diffusion

distance is as already stated $\propto t^{1/2}$. The results from two of the tensile tests are displayed in Figure 5-2.

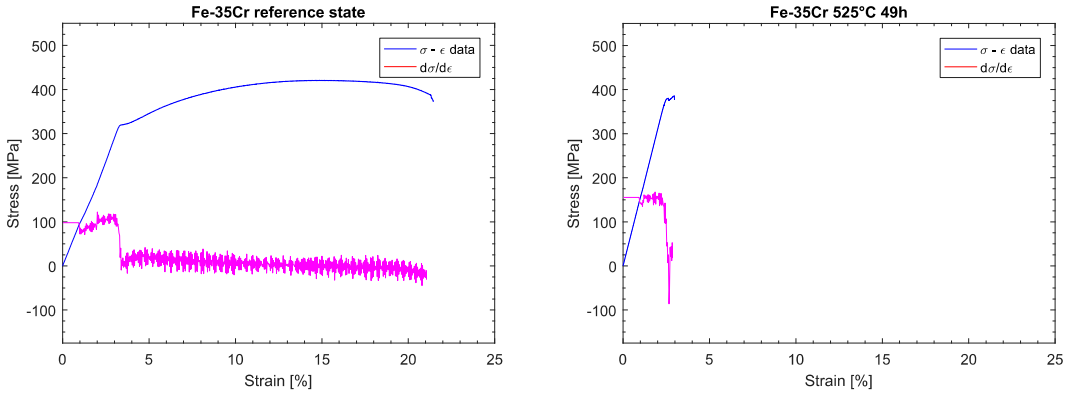

Figure 5-2. Engineering stress-strain curves of the Fe-35Cr alloys. Strain rate 0.25 mm/min and data collection rate 75Hz, on an MTS Criterion 43 with 30kN wedge grips.

At the start of the test, when the force is first applied, there is some unavoidable sliding motion between the grip and sample. This motion results in an initial overestimation of the displacement caused by the applied force, but it was corrected for by assuming linear elastic behaviour between the origin and yield point through $\partial\sigma/\partial\varepsilon$. Therefore, the first part of the $\partial\sigma/\partial\varepsilon$ curve can be seen as a straight line, where the measured values have been replaced by calculating values assuming linear elastic behaviour within this domain.

In Figure 5-2 MATLAB was used to recalculate the engineering stress-strain curves, from which the result is presented in Table 5-1. Focus from here on is solely on the Fe-35Cr, alloy even though the initial plan was to work also with the Fe-50Cr alloy. It is well-known that increasing Cr content will cause solution hardening, so it is not surprising to see that in combination with the "475°C embrittlement" ductility was consistently lost for aged samples. In Figure 5-2 is the aged Fe-35Cr sample broke as seen by brittle fracture almost immediately after the yield strength was reached.

Table 5-1. Mechanical properties of the tensile specimen Fe-35Cr.

Sample	**Thermal history**	**Hv (200g)**	**Yield Strength [MPa]**	Hv/σ_y	**Creep strain [%]**
Ref.	2h, 1100°C	208 ± 4	319	0.652	
Ref.	2h, 1100°C	209 ± 6	321	0.651	
$\sigma = 0$	49h, 525°C	343 ± 7	379	0.905	
$\sigma = 0$	49h, 525°C	290 ± 5	321	0.903	
σ = 150MPa	96h, 525°C	370 ± 5	-	-	$\overline{0.47}$
σ = 235MPa	96h, 525°C	379 ± 4	-	-	$\overline{0.93}$

It has previously been seen that coherency strain effects in the Fe-Cr system are so small that they can most often be neglected. Therefore, the applied elastic strain is assumed to dominate the effect of the elastic energy inside of the crystal. It is well-known from solid mechanics that the work done by straining a material is stored as energy inside of it, i.e. strain energy. The strain energy density can be calculated as the area under the stress-strain curve, usually approximated by a triangle in the elastic region (i.e. $U_\sigma = \frac{1}{2}((F/A_0)(\Delta L/L_0))$). Thus, we can approximate the strain energy density in our materials by knowing the initial elongation upon loading. For the lower force, the stored energy density is 4.78MJm^{-3} and the higher load is 7.75MJm^{-3}, as we estimated Young's modulus (Y) of the aged tensile specimen it is possible to obtain the total strain energy stored ($U_{st.} = FL_0/YA$) upon stress-ageing as 30.61J and 48.62Jm^{-3} respectively. Thus, what might seem conservative increments of the applied stress has noticeable effects on the internal energy. The decomposition can be directly enhanced dependent on the level of the applied load.

The μ-hardness (Hv) and the fracture strength (σ_f) of steels, in general, is often compared to the empirical relation σ_f = Hv/3 [205]. In our case, the true fracture strength has not been calculated, because we are unable to measure the area evolution of the necking. Yet from the stress-strain curve of the reference state, it seems like a reasonable estimate, given that the ultimate engineering strength is ~400MPa. It has been reported that it is the difference in elastic properties between α and α' that contributes to 75% of the hardening, thus the modulations of the nanostructure is key in predicting the critically resolved shear stress that will cause fatal fractures [20].

During long term heat treatments at elevated temperatures, macroscopic properties are reduced due to the reduction of grain boundary interactions through the Hall-Petch relation. This is a potential issue for nanostructured materials, however not for the Fe-35Cr alloys used in this work, due to their grain size (>100μm) and an ageing temperature of 525°C.

The known effect of "475°C embrittlement" on the mechanical tensile properties is that stiffness is increased, and ductility is lost. With an already small elastic region, the strain of the material is limited before yielding. Thus, estimating the yield point at intermediate temperatures entails balancing the effect of loss of ductility due to the embrittlement along with a reduction in yield strength due to the increased temperature. The reduction of yield strength of an Fe-23Cr alloy at elevated temperature in the range 500-700°C can empirically be expressed, according to by Chiu et al. [206], by:

$$\frac{S_{y,T}}{S_{y,25°C}} = a - \frac{(T-b)^n}{c} \tag{5.1}$$

Where a =0.774, b =449, c =2.47×10^8, and n = 3.35 are constants dependent on the temperature range. In the case of an ageing temperature of 525°C the result becomes: $S_{y,525°C} = 0.7738 S_{y,25°C}$, so samples aged at 525°C should have an estimated 23% lower yield strength than at room temperature.

5.1.1 Plastic orientation dependency of bcc alloys

Plastic deformation of materials is defined by shearing of atomic planes. Thus, critically resolved shear stress is key in describing the relative sliding of atomic planes. Plastic deformation of crystalline materials usually occurs by slip, i.e. relative sliding of atomic planes. The magnitude of the shear is an integral number of interatomic distances so that the lattice is left unaltered. If slip only occurs in a part of an atomic plane then there will be a boundary between slipped and un-slipped parts of the plane, i.e. a dislocation.

The understanding of slip systems is that slip direction is favoured in the direction with the shortest interatomic distance between atom-like pairs and slip planes are generally densely packed planes. Thus, planes on which relative slip occurs are slip planes, and the direction of the shear is the slip direction.

The critical resolved shear stress required for slip to begin in a crystal structure was first discovered by Schmidt [207]. A criterion for slip to occur can be set up as $\tau_{nd} = \pm\tau_c$ where the subscripts n and d indicates the normal- and direction of the slip. Slip occurs with equal ease forward as backward hence ±, this yield criterion is called Schmidt's law. It is normally written as $\tau_c = \pm\sigma_x \cos\lambda \cos\varphi$, where λ is the angle between the slip direction and the tensile axis, ϕ is the angle between the tensile axis and slip plane normal.

The slip direction in the bcc structure is always in the close-packed <111> direction. Therefore, slip in bcc has been referred to as pencil glide, i.e. slip can occur on any plane that contains the <111> direction. Slip has been observed on e.g. {101} planes all containing at least one <111> direction [208]. Figure 5-3 provides the orientation relationship of the Schmidt factor for uniaxial tension with <111> pencil glide.

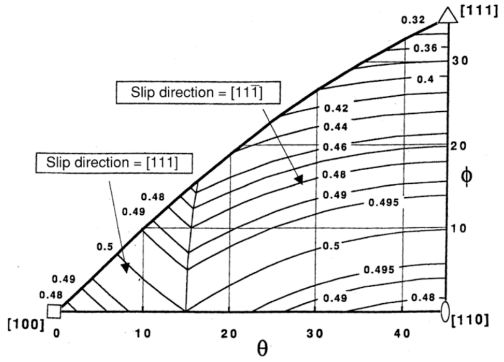

Figure 5-3. Schmidt factor dependency of [111]-direction in the [001], [110] and [111] bcc planes by Euler angles [208].

Thus, the Schmid factor in Figure 5-3 provides the relative ease of slip, depending on the crystallographic direction of the bcc crystal. What is indicated is that <111> is the easiest orientation for slip in bcc followed by <110> and <001> being the hardest direction. Knowing this the next step is to explore the orientation dependence of elastic properties.

5.1.2 Elastic behaviour of Fe-Cr alloys

Hooke's law for anisotropic materials can be expressed in terms of compliances S_{ijmn} which relates to the response of individual strain components to individual stress components. In the most general case, every strain component depends linearly on the stress components,

$$e_{ij} = S_{ijmn}\sigma_{mn} \quad \text{and} \quad \sigma_{mn} = C_{ijmn}e_{ij} \tag{5.2}$$

Where S_{ijmn} and C_{ijmn} are compliances and stiffness constants respectively as previously stated in, both are fourth rank tensors [209], [210]. In 3D, there are nine forms to express strain on a body, i.e. three eigenstrain each with two independents in-plane "shear" directions. Thus the generalized equations (5.2) leads to 81 C_{ijkl} stiffness coefficients and 81 S_{klij} compliance coefficients which form a fourth rank tensor represented by a symmetrical 9x9 array of coefficients [211].

The elastic behaviour of a lattice is described by its matrix of second-order elastic constants C_{ij} [212]. This elastic matrix, also known as the stiffness matrix, is of 6x6 size and it is symmetric. Thus, it is composed of 21 independent terms. The crystal class of the material considered yields additional symmetry constraints, further reducing the number of independent elastic constants.

The elastic response along any other set of axes may be calculated by first resolving the stress state onto the symmetry axes then using the matrices of elastic constants to the strains along the symmetry axes and finally resolving these strains onto the axes of interest.

Table 5-2. Elastic constants of Fe, Cr and Fe-Cr.

Element	Structure	a_0 [Å]	C_{11} [GPa]	C_{12} [GPa]	C_{44} [GPa]	Source
Fe	bcc	2.837	297.83	141.89	106.73	Zhang et al. [213]
Cr	bcc	2.289	354.88	70.97	100.94	Pasianot et al. [214]
Fe-10Cr	bcc	2.847	287.75	127.92	120.71	Zhang et al. [213]

The binary alloys take the main characteristic of the base element Fe, it is generally assumed that the relation: $C_{ij} = C_{ij}^{Cr} X_{Cr} + C_{ij}^{Fe}(1 - X_{Cr})$ holds for mixing elastic properties in the Fe-Cr case. For arbitrary deformation by an infinitesimal strain, the energy of the crystal is therefore given by the following quadratic form,

$$E_{elast.} = E_0 + \frac{1}{2} V_0 \sum_{i,j=1}^{6} C_{ij} \varepsilon_i \varepsilon_j + O\left(\varepsilon^3\right) \tag{5.3}$$

Where the Voigt notation is used for the indices i and j, V_0 is the volume of an unstrained sample and $O(\varepsilon^3)$ denotes terms of order 3 or higher. In a lattice of cubic symmetry, there are three independent elastic constants; C_{11}, C_{12} and C_{44}. Then the equation is reduced to,

$$\begin{aligned} E_{elast.} = \frac{1}{2} V_0 \Big[& \left(C_{11} - C_{12}\right)\left(\varepsilon_1^2 + \varepsilon_2^2 + \varepsilon_3^2\right) + C_{12}\left(\varepsilon_1 + \varepsilon_2 + \varepsilon_3\right)^2 \\ & + C_{44}\left(\varepsilon_4^2 + \varepsilon_5^2 + \varepsilon_6^2\right)\Big] + O\left(\varepsilon^3\right) \end{aligned} \tag{5.4}$$

The condition for dynamic stability is that $E_{elast.}$ is positive for any small deformation [66]. Thus, the elastic energy due to strain is highly dependent on the anisotropic nature of the elastic property.

In anisotropic materials, it is not always obvious how the material will react when load is applied in a specific direction based on the elastic constants, yet this is important for this work. To ease the understanding of elastic properties dependency on crystallographic orientation, the Young's modulus has been visualized for both Fe and Cr in Figure 5-4. Hooke's law is employed to calculate the orientation dependency [215]. A fourth-order elasticity tensor is used for the bcc crystal where the elastic constants are taken from *ab-initio* calculations. For bcc - Fe and bcc - Cr, as seen by the visual, the <100> direction in Fe is a soft direction while in Cr it is the stiffer direction. Same goes for the <111> direction in Fe, it is the stiff direction while in Cr it is the soft direction. Worth noticing is the difference in strength between Fe and

Cr, i.e. the strong Fe direction is similar in strength to the weak Cr direction. There of the increase in strength due to the addition of Cr solute atoms as shown in Figure 5-5.

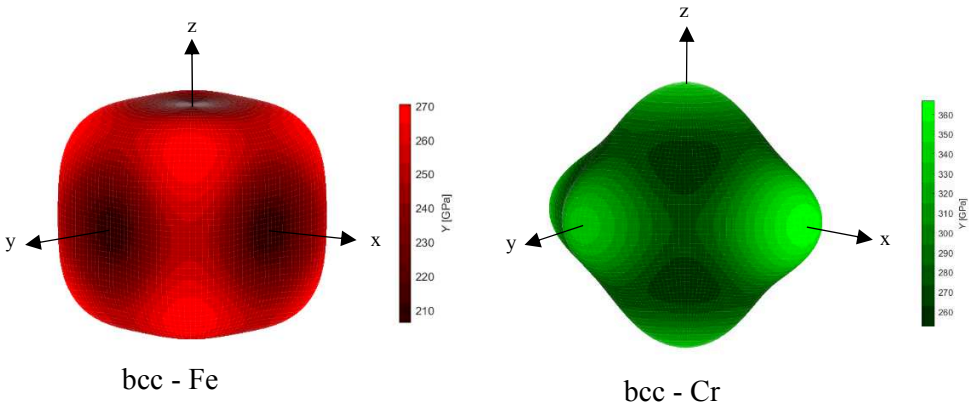

Figure 5-4. Calculation of the orientation dependence of the Young's modulus with elastic constants from *ab-initio* calculations for bcc-Fe [213] and bcc-Cr [214], the 3D calculations are based on the work by Nordman et al. [215].

Due to the limited literature review of tensile properties of decomposed high Cr alloys, a surprising issue with extremely brittleness of Fe-50Cr alloys arose. This was most likely an issue attributed to the specimen design, the heat treatments and the anisotropic elastic nature of the elements. As knowledge of elastic properties of materials is fundamental for many reasons, a theoretical investigation based on CALPHAD was made by Su et al. [216]. The composition dependence of the Young's modulus (a crucial property in this work), for the bcc Fe-Cr system is given in the graph below,

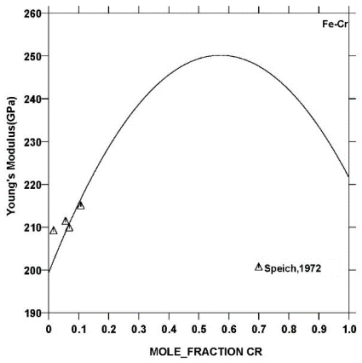

Figure 5-5. CALPHAD calculation of composition dependency at 25°C and 1atm pressure by Su et al. [216].

Thus, as seen in Figure 5-5, elasticity of the alloy is highly dependent on Cr composition. The composition dependency was optimized based on the interaction parameter $L_0 = 155.5$ for. E^{bcc}_{Fe-Cr}.. The Fe-Cr system is characteristically known to have very little coherency strain, but elastic properties are very much composition-dependent, and the anisotropic nature of bcc - Fe and bcc - Cr is very much complementary of one another with Cr being the stiffer element.

5.2 Tensile stress-ageing of Fe-35Cr alloys

The temperature at which the stress-ageing in this work will be performed is 525°C, a reason is that at this temperature the decomposition process is SD for Fe-35Cr and Fe-50Cr, but NG for Fe-20Cr. Thus, at 525°C 20at. %-Cr is still within the MG, in addition, SD begins for 35at.%-Cr at around 565°C. Therefore, Fe-35Cr is chosen for the experimental investigation because in this case at this temperature SD has reached transient growth within the first 120h, where the interconnected α - α' morphology coarsen with a time exponent m = 0.215 from 100h to 1000h, in agreement with LBM theory [113]. It is also the temperature at which the kinetic ΔTEP study has been performed, which provided us information of e.g. the apparent activation time of Cr diffusion.

In steady-state creep test or transient intermediate temperature tensile test, it is accustomed to heat the tensile specimen to the desired temperature and allow 15-30min for temperature homogenization [206], [217]. In our case, an MTS Landmark servo-hydraulic tensile rig is used, equipped with an MTS 653 furnace. The furnace is equipped with three different heat zones each controlled by a K-type thermocouple attached to the sample by a steel wire. Naturally, the lowest heating zone would be where the temperature would be the most unstable so that heat resistant cloth is used to seal any cavity around the sample. The tensile specimen needed to be at least 32cm long so that 10cm extensions were added to the original tensile specimen set-up. 15min was needed to reach 525°C, then 15min at 525°C allowed the temperature to stabilize before tensile force was applied. During the first hour, the temperature varied ±3°C before it was recorded stable at 525°C, measured every 15min throughout the experiment.

Figure 5-6. The tensile stress rig used for stress-ageing at intermediate temperature.

The instrument at INSA Rouen Figure 5-6 is used for research and teaching purposes, so time is limited to a long weekend or roughly 4 days, hence our selected target of around 100h. Upon heating and cooling, a rather low force of 150N is applied to the specimen through force control, which is a way of adjusting for the thermal expansion.

5.3 Results

5.3.1 Analysis methodology

It is assumed, based on experiment [15], [16], [218], [219] and modelling [61], [220], [221] that the elastic energy or external constraints matter when it comes to its effect and contribution to the process of spinodal decomposition. As the bcc Fe-Cr system, based on α-Fe, is elastically anisotropic in nature [222], then through analysis of the applied force orientation of the crystal would influence the induced elastic energy. In addition, the nature of the surrounding crystals would affect the internal stress level. Thus, the analyses approach is to use FIB-SEM lift-outs to extract samples with specific orientations. Naturally, the exact alignment of the crystal with the orientation axis is seldom achieved. Hence, IPF Z with a 2.5° miss orientation acceptance is used to index the orientation of the large (~200μm) grains to find representative grains with as small miss orientation parallel the APT analysis axis as possible. Keep in mind that we lift-out specimens from the centre of the grain to limit the effect of surrounding grains.

The standard APT analysis conditions of the lift-out samples were pulse fraction 20%, evaporation rate 0.30% and temperature 50K. This resulted in an acceptable specimen yield of ~70%. The benefit of using the LEAP system is the local electrode which allows for coupon to be analysed, which ease specimen preparation, the desired benefit of the reflectron configuration is the improved mass-resolution-power. In general, for this alloy with these analysis parameters ion detection events was reported as ~88% single ion event at the detector and ~12% of multiples. Analysis of multiple events can be performed by ion correlation histograms, which may provide insight into the origin of noise, the shape of mass peaks or possibly detect evaporation abnormalities [223]. In this work, ion correlation histograms were only used to make sure of no evaporation abnormalities. Thus, in this work, we mainly use the difference between single and multiple evaporation events to distinguish different crystallographic poles. Seen in Figure 5-7 is e.g. a grain indexed by EBSD as <111>, prepared by the lift-out method and then analysed in APT with the <111> direction aligned with the tip axis, as seen by the symmetry in the multiple event histogram of the evaporation sequence.

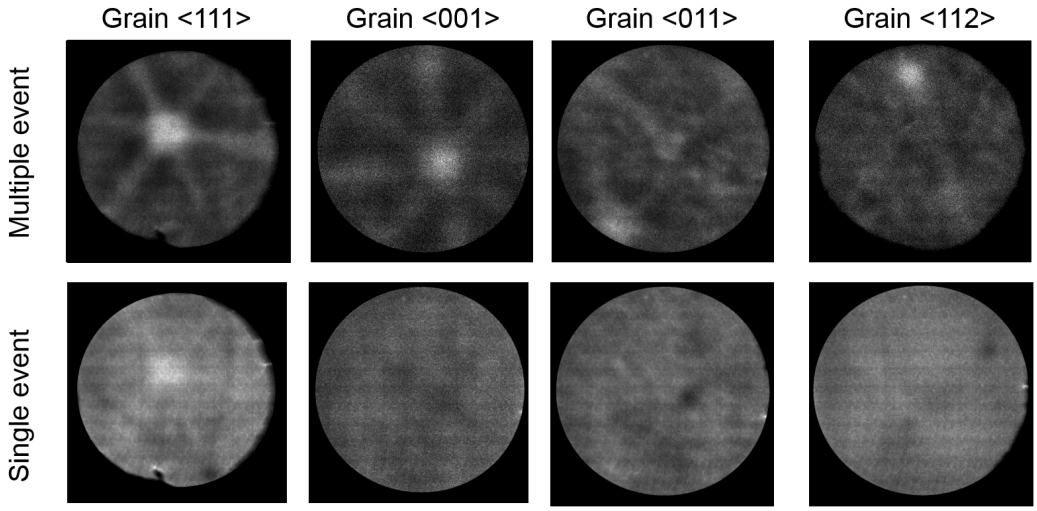

Figure 5-7. Single and multiple evaporation events from the lift-out grains with known orientations. Different poles are prone to evaporate through either single or multiple events.

As the orientation of the grains in the APT analysis is previously known, the stereographic projection of the centre pole is used to calculate the angle between the main grain orientation and minor poles. These angles are then used to recalculate the image compression factor, after which the main pole is used to calculate the interplanar distance. By this approach, it is possible to spatially and laterally optimize the reconstruction of the bcc structure [139].

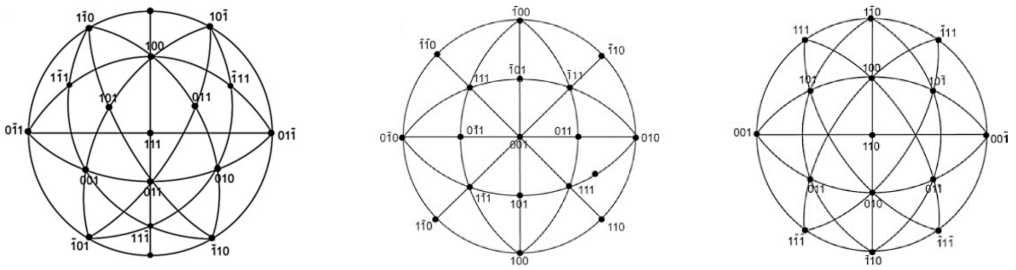

Figure 5-8. Simple standard stereographic projections of the bcc crystal [224], [225], a) <001> - pole, b) <110> - pole, c) <111> - pole and d) <112> - pole.

Characteristic of the <111> - pole projection is the threefold symmetry, seen in the multiple event histogram Figure 5-7 a). By representing the single ion events at the detector, a low impact pole is detected in the lower part of the image, the pole itself exerts two low impact symmetry lines in a V shape Figure 5-7 e). This pole is identified in the fourth quadrant of the standard projection Figure 5-8 a) as the $[\bar{1}10]$ pole. In addition, this low impact behaviour is characteristic behaviour the <011> - poles, as seen on the <011> oriented grain Figure 5-7 g). Thus, it is, therefore, possible to calculate the angle between the [111] and [110] pole in the <111> grain by equation (3.18), the result is presented in Table 5-3. The distance between the poles is easily obtained through the *xy* - coordinates. But the length of the flight path in the

reflectron compensated LEAP is more difficult to estimate. We know from the IVAS software that the distance to recalculate the ion mass is 383mm, but it is not the used to calculate magnification distance due to the focusing in the reflectron. Instead, the distance of 49.4mm has been used in this work based of internal work at GPM by C. Pareige and G. DaCosta et al., i.e. this magnification distance is equivalent of a straight flight path LEAP system which is also the distance for ions to enter the reflectron. Thus, as an example, consider the <111> oriented grain/needle given in Figure 5-7. The measured distance between the [111]-[110] poles was ~19.66mm which gives us an image compression factor of 1.625. Because this is an α-Fe based alloy we know that the interatomic plane distance in the <111> direction is 0.1657nm. The spatial distribution map implemented in the IVAS software is then used to adjust the field factor k_f . With this procedure, the accuracy of the 3D reconstruction is optimized. Similarly, for the <001> grain second [$\bar{1}03$] pole is obtained from the multiple events. In the <011> grain, the [011] pole is obtained from the single events and [010] from the multiple events and finally, for the <112> grain the [011] pole is obtained by single events. The observed angle $\theta_{obs.}$ from the samples in Figure 5-7 is provided in Table 5-3 along with the average image compression $\bar{\xi}$ and field factor $\bar{k}_f$ of the samples presented in Table 5-6.

Table 5-3. Image compression and field factor orientation dependency Fe-35Cr

Orientation	**2nd pole**	$\theta_{obs.}$	$\bar{\xi}$	$\bar{k}_f$	d_{hkl}
<001>	[103]	12.18°	1.513	4.24	0.1435nm
<011>	[010]	28.12°	1.628	4.26	0.204nm
<111>	[011]	21.69°	1.625	4.45	0.1657nm
<112>	[011]	15.98°	1.587	4.36	0.1172nm

5.3.2 The reference state and orientation-dependent ageing without stress

Reference aged samples were prepared to make comparisons with stress-aged alloys and potentially observe peculiar orientation-dependent behaviour. Thus, solution treated and aged samples at 525°C for 100h and 1000h were prepared. The alloys were analysed by EBSD to select <001>, <101>, <111> and <112> IPF Z orientations for comparison.

Metallography entailed producing high-quality surfaces for EBSD and SEM-FIB lift-out through mechanical diamond polishing followed by colloidal silicon OP-S [226]. All samples were placed in a resin and polishing was made in a semi-automatic Struers Tegramin 30 machine, following the Struers application notes for *"Preparation of ferrous metals for Electron Backscatter Diffraction (EBSD) analysis"*. As an example, the EBSD IPF Z map and pole figures of selected grains of the Fe-35Cr alloy aged for 1000h is provided in Figure 5-9.

The general approach is to select lift-outs from the centre of the grain to keep the influence of the surrounding grains to a minimum.

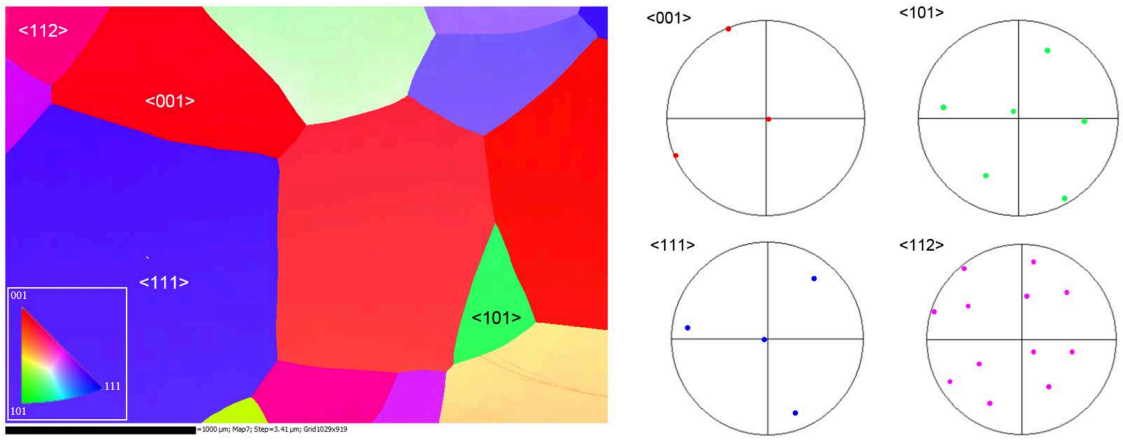

Figure 5-9. EBSD IPF Z map of the 1000h 525°C Fe-35Cr alloy and pole figures from the individually selected grains.

The parameters used to acquire the EBSD map are provided in section 3.3.3. Due to the large grain size, the approach of the EBSD analysis was to first do a quick scan for approximately 5min to index the orientation before a high-quality map was made, i.e. as in Figure 5-9. The final scanning step size is 3.41µm resulting, in an acquisition time of ~12h. The presented map is post-processed with the (*h,k,l*) CHANNEL 5 software by removal of wild spikes and 3 iterative extrapolations of six neighbours. The result is minimal removal of noise from the analysis.

The lift-out technique onto micro-tips is applied, generally, 3 tips are prepared from each lift-out to statistically have two successful APT runs. However, only one successful tip is the basis of the analysis in Table 5-4, meaning only one excellent quality data set of ~15-35million ions were collected for each condition. This is obviously a trade-off in terms of statistical basis versus the time allocation for analysis, due to the facture of tips during APT analysis, limited time and issues related to the FIB-SEM equipment.

Table 5-4. Quantitative analysis of ref. and aged alloys at 525°C, RDF volume 20nm^3, frequency analysis 20x20x60nm.

Alloy	**Time [h]**	**Orient.**	***V***	**RDF(α') [at.%Cr]**	**α' [at.%Cr]**	**RDF(λ) [nm]**	**ACF(λ) [nm]**
Fe-35Cr	Ref.	<001>	0.044	10.02	-	-	-
Fe-35Cr	Ref.	<101>	0.045	13.17	-	-	-
Fe-35Cr	Ref.	<111>	0.051	13.68	-	-	-
Fe-35Cr	Ref.	<112>	0.028	13.33	-	-	-
Fe-35Cr	100h	<101>	0.62	49.41	60.35±0.38	6.32±0.13	6.40±0.07
Fe-35Cr	100h	<111>	0.58	43.29	61.01±0.20	5.82±0.11	5.90±0.09
Fe-35Cr	1000h	<001>	1.10	64.34	65.04±0.34	8.2±0.20	8.70±0.10
Fe-35Cr	1000h	<101>	1.07	69.86	65.61±0.20	8.4±0.32	9.00±0.12
Fe-35Cr	1000h	<112>	0.98	62.07	64.14±0.61	8.5±0.18	9.60±0.10

Thus, all reference conditions have been collected as well as what later-on will be one of the more interesting directions <101> - has been analysed for all conditions. The statistical analysis presented in Table 5-4 is made from a 20x20x60nm volume from case of the frequency distribution based analysis, and 20nm^3 for RDF, ACF from concentration profile of cylinder of length 120nm radius 5nm and *dz* step size 0.3nm. What is seen is a minimal difference between the different crystallographic directions in their reference state. The Cr amplitude extracted from RDF is based on the general solution of the Cahn-Hilliard theory assuming that the periodicity of Cr exhibits cosine waves, which is not always the case [120]. In addition, the wavelength is often larger than computationally possible in IVAS or gpm3dsoft. Hence two times the "half" wavelength is presented to make the comparison, i.e. the distance separating α and α'. By extracting ion positions in (*x, y, z*) - nature, the same MATLAB script as later on will be used in the modelling section. However, due to computation time greater than 24h this approach is not systematically applied. It is merely used to validate the cosine behaviour of the periodic structure. The RDF analysis of the wavelength is a more exact measurement of a volume that is representative of approximately 2 wavelengths, in contrast to the directionally dependent concentration profile. In the case of the ACF, wavelength analysis is smoothened due to a larger number of analysed waves. However, given that the tip shape evolves during analysis some directional bias is introduced as an effect of constant ICF and k_f in the reconstruction, even though the lift-out method allows for better optimization of ICF and k_f. But it does not mean that the reconstruction of the electro-polished tips are poor as they are optimized based on interatomic plane distance of a single pole and the relation ICF $\propto k_f^{(1/3)}$ [138]. This gives us a difference of the characteristic wavelength of only 0.27nm for the Fe-35Cr alloy after 100h.

The coarsening between 100 and 1000h of ageing exhibits a time exponent of 0.215 in reasonable agreement with Soriano-Vargas et al. [18] who obtained a coarsening time exponent of 0.11-0.35 for a Fe-32Cr alloy at 500°C. In addition in the review by Danoix and Auger [11], the time exponent is also in agreement with LBM method for 20-50%Cr alloys (in the range 0.20-0.25). Thus, the coarsening of the structure follows a predictable behaviour.

The main take from the analysis compiled in Table 5-4 is that there is no significant difference depending on the orientation of the analysis that stands out. The only point is that Cr-Cr correlation as calculated by RDF is lower in the <001> direction. This could then be associated to the fact that <001> is the softer crystallographic direction of α-Fe, but more data should be acquired to confirm this trend. After 100h one cannot make any conclusions other than that <101> and <111> directions are again equivalent within their margin of error. When increasing the ageing time to 1000h the same goes for the wavelength, i.e. that it is the same for all directions within their margin of error. However, an interesting discovery is made in the <101> direction. That is frequency distribution analysis puts it at a similar level of decay to the <111> direction but the amplitude of the fluctuations looks significantly higher, i.e. we find higher Cr fluctuation amplitudes in <101> even though wavelength and V is similar to the other directions.

In the evaluation of the reference state, we have seen that concentration amplitudes are lower in the theoretically soft <001> bcc-Fe direction. It can be assumed that Fe is the dominant element for the elastic properties in the random Fe-35Cr sample due to its higher concentration.

5.3.3 Stress-ageing Fe-35Cr at 525°C

Two different stress levels applied during ageing were tested as previously described in section 5.1. This is because the reduction of yield strength is not exactly known even though it has been estimated. Creep was monitored to make sure that no micro plasticity occurs. When the lower stress level was deemed successful, a higher, yet elastic load was selected. The higher load level is naturally more interesting, as the effect of the added elastic energy is supposedly larger. Also is has been seen from modelling that very high-stress levels are required before one can see an effect of the applied stress on the morphology of the spinodal structure [16], [61].

To investigate the influence of the stress level on the mechanical properties micro-hardness, as in section 3.1, was used. The objective was to investigate if it was possible to detect a noticeable difference from ΔHv depending on stress level, see Table 5-5.

Table 5-5. Relative micro-hardness increases as a function of stress, ageing time 100h and temperature 525°C.

Alloy	Time [h]	Temperature [°C]	Stress [MPa]	ΔHv
Fe-35Cr	100	525	0.0	111.13 ± 2.44
Fe-35Cr	96	525	150	172.53 ± 1.38
Fe-35Cr	96	525	235	173.05 ± 0.54

In Table 5-5 the relative hardness increase comparing an aged sample with the stress aged samples is shown. Noticeably the addition of an applied stress enhances the hardening. Increasing the stress from 150MPa to 235MPa does not have a significant effect, however, the standard deviation/error is reduced. This supports the hypothesis that applying additional elastic energy would enhance the decomposition process, but as the Cr concentration in α' approach thermodynamic equilibrium Cr diffusion is significantly reduced [13]. Hence, only a minor increase in the micro-hardness measurements may result when changing the applied stress because ΔHv depends on Cr fluctuation.

The 150MPa alloy is also included in this APT analysis, however, the focus is on the higher stress level. This is again due to the allocation of time of the FIB-SEM equipment, specimen failure and difficulty to find grains with good orientation. Hence, only two orientations with two tips in each direction of the 150MPa stress-ageing were successfully analysed. The main objective was to obtain a better statistical basis from the higher stress level. Thus, the target was to obtain at least 3 data set from different tips of excellent quality, with > 10 million ions from each tip. Thus, fairly large tips are produced to also be able to investigate the lateral wavelength perpendicular to the applied stress as well. The statistical analyses for the stress aged samples are compiled in Table 5-6.

Table 5-6. Analysis of stress-aged samples, Fe-35Cr, aged at 525°C for 96h, RDF volumes 20nm^3 and frequency distribution analysis volume 20x20x60nm from different lift-outs.

Nr.	[MPa]	Orient.	V	χ^2/ freed.	RDF(α')*	RDF(λ)**	α' *	ACF(λ)**
2	150	<101>	0.94±0.05	412.6 / 38	54.22	10.28±0.14	62.53±1.50	-
2	150	<111>	0.82±0.04	391.4 / 35	56.79	9.85±0.17	60.62±1.23	-
3	235	<001>	1.08±0.04	716.4 / 37	68.07	10.9±0.09	70.45±1.20	11.25±1.02
5	235	<101>	1.20±0.07	965.5 / 40	74.67	11.6±0.15	74.55±0.92	12.0±0.53
3	235	<111>	1.09±0.05	516.6 / 39	64.44	11.1±0.10	64.59±0.84	11.62±1.18
3	235	<112>	1.14±0.04	581.9 / 38	72.75	11.94±0.13	69.34±1.98	12.63±1.15

*Unit: [at.%-Cr], **Unit: [nm].

Based on Cahn's theory of spinodal decomposition [38] it is expected that orientations that are elastically soft would be favoured in terms of growth of the periodic structure since the contribution of elastic energy would be at a minimum in that direction. Thus, what is expected based on published simulation results and previous APT experiment is that one would see an alignment of the periodic structure perpendicular to the axis of the applied stress [16], [32],

[61], [218], [220]. However, in the case of the Fe-Cr system (when coherent stresses between α and α' is neglected) the level of stress required for such an alignment is experimentally more than 97% of yield strength which is far from the level reached in this study [16]. But in that specific case, there is an uncertainty regarding micro plasticity effects, in addition it was a duplex (austenitic-ferritic) alloy. Based on AFT modelling presented in section 6.3 have the equivalent stain of an applied load of ~231MPa much greater effect on morphology in compression than in tension. Thus, it was also found later on in our model that for an applied tensile load to have significant effect on morphology the load level needs to exceed 95% of the elastic limit, similar behaviour was fund by CALPHAD coupled phase field modelling of Fe-Cr alloys [61]. For these reasons, it is not expected to see any orientation-dependent morphological differences in our samples as our load level was more conservative.

Two directions, each with two different APT tips were the basis of the analysis of the 150MPa stress-ageing. The statistic results are shown in Table 5-6 (also the reconstructions appear in appendix 10.3). Notice the close-packed <101> orientation is clearly further advanced in terms of the classic ways of evaluating the decomposition process. Thus, based on the separation of atoms through the V parameter, the wavelength of the decomposed structure and Cr content in the α' phase. For the χ^2 test of 150MPa the median value is based on the number of reconstructed ions, thus one χ^2 is conducted for every 10 million ions. Slip planes which favours dislocation motions are identified by high planar density this is the case of bcc-<101> [227], which is why the stiffer <111> might appear more scattered in terms of Cr distribution i.e. shorter λ and lower at.%-Cr in α'.

Focus is now on Fe-35Cr with a larger statistical basis and more orientations. Visually APT reconstructions of the α' morphology appear isotropic. Example of APT analysis from the tensile specimen aged at 235MPa <111> is given in appendix 10.4. Hence, the foundation of the analysis is compiled in Table 5-6, and smaller volumes in Figure 5-10 from each tip are extracted to visually represent the morphology of the spinodal structure.

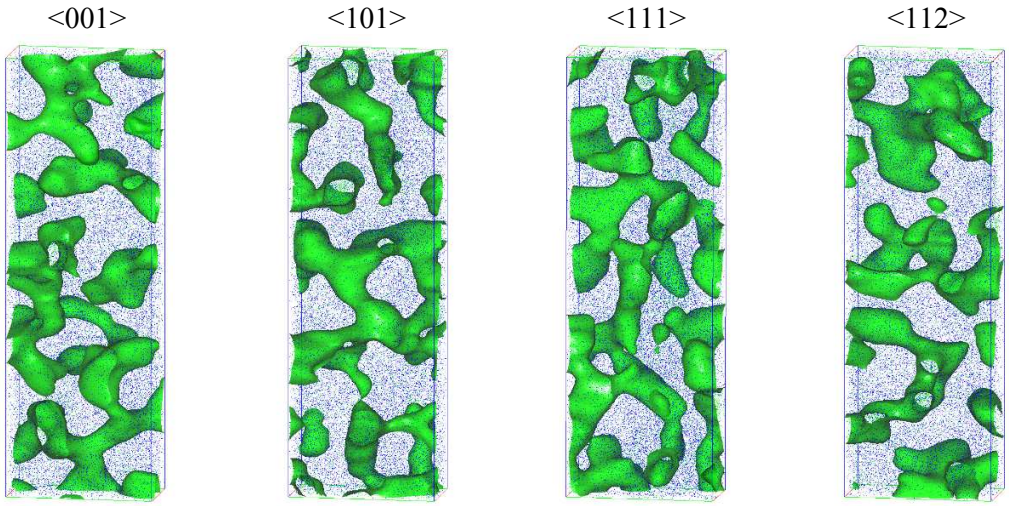

Figure 5-10. Reconstructed volumes of stress-aged samples, 235MPa, *iso*$^{th.}$ - surface, volumes 10x20x60nm.

In Figure 5-10 the 235MPa stress-aged samples are displayed in 10x20x60nm volumes using the *iso*$^{th.}$ surface. There is no noticeable directional dependency of the periodicity of the structure. However, the discrepancy between RDF and ACF evaluation of λ suggests there might be a discrepancy between depth versus lateral wavelength. The accumulated concentration profiles performed in the gpm3Dsofware revealed that for e.g. one of the <001> tip the wavelength is 0.1nm longer laterally than in-depth, and in the <111> direction the difference is 0.15nm. These distances are smaller than significant, also smaller than the lattice parameter. Thus, because the differences are small, it cannot be concluded that there is a difference in periodicity in-depth versus laterally if we compare the two supposedly extreme cases, i.e. soft versus stiff directions of the alloy. Moving a 20nm^3 box 15nm in-depth versus laterally from a centred position, performing RDF analysis only gave a deviation of 0.12nm without a preferred λ direction in <111>. Hence, λ was deemed isotropic in the APT analysis, since no preference lateral versus depth could not be confirmed in any of the orientations.

The evaluation of the average wavelength ($\bar{\lambda}$) in the samples presented in Table 5-6, based on RDF, it reveals that: $\bar{\lambda}_{001} < \bar{\lambda}_{111} < \bar{\lambda}_{101} < \bar{\lambda}_{112}$. However, $\bar{\lambda}$ in the <001> and <111> directions are within the same margin of error. As we have an α-Fe based alloy the expectation is that decomposition should be favoured in the <001> direction since it is soft, i.e. with low elastic energy. However, as indicated by the Young's modulus in Figure 5-4 <001> orientation of bcc-Cr is much stiffer than α-Fe <001>, the opposite is true for <111>. This might explain why there is no significant benefit for either direction. Similarly, such as isotropic behaviour has been seen by Dederichs and Schroeder [69]. However, the directions of the slip planes <101> and <112> [228], do favour the decomposition both in terms of Cr

concentration and wavelength. The difference between the two slip planes is that <101> has slightly shorter wavelength but higher Cr concentration in the α' phase.

Nano-indentation has been made as described in section 3.1, the interest here is to investigate the hardness as a function of the orientation by measuring it in single grains with known orientations. The purpose is to investigate the mechanical properties of the grains that have been lifted-out, as well as their surrounding grains. Thus cavities from the lift-outs made it easy to locate the grains even with the optical microscope on the instrument. The values reported in Table 5-7 is an averaged over three measurement with corresponding errors.

To stress an unfortunate turn of event, the wire saw used for machining the tensile specimen probably obliterated some of the grain structure, see Figure 5-11. The manufacturing approach was to cut a piece from the rolled sample and then solution treated before the ASTM-E8 profile was machined by a turning tool. This was made to remove the surface that had been exposed to air at 1100°C and possibly Cr depleted, as well as possible nitride formation, that can cause severe local surface embrittlement and reduce impact toughness [181]. Thus, the Fe-35Cr reference state showed a classically ferritic stress-strain curve. Compared to the Fe-50Cr alloys that were solution treated after wire saw machining had a brittle fracture before any yielding. A series of stress relaxation and homogenization heat treatments were performed in that case without any success. At best for Fe-50Cr a yield strength of ~170MPa was obtained, but with random fractures along the gauge, and even sometimes fractures appeared at the support below/above the gauge. This made potential stress-ageing very difficult to interpret, even though the higher at.%-Cr supposedly improves mechanical properties.

LOM and EBSD investigation of the Fe-35Cr tensile specimen revealed that the damage to the microstructure was made prior to stress-ageing. Thus, that no-recrystallization occurred during stress ageing at 525°C (see Figure 5-11), which suggest that the samples were not recrystallized but in the as-delivered hot-rolled state. Hence, it is assumed that the investigated grains have experienced the applied force during stress-ageing. This makes the investigation of the surrounding environment the more interesting since the grains are embedded in a smeared microstructure, but this aspect is out of the scope of this work and will not be investigated further. For the result of the nanoindentation see Figure 5-11 and corresponding Table 5-7.

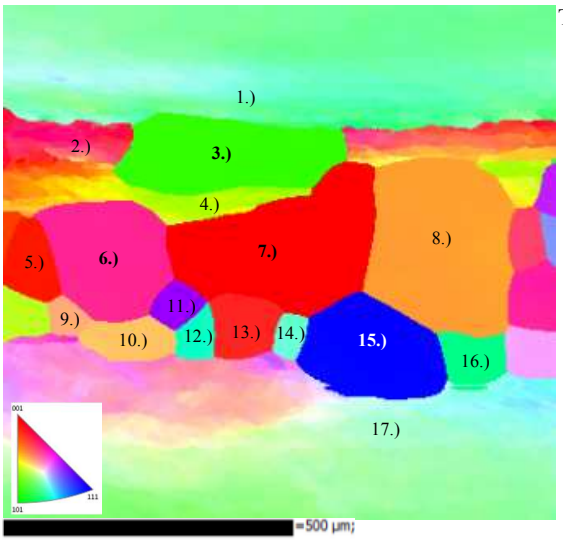

Figure 5-11. EBSD IPF Z Fe-35Cr 525°C 96h 235MPa step size 2.26µm.

Table 5-7. Nano-hardness of selected grains and environment.

Position	**Hardness (GPa)**	***E*$_r$ (GPa)**
1.)	5.95 ± 0.06	211.04 ± 9.05
2.)	5.98 ± 0.04	208.02 ± 7.47
3.) <101>	*6.11 ± 0.20*	*214.14 ± 2.36*
4.)	5.85 ± 0.06	205.39 ± 2.20
5.)	6.12 ± 0.42	211.27 ± 1.69
6.) <112>	*5.77 ± 0.07*	*208.07 ± 1.56*
7.) <001>	*5.73 ± 0.02*	*202.33 ± 4.79*
8.)	5.77 ± 0.03	207.69 ± 3.25
9.)	5.92 ± 0.07	202.02 ± 2.73
10.)	5.54 ± 0.03	200.15 ± 2.32
11.)	5.83 ± 0.09	202.88 ± 2.78
12.)	5.85 ± 0.17	202.78 ± 3.42
13.)	5.83 ± 0.12	205.97 ± 1.99
14.)	5.76 ± 0.10	203.96 ± 2.17
15.) <111>	*5.62 ± 0.12*	*203.97 ± 4.41*
16.)	5.69 ± 0.11	205.68 ± 3.56
17.)	5.69 ± 0.12	202.36 ± 1.92

Note the size of the grains in Figure 5-11 keeping in mind that a needle is made from a ~2µm^2 piece from the lift-out. In addition, to numbering of the grains, the specific orientation is placed approximately where lift-outs were carried out. Thus, the needles are considered as "bulk" samples of the specific grains with little to no interference of grain/structure boundaries. The purpose of the investigation is to see if there is any influence of the grain orientation (with respect to the load axis) on its hardness evolution. According to the measured hardness (and measurement uncertainties), it appears that it does exist an orientation dependency of grains of similar size. Regarding Young's modulus, it appears that grain 3 shows a slightly higher level. However, grain 16, which shows the same orientation is not so different from others. It, therefore, can be said that nanoindentation do not show significant differences attributed to a specific orientation. In addition, a comparison between grain 5.), 7.) and 13.) where the variation of the measurement is much smaller indicate that variation in hardness exists in grains that are oriented in the same direction. Therefore, for further understanding, it would be key to investigate the local stress variation within a specific grain dependent on its size and crystallographic environment.

What can be said of the area that embeds the <101> grain (i.e. Figure 5-11 position 1.), 2.) and 4.)) is that it is slightly stiffer than for the other grains. However, when looking at E_r one can see a larger spread of the elastic properties. In comparison with the area that embeds

the <001> grain, there is one significant difference that might be the cause of this effect. Thus, the environment surrounding the lifted-out grains does not exhibit any mechanical abnormalities to a great extent that might cause this difference. Hence, all grains seem similarly affected by their environment, i.e. there is no general trend that appears in these measurements. Of course, this is only a qualitative assessment and further investigation should involve more sophisticated 3D finite element determination of the actual stress state of each individual grain. Thus, based on the results in Table 5-7 it is clear no large abnormalities that stand out from the rest of the measurements. Hence, looking more closely at the specific grains from which the lift-outs were extracted there are differences that are larger than the variations of the measurements.

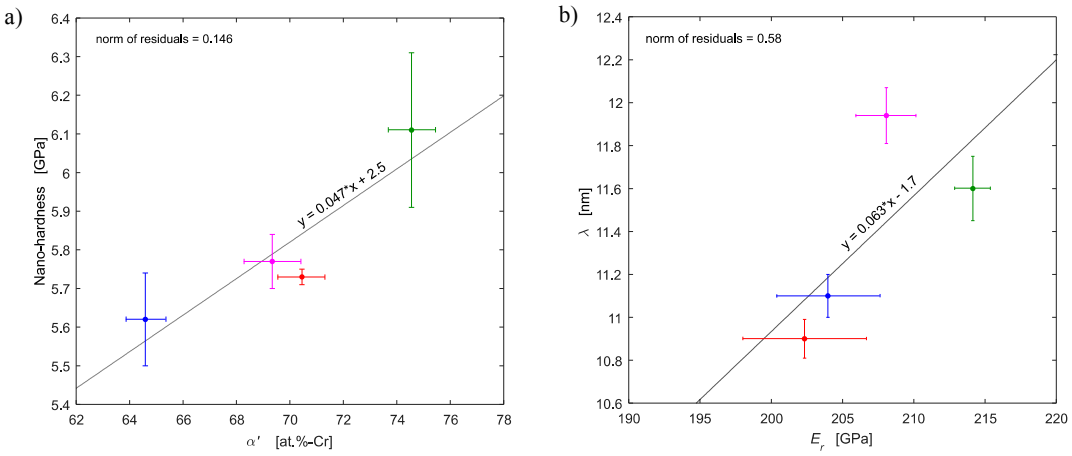

Figure 5-12. Comparison between nanoindentation and APT: a) Berkovich nano-hardness as a function of Cr in α' the colour is corresponding to the IPF Z mapping, b) characteristic wavelength as a function of orientation, c) reduced elastic modulus of the different orientations.

In Figure 5-12 is a comparison of APT analysis (Table 5-6) with the mechanical properties from nanoindentation (Table 5-7). It is possible to see that the hardness values correspond well with the at.%-Cr content in the α' phase. Meaning higher Cr content result also in a higher nano hardness value as previously seen with microhardness. Another point is that the characteristic wavelength seems to be linked with the elastic behaviour of E_r, i.e. larger λ appears to yield a higher E_r. Meaning that the periodicity of the modulated structure could possibly be related to the elasticity of that structure. Thus, nanoindentation did not reveal any significant abnormalities of the mechanical properties in the local environment of the analysed grains that might cause the difference of APT analysis. Thus, as bulk samples of large grains were selected it can be assumed that the analysed grains are representative of the stress effect on the specific orientations.

5.4 Final remarks

Based on the information that has been presented in this chapter, indeed, it appears that the addition of elastic strain does affect the decomposition process (or kinetics) in Fe-Cr alloys. To the best of knowledge and based on the two tested load levels (150 and 235MPa), the response is in direct link to the level of applied force, i.e. an enhanced external elastic force results in an evolution of the characteristic wavelength and amplitude of the Cr concentration fluctuation resolving from the SD process.

Results from the APT investigation suggest that atomically close-packed directions favour an increased amplitude of the concentration fluctuations during spinodal decomposition. This results in higher hardness, which means that they are potentially more susceptible to the embrittlement. In this work, the direction with the highest amplitude of Cr fluctuations has been identified as the close-packed <101> direction, i.e. the main slip-plane of this structure.

For the <112> direction, which is also a reported slip-plane, however with much lower atomic density than the <101> direction, the concentration fluctuations are slightly lower in amplitude in comparison with <101>. However, it is one of the elastically (E_r) softer directions after stress-ageing, and it is the direction with the longest characteristic wavelength in comparison with any of the other directions.

Comparing the principal direction <001> and <111> of the bcc structure reveals that the stiffer direction <001>, based on bcc-Cr, has a higher Cr concentration in α'. While the softer <111> direction has a longer wavelength and lower Cr content in α'. Assuming that the high Cr phase dominates the mechanical properties, because if we look to bcc - Fe the <001> orientation would be soft and thus favour a longer wavelength. Yet nanoindentation gives them approximately equivalent mechanical properties that are within the same margin of error.

Analysis of aged material revealed that alloys still show a clear SD structure characterized by an interconnected structure at 525°C after approximately 100h. In addition, coarsening of the structure between 100 and 1000h resulted in a time exponent in good agreement with LBM theory. Hence, the nanostructure is characterized with certainty as a SD structure.

After 1000h of ageing, there are minor variations in wavelength depending on crystallographic orientation. The variations are within the margin of error, this is true for the principal directions of the bcc structure. Similarly, quantifying decomposition by frequency distribution analysis (V-parameter), there is little to no significant dependence with orientation

during thermal ageing of samples without external loading. However, what could be seen is that the orientation with high atomic density, i.e. <101>, has slightly higher Cr fluctuation amplitudes, even though wavelength and *V*-parameter is almost the same.

The effect of an applied load in comparison to "stress-free" ageing seems to affect the wavelength of the structure the most, with the lower stress level yielding to a shorter increase of the wavelength. Based on the amplitude of concentration fluctuation evaluated by RDF and subsequently at.%-Cr in α' is higher than the value obtained by cluster detection This suggests that the composition of α' by cluster-method gives more of an average composition of the α' while the RDF is more representative of the core composition of α'.

Micro-hardness measurement indicates a clear effect of added external load on phase separation. However, no clear effect when increasing from 150MPa to 235MPa. The relation between Cr fluctuations and micro-hardness it well known. Thus, the fact that the cluster-method only gives ~5at.%-Cr difference between 150MPa and 235MPa in the <111> direction suggest that micro-hardness is not sensitive enough to notice a significant effect of the increased load level.

To conclude the added stress of 235MPa contributes to the ageing process by enhancing the temporal evolution of the characteristic wavelength which in time is representative on a factor of approximately 10. The softer directions result in a longer wavelength, stiffer directions with higher atomic density show higher amplitude of Cr fluctuations and slip-plane directions favour atomic motion also is favourable to the evolution of characteristic wavelength which could support that a rate-controlling mechanism for Cr motion in Fe-Cr is vacancy diffusion.

Chapter VI

Modelling phase separation

The importance of theoretical models in materials design is constantly increasing. As experimental techniques evolve, and new discoveries are made theoretical models can be validated and further evolve. The purpose of modelling is to advance development and reduce the time-to-market, through e.g. hierarchic engineering of materials. The mechanical properties of materials at macroscale are defined by their structure on a micro-scale. Hence, microstructural investigation is key in metallurgy and design of structural materials.

Downstream to bridge the gap between micro- and nanostructure, modelling is a natural aid in technical development. That is to connect first-principle calculations, electronic- and elastic- properties to the atomic structure at nanoscale. The theories of microstructural evolution have been proven valid at the nanoscale through the phase field crystal (PFC) modelling [229]. A more general formulation of the PFC approach is atomic density function (ADF) theory formulated by Khachaturyan [230]. In this chapter, we utilize an extended version of ADF to model the decomposition of an elastically constrained alloy at the atomic scale.

6.1 Atomic density function theory

In the initially developed ADF theory, the configuration of atoms is described by the density probability function $\rho(r)$. Thus, the function $\rho_\alpha(r)$ gives the probability of finding an atom α in a site *r* at a given time *t.* At the beginning ADF theory was used to describe isostructural phase transformations. In a multi-component system, $\rho_\xi(r,t)$ should be defined for each element, where the index $\xi = 1,2,...,n$ corresponds to each element. An additional condition for a binary system is that $\rho_A(r) + \rho_B(r) + \rho_{vacancies}(r) = 1$ holds.

In ADF theory the free energy functional is written as,

$$F = F(\{\rho_{\alpha\beta}(r), T) = U - TS - \sum_r \sum_{\alpha=1}^{m} \mu_\alpha \rho_\alpha(r) \tag{6.1}$$

Where U is the internal energy and S is the entropy of the system. The entropy of mixing is given as an ideal regular solution term. Thus, the internal energy in our case is given by the average model Hamiltonian,

$$U = \langle H \rangle = \frac{1}{2} \sum_{r,r'} \sum_{\alpha=1}^{m} \sum_{\beta=1}^{m} w_{\alpha\beta}(r - r') \rho_{\alpha}(r) \rho_{\beta}(r') \tag{6.2}$$

In this expression, the summation is carried out for r and r', for all components over all lattice sites.

Substituting equation (6.2) into (6.1) and writing the ideal entropy term as a function of $\rho_{\alpha}(r)$ for the binary system, gives the mean-field approximation of the Helmholtz free energy as,

$$\begin{aligned} F\left(\{\rho_{\alpha}(r)\}, T\right) &= \frac{1}{2} \sum_{r,r'} \sum_{\alpha=1}^{m} \sum_{\beta=1}^{m} w_{\alpha\beta}(r - r') \rho_{\alpha}(r) \rho_{\beta}(r') + \\ &+ k_B T \sum_{r} \left[\sum_{\alpha=1}^{m} \rho_{\alpha}(r) \ln \rho_{\alpha}(r) + \left(1 - \sum_{\alpha=1}^{m} \rho_{\alpha}(r) \right) \ln \left(1 - \sum_{\alpha=1}^{m} \rho_{\alpha}(r) \right) \right] - \sum_{r} \sum_{\alpha=1}^{m} \mu_{\alpha} \rho_{\alpha}(r) \end{aligned} \tag{6.3}$$

Minimization of this free energy expression that determines the equilibrium configuration of the system.

The equilibrium value of the probability function can be found from $\partial F / \partial \rho = 0$, it gives a Fermi-Dirac function as [230],

$$\rho_{\alpha}(r) = \left[\exp\left(\frac{-\mu_{\alpha} + \Phi_{\alpha}(r)}{k_B T} \right) + 1 \right]^{-1} \tag{6.4}$$

Where $\Phi_{\alpha}(r)$ is the mean-field potential, which is given by,

$$\Phi_{\alpha}(r) = \sum_{\beta=1}^{m} \sum_{r'} w_{\alpha\beta}(r - r') \rho_{\alpha}(r') \tag{6.5}$$

This mean-field potential is created by all atoms around a given one situated at *r*. Where $w_{\alpha\beta}(r - r')$ is the atomic interaction between the α - β atom pairs situated at position r and r' respectively.

6.1.1 Pseudo-particle approach

In 2017 a new version of the ADF theory was developed, the ADF continuum theory was called atomic fragment theory (AFT) [56] or pseudo-particle approach. In this approach, the size of the simulation grid is smaller than the distance between the neighbouring atoms. Then an atom can be seen as a sphere comprised of a finite number of atomic fragments, these fragments are treated as pseudo-particles. Thus, in AFT an atom occupies a volume within the simulation box while in ADF an atom corresponds to a single lattice site. In Figure 6-1 the atomic configuration is presented by these two approaches: a) ADF on constrained and continuous lattices, b) AFT atomic spheres comprised of atomic fragments also called "fratons". Then in the ADF method, each simulation site (each site of the Ising lattice) is occupied by an atom. However, in the AFT approach, only some numbers of simulation grids are situated inside of atomic spheres. The purpose of introducing the quasi-particle approach is because ADF theory on a constrained lattice is a discrete model unable to model phase transitions including atomic displacements.

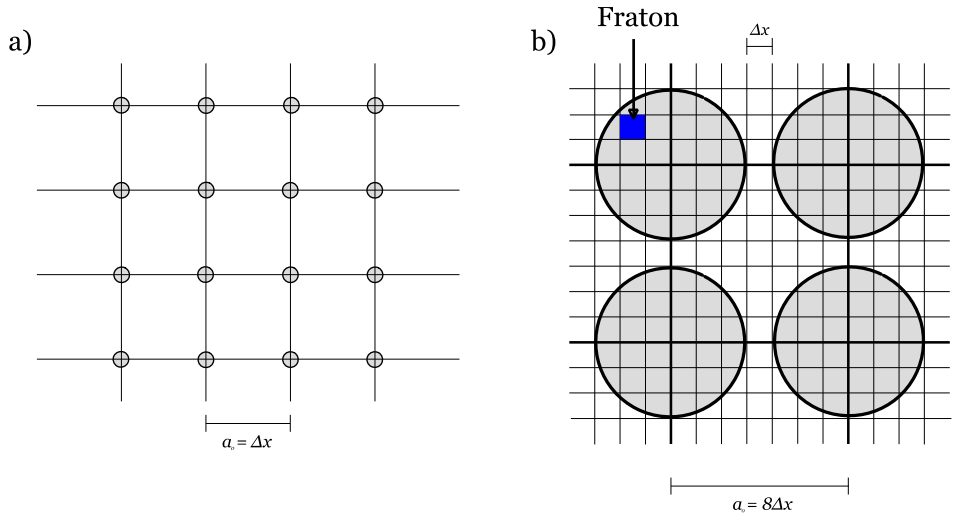

Figure 6-1. a) Illustration of the ADF theory on a rigid Ising lattice, b) illustration of AFT, fraton approach with a_0 lattice parameter of 8Δx.

In AFT similar to ADF the configuration of the system is given by the probability function. However, $\rho(r,t)$ in the ATF is the probability that a point r is situated anywhere inside any atomic sphere at that moment in time. The average density of component α in the system is then given by $\bar{\rho}_\alpha = \rho_\alpha^{at}(3/4)\pi R_\alpha^3$, where the atomic density is $\rho_\alpha^{at} = N_\alpha / V$. The volume V is the volume of the simulation box and N_α is the total number of α atoms in that box.

6.1.2 The response function and high-temperature phase stability

When referring to high-temperature phase stability one considers phase stability towards infinitesimal fluctuations of concentration. The stability condition is based on the introduction of a response function. This approach is valid for both ADF and AFT, where the free energy function can describe two types of phases: homogeneous and heterogeneous.

A critical temperature T_c defines phase transition so that at $T > T_c$ the homogeneous phase is stable towards all fluctuations of the fraton density $\Delta\rho_\alpha$. Because all of these fluctuations increase the energy of the system. In the other case when $T < T_c$, fluctuations grow, and the phase become heterogeneous. Thus, it is possible to study the free energy variation $\Delta F = F[\rho_\alpha(r)] - F[\bar{\rho}_\alpha]$ based on the spatial variations of the fraton density $\Delta\rho_\alpha(r)$. At temperatures near the temperature of phase transition, we obtain the free energy variation, ΔF where F is given by equation (6.3). ΔF can be expanded in Taylor series around $\bar{\rho}_\alpha$, i.e. with respect to small fluctuations.

When $\Delta F > 0$, all fluctuations of $\rho_\alpha(r)$ increase the energy and the homogeneous system is stable. When $\Delta F < 0$ some fluctuations decrease the energy and the system becomes unstable towards such fluctuations. In close proximity to T_c the amplitudes of fluctuations are small and therefore the Taylor expansion is limited to the second-order term. As we are studying the system at equilibrium the first term in the Taylor expansion is zero, i.e. $\delta F / \delta\rho_\alpha(r) = 0$. Thus, the reduced term of the Taylor expansion describing the change in free energy due to infinitesimal fluctuations around $\bar{\rho}_\alpha$ is,

$$\Delta F = \frac{1}{2}\sum_{r,r'}\sum_{\alpha,\beta}\left.\frac{\partial^2 F}{\partial\rho_\alpha(r)\partial\rho_\beta(r')}\right|_{\bar{\rho}_\alpha\bar{\rho}_\beta}\Delta\rho_\alpha(r)\Delta\rho_\beta(r') \tag{6.6}$$

With,

$$\left.\frac{\partial^2 F}{\partial\rho_\alpha(r)\partial\rho_\beta(r')}\right|_{\bar{\rho}_\alpha\bar{\rho}_\beta} = V_{\alpha\beta}(r-r') + \left.\frac{\partial^2 S}{\partial\rho_\alpha(r)\partial\rho_\beta(r')}\right|_{\bar{\rho}_\alpha\bar{\rho}_\beta} k_B T \tag{6.7}$$

Where S is the ideal entropy of mixing, considering a regular solution.

To define the crystal structure and the long-range periodicity of the structure we assume that the concentration fluctuations $\Delta\rho_\alpha(r)$ are periodic. Thus, the fluctuations can be described by a Fourier series,

$$\Delta\rho_\alpha(r) = \bar{\rho}_\alpha + \sum_k \Delta\tilde{\rho}_\alpha(k) e^{ikr} \tag{6.8}$$

By this notation $\Delta\rho_\alpha(r)$ is represented as a static concentration wave, this representation of atomic density fluctuations was introduced by A.G. Khachaturyan [230]. Where $\Delta\tilde{\rho}_\alpha(k) = \sum_r \Delta\rho_\alpha(r) e^{-ikr}$ is the Fourier amplitude of the concentration wave. It is now possible to express the ADF equilibrium energy in reciprocal space as a function of amplitude for concentration waves,

$$\Delta F = \frac{1}{2}\sum_k \sum_{\alpha,\beta} D_{\alpha\beta}(k, T, \{\bar{\rho}_\alpha\}) \Delta\tilde{\rho}_\alpha(k) \Delta\tilde{\rho}^*_\beta(k) \tag{6.9}$$

Where,

$$D_{\alpha\beta}(k, T, \{\bar{\rho}_\alpha\}) = V_{\alpha\beta}(k) + \left.\frac{\partial^2 S}{\partial\rho_\alpha(r)\partial\rho_\beta(r')}\right|_{\bar{\rho}_\alpha\bar{\rho}_\beta} k_B T \tag{6.10}$$

The function $D_{\alpha\beta}(k, T, \{\bar{\rho}_\alpha\})$ is called the response function and it characterizes the inter properties of the system at temperature T with mean concentration $\bar{\rho}_\alpha$. It is defined by the interaction potential $V_{\alpha\beta}(k) = \sum V(r)\exp(ikr)$.

At high temperature, the structure factor $s(k)$ obtained from X-ray diffraction is proportional to $\left\langle \Delta\tilde{\rho}_\alpha(k) \cdot \Delta\tilde{\rho}^*_\beta(k) \right\rangle$ the angular brackets indicate the average thermodynamic intensity. Thus, the structure factor is then directly related to the response function as,

$$s(k) = \frac{k_B T}{D_{\alpha\beta}(k, T, \{\bar{\rho}_\alpha\})} \tag{6.11}$$

The response function can be directly determined from experimental results [153] or extracted from MD simulations.

The response function defined as equation (6.10) is an element of the $\hat{D}(k, T, \{\bar{\rho}_\alpha\})$ matrix with complex values $m \times m$ where m represents the total number of independent components in the system. The matrix is defined as,

$$\hat{D}(k, T, \{\bar{\rho}_\alpha]\}) = \begin{pmatrix} D_{11} & D_{12} & \cdots & D_{1m} \\ D_{12} & D_{22} & \cdots & D_{2m} \\ \vdots & \vdots & \ddots & \vdots \\ D_{1m} & D_{2m} & \cdots & D_{mm} \end{pmatrix} \tag{6.12}$$

The matrix $\hat{D}$ is Hermitian. In this case with two independent components $\hat{D}$ has two eigenvalues corresponding two, two-by-two orthogonal eigenvectors for the same *k*.

As we are interested in the free energy variation ΔF, equation (6.9), can be expressed in normal mode representation. In this representation, the system is broken down into normal modes where each mode is independent from the other. The normal mode represents oscillations of the system on different sub-networks. Meaning that the density fluctuation, $\Delta\rho_\alpha(r)$, can be written as the superposition of static waves with normal concentration modes $\Psi_\alpha(s,k)$,

$$\Delta\rho_\alpha(r) = \sum_{s=1}^{m}\sum_{k} Q(s,k)\Psi_\alpha(s,k) \tag{6.13}$$

Where the amplitude of the normal concentration waves, $\Psi_\alpha(s,k)$, is given by $Q(s,k)$. The normal mode characterizes the relative vibrations of different atoms on different sub-lattices. The static wave of normal concentration is defined by,

$$\Psi_\alpha(s,k) = v_\alpha(s,k)e^{ikr} \tag{6.14}$$

Where $v_\alpha(s,k)$ is the equivalent of a "polarization vector" of mode s of the component α. Utilizing equations (6.9), (6.13) and (6.14) it is possible to rewrite the equation of free energy ΔF in reciprocal space as a function of the normal concentration waves,

$$\Delta F = \frac{1}{2}\sum_{s=1}^{m}\sum_{k}\sum_{\alpha,\beta} D_{\alpha\beta}(k,T,\{\bar{\rho}_\alpha\})\Psi_\alpha(s,k)\Psi^*_\beta(s,k)\left|Q(s,k)\right|^2 \tag{6.15}$$

A consequence of utilizing the normal mode representation is that the static normal concentration $\Psi_\alpha(s,k)$ is an eigenvector of the matrix $\hat{D}(k,T,\{\bar{\rho}_\alpha\})$. Therefore, by linear algebra one can construct the relation,

$$\hat{D}(k,T,\{\bar{\rho}_\alpha\})\Psi_\alpha(s,k) = \lambda_s(k,T,\{\bar{\rho}_\alpha\})\Psi_\alpha(s,k) \tag{6.16}$$

Where $\lambda_s(k,T,\{\bar{\rho}_\alpha\})$ is the eigenvalue of the matrix $\hat{D}(k,T,\{\bar{\rho}_\alpha\})$ with corresponding eigenvectors $\Psi_\alpha(s,k)$ to the mode s . All eigenvalues are roots of the characteristic polynomial defined by,

$$\det\left\|\hat{D}(k,T,\{\bar{\rho}_\alpha\}) - \lambda_s(k,T,\{\bar{\rho}_\alpha\})\hat{I}\right\| = 0 \tag{6.17}$$

Where "det" is the determinant and $\hat{I}$ is the identity matrix. The properties $\hat{D}$ are orthogonal two-by-two eigenvectors, it is possible to simplify the free energy equation (6.15) to,

$$\Delta F = \frac{1}{2}\sum_{k}\sum_{s}\lambda_s(k,T,\{\bar{\rho}_\alpha\})\left|Q(s,k)\right|^2 \tag{6.18}$$

The sum of the energy variation, equation (6.18), depending on the sign of the eigenvalue $\lambda_s(k,T,\{\bar{\rho}_\alpha\})$, i.e. it determines whether or not the homogenous solution is stable or unstable towards infinitesimal fluctuations. If all $\lambda_s(k,T,\{\bar{\rho}_\alpha\})$ are positively defined, for all wave vectors *k***,** then any fluctuation will increase ΔF, since $\left|Q(s,k)\right|^2$ always is positive. Thus, the stable state will remain the homogenous state. However, if there exists a unique wave vector k_0 such that $\lambda_s(k_0,T,\{\bar{\rho}_\alpha\})$ is negative it means that the energy will decrease for this fluctuation and this motivates phase transition to proceed. It is possible to obtain several wave vectors such that $\lambda_s(k,T,\{\bar{\rho}_\alpha\})$ is negative. If that is the case then the system becomes unstable to this whole range of fluctuations, but fluctuations corresponding to the absolute minimum of $\lambda_s(k,T,\{\bar{\rho}_\alpha\})$ will grow faster and dominate the structure.

The temperature at which the system becomes unstable with respect to infinitesimal fluctuations is the absolute temperature of instability T_c, thus the system is either stable or metastable above T_c. At $T = T_0$ the lowest branch of the spectrum $\lambda_s(k,T,\{\bar{\rho}_\alpha\})$ reach zero at $k = k_0$, thus the system loses its stability towards fluctuations of periodicity k_0.

In conclusion, solving the characteristic polynomial, equation (6.17), for the diagonal matrix $\hat{D}$ allows us to determine eigenvalues of the system. The smallest eigenvalue, $\lambda_s(k,T,\{\bar{\rho}_\alpha\})$, gives us the temperature that allows solidification of the system, for a fixed concentration and the corresponding eigenvector gives the periodicity of growth fluctuations.

6.1.3 Model potential

As already stated the Helmholtz free energy is given as a function of site occupation probabilities. The creation of a periodic solid-state relies upon an appropriate choice of the Hamiltonian. It should describe;

- the condensation of atomic fragments into spheres
- spontaneous minimization of free energy into the desired equilibrium atomic configuration.

Thus, the model potential $w_{\alpha\beta}(r-r')$ is constructed in two parts. The short-range potential treating the formation of atoms and the long-range potential describing the periodicity of the system. The Fourier transform of the model potential is,

$$\tilde{w}_{\alpha\beta}(k)=\frac{1}{N_0}\sum_r w_{\alpha\beta}(r)e^{-ikr} \tag{6.19}$$

Where N_0 is the number of points on the simulation grid (Ising lattice) permitted by the periodic boundary conditions. Thus, the summation is carried out over all lattice sites, *k* is the wave vector defined in the first Brillouin zone of the computational grid. To take into account the interatomic bonds in our mean-field potential we introduce the concept of clusters and cluster amplitudes.

The short-range potential, $V^{Sr}(r)$ describe the fraton-fraton interaction, it should guarantee the condensation of an initially homogeneous fraton distribution into spherical atoms. This is also a simple way to introduce a radius (r_i) of these spheres, given in real space by a step function,

$$V^{Sr}(r)=\begin{cases}-1 & if \quad r<r_i\\ \xi & if \quad r\le r_i+\Delta r\\ 0 & if \quad r>r_i+\Delta r\end{cases} \tag{6.20}$$

Here ζ and Δr represent the height and width of the potential barrier, see Figure 6-2 for a schematic illustration. Utilizing the substitution $\tilde{r}=r_i+\Delta r$ the Fourier transform of the short-range potential in reciprocal space is given by,

$$\begin{aligned}V^{Sr}(k)=&\frac{4\pi}{k^3}\{-\sin(kr_i)+kr_i\cos(kr_i)\\ &+\xi\left[\sin(k\tilde{r})-k\tilde{r}\cos(k\tilde{r})-\sin(kr_i)+kr_i\cos(kr_i)\right]\}\end{aligned} \tag{6.21}$$

Thus, in reciprocal space ξ is a scalar that defines the amplitude of the repulsive part in the short-range potential, Figure 6-2 b. The first term in equation (6.21) represent condensation of fratons into atomic spheres and the second term is the repulsion between atomic spheres.

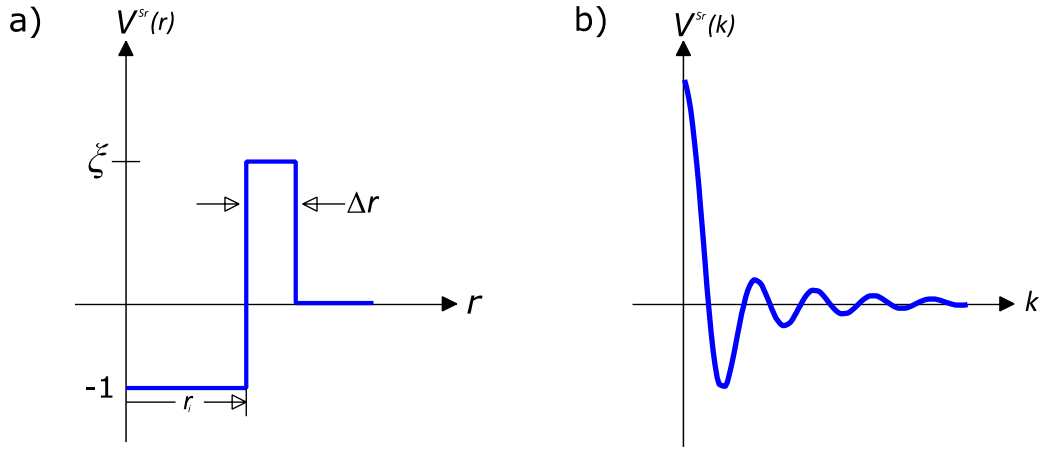

Figure 6-2. a) The short-range potential in real space, b) the short-range potential in reciprocal space.

In the construction of the long-range potential, $V^{Lr}(k)$ we rely on the cluster notation. In this instance, a cluster is defined as the minimum number of atoms that can reproduce the desired periodic structure of α atoms. Thus, a vector $\vec{r}_{j_{\alpha\in\beta}}$ defines the position of an α atom in a β cluster, with this notation we can define our cluster function in reciprocal space as,

$$\psi_{\alpha}^{cluster}(k) = \sum_{j_{\alpha\in\beta}} w_j(\alpha,k) e^{-ikr_{j_{\alpha\beta}}} \tag{6.22}$$

Where the summation is carried out overall points j on the vector $\vec{r}_{j_{\alpha\beta}}$ in the β cluster. The constants $w_j(\alpha,k)$ is a weight of the contribution of each atom to the amplitude of the cluster, chosen to reproduce the thermodynamic and mechanical properties of the simulated structure. Finally, the long-range potential is defined in Fourier space as the product of the cluster function equation (6.22) and its complex conjugate.

To conclude the model potential, consist of two terms, a short-range potential describing the condensation of fratons, the long-range potential describing the crystallographic structure. Thus, the equation of the total model potential of a component α is given by,

$$\tilde{w}_{\alpha\beta}(k) = \lambda^{Sr} V_{\alpha}^{Sr}(k) + \lambda^{Lr} V_{\alpha\beta}^{Lr}(k) \tag{6.23}$$

Where each term is weighted by the coefficients λ^{Lr} and λ^{Sr} which represent the strength of the long-range and short-range potentials respectively.

As an example, the bcc structure has 8 nearest neighbours, with a lattice parameter given by a_0. The first neighbour distance between atoms in bcc is then given by $d = a_0\sqrt{3}/2$,

viz. the maximum radius of an atom is half of the nearest neighbour distance. This gives us the condition $r_i + \Delta r \le a_0\sqrt{3}/4$ in the step function (6.20).

In the case of the single component the α-Fe crystal $V^{Lr}(k)$ has great influence on the periodic distribution of atoms, it is fitted to the structure factor from X-ray diffraction experiments through the equation,

$$V^{Lr}(k) = V_0\left(1 - \frac{k^4}{\left(k^2 - k_1^2\right)^2 + k_2^4}\right) \tag{6.24}$$

Where V_0 is a scalar used to define an appropriate free energy scale [153], k_1 and k_2 are constants used to fit s(k). The relation between the long-range potential and the structure factor $s(k)$ is essentially given by: $V^{Lr}(k) = s^{-1}(k)$, i.e. the inverse function in reciprocal space. Thus, the position of the minimum, k_0, of $V^{Lr}(k)$ is given by,

$$k_0 = \frac{\sqrt{k_1^4 + k_2^4}}{k_1} \tag{6.25}$$

Where by the function (6.24) k_1 and k_2 are defined as $k_1 = 0.435k_0$ and $k_2 = 0.626k_0$. The Fourier representation of bcc in reciprocal space is given by the fcc structure, which means that the lattice parameter of the reciprocal lattice is given by $4\pi/a_0$. So, the position of the k_0 minima, representing the nearest neighbour distance of the simulation in reciprocal space is given by,

$$k_0 = \frac{2\sqrt{2}\pi}{a_0} \tag{6.26}$$

It was shown by Vaugeois [231] that using this potential with appropriate input parameters of $\bar{\rho}_\alpha$, ξ, r_i and Δr the bcc structure/s(k) is successfully reproduced at a given temperature. In the thesis of Vaugeois, it was also shown that the bcc structure can be successfully modelled using a simpler Gaussian distribution for the long-range potential accordingly,

$$V^{Lr}(k) = \exp\left(-\frac{(k-k_0)^2}{2\sigma^2}\right) \tag{6.27}$$

Let us remark that in AFT the choice of discretization of the simulation mesh, Δx, is important to minimize the effect of numerical artefacts. Hence, the discretization of the simulation box

must be kept at a reasonable size due to allocation of supercomputing power. The simulations have been run at the regional supercomputer Myria, i.e. at Centre Régional Informatique et d'Applications Numériques de Normandie (CRIANN). Current simulations run with a parallel-MPI, 32 cores each with 500MB memory dedicated for ~52h. Much larger simulation volumes would increase waiting and computation time, i.e. drastically decreasing the number of explored conditions for our five variables.

In the case of spinodal decomposition periodicity is important, i.e. to have a large simulation box. Hence a good compromise is $a_0 = 8\Delta x$, which also allows for displacements of atoms on the quasi-continuous network. The lattice parameter of α-Fe is 2.87Å, so that $\Delta x = 0.36$Å . Naturally, displacements smaller than the discretization of the simulation grid is cumbersome. Once the lattice parameter is chosen the values of k_1 and k_2 is automatically calculated from k_0. The parameters of the short-range potential are selected as $r = 3.2$, $\Delta r = 0.17r$ and $\zeta = 4$. In these simulations, the model potential is given by the sum of the short-range and long-range potentials accordingly,

$$\tilde{w}_{\alpha\beta} = \lambda^{Sr}\frac{V^{Sr}(k)}{V^{Sr}_{\max} - V^{Sr}_{\min}} + \lambda^{Lr}\frac{V^{Lr}(k)}{V^{Lr}_{\max} - V^{Lr}_{\min}} \tag{6.28}$$

The potential is normalized and weighted by the constants $\lambda^{sr} = 1$ and $\lambda^{Lr} = 0.5$ to simplify the relative parameterization of each interaction.

6.1.4 The kinetic calculations

To model the kinetics of phase separation the microscopic kinetic equation has been used [230],

$$\frac{\partial \rho_\alpha(r,t)}{\partial t} = -\sum_{\beta=1}^{n}\sum_{r'} div\left\{ L^{ons.}_{\alpha\beta}(r-r')\overrightarrow{\text{grad}}\left(\frac{\delta F}{\delta \rho_\beta(r',t)}\right)\right\} \tag{6.29}$$

Where the indexes $(\alpha,\beta) \in \{1,\ldots,n\}^2$ correspond to the independent components, $L_{\alpha\beta}$ is the mobility matrix coefficients, F is the free energy of the system. The derivative of free energy is the driving force for phase transformation. To be conservative the equation (6.29) should satisfy the condition: $\sum_r \partial\rho_\alpha(r)/\partial t = 0$, this condition imposes that $\sum_r L_{\alpha\beta}(r-r') = 0$.

To study the temporal evolution of a binary A-B system it is necessary to introduce three fraton density functions: $\rho_A(r,t)$, $\rho_B(r,t)$ and $\rho_{vacancies}(r,t)$, under the condition that $\overline{\rho}_A + \overline{\rho}_B + \overline{\rho}_{vacancies} = 1$ holds. Still, as previously only two of the functions are independent, and

$\rho_B(r,t)$. The interactions in the system is modelled by six interaction potentials, i.e. V_{AA}, V_{AV}, V_{BB}, V_{BV}, V_{AB} and V_{VV}. It is assumed that there is no interaction between the atoms in the system and vacancies, as well as in-between vacancies themselves. Thus, $V_{AV} = V_{BV} = V_{CV} = 0$ and the free energy functional (6.3) can be written as,

$$\begin{aligned} F[\rho(r,t)] = \frac{1}{2}\sum_{rr'}\begin{bmatrix} V_{AA}(r-r')\rho_A(r,t)\rho_A(r,t) + V_{AB}(r-r')\rho_A(r,t)\rho_B(r,t) \\ +V_{BB}(r-r')\rho_B(r,t)\rho_B(r,t) \end{bmatrix} \\ +k_BT\sum_r\begin{bmatrix} \rho_A(r,t)\ln\rho_A(r,t) + \rho_A(r,t)\ln\rho_A(r,t) \\ +\left(1-\rho_A(r,t)-\rho_B(r,t)\right)\ln\left(1-\rho_A(r,t)-\rho_B(r,t)\right) \end{bmatrix} \end{aligned} \tag{6.30}$$

To estimate the stability of the system with respect to fluctuations of $\Delta\rho_A$ and $\Delta\rho_B$, we return to the response function $\hat{D}(k)$. Which for this binary system is expressed by the following symmetric matrix,

$$\hat{D}(k,T,\bar{\rho}_A,\bar{\rho}_B) = \begin{pmatrix} D_{AA}(k,T,\bar{\rho}_A,\bar{\rho}_B) & D_{AB}(k,T,\bar{\rho}_A,\bar{\rho}_B) \\ D_{AB}(k,T,\bar{\rho}_A,\bar{\rho}_B) & D_{BB}(k,T,\bar{\rho}_A,\bar{\rho}_B) \end{pmatrix} \tag{6.31}$$

Where,

$$D_{AA}(k,T,\bar{\rho}_A,\bar{\rho}_B) = V_{AA}(k) + k_BT\frac{1-\bar{\rho}_B}{\bar{\rho}_A(1-\bar{\rho}_A-\bar{\rho}_B)} \tag{6.32}$$

$$D_{BB}(k,T,\bar{\rho}_A,\bar{\rho}_B) = V_{BB}(k) + k_BT\frac{1-\bar{\rho}_A}{\bar{\rho}_B(1-\bar{\rho}_A-\bar{\rho}_B)} \tag{6.33}$$

$$D_{AB}(k,T,\bar{\rho}_A,\bar{\rho}_B) = V_{AB}(k) + k_BT\frac{1}{1-\bar{\rho}_A-\bar{\rho}_B} \tag{6.34}$$

As was shown previously, to determine the temperature of instability it is necessary to solve for the eigenvalues of the characteristic equation of the system, equation (6.17). If the values are negative then the system loses its stability. Thus, there is the case two components two solutions to the characteristic equation given by,

$$\lambda_{1,2}(k,\mathrm{T},\bar{\rho}_A,\bar{\rho}_B) = \frac{D_{AA}+D_{BB} \pm \sqrt{\left(D_{AA}-D_{BB}\right)^2 + 4D_{AB}^2}}{2} \tag{6.35}$$

As the third term in this equation always is positively defined or zero the minimum of the expression is given by "-" in the right part so that the order-disorder transition is given by the condition $\min(\lambda_2(k,\mathrm{T}_c)) = 0$.

Hence, the temporal evolution of this two-component system is given by two kinetic equations, expressed in reciprocal space as,

$$\frac{\partial \rho_A(k,t)}{\partial t} = L_{AA}^{ons.} k^2 \left[V_{AA}(k)\rho_A(k,t) + V_{AB}\rho_B(k,t) + k_B T \left\{ \ln \frac{\rho_A(r,t)}{1-\rho_A(\mathrm{r,t})-\rho_B(r,t)} \right\}_{FT} \right]$$
$$+ L_{AB}^{ons.} k^2 \left[V_{AB}(k)\rho_A(k,t) + V_{BB}(k)\rho_B(k,t) + k_B T \left\{ \ln \frac{\rho_B(r,t)}{1-\rho_A(\mathrm{r,t})-\rho_B(r,t)} \right\}_{FT} \right] \quad (6.36)$$

and,

$$\frac{\partial \rho_B(k,t)}{\partial t} = L_{AB}^{ons.} k^2 \left[V_{AA}(k)\rho_A(k,t) + V_{AB}\rho_B(k,t) + k_B T \left\{ \ln \frac{\rho_A(r,t)}{1-\rho_A(\mathrm{r,t})-\rho_B(r,t)} \right\}_{FT} \right]$$
$$+ L_{BB}^{ons.} k^2 \left[V_{AB}(k)\rho_A(k,t) + V_{BB}(k)\rho_B(k,t) + k_B T \left\{ \ln \frac{\rho_B(r,t)}{1-\rho_A(\mathrm{r,t})-\rho_B(r,t)} \right\}_{FT} \right] \quad (6.37)$$

To introduce the kinetic coefficients. In the case of a system with two independent components the matrix of kinetic coefficients is given by,

$$L^{ons.} = \begin{pmatrix} L_{AA}^{ons.} & L_{AB}^{ons.} \\ L_{BA}^{ons.} & L_{BB}^{ons.} \end{pmatrix} \quad (6.38)$$

This symmetric matrix is positively defined and each $L_{\alpha\beta}^{ons.}$ is dimensionless. The values of the coefficients are dimensionless coefficients corresponding to $L_{AA}^{ons.} = L_{BB}^{ons.} = 1$ and $L_{AB}^{ons.} = -0.5$.

6.1.5 Calculation of elastic properties

Validation of appropriate input parameters of the potentials is made through the calculation of the elastic properties of the investigated system. Thus, it is necessary to utilize tensors to obtain elastic constants at the atomic scale. For small deformations where materials exhibit linear elastic behaviour Hooke's law, $\hat{\sigma} = \hat{C}\hat{\varepsilon}$, holds. The stress tensor, $\hat{\sigma}$, and strain tensor, $\hat{\varepsilon}$, are both field tensors of rank 2 coupled by a material tensor, $\hat{C}$, of rank 4 characterizing the elastic properties/stiffness of the material. It is possible to use the flexibility tensor $\hat{S}$ to connect stress, strain and stiffness, $\hat{\varepsilon} = \hat{S}\hat{\sigma}$.

Hooke's law by Voigt notation for cubic crystal is [232],

$$\begin{pmatrix}\sigma_1\\ \sigma_2\\ \sigma_3\\ \sigma_4\\ \sigma_5\\ \sigma_6\end{pmatrix} = \begin{pmatrix} C_{11} & C_{12} & C_{12} & 0 & 0 & 0 \\ & C_{11} & C_{12} & 0 & 0 & 0 \\ & & C_{11} & 0 & 0 & 0 \\ & & & C_{44} & 0 & 0 \\ & & & & C_{44} & 0 \\ & & & & & C_{44} \end{pmatrix} \begin{pmatrix}\varepsilon_1\\ \varepsilon_2\\ \varepsilon_3\\ 2\varepsilon_4\\ 2\varepsilon_5\\ 2\varepsilon_6\end{pmatrix} \tag{6.39}$$

There are three independent elastic constants in the cubic system: C_{11} , C_{12} and C_{44}. The stiffness tensor $\hat{C}$ and flexibility tensor $\hat{S}$ are the inverse of one and other, they also have the same symmetry properties. Thus, in the case of our cubic system it is possible to obtain the relationship between stiffness and flexibility as,

$$\begin{aligned} C_{11} &= \frac{S_{11}+S_{12}}{(S_{11}-S_{12})(S_{11}+2S_{12})} \\ C_{12} &= \frac{-S_{12}}{(S_{11}-S_{12})(S_{11}+2S_{12})} \\ C_{44} &= \frac{1}{S_{44}} \end{aligned} \tag{6.40}$$

The free energy of a system depends upon the deformation of the system, under the assumption that we have small deformations. Assuming that the initial state of the system is unconstrained it is possible to calculate the free energy with respect to ε_k in a Taylor series [66],

$$F(\{\varepsilon_k\}) = F_0 + \frac{V_0}{2}\sum_{m,n=1}^{6} C_{mn}\varepsilon_m\varepsilon_n \tag{6.41}$$

Where F_0 is the total free energy and V_0 is the initial volume of the system before deformation. From equation (6.41) it is evident that the elastic constants are proportional to the free energy contribution, that is

$$C_{mn} = \frac{\partial^2 F}{\partial\varepsilon_m\partial\varepsilon_n} \tag{6.42}$$

Thus, the elastic constants of the systems are calculated through the change in free energy of the system due to deformation of the crystal. To do this three characteristic deformations are defined in compression/expansion [153]:

1) hydrostatic, $(x, y, z) \rightarrow (1-\varepsilon)x, (1-\varepsilon)y, (1-\varepsilon)z$,
2) orthorhombic, $(x, y, z) \rightarrow (1+\varepsilon)x, (1-\varepsilon)y, z$

3) monoclinic $(x, y, z) \rightarrow x + \varepsilon y, y, z$

These deformation transformations can be presented by their corresponding deformation matrix $\hat{D} = \hat{I} + \bar{\varepsilon}$ where $\hat{I}$ is the identity matrix and $\bar{\varepsilon}$ is the strain vector. Thus ΔF of the system due to deformation is defined by the displacement of the interaction potential given by the model Hamiltonian (equation (6.2)) as: $w(r) \rightarrow w\left(\left(\hat{I} + \bar{\varepsilon}\right) r\right)$.

Given that r is the position vector in real space of a fraton before deformation, defined by Cartesian coordinates (*x, y, z*), and r' given by (x', y', z') is the position vector after deformation $\hat{D}$ in real space we get the deformation relation: $r' = \hat{D}r$, where $\hat{D}$ is a 3x3 matrix. Similarly, in Fourier space we have the position vector $\bar{k}$ composed of $\left(k_x, k_y, k_z\right)$ before and k' as $\left(k'_x, k'_y, k'_z\right)$ after deformation. Thus by definition of our simulations $\vec{k}\ \vec{r}^{\,T} = \vec{k}'\ \vec{r}'^{\,T} = 2\pi$, where $\vec{k}$ is a row vector and the transpose $\vec{k}^{\,T}$ is a colon vector. So that,

$$\vec{k}\ \vec{r}^{\,T} = \vec{k}\left(\hat{D}^{-1}\hat{D}\right)\vec{r}^{\,T} = \left(\vec{k}\hat{D}^{-1}\right)\left(\hat{D}\vec{r}^{\,T}\right) = \vec{k}'\ \vec{r}'^{T} \tag{6.43}$$

From this expression we obtain that the vector after deformation is related to the displacement by $\vec{k}' = \vec{k}\ \hat{D}^{-1}$ in reciprocal space. The corresponding deformation matrices are,

$$\hat{D}^{-1}_{cubic.} = \frac{1}{1+\varepsilon}\begin{pmatrix} 1 & 0 & 0 \\ 0 & 1 & 0 \\ 0 & 0 & 1 \end{pmatrix},\ \hat{D}^{-1}_{orthor.}\begin{pmatrix} 1/(1+\varepsilon) & 0 & 0 \\ 0 & 1/(1-\varepsilon) & 0 \\ 0 & 0 & 0 \end{pmatrix},\ \hat{D}^{-1}_{monoc.} = \begin{pmatrix} 1 & -\varepsilon & 0 \\ 0 & 1 & 0 \\ 0 & 0 & 0 \end{pmatrix} \tag{6.44}$$

Hence it is possible to express the free energy associated with the three deformations as a function of the strain according to equation (6.41), resulting in the following equations [17],

$$F_{cubic.}(\varepsilon) = F_0 + V_0 \frac{3}{2}\left(C_{11} + 2C_{12}\right)\varepsilon^2 \tag{6.45}$$

$$F_{orthor.}(\varepsilon) = F_0 + V_0\left(C_{11} - C_{12}\right)\varepsilon^2 \tag{6.46}$$

$$F_{monoc.}(\varepsilon) = F_0 + V\frac{C_{44}}{2}\varepsilon^2 \tag{6.47}$$

Thus, it is necessary to determine the elastic constants in order to determine the system response to deformation. Hydrostatic deformation of a system is directly related to its incompressibility, i.e. the bulk modulus (*B*). The modulus *B* is a thermodynamic quantity defined as the ratio between an infinitesimal pressure change resulting in a relative volume change, $B = -V(\partial p / \partial V)$. The pressure variation is caused by stress tensor ($\hat{\sigma}$) and the

volume variation caused by the deformation. The volume variation is then given by the trace of the strain tensor, $\Delta V / V = Tr(\hat{\varepsilon})$. In this case both $\hat{\sigma}$ and $\hat{\varepsilon}$ diagonal matrices, so that the expression of the strain tensor given by the flexibility tensor is given by,

$$\hat{\varepsilon} = \hat{S}\hat{\sigma} = (S_{11} + 2S_{12})\sigma \begin{pmatrix} 1 & 0 & 0 \\ & 1 & 0 \\ & & 1 \end{pmatrix} \tag{6.48}$$

Thus,

$$B = -\frac{\Delta p}{\Delta V / V} = \frac{1}{3(S_{11} + 2S_{12})} \tag{6.49}$$

Utilizing the relation between C_{mn} and S_{mn}, equation (6.40), it is possible to obtain the bulk modulus as $B = (C_{11} + 2C_{12})/3$. It is convenient to use the notation of the C' elastic variable, defined as $C' = (C_{11} - C_{12})/2$. Using these substitutions it is possible to calculate the change in free energy of the system as defined by equations (6.45)–(6.47), with the new elastic coefficient as,

$$F_{cubic.} = F_0 + V_0 \frac{9}{2} B\varepsilon^2 \tag{6.50}$$

$$F_{ortho.}(\varepsilon) = F_0 + V_0 2C'\varepsilon^2 \tag{6.51}$$

$$F_{monoc.}(\varepsilon) = F_0 + V_0 \frac{C_{44}}{2}\varepsilon^2 \tag{6.52}$$

The Zener anisotropy ratio (A_{Zn}) is used for cubic crystals to quantify the relation between the elastic constants as follows,

$$A_{Zn} = \frac{2C_{44}}{C_{11} - C_{12}} = \frac{C_{44}}{C'} \tag{6.53}$$

Thus, an A_{Zn} value of 1 corresponds to an isotropic material. The α-Fe crystal in our model is anisotropic, in addition even if the potentials in our model are symmetric the elastic properties in compression/tension are not. A $128\Delta x^3$ simulation with lattice parameter $a_0 = 16\Delta x$, short-range potential inputs $r_i = 6.4$, $\Delta r = 0.17 r_i$, $\xi = 4$, long-range input $\sigma = 0.3$, for the k^4 potential (equation (6.24)) the long-range its depth was $k_0 = -0.01$ and density $\rho_A = 0.105$ and for the Gauss potential the only difference was $k_0 = -0.005$ and $\rho_A = 0.125$, the elastic properties of our model is given in Table 6-1 with two potentials, Gaussian (6.27) and k^4 (6.24).

Table 6-1. Elastic constants of bcc Fe from ADF modelling and *ab-initio*, units in [GPa].

	Type	C_{44}	C'	B	A_{Zn}	B/C_{44}
This work k^4 pot.	ADF	116	49	112	2.37	0.97
This work Gauss pot.	ADF	116	49	130	2.37	1.12
Müller [233] Theory	*ab-initio*	96	65	190	1.48	1.53
Müller [233] Exp.	-	116	43	169	2.69	1.53
Mendeleev et al. [234]	*ab-initio*	116	49	178	2.37	1.53

Table 6-1 compiles the elastic constants of α-Fe which is the main element of our simulations. There are differences in the *ab-initio* methods e.g. Müller [233] is based on DFT and Mendeleev [234] is based on embedded-atom method potential, hence discrepancies. In this work, target has been to reproduce elastic anisotropy in good agreement with experiment and Mendeleev [234]. As hydrostatic loading is of less concern to us it is more important to obtain good values for C_{44} and C'.

6.1.6 Elastic constraints of the system

The total strain $\varepsilon_{ij}(r)$ of a multi-component system is as defined by Khachaturyan [230] contributed to two effects: configurationally dependent strain-induced interaction among concentration heterogeneities, dependent on the mutual arrangement of heterogeneities and configurationally independent self-energy. Thus, $\varepsilon_{ij}(r)$ might be represented as the sum of homogenous $\overline{\varepsilon}_{ij}$ and heterogeneous strain $\delta\varepsilon_{ij}(r)$, i.e. $\varepsilon_{ij}(r) = \overline{\varepsilon}_{ij} + \delta\varepsilon_{ij}(r)$. The homogenous strain is defined as integrated over the volume. This total strain $\varepsilon_{ij}(r)$ in a simulation volume is the macroscopic shape and volume change associated with a deformation.

As was shown previously by Provatas [229] to model the effect of applied elastic stress of the system, the interatomic potential have been deformed. In our case, the long-range potentials $V_{AA}^{lr}(k)$, $V_{BB}^{lr}(k)$ has been subjected to the constraint, while the $V_{AB}^{lr}(k)$ remains unchanged. This has been done by introducing an atomic distortion coefficient ε. It is difficult to obtain an absolute value of ε, since the continuous displacement field of the system has not been parameterized to any real system. In addition, in our modelling, the discretization of space is limited by the efficiency of our code. So, the size of the simulation grid is higher than the real value of applied deformations. However, it will be shown later that this approach can give an insight into the behaviour of the system under small applied stresses.

From the calculation of elastic constants we obtained an expression for the relation between the deformed structure ($\hat{k}'$), wave vector ($\hat{k}$) and deformation matrix ($\hat{D}$).

$$\hat{k}' = \hat{k}\hat{D}^{-1} \tag{6.54}$$

Where the deformation matrix of uniaxial loading in *z*-direction becomes,

$$\hat{D}^{-1} = \begin{pmatrix} 1 & 0 & 0 \\ 0 & 1 & 0 \\ 0 & 0 & 1/(1+\varepsilon) \end{pmatrix} \tag{6.55}$$

As the potentials $V_{AA}^{lr}(k)$ and $V_{BB}^{lr}(k)$ are defined in reciprocal space then compression of the system is given by $\varepsilon > 0$ and dilatation of the system is given by $\varepsilon < 0$. Thus, for e.g. compression the effect of equation (6.55) is that the equilibrium position of the potential (k_0) will be shifted to a larger value in reciprocal space, equivalent to shorter distance in real space. Hence, as illustrated in Figure 6-3 displacement in reciprocal space is reversibly proportional to real space. Thus, displacements of the wave vector to larger k_0's result in real compression and smaller k_0's result in tension.

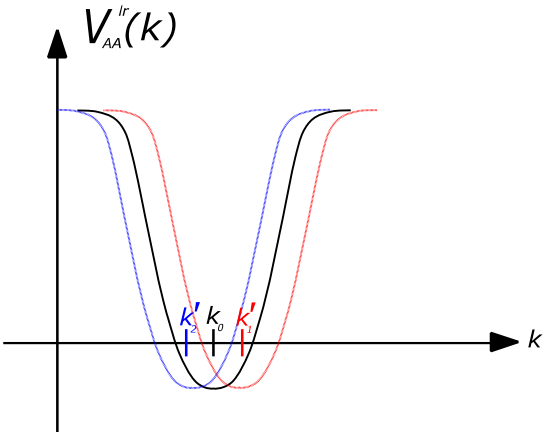

Figure 6-3. Uniaxial constraints of the AA long-range potential, in tension k_2', unstrained equilibrium position k_0 and compression k_1'.

The deformation matrix in reciprocal space (6.55) assumes that we have a linearly elastic material since which follows Hooke's law, where strain ε is restricted to infinitesimal displacements: $\varepsilon = dl + 1$, dl is the stretch ratio of the simulation volume. Still, as we underline earlier, we are unable to treat displacements over the simulation volume that are smaller than the lattice discretization (i.e. if $\varepsilon < \Delta x$). In addition, uniaxial loading in reciprocal space have a $1/(1+\varepsilon)$ dependency which is not symmetric around 1. Therefore, ε has been adjusted to reproduce equivalent deformation of the simulated volume in compression/tension.

A well-known behaviour of linearly elastic materials is that the strain energy contribution to the free energy is proportional to ε^2. In addition, Zener anisotropy provides an insight into the ratio of elastic properties the bcc crystal through small axial and shear displacements. Thus, entering a plastic deformation domain could be seen as an elastic anisotropy collapse of the crystal, by shearing of atomic planes. Hence, by investigating the $\Delta F_{mono./ortho}$ ratio between orthorhombic (axial) / monoclinic (shear) of our single component "α-Fe" structure in response to linear strain it is possible to obtain the extreme values of elastic deformation related to the strain limits of the structure, see Figure 6-4 where ΔF is given by,

$$\Delta F = \left| \frac{2(F_{mono.} - F_0)/\varepsilon^2}{0.5(F_{ortho.} - F_0)/\varepsilon^2} \right| \tag{6.56}$$

This ΔF ratio is obtained from equations (6.51) and (6.52). It is the input parameters of the bcc structure that defines its elastic properties, thus these extreme points are also defining for the two-component system with the same parameters. What we obtain from these calculations is that strain in reciprocal space ε_k is symmetric maximum at $\varepsilon_k = \pm 0.59$ in reciprocal space for tensile/compressive strain. Beyond this point elastic deformation of this system is highly unstable, see Figure 6-4. However, the effect on free energy is non-symmetric. In tension we reach an extreme value at $\varepsilon_k = -0.137$ and the second minima i.e. the simulation limit at $\varepsilon_k = -0.59$. In the range $-0.137 \le \varepsilon_k \le 0.0$ we have similar behaviour of tension/compression in response to the imposed deformation. Between $-0.59 \le \varepsilon_k \le -0.137$ ΔF is first increased before the elastic limit is reached. This difference is of course in part attributed to the stretch ratio of our system which is not symmetric in reciprocal space. Thus, the compressive case which is positively defined is used to recalculate equivalent stretch rations, i.e. equivalent real space deformation of our system. Hence, different absolute strain values are used in reciprocal space to obtain equivalent tensile/compressive deformation levels. Therefore, the yield limit in compression is defined by $\varepsilon_k = -0.59$ allowing 37% deformation of the system, the equivalent deformation in tensile direction is given by $\varepsilon_k = -0.27$. Exceeding this limit to e.g. $\varepsilon = -0.45$ and the atomic spheres lose their structural integrity.

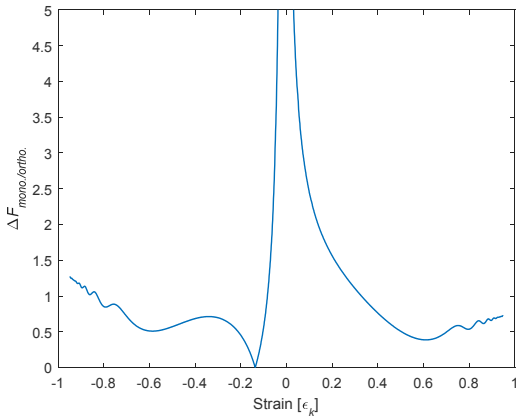

Figure 6-4. Elastic anisotropy energy contribution to free energy as a function of strain ε_k in reciprocal space. Deformation of a $128\Delta x^3$ volume, single component bcc-A, lattice parameter a_0=16Δx, density ρ_A=0.125.

The Green-Lagrange strain tensor is commonly used in finite element methods (FEM) to describe large displacements as it is valid for linear and quadratic terms. In that case strain ε_{gl} is given by,

$$\varepsilon_{gl} = \frac{1}{2}\left(dl^2 - 1\right) \tag{6.57}$$

Here strain ε_{gl} is symmetric and positively defined, the stretch ratio dl is representative of the elongation/deformation of the volume. Thus, in reciprocal space tensile elongation, *dl*, of the volume follows a parabolic curve that goes towards infinity as $\varepsilon_{gl} \to -0.5$. With ε_{gl} notation compression is limited in reciprocal space to ~32% elongation at $\varepsilon_{gl} = 0.59$, and 32% elongation in tension is given by $\varepsilon_{gl} = -0.213$. Thus, the ε_{gl} strain better describes our A-35B system under applied strain, as a linear strain of $\varepsilon = -0.25$ is so high that this strain completely obliterates the spinodal structure so that our A and B distributions appear random. Hence, by the ε_{gl} notation we can model tensile strain all the way up to the yield point which is necessary to see an alignment of the spinodal structure by tensile strain, as seen in experiment by Zhou et al. [16] who applied a load equivalent 97% of their elastic limit. Thus, as we in section 5.1 have evaluated the elastic yield limit σ_y of Fe-35Cr to 310MPa we can for simplicity say that in our A-35B system the yield limit given by the $\varepsilon_{gl} = -0.213$ strain is the equivalent of applying 310MPa load. Therefore, from here on we refer to the level of applied load in terms of % of the elastic limit σ_y or its value in MPa.

Interatomic distance is dependent on crystal orientation thus it is obvious that the system has different elastic properties depending on orientation as it is a crystalline structure scaled towards α-Fe. It has previously been suggested that "soft" directions should favour phase separation in experiment and theory as they have low elastic energy [15], [235]. Hence crystallographic orientation dependence is important for the system response to strain.

Thus, to investigate this influence we simulated phase separation in binary system in different directions for compression and tensions. To change the direction of the stress in our model we rotate our crystal. First a 2D rotation around the *z*-axis according to,

$$R_{001}(\psi) = \begin{pmatrix} \cos\psi & -\sin\psi & 0 \\ \sin\psi & \cos\psi & 0 \\ 0 & 0 & 1 \end{pmatrix} \tag{6.58}$$

As we ought to analyse more complex rotations as the <111> and <112> direction it is necessary to a fully 3D rotation matrix as,

$$\begin{aligned} \Re(\varphi,\Theta,\psi) &= R_{100}(\varphi) * R_{010}(\Theta) * R_{001}(\psi) \\ &= \begin{pmatrix} \cos\psi\cos\Theta & -\sin\psi\cos\varphi + \cos\psi\sin\Theta\sin\varphi & \sin\psi\sin\varphi + \cos\psi\sin\Theta\cos\varphi \\ \sin\psi\cos\Theta & \cos\psi\cos\varphi + \sin\psi\sin\Theta\sin\varphi & -\cos\psi\sin\varphi + \sin\psi\sin\Theta\cos\varphi \\ -\sin\Theta & \cos\Theta\sin\varphi & \cos\Theta\cos\varphi \end{pmatrix} \end{aligned} \tag{6.59}$$

Using this matrix, the position of the atomic configuration is rotated in the crystal.

6.2 Spinodal decomposition in a binary system

To model a binary A-B system we need to introduce some new parameters to describe among other things the chemical nature of the AA, BB, AB interaction in the system. AFT has previously been used to model complex binary systems [56], however here we need a general method to describe two phases without a periodic structure in-between them.

Thus, in section 6.1.3 we treat the transformation of a random distribution of A fratons into an ordered crystal structure. However, in a two-component system we need to introduce a new potential for the interaction between A-B. As we consider an ideal bcc system in two cases composed of A-35B and A-50B regular solutions. Thus, to describe phase separation between A-B we use a Gaussian potential centred at zero position. The Gaussian potential is selected for its simplicity, given by the equation,

$$V_{AB}(k) = -\mu \cdot \exp\left(\frac{-k^2}{2\sigma^2}\right) \tag{6.60}$$

The minimum of this potential is reached when $k \to 0$. Since in reciprocal space $k = 2\pi / r$ the equilibrium distance between A and B in real space is obtained by $r \to \infty$, meaning that during phase separation the phases are enriched in A and B respectively. The dimensionless coefficient μ influence the value of $\lambda(k)$, defined in section 6.1.2, and thus the driving force for phase separation. It can be considered as the interaction strength between the A and B atoms. Therefore, the selection of μ influences the choice of time step *dt*. Hence, in these simulations of a regular A-B solution it is fixed to $\mu = 0.08$.

The aim here is to study phase separation in comparison to the Fe-Cr system, in order to do so simplifications of the system has been made. As a start, Fe and Cr are both of bcc structures with a lattice parameter of 2.87Å and 2.89Å respectively. In addition, their atomic radii are 128 and 126pm respectively. Therefore, the atomic radius and the long-range interaction potentials $V_{AA}^{lr}(k)$ and $V_{BB}^{lr}(k)$ are chosen to be identical with the same lattice parameter. The size difference between atoms is considered insignificant, which means that the short-range potentials are the same. The elastic properties were not parameterized based on the real Fe-Cr system but rather on the α-Fe system as Fe would be the main constituent in the A-35B system. The long-range potentials are thus given by,

$$V_{AA}^{lr}(k) = V_{BB}^{lr}(k) = \exp\left(-\frac{(k-k_0)^2}{2\sigma^2}\right) \tag{6.61}$$

Where k_0 is the first minima of the function in reciprocal space, already defined by equation (6.26). The "width" of the Gaussian is defined by $\sigma = 0.15$, the mesh parameter and discretization is $a_0 = 8\Delta x$ and $\Delta x = 1$. The parameters used in the short-range potential is $r_i = 3.2$, $\Delta r = 0.17 r_i$ and $\zeta = 4$, the average concentration of fratons are for A-35B $\bar{\rho}_A = 0.052$, $\bar{\rho}_B = 0.028$ and for A-50B $\bar{\rho}_A = \bar{\rho}_B = 0.04$. These parameters describe the bcc crystal with corresponding elastic constants given in Table 6-1. The initial state for these simulations corresponds to randomly distributed A and B fratons on the sites of bcc lattice. The solution of the kinetic equation (6.29) gives the kinetic evolution of the fraton densities.

6.3 Quantitative results

To make sure that the crystallographic structure of the simulated A-35B system is well defined, the intensity of the density function is calculated by $I(k) = \rho(k)\rho^*(k)$ to attain the diffraction pattern.

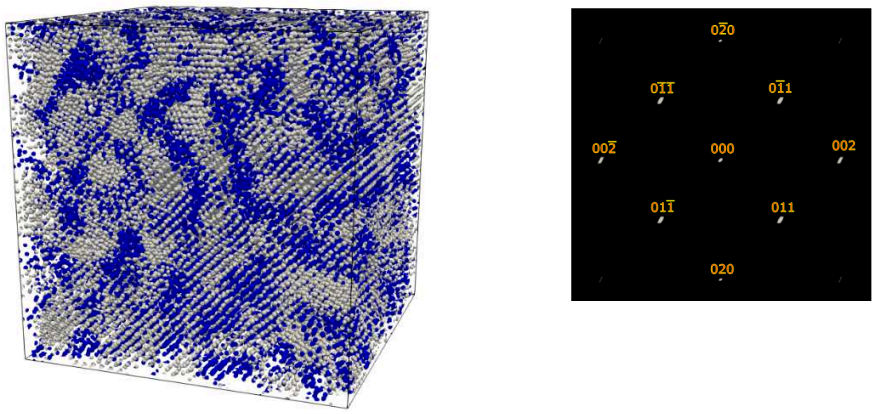

Figure 6-5. Simulation of spinodal decomposition in a $256\Delta x^3$ volume, lattice parameter $a_0 = 8\Delta x$, $\rho_A = 0.028$, $\rho_B = 0.052$ at time $t = 2 \cdot 10^6$ time steps, A atoms are represented by blue and B atoms by green colour and diffraction pattern of the bcc <001> plane.

From the intensity function is it possible to obtain the diffraction pattern on the {100} - plane. In this projection we have the <011> - poles at a 45° angle from the (0, 0, 0) centre, and at 90° from the centre we obtain the <002> - poles. Thus, the simulation has successfully reproduced a bcc structure, the surrounding low-intensity circle reflects the long-range periodicity of the structure.

The static structure factor $s(k)$ is a thermodynamically important entity for systems described by pairwise interaction potentials as it can provide the potential energy, pressure and atomic ordering by the distribution of atoms. It is defined as,

$$s(k) = \frac{1}{N}\left\langle \left|\rho(k)\right|^2 \right\rangle \tag{6.62}$$

The response function of our simulations can be directly related to the structure factor according to the relation,

$$s(k) = k_B T D^{-1}(k) \tag{6.63}$$

Thus, the structure factor is a way of representing the density correlation function in reciprocal space, i.e. it corresponds to the periodicity in atomic distribution. The relation between the radial distribution function, $g(r)$, and the structure factor is a well-known relation given by,

$$\mathrm{s}(k) = 1 + \rho \int \left(g(r) - 1 \right) e^{ik^* r} dr \tag{6.64}$$

In real space the radial distribution function, $g(r)$ or RDF as earlier defined by equation (3.24), can describe short-range correlation affinity or preferred separation distance. From our AFT simulations, we can extract data sets with (*x, y, z*) - coordinates of the atomic positions in real space. Thus $g(r)$ can be re-written as,

$$g(r) = \frac{1}{nN} \left\langle \sum_{i=1}^{N} \sum_{j \neq i=1}^{N} \delta\left(r + r_j - r_i \right) \right\rangle \tag{6.65}$$

One of the points of the experimental investigation is to determine the limits of the miscibility gap, which means investigating the evolution of the structure by $g(r)$ and $\mathrm{s}(k)$ in close proximity to the spinodal limit. In Figure 6-6 is this evolution displayed in the A-35B system, and the more quantitative temperature dependency is provided in Figure 6-7.

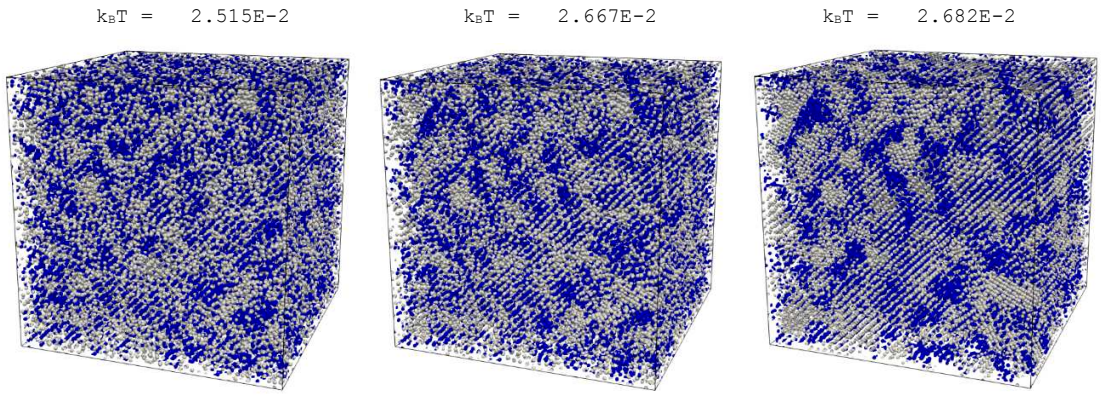

Figure 6-6. Evolution of the structure depending on temperature: $\lambda^{g(r)}_{k_BT=2.51E-2} = 1.56a_0$, $\lambda^{g(r)}_{k_BT=2.67E-2} = 1.83a_0$, $\lambda^{g(r)}_{k_BT=2.68E-2} = 2.74a_0$ with the consolute temperature $k_BT = 2.684E-2$. Volume 256Δx^3, ρ_A = 0.052, ρ_B = 0.028 at t = $2 \cdot 10^6$ time steps. A atoms are represented by blue and B atoms by grey colour, the initial structure is a random fraton distribution with fluctuation amplitude $\Delta\rho_A = \Delta\rho_B = 0.035$.

In ADF theory [230] the difference between two metastable α and β phases in a miscibility gap is temperature dependent. As the critical dissolution temperature T_c is approached the homogenization between α and β is given by: $(1-2C_\alpha)\tan(\chi)^{-1}$, where C_α is the concentration of A in the α matrix and $\chi = (\partial C(x)/\partial x)_{C=1/2}$. This homogenization tendency is in proximity

to a dissolution temperature is similarly described by the non-classical nucleation theory. Thus, as we here model our system at the atomic scale we have no interface to speak of, instead, we see an increase of the characteristic wavelength that described the α/β periodicity. In our case with AFT simulations, the behaviour is an exponential function given by quantitative by $s(k)$ of the simulated volumes in Figure 6-7. This temperature-dependent evolution of the system is similar to the Cahn-Hilliard (CH) theory (section 2.3.2) in terms of an exponential increase of the length between α and α' that goes towards infinity in close proximity to the limit of the miscibility gap (i.e. T_c).

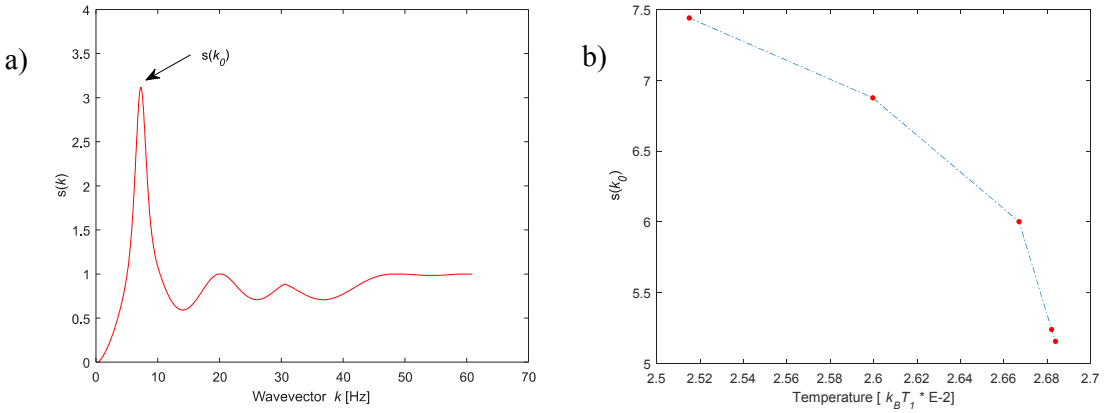

Figure 6-7. Evolution of the structure periodicity with temperature, AFT theory a) the structure factor in reciprocal space, b) evolution of s(k_0) with temperature including the consolute temperature k_BT=2.684E-2.

As we in our model allow for complete separation between A and B atoms, meaning that α and β composition is either 100% A or B, we investigate the temperature-dependent periodicity rather than a decreased composition gradient between α and β. Thus, since the composition of our system is conserved, we see an increase of the characteristic wavelength. This behaviour has been reproduced both by A-50B and A-35B simulations. The s(k) in Figure 6-7 is obtained from the density function of our model, i.e. equation (6.63), $g(r)$ in real space has also been performed to verify this trend. The "real" shape or limits of the miscibility gap in our model would relate to the volume fraction of α and β. In essence, the periodicity of the structure corresponds to the volume fraction of the phases in equilibrium, hence it is easy to relate to the shape of the miscibility gap through the lever rule. Thus, changing the composition only changes the length of the characteristic wavelength not the behaviour of the system.

If the periodicity were to be highly anisotropic then RDF and s(k) are not suitable for describing orientation dependency of the structures, as it represents the mean intensity in the volume. Instead, a simpler yet effective method to quantify the structure is to consider the average density profile in a specific direction in real space is calculated as,

$$\bar{\rho}_{B_z} = \frac{1}{n_x n_y \Delta z} \cdot \sum_{r \in \Delta z} \rho(r) \tag{6.66}$$

Where Δz is one segmentation ("slice") of the volume in z-direction, here $\Delta z = 3n_z$. To reduce noise from the concentration profile autocorrelation has been used to estimate the waves in the volume so that Δz is chosen appropriately. Then for better accuracy of the average wavelength in the volume fast Fourier transform of $\bar{\rho}_{B_z}$ (equation (6.67)) is used to produce its frequency domain of $\bar{\rho}_{B_z}$. Then a Gauss distribution with 95% confidence is fitted to this frequency domain, to obtain the characteristic frequency $\bar{\lambda}(k_0)$. To benchmark the $\bar{\lambda}(k_0)$ measurements a comparison with the result from equation (6.63) is made in an isotropic reference state: the result is $\bar{\lambda}(k_0) = 0.156 \pm 0.016k$ and $s(k_0) = 0.12k$ respectively. Thus, the inverse of $\bar{\lambda}(k_0)$ is in real space representative of the characteristic wavelength, however, a minor overestimation by the Δz segmentation of the volume should be noted.

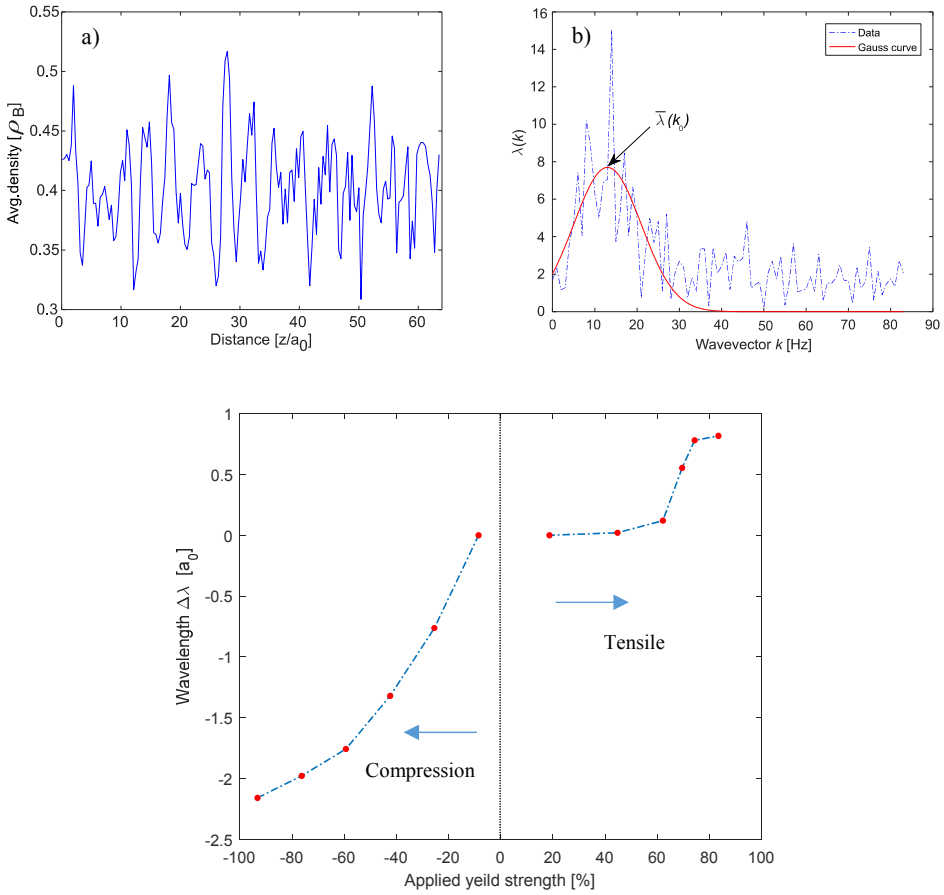

Figure 6-8. The analysis method of the effect of an applied loading a) average concentration profile in the direction of applied load, b) the Fourier transform of the concentration profile fitted by a Gaussian distribution with 95% confidence, c) the effect of applied load positive in tension and negative in compression t = $2*10^6$.

In Figure 6-8 c) is the effect of pure axial-loading on the periodicity of the decomposition analysed through the relative change of the characteristic wavelength. The analysis is based on the $\bar{\lambda}(k_0)$ method with the concentration profiles in z-direction, i.e. in the same direction as the applied loading over $64\,a_0$. It is observed that when the system decomposes under compressive strain it leads to a decrease in $\bar{\lambda}$ due to the formation of a plate-like structure, it is aligned perpendicular to the applied strain. If the strain is applied in the tensile direction the structure will first coarsen while remaining isotropic. But when strain is further increased beyond a critical point at ~185MPa the structure starts to align itself perpendicular to the applied strain. However, this alignment is not as obvious by ocular examination as in the case of compression. Thus, if a cubic volume is extracted to analyse the wavelength perpendicular to the applied load the effect of the wavelength parallel to the applied load is non-significant. However, the effect on the wavelength perpendicular to the applied load exhibits the same strain-dependent trend as in Figure 6-8 c). To further confirm this anisotropic alignment of the structure the diffraction pattern is used.

In Figure 6-9 is the (0,0,0) pole of the <100> plane when applying tensile load in the <001> direction, i.e. the plane with its normal direction perpendicular to the applied strain. When increasing the stress one can see that strikes of diffusion scattering appear, these strikes are parallel to the applied strain. As this is represented in Fourier space it means that in real space there is an alignment of the intensity perpendicular to the applied load, as expected.

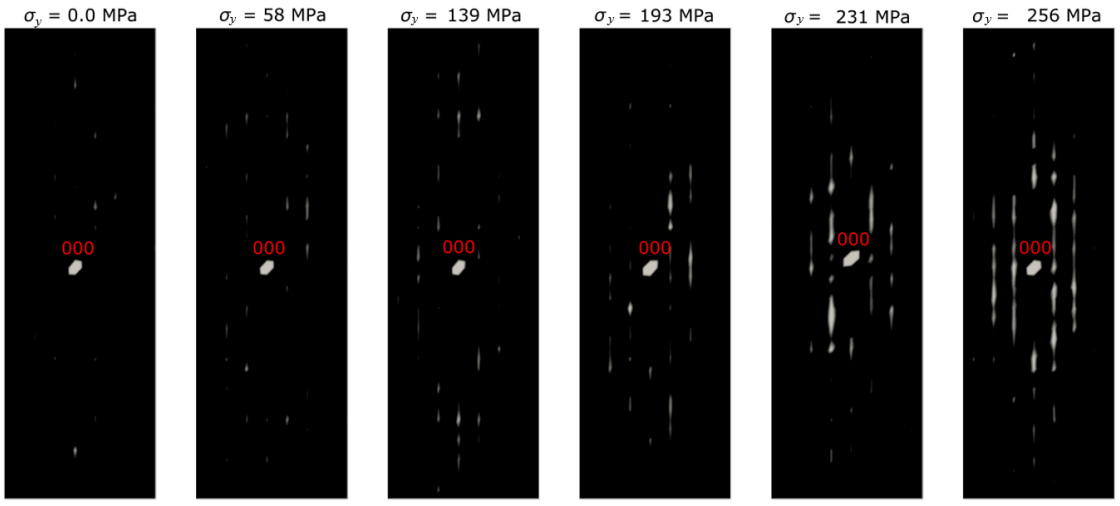

Figure 6-9. Diffraction pattern on the {100} plane, <001> strain direction, cantering the (0, 0, 0) pole. Intensity lines appear around the pole parallel the direction of the applied stress, thus in real space, the periodicity is prone to alignment perpendicular to the direction of the applied stress.

Thus, the strain/deformation of an applied load is not reversely proportional in compression/tension, since the free energy response to strain of the material does not react in

the same way. Under compression, the repulsive forces between atoms restrict how closely atoms can be compressed. Thus, energy per unit-volume would then in a compressed volume increase, potentially causing the greater response to the applied strain. During dilatation, volume is stretched, furthering the distance between atomic sites. This has a great effect on the characteristic wavelength, in relation to an unstrained reference state, it is dramatically reduced even at only 1.35MPa load. Thus, for our modelling, we are interested in the relative change of the system due to increased tensile loading. The system first responds by coarsening the characteristic wavelength, directly related to the applied load level. However, when the added strain is large enough it starts to affect the morphology of the structure. First by a much wider Gaussian distribution of representing the $\bar{\lambda}(k_0)$, then by aligning itself in directions that are energetically favourable this often means perpendicular to the applied forces as seen by Figure 6-9. This change in morphology is related to the energy minima in Figure 6-4 at $\varepsilon_k = -0.137$ i.e. 185MPa it falls in-between $\sigma_y = 139\text{-}193$ MPa where the change in morphology occurs.

In light of this, it is increasingly interesting to also investigate the influence of orientation of the stressed volume during decomposition, as the interatomic distance/plane-density is dependent on orientation. In addition, the anisotropic elastic nature of the bcc structure means that the elastic energy contribution would depend upon the interatomic distance of the orientation of the crystal. This, in turn, could potentially have an effect on the morphology and rate of decomposition. Thus, the principal directions of the bcc structure, as well as the <112> direction, has been selected for the orientation-dependent analysis, for direct comparison with the experimental results.

The rotation matrix (6.59) is used to rotate the bcc crystal so that the applied load is oriented in the right directions, i.e. so that the desired crystallographic orientation is aligned parallel to the applied force in the *z*-direction of the volume. The rotation of the crystal is given in Table 6-2. The $\bar{\lambda}(k_0)$ characteristic wavelength of the structure in the *z*-direction is given in Ångström in the same table, the length is approximated by the lattice parameter of α-Fe.

Table 6-2. The effect of crystallographic orientation on wavelength under tensile load ~74.4% of yield strength.

Rotation	**Ref.**	**(0,0,0)**	**(45°,0,0)**	**(45°,35.26°,0)**	**(45°,30°,0)**
Orientation of z-axis	<001>	<001>	<101>	<111>	<112>
Stress	0.0	231 MPa	231 MPa	231 MPa	231 MPa
Wavelength	14.12Å	13.59Å	13.98Å	12.15Å	14.05Å

Images in Figure 6-10 display the (*x, z*) - plane of the simulation box, the desired orientation is aligned parallel to the *z*-axis. Then pure axial load is applied in the *z*-direction, thus the

displayed morphological difference is also dependent on the difference in crystallographic orientation.

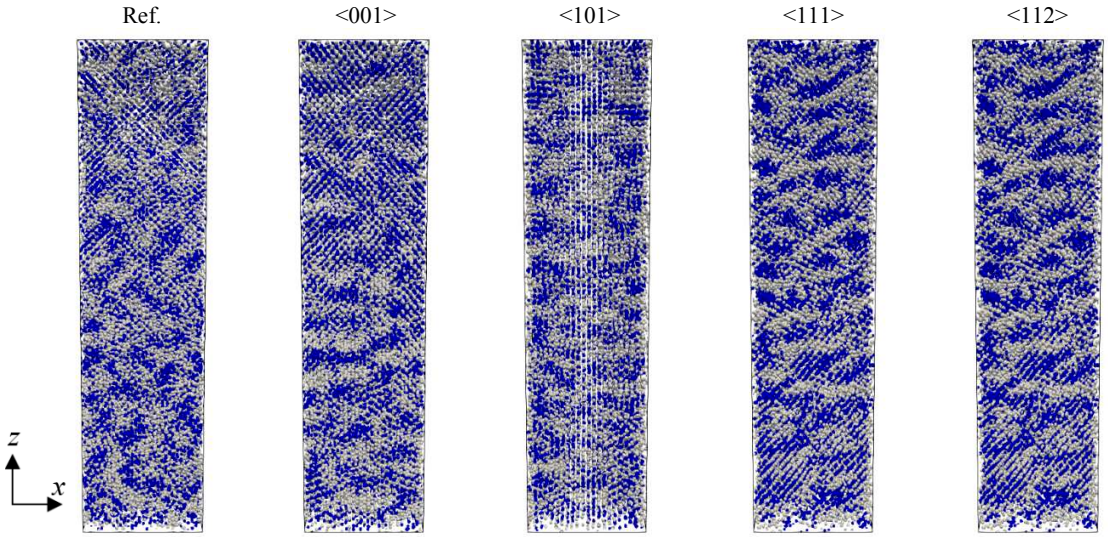

Figure 6-10. Orientation dependent decomposition of A-35B ($\rho_A = 0.052$, $\rho_B = 0.028$), at time step $t = 2 \cdot 10^6$, tensile yield strain is 75%, the characteristic wavelength is compiled in Table 6-2.

Strain in the "soft" α -Fe <001> direction produce a slight alignment of the $\bar{\lambda}(k_0)$ periodicity, in relation to the isotropic reference state. This alignment produces a relative decrease of the characteristic wavelength. The <101> is a close-packed slip-plane and thus it reacts stronger to the applied stress, hence in this principal direction is where we find the 2nd longest characteristic wavelength. The <111> direction is elastically stiffest of them all with a threefold symmetry and shorter interatomic plane distance than <101>. This direction responds by a higher degree of A and B separation into α and β, thus A/B separation has progressed the furthest with the shortest $\bar{\lambda}(k_0)$ wavelength. Finally, the low density <112> slip plane has surprisingly great response to the applied load, it is the low-density slip-direction with the shortest interatomic plane distance. There is an obvious alignment of the structure seen in Figure 6-10 however obviously not always perpendicular to the applied load direction, hence the diffraction pattern is further analysed in Figure 6-11.

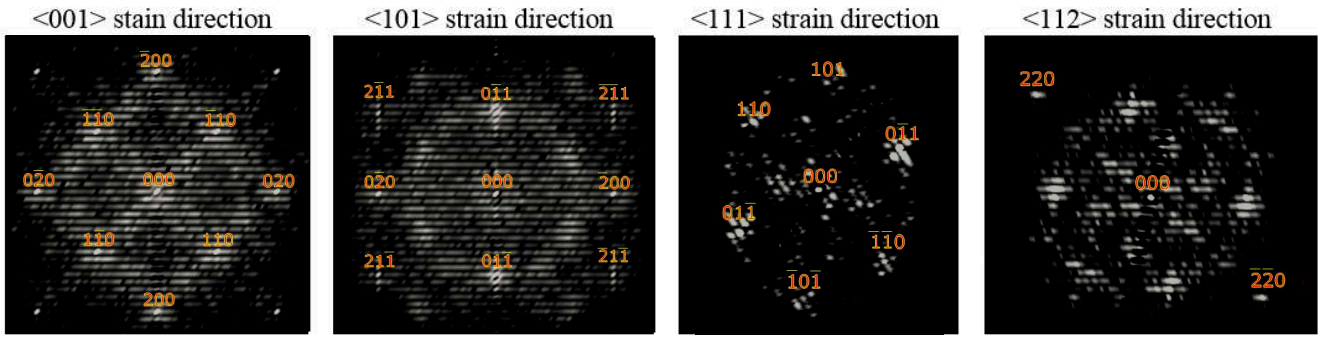

Figure 6-11. Orientation dependent orientation the diffraction pattern is of the {100} -plane of the simulation box with the indicated crystallographic orientation aligned parallel with the {001} direction of the simulation box which is strained.

These diffraction patterns display the planes whose normal direction is in the direction of the applied load. Thus, the diffraction of the <001> direction display higher intensity lines towards the (0,1,1) and (0,2,0) poles. Which means that in plate-like morphology is fairly isotropic with some aligned in the <100> direction. In the <101> direction, there is higher intensity at the (0,2,0) and (0,1,1) poles, but clearly the highest intensity is found in the <011> directions, i.e. perpendicular to the applied load. Visually and by diffraction of <111> and <112> strain we can see some rotation of structure in real space and in the diffraction pattern. From diffraction, this angle appears greater for the <112> orientation with alignment towards the <111> direction. For the <111> direction the alignment of the structure is in a ~45° angle of the <101> orientation. Observed from $s(k_0)$ analysis is that <111> has more well-defined transitions between high and low-intensity regions, i.e. the preferred separation distances. Thus, the <112> has a slightly wider range of composition fluctuations. The result is a smaller structure factor $s(k_0)_{<112>} = 0.23k$ versus $s(k_0)_{<111>} = 0.237k$, which means that in real space the characteristic wavelength of <111> is shorter.

As the ferritic stainless steel often is structural materials with more complex stress states than axial-loading it is interesting to investigate the effect of the principal stress states. In addition, these steels are polycrystalline materials, so often characterized by a random grain orientation distribution. Hence, the exact stress state inside a grain influenced by the stiffness of its surrounding environment is hard to determine. Even though it is possible to manufacture materials with a texture the exact stress state depends on the local chemical composition and grain boundaries.

As an example, consider duplex stainless steels often used as structural materials in welding applications, it consists of ferrite (bcc) and austenite (fcc). Austenite has a greater linear thermal expansion and solidification density then ferrite [236]. Thus, in service at intermediate temperature it is plausible that the ferrite is constrained in the duplex system, which may lead to complex compressive/shear forces. Therefore, a comparison between tensile,

compressive and shear strain has been made during an external loading of 231MPa, the result is presented in Figure 6-12.

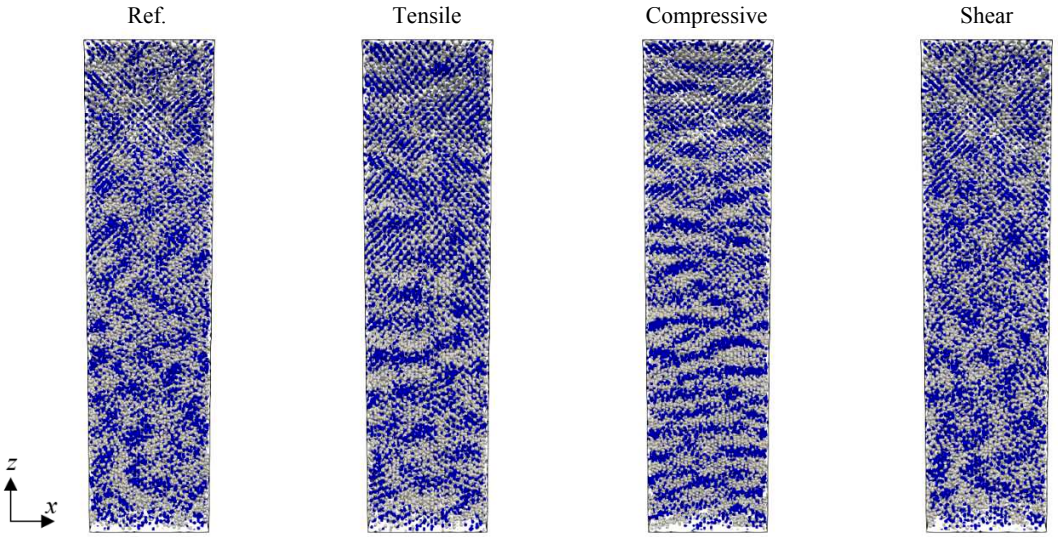

Figure 6-12. View of the {010}-plane with <001> - strain direction, loading 75% of yield limit in tension/compression. The characteristic wavelength is for: reference state 14.12Å, tensile 13.35Å, compression 8.40Å and shear 11.68Å.

These simulations confirm that the stress state effect morphology and the kinetics of decomposition. In all these cases the pure axial load is applied in the <001> direction, thus it is obvious that compression is the stress state in our model with the greatest response to the applied load. Tensile stress has a similar effect on morphology as compression, however less obvious, we have already seen the effect of tensile load level on periodicity and morphology Figure 6-8 and Figure 6-9 respectively. Still separation between A-B atoms has progressed the furthest by compression. Shear in this A-35B alloy appear visually isotropic from this point of view, however, from previous A-50B simulations we have seen significant morphological anisotropy dependent on shear. Thus, in this case of shear loading in the (y, z) - plane, we

expect some anisotropy. Hence the diffraction pattern on the {100} - plane is investigated in Figure 6-13.

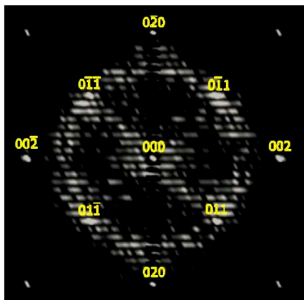

Figure 6-13. Diffraction pattern of the {100}-plane, shearing in the *yz*-plane result in an alignment in the <011> direction.

The point to be highlighted in Figure 6-13 is the high-intensity region aligned at a 45° angle, in real space, this alignment is obviously inverse. Thus, shearing of the (*y*,*z*) - plane result in high-intensity regions in <110> direction, not ideal for visual representation but still present.

6.4 Final remarks

In this chapter dedicated to modelling, ADF theory has been used to model decomposition and influence of applied stress on the microstructure evolution in Fe-Cr alloys. ADF theory is constrained to a rigid Ising lattice, thus the extended quasi-particle approach AFT was used to model the effect of applied strain. The temporal evolution of the system is governed by the density function of atomic fragments, which determines the probability of whether a simulation grid belongs to an atomic sphere or not.

In order to model our crystalline structures two types of interaction potentials have been introduced. The short-range interaction potential which represents the condensation of fratons into spherical atoms. The second part is the long-range potential which determines the periodicity of atomic spheres. The long-range interaction periodicity is based on cluster notation, where each cluster element represents an interatomic bond.

The elastic constraint of the long-range potential is introduced by a deformation matrix acting on the wave vector *k* which defines the system. The deformation matrix is the sum of the identity matrix and a strain tensor. Thus, different strain tensors can be used to describe the displacement of the wave vector to apply different stress states and stress levels. The limit of deformation is evaluated by the change of elastic energy during deformation. In essence, in

reference to an unstrained state, we alter the interatomic distances by small deformations, which in turn affect the interatomic bond and subsequently the free energy defined by the elastic properties of the system. The applied load in modelling was linked to the real units through the reaction to deformation of the volume. To investigate the influence of crystallographic orientations a rotation matrix successfully used to rotate the crystal so that the desired orientation is aligned with the applied load, the result shows good agreement between AFT and APT experiment.

The AFT method has shown great potential in describing the influence of external constraints of spinodal decomposition. Since the elastic properties are defined by the nearest neighbour interaction it is not necessary to impose a composition-dependent elastic modulus of the system, as it is for phase field methods. The ability to vary the stress state and orientation of the crystal structure greatly enhances the versatility of the model.

The effect of tensile, compressive and shear stress states has successfully been modelled by the AFT method. During uniaxial loading, the periodicity increase as a function of the applied load with error function behaviour, when this deformation is reversed into compression the periodicity is exponentially decreased. The decomposed structure becomes plate-like aligned perpendicular to the applied load at high strain levels. In the case of shear stresses the structure aligns itself in a 45° angle in comparison to the shearing surfaces.

Chapter VII

Discussion of main results

The novel aspect of this work is the investigation of the influence of an external force on phase separation in Fe-Cr alloys. To achieve this objective a combination of atomistic modelling and the state-of-the-art experimental techniques was used. The experimental investigations focused on the early stages of phase separation in combination with elastic tensile forces at intermediate temperature, the work was then extended into different stress states through ADF modelling. In order to do so, the limits of the metastable Fe-Cr MG were first investigated, along with a kinetic study of NG/SD. Even though the Fe-Cr system is well known its exact phase diagrams is not well reproduced by existing models. Hence, a new optimization was presented in this work based on direct observations of α' formation in 3D at the atomic scale.

7.1 Highlights from experimental work

The limit of the MG was defined as the limit of α' formation after 120h ageing. Thus, by favouring the kinetics with higher than normal temperature the upper limit of phase separation was determined for Fe-x$Cr_{(x=20,35,50)}$ alloys. Utilizing a high precision furnace, the limit of phase separation for these alloys could be determined, first by exploring the temporal evolution of mechanical properties. Then NG/SD phase separation mechanisms were investigated by APT. For Fe-20Cr the limit of NG was found at 540 ± 1.5°C. For Fe-35Cr alloy it was possible to locate the limit of the MG at 570 ± 1°C which according to Cahn-Hilliard theory is close to the spinodal limit, and for the Fe-50Cr alloy, the MG consulate temperature was found at 580 ± 1°C.

A literature review of the metastable Fe-Cr phase diagram was compiled to establish consensus of the latest Fe-Cr MG description, and large discrepancies were found. The Fe-Cr system is complex, in part due to the treatment of magnetic momentum and equilibrium solubility's of the low-temperature MG. However, the upper limit of α' formation was more consistent in published experiments. With the addition of these new data, a re-optimization of the metastable MG was conducted. Based on Cr solubility in α above 325°C and data concerning the location of the upper limit of the MG. In combination with new *ab-initio* calculations of the unary descriptions, the re-optimization could better capture the behaviour of Cr solubility and thus the location of the MG as it is presented in this work.

We have observed experimental results of the free energy dependency of the critical wavelength in an SD structure as described by the Cahn-Hilliard theory. It was observed that as the spinodal line is approached from within the spinodal regime the characteristic wavelength increased exponentially towards infinity in Fe-35Cr.

The nominal composition dependency of α' formation during isothermal heat treatments showed an increase in volume fraction α' with increasing Cr content. Thus, alloys with a higher volume fraction α' /higher Cr-content results in a shorter characteristic wavelength. Naturally, this trend is restricted to 50at.%-Cr in a binary system, as α would be the precipitating phase in the case at.%-Cr > 50%. The time exponent of the characteristic wavelengths, however, exhibits good agreement with LBM theory for both Fe-35Cr and Fe-50Cr (i.e. SD).

Thermoelectric power (TEP) is a simple yet efficient non-destructive way of investigating the kinetics of phase separation in Fe-Cr. A difference in kinetic behaviour between alloys with different decomposition mechanisms (i.e. NG/SD) was observed. This is most likely linked to Cr atoms leaving the α matrix, but also in part due to the magnetic properties of the precipitating phase relative to their solution treated state. By correlative APT-TEP investigation, we found that the evolution of volume fraction of α' and the variation in TEP could be attributed to the activation of Cr diffusion in α-Fe. Thus, TEP has shown great potential of possibly discriminating the kinetic behaviour of NG/SD, which must now be proved.

Cr-Cr clustering above the MG in Fe-Cr has been investigated. It was seen that the amount of clustering was stable in time, however, it decreased with increasing temperature. The decreasing trend in the clustering could correlate well with a quasi-chemical model for the bond probability distribution above the MG, which also indicated that significant clustering would be present at the α' dissolution temperature. Thus, clustering is temperature-dependent above the MG, this is most likely an entropy dependent phenomenon. Since the degree of clustering decreases with increasing temperature as the entropy contribution (-TS) become more dominant.

There is a small effect of crystallographic orientation and the degree of SD in polycrystalline Fe-Cr alloys. For an unstrained sample, the difference between the principal bcc directions are within the margin of error, for a stress-aged sample the principal directions show small differences just beyond the margin of error. This small effect on unstrained samples

could possibly be due to the small size difference between the pure Fe/Cr elements, the effect on strained samples could potentially be linked to the difference in elastic anisotropy.

Stress-ageing showed that higher load levels noticeably further enhanced decomposition. Based on the statistical analysis of high load stress-ageing the characteristic wavelength of the periodic structure depends on orientation from smallest to largest: <001>, <111>, <101>, <112>. As is known Cr, is significantly stiffer in <001> than Fe, thus what we see from this analysis is that <001> direction behaves as the stiff direction and <111> is the softer direction. But it appears that Fe slip directions are the most favourable for decomposition and specifically the <101> direction. The low-density slip plane <112> tends to favour a longer wavelength. Stiff and close-packed directions, i.e. <001> and <101>, tend to favour higher Cr concentration in α'. The "soft" <111> direction is where we find the lowest Cr concentration in α', similarly, in the low-density slip plane <112> we have lower Cr in α' than in <101>.

Evaluation of nano-hardness in combination with APT show that orientations with higher at.%-Cr in α' results in higher hardness. Hardness dependency on orientation from softest to hardest is: <111>, <001>, <112>, <101>. Analysis of the surrounding environment does not exhibit large variation in hardness that may cause the difference between these grains. The hardness difference of the surroundings does not show a significant spread or correlation with the hardness of the individual grains. Thus, the difference between the crystallographic orientations cannot be related to the immediate environment in which the grains were embedded. It is more probably an effect of the orientation dependence of elastic properties, thus the difference is very small. The case which stands out is the <101> grain, where the hardness is noticeably higher than in its surroundings. Hence, it is natural that this would affect the immediate surroundings so that the hardness is marginally higher than in the environment surrounding other grains.

7.2 Highlights from AFT modelling

The pseudo-particle approach, i.e. Atomic fragment theory (AFT) [50], is a continuous model that allows for modelling of physical phenomenon at the atomic scale. The timescale of this model correspond to a typical diffusion time, which could vary from a fraction of a second to years. The model relies on mainly two principals: 1.) Introduction of the pseudo-particles that describe two configurational states of each point of continuum space, i.e. a non-ideal gas whose "condensation" describes a diffusional self-assembling of atomic systems, 2.) a structural cluster function describing the directions, length and strength of interatomic bonds. The

introduction of the cluster concept allows to formulate a simple Hamiltonian that is proportional to a bilinear expansion in these cluster function. The model Hamiltonian provides the formation of a predetermined atomic structure and has enough flexibility to describe the desired mechanical and thermodynamic properties of this structure. This model is very versatile with the possibility of describing different levels of topological complexity [56]. In this work, we have constructed single and two-component bcc structures in equilibrium configuration, from solidification and phase separation.

This AFT approach enables modelling of A-B phase separation in a single bcc crystal during tension, compression, shear and hydrostatic dilatation/compression. Beneficial for this model is that the initial nuclei can be rotated freely in the simulation box by a 3D rotation matrix. Therefore, different crystallographic directions could be aligned parallel to the applied strain and investigated.

The Green-Lagrange strain tensor is introduced as it directly gives the half-square distance of displacement, i.e. it is a positively defined symmetric tensor. Naturally, the deformation introduced by a displacement in reciprocal space is not the same in tension/compression, thus the absolute value has consistently been recalculated to obtain equivalent levels of deformation. The elastic limits of our model have been defined by the shear and axial strain effect on the free energy. If the elastic limits are exceeded the energy response to deformation starts to oscillate (beyond $\varepsilon > \pm 0.59$ as seen Figure 6-4) and the simulation does not stabilize.

It has been seen that the influence of the temperature alters the periodicity of the structure as the limit of instability is approached. It increases exponentially very close to the limit of instability when it is reached a homogenous bcc structure is obtained on two superimposed bcc lattices. The nominal composition in our simulation is conserved so that the temperature-dependent volume fraction of α and β can be considered constant.

One point is that weights can be put on the potential to limit the degree of separation to a predetermined equilibrium composition. However, the general approach in this work has been to allow for the complete separation between A and B atoms. Meaning that one lattice site in the simulation volume is occupied only by one type of atom. The versatility of the model is then further explored as it would be possible to obtain phase compositions of the modulated structure with the AFT approach. However, here the focus has been on atomic modelling and therefore by simplicity an atom site is solely occupied by one type of frosting.

The AFT modelling has shown to be very versatile in the modelling of elastic constraints of the system. This is because elastic properties are defined at the atomic scale and neighbour interaction is naturally considered and therefore no composition dependency of the elastic properties needs to be pre-defined. Thus, constraints to the wave vector describing the interaction potential can easily be added. By doing so we have successfully modelled uniaxial and hydrostatic compression/tension and shear. In addition, by the introduction of a rotation matrix, uniaxial loading in different crystallographic directions can be achieved. There is a noticeable difference dependent on orientation as interatomic distance as a direct response to the alteration of free energy. Considering the bcc structure, the wavelength of the periodic structure depends on the orientation of the structure from smallest to largest: $\lambda_{111} < \lambda_{001} < \lambda_{101} < \lambda_{112}$. From the calculation of elastic constants of our model, we know that for bcc-Fe <001> is an elastically soft direction and <111> is the stiffest direction, <101> is a slip-plane that falls in-between, as well as the <112> slip-plane, does in terms of elastic stiffness. However, <112> slip plane is of lower atomic density thus it exhibits a longer wavelength than <101>.

7.3 Comparing modelling with experiment: influence of uniaxial tensile load on spinodal decomposition

Due to the difficulty to accurately control the local stress distribution of a single grain in a polycrystalline material the experimental investigation was restricted to uniaxial tensile loading. This allows us to control an "average" axial force during ageing without the need to consider the effects of bending or shearing in the contact surface between sample and support. In a very large grain, the average stress can be approximated as homogeneous.

Figure 7-1 illustrates the correlation between our model and the experimental work, tensile strain is intended to serve as a reference for this comparison. Ultimately high morphological anisotropy for high tensile load levels has been seen before by APT in duplex Fe-Cr alloys by Zhou et al. [16]. This phenomenon has not been observed in our experimental investigation of purely ferritic Fe-Cr alloys with more conservative load levels to maintain purely elastic conditions. Hence, no clear morphological anisotropy could be determined in our case, however, we still have good agreement in the system's response to the applied load regarding its effect on the characteristic wavelength and Cr composition amplitudes.

In Figure 7-1 there is the obvious difference in volume fraction of α'/β represented by green atoms for APT and AFT respectively. The volume fraction β is roughly ~0.40 while α'

is ~0.1 even though the nominal composition solute is in both cases 35%. This difference is due to the construction of the miscibility gap in the model. In experiment α' composition consist of ~80at.%-Cr, while in the model it is 100%-B in β. Therefore, one observes a longer characteristic wavelength in the experimental investigation, because the matrix contains at least 14at.%-Cr when phase separation is close to equilibrium [192]. Observed by AFT is that greater volume fraction of β in A-35B versus A-50B leads to greater morphological response to the applied load.

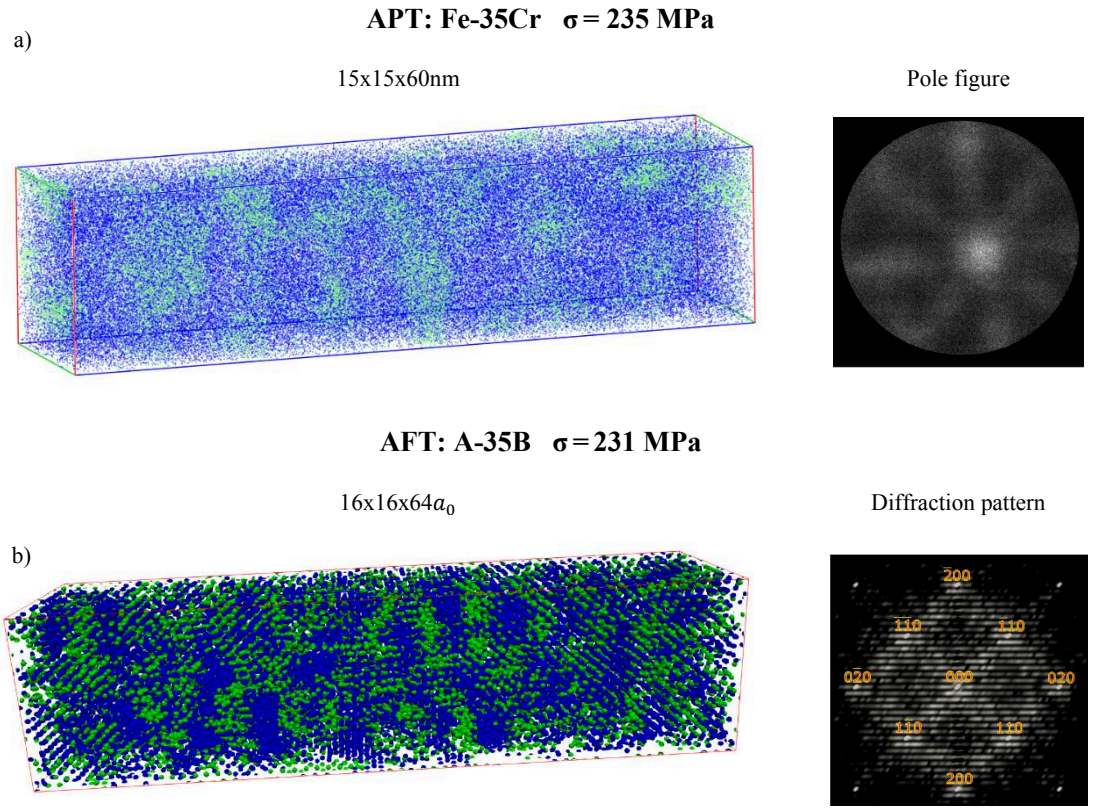

Figure 7-1. Comparison between a) APT experiment σ = 235MPa in <001> direction, it is 75.8% of yield strength at room temperature for this Fe-35Cr alloy, b) AFT modelling with σ = 231MPa in <001> direction.

The elastic properties of A and B elements in the A-B system are both fitted to α-Fe. This is motivated by the fact that α-Fe is the base element of Fe-35Cr alloy, which is used for comparison. Thus, no difference in elastic behaviour between A and B atoms is modelled, even though that is clearly the case of the real Fe-Cr system. Still observed during tensile strain modelling is that at small strain levels increase the characteristic wavelength of the structure. This was also the case when increasing the tensile stress in the experimental investigation from 150MPa to 235MPa. In experiment no, evident morphological alignment depends on the applied strain could be defined as these intermediate stress levels. But still, there are regions with weak tendencies to elongate α' perpendicular to the applied stress as seen in Figure 7-1

a), in that case <001> tensile strain at 235MPa is applied for 100h with results in good agreement between APT and AFT. The difference attributed to the fact that known from AFT modelling is that greater volume fraction β and level of applied load has a greater effect on the system response and α' morphology. In Figure 7-1 is also the diffraction pattern/pole figure of the <001> direction in which the external load was applied. Naturally with a few degrees' deviation from the pure <001> orientation in the experimental case. Based on the morphology and behaviour dependent on the applied load of specific crystallographic orientation, we have a good agreement between ATF and APT as well. The difference between <001>, <101>, <111> and <112> is very small both here in modelling and in our experiment, thus no definitive conclusion can be made with high confidence. However, the trend we find in modelling is that: $\bar{\lambda}_{111} < \bar{\lambda}_{001} < \bar{\lambda}_{101} < \bar{\lambda}_{112}$ (the difference between <111> and <001> being 0.14nm) and in experiment: $\bar{\lambda}_{001} < \bar{\lambda}_{111} < \bar{\lambda}_{101} < \bar{\lambda}_{112}$ (the difference between <111> and <001> being 0.11nm). Thus, <001> and <111> are within one σ error of the measurements. However, we find that the slip planes produce a longer characteristic wavelength in both cases and that the stiff crystallographic direction in modelling produces a shorter wavelength. As we only consider the elastic properties of α-Fe in our model and we know that bcc-Cr is much stiffer in the <001> direction this effect might explain why $\bar{\lambda}_{001} < \bar{\lambda}_{111}$ in experiment which is opposite from the result on our model. It should also be empathized that we know from nanoindentation that <001> is harder than <111> in the experiment. In addition, the morphology of all directions appears isotropic by APT experiments. The effect of compression and shear stress-ageing is yet to be verified by experiments.

a) APT: Experiment

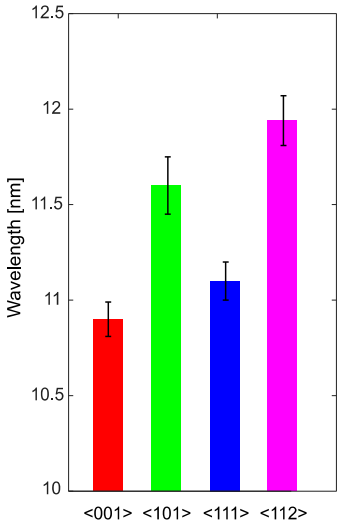

b) AFT: Modelling

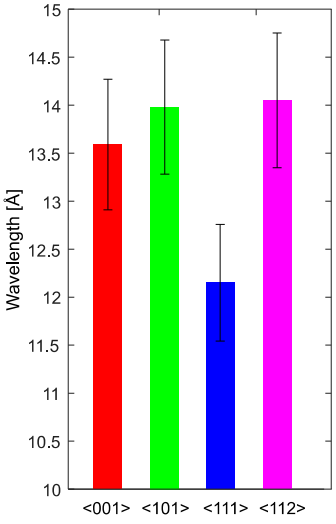

Figure 7-2. Comparison between experiment and modelling of the influence of crystallographic orientation on stress-ageing. a) experimental results from a polycrystalline material, b) modelling of a single crystal.

Chapter VIII

Conclusions and perspective

8.1 Conclusions based on experimental work

- The limit of metastable nucleation and growth is located between 537°C and 540°C for Fe-20Cr alloys.

- The limit of unstable spinodal decomposition is located between 568°C and 570°C for Fe-35Cr alloys.

- The limit of spinodal decomposition is more difficult to determine in Fe-50Cr alloys, thus between 575°C and 580°C there is a rapid homogenization of the alloy, between 580°C and 595°C there is a gradual homogenization of the alloy but no α' or effect on microhardness.

- The Cahn-Hilliard theory of spinodal decomposition can accurately describe the evolution in nano-morphology in Fe-35Cr in close proximity to the spinodal line.

- The homogeneity of α in Fe-35Cr is stable in time at 650°C for 250h but decrease with increasing temperature up to 850°C.

- Decomposition in Fe-35Cr at 525°C 100-1000h occur through spinodal decomposition in good agreement with LBM theory, the time exponent of the characteristic wavelength was in this case m=0.215.

- The effect of Cr on spinodal decomposition Fe-35Cr versus Fe-50Cr at 525°C 100-300h revealed that Fe-35Cr has a longer characteristic wavelength and that Fe-50Cr wavelength evolves faster, while decomposition of the alloy through the variance parameter progress at a similar rate.

- The temporal evolution of thermoelectric power (TEP) is dependent on the Cr content of the alloy during decomposition.

- In an aged Fe-35Cr alloy the effect of crystallographic orientation does not significantly favour any close-packed or "soft" directions.

- Adding external elastic stress to an Fe-35Cr alloy enhances the decomposition process in proportion to the added stress.

- In stress-aged Fe-35Cr local variation in nano-hardness between differently oriented grains is directly related to the Cr concentration of α' in those regions.

8.2 Conclusions based on AFT modelling

- By AFT simulations it is possible to exactly reproduce the elastic Zener anisotropy with corresponding C_{11} and C_{12} elastic constants of bcc-Fe from *ab-initio* calculations.

- It is possible to model spinodal decomposition in a binary system at high temperature.

- The characteristic wavelength is temperature-dependent and increases exponentially when the critical temperature of instability is approached from within the miscibility gap.

- AFT allows for the modelling of elastic constraint of an unstable binary system by displacement of the atomic equilibrium configuration.

- The elastic displacement of interatomic distances affects the free energy response and subsequently morphology of the decomposed structure based on stress-state and crystallographic orientation.

8.3 Prospective

The next step to further advance this work from a modelling perspective would be to include the stress distribution in a polycrystalline material that from a starting point is without texture. Thus, a polycrystalline structure could potentially be generated by a program such as *"Neper: polycrystal generation and meshing"* followed by FEM simulation of the mechanical testing, to obtain the stress distribution at a microscopic scale. Natural grain size distribution would ideally be imported from e.g. EBSD of the alloy in question. The target would be to correlate this to the 3D experimental stress distribution similar to what's been conducted by Raabe and Sachtleber [237]. One of the difficulties than would be to accurately reproduce the grain boundaries in FEM tensile test simulations as pointed out by Carlsson [238]. Another possibility would be to introduce multiple grains in the ADF modelling to be able to circumvent the issue. However, computational power is that case an issue for the size of the grains. It would be possible to introduce multiple grains with a predetermined orientation, however, at present the simulation volume is restricted to 5-15 grains as in the PhD thesis of Vaugeois [231]. Still, the accurate grain boundary reproduction is desirable. Grain size distribution is one point that could be taken into consideration. As the strength of the material would benefit from a smaller grain size the orientation and polycrystalline nature of the structure would benefit. In addition, different vacancy densities to see how the kinetics of the decomposition would be affected both with and without added strain is an interesting point to pursue. The correlative experimental technique would be X-ray diffraction contrast tomography, it is a non-destructive 3D mapping of poly-crystals at a scale up towards 1mm [239]. Used to import the real grain distribution into the FEM simulation to obtain the stress state of individual grains would be sort of a graal.

The AFT model has proven to be successful in reproducing the behaviour of the Fe-Cr system. It is true for the behaviour of the system in terms of temperature dependence and elastic constraint. What would be interesting is to better restrict the limits of the α/β phase in the miscibility gap so that the result is not complete separation between A and B atoms in α and β. The approach would be to define a new potential that would allow for the occupation of one lattice site not only by binary options but with a fraction so that the composition of the individual α and β phases could be defined.

Microscopic modelling coupled with CALPHAD is the natural extension of ADF modelling. This would allow for the connection between atomistic modelling and experiment from the nanometre scale to mesoscale. However, an assumption regarding the elastic properties of the alloy based on composition fluctuations and mechanical equilibrium is necessary which makes the response to an externally applied elastic load somewhat uncertain.

Yet it is necessary to resolve to CALPHAD in order to make predictions of a multi-component system which is too cumbersome to treat by ADF. Thus, ADF is useful as a benchmark for simple systems at the atomic scale, from which modelling at a larger scale can be derived.

Experimentally more work on the tensile properties at elevated temperature would be interesting to pursue. This would allow for more exact control of the applied load level, as a result, extreme service conditions could be investigated giving a better foundation for making predictions. In addition, the response of the elastic load could be investigated more carefully. It would, of course, be beneficial to perform these experiments in a controlled environment to be sure no contamination. Compression and torsion ageing would be the other two stress states interesting to investigate in order to get an understanding of compressive and shear forces on effect on the decomposition. This is important for more complex alloys as duplex steels. The difference in thermal expansion/solidification volume could potentially induce compressive forces acting on the ferrite grains and enhancing the decomposition process. Therefore, it would be interesting to investigate the effect of pure compression. The experimental procedure employed in this work has shown success in selecting the specific grain orientation and optimizing the APT reconstruction after the crystal structure. It has been seen in more complex alloys such as austenitic-ferritic and martensitic that the higher applied load affect the anisotropy of the SD structure [15], [16]. Thus, it would be interesting to peruse Fe-Cr-Ni-C/Fe-Cr-Mn-C steels [240], with improved mechanical properties to allow for higher load levels while avoiding the complex duplex microstructure and the martensitic microstructure which would make it very difficult to conduct the orientation-dependent analysis.

Acknowledgements

I would like to express my sincere gratitude to my thesis director Prof. Helena Zapolsky for her belief in me and her administrative assistance in making this move possible for me. I am also grateful for her patience, immense knowledge, and discussion, guidance throughout my PhD and for making my time in France an enjoyable experience outside of work.

I am very grateful for my main supervisor Dr Frederic Danoix for his invaluable experimental experience and knowledge of the field. I am thankful for his work and assistance in making this research possible, for his trust and encouragement to advance my research. For providing me the possibilities to be a part of collaborations, workshops and conferences.

I would like to thank the project collaborators Assoc. Prof. Peter Hedström and Assoc. Prof. Joakim Odqvist for recommending me this experience. For their discussions and guidance to advance my work and making my visits to KTH fruitful. Also, for their belief in this work and the discussions and input from Prof. Malin Selleby and Dr Wei Xiong.

I am thankful for the collaborators of this project at ISNA Lyon, Mathilde Labonne for her assistance in conducting experiments, providing experimental results and making my visit to Lyon an enjoyable experience. Dr Sophie Cazottes for inviting me and making this collaboration possible, Prof. Michel Perez for his discussions and suggestions, Prof. Veronique Massardier for discussions and providing experimental results.

I would like to thank the doctoral school, administrative and technical staff at the GPM laboratory directed by Prof. Philippe Pareige for providing the means and resources to make this work possible. I am especially thankful to Prof. Alain Guillet and Dr Clément Keller for their guidance and assistance during mechanical testing at INSA Rouen. Fabien Cuvilly and Emmanuel Cardel for their help with SEM/FIB/EBSD/EDS and Ivan Blum for LEAP assistance at the GPM laboratory. In addition, Charly Vadulon and Romain Fleury with their help with making my samples and Renaud Patte for his help with my simulations.

Finally, I would like to thank all the PhD students and Postdocs in the laboratory for their friendship, warm welcome and creating a stimulating environment especially my office mates and those in the ERAFEN research group. Of course, I am very grateful for my family and friends back home for their continuous support and encouragement.

Bibliography

[1] H. M. Cobb, *The History of Stainless Steel*, First printing. Materials Park, OH 44073-0002: ASM International, 2010.

[2] D. Peckner and I. Bernstein Melvin, *Handbook of stainless steels*. University of Michigan: McGraw-Hill, 1977.

[3] "Fifth Assessment Report - Mitigation of Climate Change." [Online]. Available: https://www.ipcc.ch/report/ar5/wg3/. [Accessed: 16-Jan-2018].

[4] M. A. Pouchon, M. Doebeli, R. Schelldorfer, J. Chen, W. Hoffelner, and C. Degueldre, "ODS Steel As A Structural Material For High Temperature Nuclear Reactors," 2005.

[5] C. Gindorf, L. Singheiser, and K. Hilpert, "Chromium vaporisation from Fe,Cr base alloys used as interconnect in fuel cells," *Steel Research*, vol. 72, no. 11–12, pp. 528–533, Nov. 2001.

[6] A. B. Stambouli and E. Traversa, "Solid oxide fuel cells (SOFCs): a review of an environmentally clean and efficient source of energy," *Renewable and Sustainable Energy Reviews*, vol. 6, no. 5, pp. 433–455, Oct. 2002.

[7] "Materials Genome Initiative | WWW.MGI.GOV." [Online]. Available: https://www.mgi.gov/. [Accessed: 02-Mar-2018].

[8] A. L. Schaeffler, "Constitution diagram for stainless steel weld metal," *Metal Progress*, vol. 1949, no. 56(11), p. 680.

[9] W. DeLong, G. Ostrom, and E. Szumachowiski, "Measurement and calculation of Ferrite in Stainless Steel Weld Metal," *The Welding Jornal*, vol. 1956, no. 35 (11), pp. 526–533.

[10] H. D. Newell, "Properties and characteristics of 27% chromium-iron," no. 49, pp. 977–1006, 1949.

[11] F. Danoix and P. Auger, "Atom Probe Studies of the Fe–Cr System and Stainless Steels Aged at Intermediate Temperature: A Review," *Materials Characterization*, vol. 44, no. 1–2, pp. 177–201, Jan. 2000.

[12] W. Xiong, P. Hedström, M. Selleby, J. Odqvist, M. Thuvander, and Q. Chen, "An improved thermodynamic modeling of the Fe–Cr system down to zero kelvin coupled with key experiments," *Calphad*, vol. 35, no. 3, pp. 355–366, Sep. 2011.

[13] T. Barkar, L. Höglund, J. Odqvist, and J. Ågren, "Effect of concentration dependent gradient energy coefficient on spinodal decomposition in the Fe-Cr system," *Computational Materials Science*, vol. 143, pp. 446–453, Feb. 2018.

[14] J. Zhou, J. Odqvist, L. Höglund, M. Thuvander, T. Barkar, and P. Hedström, "Initial clustering – a key factor for phase separation kinetics in Fe–Cr-based alloys," *Scripta Materialia*, vol. 75, pp. 62–65, Mar. 2014.

[15] F. Danoix, J. Lacaze, A. Gibert, D. Mangelinck, K. Hoummada, and E. Andrieu, "Effect of external stress on the Fe–Cr phase separation in 15-5 PH and Fe–15Cr–5Ni alloys," *Ultramicroscopy*, vol. 132, pp. 193–198, Sep. 2013.

[16] J. Zhou, J. Odqvist, M. Thuvander, S. Hertzman, and P. Hedström, "Concurrent phase separation and clustering in the ferrite phase during low temperature stress aging of duplex stainless steel weldments," *Acta Materialia*, vol. 60, no. 16, pp. 5818–5827, Sep. 2012.

[17] K. R. Elder and M. Grant, "Modeling elastic and plastic deformations in nonequilibrium processing using phase field crystals," *Phys. Rev. E*, vol. 70, no. 5, p. 051605, Nov. 2004.

[18] O. Soriano-Vargas, E. O. Avila-Davila, V. M. Lopez-Hirata, N. Cayetano-Castro, and J. L. Gonzalez-Velazquez, "Effect of spinodal decomposition on the mechanical behavior of

Fe–Cr alloys," *Materials Science and Engineering A*, vol. 527, no. 2010, pp. 2910–2914, Jan. 2010.
[19]A. Pineau and J. Besson, "Thermal Embrittlement of Cast Duplex Stainless Steels: Observations and Modeling," in *Duplex Stainless Steels*, I. Alvarez-Armas and S. Degallaix-Moreuil, Eds. John Wiley & Sons, Inc., 2013, pp. 161–208.
[20]C. Capdevila, M. K. Miller, I. Toda, and J. Chao, "Influence of the α–α′ phase separation on the tensile properties of Fe-base ODS PM 2000 alloy," *Materials Science and Engineering: A*, vol. 527, no. 29–30, pp. 7931–7938, Nov. 2010.
[21]K. H. Lo, C. H. Shek, and J. K. L. Lai, "Recent developments in stainless steels," *Materials Science and Engineering: R: Reports*, vol. 65, no. 4–6, pp. 39–104, mai 2009.
[22]C. Capdevila, M. K. Miller, and J. Chao, "Phase separation kinetics in a Fe–Cr–Al alloy," *Acta Materialia*, vol. 60, no. 12, pp. 4673–4684, juillet 2012.
[23]J. Wallenius, P. Olsson, L. Malerba, and D. Terentyev, "Simulation of thermal ageing and radiation damage in Fe–Cr," *Nuclear Instruments and Methods in Physics Research Section B: Beam Interactions with Materials and Atoms*, vol. 255, no. 1, pp. 68–74, Feb. 2007.
[24]K. L. Wong, H.-J. Lee, J.-H. Shim, B. Sadigh, and B. D. Wirth, "Multiscale modeling of point defect interactions in Fe–Cr alloys," *Journal of Nuclear Materials*, vol. 386–388, pp. 227–230, avril 2009.
[25]D. Terentyev, L. Malerba, and A. v. Barashev, "On the correlation between self-interstitial cluster diffusivity and irradiation-induced swelling in Fe-Cr alloys," *Philosophical Magazine Letters*, vol. 85, no. 11, pp. 587–594, Nov. 2005.
[26]S. M. Dubiel and J. Cieslak, "Sigma-phase in Fe-Cr and Fe-V alloy systems and its physical properties," *Critical Reviews in Solid State and Materials Sciences*, vol. 36, no. 4, pp. 191–208, Oct. 2011.
[27]M. J. Cieslak, A. M. Ritter, and W. F. Savage, "Chi-Phase Formation During Solidification and Cooling of CF-8M Wels Metal," *WELDING RESEARCH SUPPLEMENT*, p. 133.
[28]D. M. Escriba, E. Materna-Morris, R. L. Plaut, and A. F. Padilha, "Chi-phase precipitation in a duplex stainless steel," *Materials Characterization*, vol. 60, no. 11, pp. 1214–1219, Nov. 2009.
[29]L. E. Larsson, "Pre-precipitation and precipitation phenomena in the Al-Zn system," *Acta Metallurgica*, vol. 15, no. 1, pp. 35–44, Jan. 1967.
[30]R. Baur and V. Gerold, "The existence of a metastable miscibility gap in aluminium-silver alloys," *Acta Metallurgica*, vol. 10, no. 6, pp. 637–645, Jun. 1962.
[31]J. L. Meijering, "On the thermodynamics of the Au-Pt system," *Journal of Physics and Chemistry of Solids*, vol. 18, no. 2, pp. 267–268, Feb. 1961.
[32]S. Ahn and T. Tsakalakos, "The Effect of Applied Stress of the Decomposition Cu-15Ni-8Sn Spinodal Alloy," in *Symposium GREECE – Phase Transformations in Solids*, 1983, vol. 21.
[33]J. E. Woodilla and B. L. Averbach, "Modulated structures in Au□Ni alloys," *Acta Metallurgica*, vol. 16, no. 2, pp. 255–263, Feb. 1968.
[34]J. W. Gibbs, *THE SCIENTIFIC PAPERS OF J. WILLARD GIBBS,PH.D., LL.D.*, vol. VOL. 1 THERMODYNAMICS, 2 vols. 39 PATERNOSTER ROW, LONDON: LONGMANS, GREEN, AND CO., 1906.
[35]M. H. Hillert, "A theory of nucleation for solid metallic solutions," Thesis, Massachusetts Institute of Technology, 1956.
[36]J. W. Cahn, "On spinodal decomposition," *Acta Metallurgica*, vol. 9, no. 9, pp. 795–801, Sep. 1961.

[37]J. W. Cahn and J. E. Hilliard, “Free Energy of a Nonuniform System. I. Interfacial Free Energy,” *The Journal of Chemical Physics*, vol. 28, no. 2, pp. 258–267, Feb. 1958.
[38]J. W. Cahn, “Phase Separation by Spinodal Decomposition in Isotropic Systems,” *The Journal of Chemical Physics*, vol. 42, no. 1, pp. 93–99, Jan. 1965.
[39]J. S. Langer and M. Bar-on, “Theory of early-stage spinodal decomposition,” *Annals of Physics*, vol. 78, no. 2, pp. 421–452, Jun. 1973.
[40]M. Bonvalet, “Precipitation kinetic paths in solids,” Theses, Normandie Université, 2015.
[41]D. Kachchiev, *Nucleation*. Butterworth - Heinemann, 2000.
[42]K. C. Russell, “Nucleation in solids: The induction and steady state effects,” *Advances in Colloid and Interface Science*, vol. 13, no. 3, pp. 205–318, Sep. 1980.
[43]S. Schönecker, S. K. Kwon, B. Johansson, and L. Vitos, “Surface parameters of ferritic iron-rich Fe–Cr alloy,” *J. Phys.: Condens. Matter*, vol. 25, no. 30, p. 305002, 2013.
[44]A. Borgenstam, L. Höglund, J. Ågren, and A. Engström, “DICTRA, a tool for simulation of diffusional transformations in alloys,” *JPE*, vol. 21, no. 3, p. 269, May 2000.
[45]S. Novy, “Atomic scale observation of phase transformation in long term thermally aged duplex stainless steels,” Theses, Université de Rouen, 2009.
[46]W. Ostwald, “Studien über die Bildung und Umwandlung fester Körper,” *Zeitschrift für Physikalische Chemie*, vol. 22U, no. 1, pp. 289–330, 1897.
[47]R. Wagner, R. Kampmann, and P. W. Voorhees, “Homogeneous Second-Phase Precipitation,” in *Phase Transformations in Materials*, G. Kostorz, Ed. Wiley-VCH Verlag GmbH & Co. KGaA, 2001, pp. 309–407.
[48]A. Baldan, “Review Progress in Ostwald ripening theories and their applications to nickel-base superalloys Part I: <Emphasis Type="Italic">Ostwald ripening theories</Emphasis>,” *Journal of Materials Science*, vol. 37, no. 11, pp. 2171–2202, Jun. 2002.
[49]I. M. Lifshitz and V. V. Slyozov, “The kinetics of precipitation from supersaturated solid solutions,” *Journal of Physics and Chemistry of Solids*, vol. 19, no. 1, pp. 35–50, avril 1961.
[50]J. W. Cahn, “Free Energy of a Nonuniform System. II. Thermodynamic Basis,” *The Journal of Chemical Physics*, vol. 30, no. 5, pp. 1121–1124, May 1959.
[51]J. W. Cahn and J. E. Hilliard, “Free Energy of a Nonuniform System. III. Nucleation in a Two-Component Incompressible Fluid,” *The Journal of Chemical Physics*, vol. 31, no. 3, pp. 688–699, Sep. 1959.
[52]F. K. LeGoues, Y. W. Lee, and H. I. Aaronson, “Influence of crystallography upon critical nucleus shapes and kinetics of homogeneous F.C.C.-F.C.C. nucleation—II. The non-classical regime,” *Acta Metallurgica*, vol. 32, no. 10, pp. 1837–1843, Oct. 1984.
[53]A. K. da Silva *et al.*, “Phase nucleation through confined spinodal fluctuations at crystal defects evidenced in Fe-Mn alloys,” *Nature Communications*, vol. 9, no. 1, p. 1137, Mar. 2018.
[54]J. Zhou, “An Atom-Probe Tomography Study of Phase Separation in Fe-Cr Based Steels,” Doctoral Thesis, Royal Institute of Technology (KTH), Department of Materials Science and Engineering,SE-100 44 Stockholm, Sweden, 2014.
[55]H. E. Cook, “Brownian motion in spinodal decomposition,” *Acta Metallurgica*, vol. 18, no. 3, pp. 297–306, Mar. 1970.
[56]M. Lavrskyi, H. Zapolsky, and A. G. Khachaturyan, “Fraton Theory and Modelling of Self-Assembling of Complex Structures,” *arXiv:1411.5587 [cond-mat]*, Nov. 2014.
[57]J. W. Cahn, “The later stages of spinodal decomposition and the beginnings of particle coarsening,” *Acta Metallurgica*, vol. 14, no. 12, pp. 1685–1692, Dec. 1966.
[58]J. S. Langer, “Metastable states,” *Physica*, vol. 73, no. 1, pp. 61–72, Apr. 1974.

[59]J. Ågren, "Calculation of phase diagrams: Calphad," *Current Opinion in Solid State and Materials Science*, vol. 1, no. 3, pp. 355–360, Jun. 1996.
[60]M. Hättestrand, P. Larsson, G. Chai, J.-O. Nilsson, and J. Odqvist, "Study of decomposition of ferrite in a duplex stainless steel cold worked and aged at 450–500°C," *Materials Science and Engineering: A*, vol. 499, no. 1, pp. 489–492, Jan. 2009.
[61]Y.-S. Li, H. Zhu, L. Zhang, and X.-L. Cheng, "Phase decomposition and morphology characteristic in thermal aging Fe–Cr alloys under applied strain: A phase-field simulation," *Journal of Nuclear Materials*, vol. 429, no. 1–3, pp. 13–18, Oct. 2012.
[62]L. Zhang *et al.*, "Spinodal Decomposition in Fe-25Cr-12Co Alloys under the Influence of High Magnetic Field and the Effect of Grain Boundary," *Nanomaterials*, vol. 8, no. 8, p. 578, Jul. 2018.
[63]S. Y. Hu and L. Q. Chen, "A phase-field model for evolving microstructures with strong elastic inhomogeneity," *Acta Materialia*, vol. 49, no. 11, pp. 1879–1890, Jun. 2001.
[64]D. J. Seol, S. Y. Hu, Y. L. Li, J. Shen, K. H. Oh, and L. Q. Chen, "Computer simulation of spinodal decomposition in constrained films," *Acta Materialia*, vol. 51, no. 17, pp. 5173–5185, Oct. 2003.
[65]M. P. Gururajan and A. Lahiri, "Elastic stress effects on microstructural instabilities," *arXiv:1607.00599 [cond-mat]*, Jul. 2016.
[66]G. Grimvall, B. Magyari-Köpe, V. Ozoliņš, and K. A. Persson, "Lattice instabilities in metallic elements," *Rev. Mod. Phys.*, vol. 84, no. 2, pp. 945–986, Jun. 2012.
[67]D. Vasilyev and A. Udovsky, "Calculation of the miscibility gap and specific heat of bcc Fe-Cr alloys by using physical – empirical models | Request PDF," *Proceedings of the International Conference on Solid-Solid Phase Transforations in Inorganic Materials*, vol. 2015, pp. 799–800.
[68] null Maroudas and null Brown, "Analysis of point-defect diffusion and drift in cubic-type lattices: Constitutive modeling," *Phys. Rev., B Condens. Matter*, vol. 44, no. 6, pp. 2567–2581, Aug. 1991.
[69]P. H. Dederichs and K. Schroeder, "Anisotropic diffusion in stress fields," *Phys. Rev. B*, vol. 17, no. 6, pp. 2524–2536, Mar. 1978.
[70]P. Shewmon, Ed., *Diffusion in Solids*, 2nd ed. Springer International Publishing, 2016.
[71]A. V. Nazarov and A. A. Miheev, "Effect of Elastic Stress Field on Diffusion," *Defect and Diffusion Forum*, 1997. [Online]. Available: https://www.scientific.net/DDF.143-147.177. [Accessed: 02-Oct-2018].
[72]A. V. Nazarov and A. A. Mikheev, "Diffusion under a stress in fcc and bcc metals," *J. Phys.: Condens. Matter*, vol. 20, no. 48, p. 485203, 2008.
[73]M.-W. Lui and I. Le May, "On the 'Friedel relation' in precipitation hardening," *Scripta Metallurgica*, vol. 9, no. 6, pp. 587–589, Jun. 1975.
[74]E. Rizzi and P. Hähner, "On the Portevin–Le Chatelier effect: theoretical modeling and numerical results," *International Journal of Plasticity*, vol. 20, no. 1, pp. 121–165, Jan. 2004.
[75]Y. Brechet and Y. Estrin, "On the influence of precipitation on the Portevin-Le Chatelier effect," *Acta Metallurgica et Materialia*, vol. 43, no. 3, pp. 955–963, Mar. 1995.
[76]A. van den Beukel, "The influence of static and dynamic strain aging on the temperature dependence of the flow stress in solid solutions," *Scripta Metallurgica*, vol. 17, no. 5, pp. 659–663, May 1983.
[77]Y. Estrin and L. P. Kubin, "Local strain hardening and nonuniformity of plastic deformation," *Acta Metallurgica*, vol. 34, no. 12, pp. 2455–2464, Dec. 1986.

[78]S. MIURA and M. KOUSHIMA, “Deformation Mechanism of [001] Oriented Fe-30%Cr Alloy Single Crystals,” *Journal of the Society of Materials Science, Japan*, vol. 50, no. 11, pp. 1223–1227, 2001.
[79]A. F. Jankowski, “Strain Energy Effects in the Spinodal Decomposition of Cu-Ni(Fe) Nanolaminate Coatings,” *Coatings*, vol. 5, no. 3, pp. 246–262, Jun. 2015.
[80]D. Wagner, J. C. Moreno, and C. Prioul, “Influence of Post Weld Heat Treatment on the Dynamic Strain Aging of C-Mn Steels,” *J. Phys. IV France*, vol. 06, no. C8, pp. C8-159-C8-162, Dec. 1996.
[81]S. M. Dubiel and J. Zukrowski, “Phase decomposition in an Fe-Cr alloy at 402 deg C: M\"ossbauer spectroscopic study,” *Materials Characterization*, vol. 129, pp. 282–287, Jul. 2017.
[82]H. Kuwano, “Mössbauer Effect Study on the mechanism of phase decomposition in Iron-Chromium alloys,” *Transaction of the Japan Institute of Metals*, vol. Vol. 26, no. 7, pp. 482–491, 1985.
[83]J. Krzywon, “Small Angle Neutron Scattering (SANS),” *NIST*, 25-Apr-2017. [Online]. Available: https://www.nist.gov/ncnr/neutron-instruments/small-angle-neutron-scattering-sans. [Accessed: 08-Nov-2018].
[84]J. C. LaSalle and L. H. Schwartz, “SPINODAL DECOMPOSITION IN Fe-52Cr,” in *Decomposition of Alloys: the Early Stages*, P. HAASENV. GEROLDR. WAGNERM. F. ASHBY, Ed. Pergamon, 1984, pp. 104–109.
[85]K. a. Hawick, J. e. Epperson, C. g. Windsor, and V. s. Rainey, “Chemical Phase Separation in Binary Iron-Chromium Alloys,” in *Symposium F – Kinetics of Phase Transformations*, 1990, vol. 205.
[86]“Vickers Hardness Test - Leaving Certificate Engineering Notes.” [Online]. Available: https://sites.google.com/site/gobanengineeringnotes/materials-testing/hardness-testing/vickers-hardness-test. [Accessed: 30-Aug-2018].
[87]M. Yovanovich, “Micro and Macro Hardness Measurements, Correlations, and Contact Models,” in *44th AIAA Aerospace Sciences Meeting and Exhibit*, Reno, Nevada, 2006.
[88]*TI 950 TriboIndenter User Manual*, Revision 9.3.0314. Hysitron Incorporated, 2014.
[89]F.-C. Anthony C., *Nanoindentation*. Springer Science & Business Media, 2004.
[90]“1461-1465_ijmr110198 1461..1465 - Perez09.pdf.” [Online]. Available: http://michel.perez.net.free.fr/Perez09.pdf. [Accessed: 15-Sep-2016].
[91] von L. Nordheim and C. J. Gorter, “Bemerkungen über thermokraft und widerstand,” *Physica*, vol. 2, pp. 383–390, 1935.
[92]A. Matthiessen and C. Vogt, “IV. On the influence of temperature on the electric conducting-power of alloys,” *Phil. Trans. R. Soc. Lond.*, vol. 154, pp. 167–200, Jan. 1864.
[93]X. Kleber, P. Roux, and M. Morin, “Sensitivity of the thermoelectric power of metallic materials to an elastic uniaxial strain,” *Philosophical Magazine Letters*, vol. 89, no. 9, pp. 565–572, Sep. 2009.
[94]J. M. Pelletier, G. Vigier, and P. Guyot, “Electrical resistivity and thermoelectric power during clustering in aluminium solid solutions,” *Acta Metallurgica*, vol. 29, no. 7, pp. 1335–1342, Jul. 1981.
[95]T. Fukasawa and T. Sato, “Versatile application of indirect Fourier transformation to structure factor analysis: from X-ray diffraction of molecular liquids to small angle scattering of protein solutions,” *Phys Chem Chem Phys*, vol. 13, no. 8, pp. 3187–3196, Feb. 2011.
[96]R. Reichelt, “Scanning Electron Microscopy,” in *Science of Microscopy*, Springer, New York, NY, 2007, pp. 133–272.

[97]J. I. Goldstein *et al.*, "The SEM and Its Modes of Operation," in *Scanning Electron Microscopy and X-ray Microanalysis*, Springer, Boston, MA, 2003, pp. 21–60.
[98]JEOL, "Energy table for EDS analysis." [Online]. Available: https://www.unamur.be/services/microscopie/sme-documents/Energy-20table-20for-20EDS-20analysis-1.pdf. [Accessed: 15-Nov-2018].
[99]J. I. Goldstein *et al.*, "Qualitative X-Ray Analysis," in *Scanning Electron Microscopy and X-ray Microanalysis*, Springer, Boston, MA, 2003, pp. 355–390.
[100] D. Drouin, A. Couture, D. Joly, N. Poirier-Demers, and H. Demers, "Monte Carlo simulation of electron trajectory in solids," *Casino Version 3.3.0.4*, vol. 2016.
[101] E. W. Müller, "Das Feldionenmikroskop," *Z. Physik*, vol. 131, no. 1, pp. 136–142, Mar. 1951.
[102] E. W. Müller and K. Bahadur, "Field Ionization of Gases at a Metal Surface and the Resolution of the Field Ion Microscope," *Phys. Rev.*, vol. 102, no. 3, pp. 624–631, May 1956.
[103] M. K. Miller and R. G. Forbes, *Atom-Probe Tomography*. Boston, MA: Springer US, 2014.
[104] M. K. Miller, A. Cerezo, M. G. Hetherington, and G. D. W. S. FRS, *Atom Probe Field Ion Microscopy*. Oxford, New York: Oxford University Press, 1996.
[105] A. Cerezo, T. J. Godfrey, and G. D. W. Smith, "Application of a position-sensitive detector to atom probe microanalysis," *Review of Scientific Instruments*, vol. 59, no. 6, pp. 862–866, Jun. 1988.
[106] E. W. Müller, J. A. Panitz, and S. B. McLane, "The Atom-Probe Field Ion Microscope," *Review of Scientific Instruments*, vol. 39, no. 1, pp. 83–86, Jan. 1968.
[107] F. Danoix, G. Grancher, A. Bostel, and D. Blavette, "Standard deviations of composition measurements in atom probe analyses—Part II: 3D atom probe," *Ultramicroscopy*, vol. 107, no. 9, pp. 739–743, Sep. 2007.
[108] F. Danoix, G. Grancher, A. Bostel, and D. Blavette, "Standard deviations of composition measurements in atom probe analyses. Part I: Conventional 1D atom probe," *Ultramicroscopy*, vol. 107, no. 9, pp. 734–738, Sep. 2007.
[109] G. Da Costa, F. Vurpillot, A. Bostel, M. Bouet, and B. Deconihout, "Design of a delay-line position-sensitive detector with improved performance," *Review of Scientific Instruments*, vol. 76, no. 1, p. 013304, Dec. 2004.
[110] F. Vurpillot, M. Gilbert, and B. Deconihout, "Towards the three-dimensional field ion microscope," *Surface and Interface Analysis*, vol. 39, no. 2–3, pp. 273–277, Feb. 2007.
[111] M. K. Miller and M. G. Hetherington, "Morphology and scaling behavior of ultrafine isotropic microstructures in Fe-Cr alloys from atom probe field ion microscopy data," *Scripta Metallurgica et Materialia*, vol. 24, no. 7, pp. 1375–1380, Jul. 1990.
[112] M. K. Miller and M. G. Hetherington, "Local magnification effects in the atom probe," *Surface Science*, vol. 246, no. 1, pp. 442–449, Apr. 1991.
[113] M. K. Miller, A. Cerezo, M. G. Hetherington, and J. M. Hyde, "Estimation of composition amplitude: Pa and LBM versus V," *Surface Science*, vol. 266, no. 1, pp. 446–452, Apr. 1992.
[114] S. Novy, P. Pareige, and C. Pareige, "Atomic scale analysis and phase separation understanding in a thermally aged Fe–20 at.%Cr alloy," *Journal of Nuclear Materials*, vol. 384, no. 2, pp. 96–102, février 2009.
[115] M. K. Miller, "THE EFFECTS OF LOCAL MAGNIFICATION AND TRAJECTORY ABERRATIONS ON ATOM PROBE ANALYSIS," *J. Phys. Colloques*, vol. 48, no. C6, pp. C6-565-C6-570, Nov. 1987.

[116] F. Vurpillot, A. Bostel, and D. Blavette, "Trajectory overlaps and local magnification in three-dimensional atom probe," *Applied Physics Letters*, vol. 76, no. 21, pp. 3127–3129, May 2000.

[117] S. Parviainen, F. Djurabekova, S. P. Fitzgerald, A. Ruzibaev, and K. Nordlund, "Atomistic simulations of field assisted evaporation in atom probe tomography," *J. Phys. D: Appl. Phys.*, vol. 49, no. 4, p. 045302, 2016.

[118] D. J. Larson, T. J. Prosa, R. M. Ulfig, B. P. Geiser, and T. F. Kelly, *Local Electrode Atom Probe Tomography: A User's Guide*. New York: Springer-Verlag, 2013.

[119] A. Cerezo, T. J. Godfrey, S. J. Sijbrandij, G. D. W. Smith, and P. J. Warren, "Performance of an energy-compensated three-dimensional atom probe," *Review of Scientific Instruments*, vol. 69, no. 1, pp. 49–58, Jan. 1998.

[120] J. Zhou, J. Odqvist, M. Thuvander, and P. Hedström, "Quantitative Evaluation of Spinodal Decomposition in Fe-Cr by Atom Probe Tomography and Radial Distribution Function Analysis," *Microscopy and Microanalysis*, vol. 19, no. 03, pp. 665–675, Jun. 2013.

[121] S. Lozano-Perez, D. W. Saxey, T. Yamada, and T. Terachi, "Atom-probe tomography characterization of the oxidation of stainless steel," *Scripta Materialia*, vol. 62, no. 11, pp. 855–858, Jun. 2010.

[122] M. Meisnar, M. Moody, and S. Lozano-Perez, "Atom probe tomography of stress corrosion crack tips in SUS316 stainless steels," *Corrosion Science*, vol. 98, pp. 661–671, Sep. 2015.

[123] M. Thuvander, M. Andersson, and K. Stiller, "Atom probe tomography investigation of lath boundary segregation and precipitation in a maraging stainless steel," *Ultramicroscopy*, vol. 132, pp. 265–270, Sep. 2013.

[124] G. Ehrlich, "Direct observation of individual atoms on metals," *Surface Science*, vol. 63, pp. 422–447, Mar. 1977.

[125] G. L. Kellogg, "Determining the field emitter temperature during laser irradiation in the pulsed laser atom probe," *Journal of Applied Physics*, vol. 52, no. 8, pp. 5320–5328, Aug. 1981.

[126] B. Gault, F. Danoix, K. Hoummada, D. Mangelinck, and H. Leitner, "Impact of directional walk on atom probe microanalysis," *Ultramicroscopy*, vol. 113, pp. 182–191, Feb. 2012.

[127] B. Gault, M. P. Moody, J. M. Cairney, and S. P. Ringer, *Atom Probe Microscopy*. Springer Science & Business Media, 2012.

[128] M. Wada, "On the thermally activated field evaporation of surface atoms," *Surface Science*, vol. 145, no. 2, pp. 451–465, Oct. 1984.

[129] F. Vurpillot, A. Bostel, A. Menand, and D. Blavette, "Trajectories of field emitted ions in 3D atom-probe," *The European Physical Journal - Applied Physics*, vol. 6, no. 2, pp. 217–221, May 1999.

[130] F. Vurpillot, B. Gault, B. P. Geiser, and D. J. Larson, "Reconstructing atom probe data: A review," *Ultramicroscopy*, vol. 132, pp. 19–30, Sep. 2013.

[131] P. Bas, A. Bostel, B. Deconihout, and D. Blavette, "A general protocol for the reconstruction of 3D atom probe data," *Applied Surface Science*, vol. 87–88, pp. 298–304, Mar. 1995.

[132] B. Gault *et al.*, "Advances in the calibration of atom probe tomographic reconstruction," *Journal of Applied Physics*, vol. 105, no. 3, p. 034913, Feb. 2009.

[133] B. Gault *et al.*, "Advances in the reconstruction of atom probe tomography data," *Ultramicroscopy*, vol. 111, no. 6, pp. 448–457, May 2011.

[134] T. J. Prosa, D. Olson, B. Geiser, D. J. Larson, K. Henry, and E. Steel, "Analysis of implanted silicon dopant profiles," *Ultramicroscopy*, vol. 132, pp. 179–185, Sep. 2013.
[135] L. Yao, "A filtering method to reveal crystalline patterns from atom probe microscopy desorption maps," *MethodsX*, vol. 3, pp. 268–273, Jan. 2016.
[136] Z. Peng, F. Vurpillot, P.-P. Choi, Y. Li, D. Raabe, and B. Gault, "On the detection of multiple events in atom probe tomography," *Ultramicroscopy*, vol. 189, pp. 54–60, Jun. 2018.
[137] M. Thuvander *et al.*, "Quantitative atom probe analysis of carbides," *Ultramicroscopy*, vol. 111, no. 6, pp. 604–608, May 2011.
[138] F. Vurpillot, M. Gruber, G. Da Costa, I. Martin, L. Renaud, and A. Bostel, "Pragmatic reconstruction methods in atom probe tomography," *Ultramicroscopy*, vol. 111, no. 8, pp. 1286–1294, juillet 2011.
[139] M. P. Moody, B. Gault, L. T. Stephenson, D. Haley, and S. P. Ringer, "Qualification of the tomographic reconstruction in atom probe by advanced spatial distribution map techniques," *Ultramicroscopy*, vol. 109, no. 7, pp. 815–824, Jun. 2009.
[140] null Hellman, null Vandenbroucke, null Rüsing, null Isheim, and null Seidman, "Analysis of Three-dimensional Atom-probe Data by the Proximity Histogram," *Microsc. Microanal.*, vol. 6, no. 5, pp. 437–444, Sep. 2000.
[141] R. W. O'Neill, D. J. Larson, K. Thompson, T. C. Kunicki, and B. Geiser, "Measuring the Roughness of Buried Interfaces in Nanostructures by Local Electrode Atom Probe (LEAP®) Analysis," *Microscopy and Microanalysis*, vol. 12, no. S02, pp. 1746–1747, Aug. 2006.
[142] K. Kaluskar and K. Rajan, "Gaussian Kernel Density Estimator for Voxel Size Selection in Atom Probe Tomography," *Microscopy and Microanalysis*, vol. 19, no. S2, pp. 992–993, Aug. 2013.
[143] C. M. Parish and M. K. Miller, "Multivariate statistical analysis of atom probe tomography data," *Ultramicroscopy*, vol. 110, no. 11, pp. 1362–1373, Oct. 2010.
[144] S. Srinivasan, K. Kaluskar, S. Dumpala, S. Broderick, and K. Rajan, "Automated voxelization of 3D atom probe data through kernel density estimation," *Ultramicroscopy*, vol. 159, pp. 381–386, Dec. 2015.
[145] L. T. Stephenson, M. P. Moody, P. V. Liddicoat, and S. P. Ringer, "New Techniques for the Analysis of Fine-Scaled Clustering Phenomena within Atom Probe Tomography (APT) Data," *Microscopy and Microanalysis*, vol. 13, no. 06, pp. 448–463, Dec. 2007.
[146] M. P. Moody, L. T. Stephenson, A. V. Ceguerra, and S. P. Ringer, "Quantitative binomial distribution analyses of nanoscale like-solute atom clustering and segregation in atom probe tomography data," *Microsc. Res. Tech.*, vol. 71, no. 7, pp. 542–550, juillet 2008.
[147] M. Dumont, W. Lefebvre, B. Doisneau-Cottignies, and A. Deschamps, "Characterisation of the composition and volume fraction of η′ and η precipitates in an Al–Zn–Mg alloy by a combination of atom probe, small-angle X-ray scattering and transmission electron microscopy," *Acta Materialia*, vol. 53, no. 10, pp. 2881–2892, Jun. 2005.
[148] D. Blavette, F. Vurpillot, P. Pareige, and A. Menand, "A model accounting for spatial overlaps in 3D atom-probe microscopy," *Ultramicroscopy*, vol. 89, no. 1, pp. 145–153, Oct. 2001.
[149] W. Guo, D. A. Garfinkel, J. D. Tucker, D. Haley, G. A. Young, and J. D. Poplawsky, "An atom probe perspective on phase separation and precipitation in duplex stainless steels," *Nanotechnology*, vol. 27, no. 25, p. 254004, 2016.

[150] F. D. Geuser, “Interprétation et traitement des données de sonde atomique tomographique : application à la precipitation dans les Al-Mg-Si,” phdthesis, Université de Rouen, 2005.
[151] K. Zhang, “On the Concept of Static Structure Factor,” *arXiv:1606.03610 [cond-mat]*, Jun. 2016.
[152] X. Xu *et al.*, “Structural Characterization of Phase Separation in Fe-Cr: A Current Comparison of Experimental Methods,” *Metall and Mat Trans A*, vol. 47, no. 12, pp. 5942–5952, Dec. 2016.
[153] O. Kapikranian, H. Zapolsky, R. Patte, C. Pareige, B. Radiguet, and P. Pareige, “Point defect absorption by grain boundaries in α-iron by atomic density function modeling,” *Physical Review B*, vol. 92, no. 22, Dec. 2015.
[154] N. Lecoq, H. Zapolsky, and P. Galenko, “Evolution of the structure factor in a hyperbolic model of spinodal decomposition,” *Eur. Phys. J. Spec. Top.*, vol. 177, no. 1, pp. 165–175, Oct. 2009.
[155] D. Blavette, G. Grancher, and A. Bostel, “STATISTICAL ANALYSIS OF ATOM-PROBE DATA (I) : DERIVATION OF SOME FINE-SCALE FEATURES FROM FREQUENCY DISTRIBUTIONS FOR FINELY DISPERSED SYSTEMS,” *Journal de Physique Colloques*, vol. 49, no. C6, pp. C6-433-C6-438, 1988.
[156] S. S. Brenner, M. K. Miller, and W. A. Soffa, “Spinodal decomposition of iron-32 at.% chromium at 470°C,” *Scripta Metallurgica*, vol. 16, no. 7, pp. 831–836, Jul. 1982.
[157] F. Bley, “Neutron small-angle scattering study of unmixing in Fe□Cr alloys,” *Acta Metallurgica et Materialia*, vol. 40, no. 7, pp. 1505–1517, Jul. 1992.
[158] J.-O. Andersson and B. Sundman, “Thermodynamic properties of the Cr□Fe system,” *Calphad*, vol. 11, no. 1, pp. 83–92, Jan. 1987.
[159] M. K. Miller, J. M. Hyde, M. G. Hetherington, A. Cerezo, G. D. W. Smith, and C. M. Elliott, “Spinodal decomposition in Fe-Cr alloys: Experimental study at the atomic level and comparison with computer models—I. Introduction and methodology,” *Acta Metallurgica et Materialia*, vol. 43, no. 9, pp. 3385–3401, Sep. 1995.
[160] T. de Nys and P. M. Gielen, “Spinodal decomposition in the Fe−Cr system,” *MT*, vol. 2, no. 5, pp. 1423–1428, May 1971.
[161] M. Avrami, “Kinetics of Phase Change. I General Theory,” *The Journal of Chemical Physics*, vol. 7, no. 12, pp. 1103–1112, Dec. 1939.
[162] W. L. Jungers, “Scaling. Why is animal size so important? By K. Schmidt-Nielsen. New York: Cambridge University Press. 1984. xi + 241 pp., figures, tables, appendices, references, index. $29.95 (cloth), $9.95 (paper),” *American Journal of Physical Anthropology*, vol. 69, no. 1, pp. 129–130, Jan. 1986.
[163] C. Zener, “Theory of Growth of Spherical Precipitates from Solid Solution,” *Journal of Applied Physics*, vol. 20, no. 10, pp. 950–953, Oct. 1949.
[164] J. M. Hyde, M. K. Miller, M. G. Hetherington, A. Cerezo, G. D. W. Smith, and C. M. Elliott, “Spinodal decomposition in Fe-Cr alloys: Experimental study at the atomic level and comparison with computer models—II. Development of domain size and composition amplitude,” *Acta Metallurgica et Materialia*, vol. 43, no. 9, pp. 3403–3413, Sep. 1995.
[165] C. Wagner, “Theorie der Alterung von Niederschlägen durch Umlösen (Ostwald-Reifung),” *Zeitschrift für Elektrochemie, Berichte der Bunsengesellschaft für physikalische Chemie*, vol. 65, no. 7–8, pp. 581–591, Sep. 1961.
[166] D. Blavette and P. Auger, “Fine scale investigation of some phenomena in metallic alloys by field ion microscopy and atom probe microanalysis,” *Microsc. Microanal. Microstruct.*, vol. 1, no. 5–6, pp. 481–492, Oct. 1990.

[167] T. Philippe and D. Blavette, "Nucleation pathway in coherent precipitation," *Philosophical Magazine*, vol. 2011, no. 36, p. p.4606-4622, 09 May.
[168] F. Li and J. S. Lannin, "Radial distribution function of amorphous carbon," *Phys. Rev. Lett.*, vol. 65, no. 15, pp. 1905–1908, Oct. 1990.
[169] Z. Yan, Y. Li, X. Zhou, Y. Zhang, and R. Hu, "Evolution of nanoscale Cr-rich phase in a Fe-35 at.% Cr alloy during isothermal aging," *Journal of Alloys and Compounds*, vol. 725, pp. 1035–1043, Nov. 2017.
[170] "Piecewise Cubic Hermite Interpolating Polynomial (PCHIP) - MATLAB pchip - MathWorks France." [Online]. Available: https://fr.mathworks.com/help/matlab/ref/pchip.html. [Accessed: 24-Oct-2018].
[171] W. Xiong, M. Selleby, Q. Chen, J. Odqvist, and Y. Du, "Phase Equilibria and Thermodynamic Properties in the Fe-Cr System," *Critical Reviews in Solid State and Materials Sciences*, vol. 35, no. 2, pp. 125–152, mai 2010.
[172] R. O. Williams, "The Miscibility Gap in the Iron-Chromium System," *Metallurgical Transactions*, vol. Volume 5, no. 967, 1974.
[173] J. M. Pelletier, G. Vigier, J. Merlin, P. Merle, F. Fouquet, and R. Borrelly, "Precipitation effects on thermopower in Al-Cu alloys," *Acta Metallurgica*, vol. 32, no. 7, pp. 1069–1078, Jul. 1984.
[174] L. Piraux, A. Fert, P. A. Schroeder, R. Loloee, and P. Etienne, "Large magnetothermoelectric power in Co/Cu, Fe/Cu and Fe/Cr multilayers," *Journal of Magnetism and Magnetic Materials*, vol. 110, no. 3, pp. L247–L253, May 1992.
[175] B. Loegel, "Magnetic transitions in the chromium-iron system," *J. Phys. F: Met. Phys.*, vol. 5, no. 3, p. 497, 1975.
[176] A. V. Ruban and V. I. Razumovskiy, "First-principles based thermodynamic model of phase equilibria in bcc Fe-Cr alloys," *Phys. Rev. B*, vol. 86, no. 17, p. 174111, Nov. 2012.
[177] V. Raghavan, "Cr-Fe-N (chromium-iron-nitrogen)," *JPE*, vol. 14, no. 5, pp. 625–626, Oct. 1993.
[178] N. Pettersson, R. F. A. Pettersson, and S. Wessman, "Precipitation of Chromium Nitrides in the Super Duplex Stainless Steel 2507," *Metall and Mat Trans A*, vol. 46, no. 3, pp. 1062–1072, Mar. 2015.
[179] D. K. Yoo, H. J. Lee, C. Y. Kang, K. H. Kim, Y. H. Kim, and J. H. Sung, "A Study on Nitrogen Permeation and Tempering Heat Treatment of AISI Type 409L Ferritic Stainless Steel," *Solid State Phenomena*, 2006. [Online]. Available: https://www.scientific.net/SSP.118.149. [Accessed: 25-Oct-2018].
[180] M. Labonne *et al.*, "Precipitation Kinetics in a Nb-stabilized Ferritic Stainless Steel," *Metall and Mat Trans A*, vol. 48, no. 8, pp. 3655–3664, Aug. 2017.
[181] N. Pettersson, K. Frisk, and R. Fluch, "Experimental and computational study of nitride precipitation in a CrMnN austenitic stainless steel," *Materials Science and Engineering: A*, vol. 684, pp. 435–441, Jan. 2017.
[182] H. W. Paxton and T. Kunitake, "Diffusion in the Iron-Chromium System," *Trans. Met. Soc. AIME*, vol. 218, no. 1003, 1960.
[183] Q. Chen and B. Sundman, "Modeling of thermodynamic properties for Bcc, Fcc, liquid, and amorphous iron," *JPE*, vol. 22, no. 6, pp. 631–644, Nov. 2001.
[184] H. Kuwano, "Mössbauer Effect Study on the Miscibility Gap of the Iron-Chromium Binary System," *Transaction of the Japan Institute of Metals*, vol. 26, no. 7, pp. 473–481, 1985.
[185] R. Vilar and G. Cizeron, "Analyse des evolutions structurales affectant des alliages Fe – x Cr ($15 \leq x \leq 80\%$ pds) initialment dans l'etat tempere," *Memories et etudes revenue de metallurgie*, 1982.

[186] R. O. Williams and H. W. Paxton, "The nature of aging of binary iron chromium alloys around 500°C," *J. Iron Steel Inst.*, vol. 185, p. 358, 1957.
[187] Y. Ustinovshikov and B. Pushkarev, "Alloys of the Fe–Cr system: the relations between phase transitions 'order–disorder' and 'ordering-separation,'" *Journal of Alloys and Compounds*, vol. 389, no. 1–2, pp. 95–101, Mar. 2005.
[188] M. Yu. Lavrentiev, R. Drautz, D. Nguyen-Manh, T. P. C. Klaver, and S. L. Dudarev, "Monte Carlo study of thermodynamic properties and clustering in the bcc Fe-Cr system," *Phys. Rev. B*, vol. 75, no. 1, p. 014208, Jan. 2007.
[189] D. Chandra and L. H. Schwartz, "Mössbauer effect study of the 475‡C decomposition of Fe-Cr," *MT*, vol. 2, no. 2, pp. 511–519, Feb. 1971.
[190] F. Bergner, A. Ulbricht, and C. Heintze, "Estimation of the solubility limit of Cr in Fe at 300 °C from small-angle neutron scattering in neutron-irradiated Fe–Cr alloys," *Scripta Materialia*, vol. 61, no. 11, pp. 1060–1063, Dec. 2009.
[191] S. Katano and M. Iizumi, "Decomposition kinetics in iron-chromium alloys," *Physica B+C*, vol. Volume 120, no. Issue 1, pp. 392–396, May 1983.
[192] S. M. Dubiel and G. Inden, "On the miscibility gap in the Fe- Cr system: a Mössbauer study on long term annealed alloys," *Z. Metallkd.*, vol. 1987, no. 78, p. 544.
[193] M. Hédin, "Sensibilité aux conditions initiales de l'évolution structurale de la ferrite d'aciers austéno-ferritiques vieillis dans le domaine 300– 4008C.," Thèse de doctorat, Université de Rouen, Rouen, France, 1998.
[194] N. Holländer Pettersson, "Precipitation in Advanced Stainless Steels," 2018.
[195] STRUCTURES, MSE, KTH., "Internal report, unpublished work." .
[196] A. D. Pelton, S. A. Degterov, G. Eriksson, C. Robelin, and Y. Dessureault, "The modified quasichemical model I—Binary solutions," *Metall and Materi Trans B*, vol. 31, no. 4, pp. 651–659, Aug. 2000.
[197] A. F. Padilha, R. L. Plaut, P. R. Rios, R. L. Plaut, and P. R. Rios, "Stainless Steel Heat Treatment," *Steel Heat Treatment*, 28-Sep-2006. [Online]. Available: https://www.taylorfrancis.com/. [Accessed: 24-Oct-2018].
[198] S. Medina *et al.*, "Theoretical and Experimental Nucleation and Growth of Precipitates in a Medium Carbon–Vanadium Steel," *Metals*, vol. 7, no. 2, p. 45, Feb. 2017.
[199] Y. Shibuta, K. Oguchi, T. Takaki, and M. Ohno, "Homogeneous nucleation and microstructure evolution in million-atom molecular dynamics simulation," *Scientific Reports*, vol. 5, p. 13534, Aug. 2015.
[200] T. Manninen, "Mechanical Properties of Ferritic Stainless Steels at Elevated Temperature." [Online]. Available: https://www.academia.edu/9039435/Mechanical_Properties_of_Ferritic_Stainless_Steels_at_Elevated_Temperature. [Accessed: 01-Dec-2015].
[201] G. Kanou, N. Harima, S. Takaki, and K. Abiko, "Mechanical Properties of a High-Purity 60 mass%Cr–Fe Alloy," *Mater. Trans., JIM*, vol. 41, no. 1, pp. 197–202, 2000.
[202] N. Matsui, K. Matsui, K. Kobayashi, A. Sugiyama, and K. Ozaki, "Effects of Cr Content on Mechanical Properties of Fe-Cr Alloy," *J. Jpn. Soc. Powder Powder Metallurgy*, vol. 46, no. 11, pp. 1179–1184, Nov. 1999.
[203] R. Braun and M. Feller-Kniepmeier, "Diffusion of chromium in α-iron," *phys. stat. sol. (a)*, vol. 90, no. 2, pp. 553–561, août 1985.
[204] J. Chen, B. Young, and B. Uy, "Behavior of High Strength Structural Steel at Elevated Temperature," *Journal of Structural Engineerin*, vol. 2006, no. 132(12), pp. 1948–1954.
[205] S. Qu *et al.*, "Tensile and compressive properties of AISI 304L stainless steel subjected to equal channel angular pressing," *Materials Science and Engineering: A*, vol. 475, no. 1–2, pp. 207–216, Feb. 2008.

[206] Y.-T. Chiu, C.-K. Lin, and J.-C. Wu, "High-temperature tensile and creep properties of a ferritic stainless steel for interconnect in solid oxide fuel cell," *Journal of Power Sources*, vol. 196, no. 4, pp. 2005–2012, Feb. 2011.
[207] E. Schmid, vol. Delft (1924), pp. 342–353.
[208] W. F. Hosford, *Mechanical Behavior of Materials*. Cambridge University Press, 2010.
[209] W. A. Wooster, *A Textbook on Crystal Physics*. UK.: Cambridge University Press.
[210] J. F. Nye, *Physical Properties of Crystals – Their Representation by Tensors and Matric*. UK.: Oxford University Press.
[211] P. Burnley, "Tensors, Stress, Strain, Elasticity," *Mineral Physics*. [Online]. Available: https://serc.carleton.edu/NAGTWorkshops/mineralogy/mineral_physics/tensors.html. [Accessed: 27-Sep-2018].
[212] F. Mouhat and F.-X. Coudert, "Necessary and Sufficient Elastic Stability Conditions in Various Crystal Systems," *Physical Review B*, vol. 90, no. 22, Dec. 2014.
[213] H. Zhang, M. P. J. Punkkinen, B. Johansson, S. Hertzman, and L. Vitos, "Single-crystal elastic constants of ferromagnetic bcc Fe-based random alloys from first-principles theory," *Phys. Rev. B*, vol. 81, no. 18, p. 184105, May 2010.
[214] R. Pasianot, D. Farkas, and E. J. Savino, "Empirical many-body interatomic potential for bcc transition metals," *Phys. Rev. B*, vol. 43, no. 9, pp. 6952–6961, Mar. 1991.
[215] J. Nordmann, M. Aßmus, and H. Altenbach, "Visualising elastic anisotropy: theoretical background and computational implementation," *Continuum Mech. Thermodyn.*, vol. 30, no. 4, pp. 689–708, Jul. 2018.
[216] D. Su, Y.-L. He, J.-Q. Liu, and X.-G. Lu, "Establishment of the Elastic Property Database of Fe-base Alloys," *Advances in Intelligent Syst ems Research*, vol. 2015, no. Volume 126, p. 2065.
[217] D.-S. Sun, T. Yamane, and K. Hirao, "Intermediate-temperature brittleness of a ferritic 17Cr stainless steel," *J Mater Sci*, vol. 26, no. 3, pp. 689–694, Feb. 1991.
[218] S. S. Chou, T. S. Chin, and L. C. Yang, "Effect of stress-aging on spinodal decomposition and magnetic properties of Fe□Cr□Co□Ti alloys," *Scripta Metallurgica*, vol. 18, no. 2, pp. 121–125, Feb. 1984.
[219] M. Thuvander, J. Zhou, J. Odqvist, S. Hertzman, and P. Hedstro¨m, "Observations of Copper Clustering in a 25cr-7ni Super Duplex Stainless Steel During Low-temperature Aging Under Load," *Philosophical Magazine Letters*, vol. 92, no. 7, pp. 336–343, Jan. 2012.
[220] S. M. Wise, J. S. Kim, and W. C. Johnson, "Surface-directed spinodal decomposition in a stressed, two-dimensional, thin film," *Thin Solid Films*, vol. 473, no. 1, pp. 151–163, février 2005.
[221] A. Vidyasagar, S. Krödel, and D. M. Kochmann, "Microstructural patterns with tunable mechanical anisotropy obtained by simulating anisotropic spinodal decomposition," *Proc. R. Soc. A*, vol. 474, no. 2218, p. 20180535, Oct. 2018.
[222] H. Hasegawa, M. W. Finnis, and D. G. Pettifor, "A calculation of elastic constants of ferromagnetic iron at finite temperatures," *J. Phys. F: Met. Phys.*, vol. 15, no. 1, p. 19, 1985.
[223] D. W. Saxey, "Correlated ion analysis and the interpretation of atom probe mass spectra," *Ultramicroscopy*, vol. 111, no. 6, pp. 473–479, May 2011.
[224] S. Suwas and R. K. Ray, *Crystallographic Texture of Materials*. London: Springer-Verlag, 2014.
[225] G. Monnet, B. Bacroix, J.-L. Lebrun, and T. Ungar, "Three-dimensional investigation of long-range internal stresses in a single crystal deforming by nonsymmetrical slip," *Metall and Mat Trans A*, vol. 33, no. 3, pp. 591–596, Mar. 2002.

[226] M. M. Nowell, R. A. Witt, and B. W. True, "EBSD Sample Preparation: Techniques, Tips, and Tricks," *Microscopy Today*, vol. 13, no. 4, pp. 44–49, Jul. 2005.
[227] C. R. Weinberger, B. L. Boyce, and C. C. Battaile, "Slip planes in bcc transition metals," *International Materials Reviews*, vol. 58, no. 5, pp. 296–314, Jun. 2013.
[228] C. Marichal, H. V. Swygenhoven, S. V. Petegem, and C. Borca, "{110} Slip with {112} slip traces in bcc Tungsten," *Scientific Reports*, vol. 3, p. 2547, Aug. 2013.
[229] N. Provatas *et al.*, "Using the phase-field crystal method in the multi-scale modeling of microstructure evolution," *JOM*, vol. 59, no. 7, pp. 83–90, Jul. 2007.
[230] A. G. Khachaturyan, *Theory of structural transformations in solids*, vol. 1983. New York: Wiley.
[231] A. Vaugeois, "Modélisation de l'influence de la structure des joints de grains sur les phénomènes de ségrégation.," phdthesis, Normandie Université, 2017.
[232] M. Jamal, S. Jalali Asadabadi, I. Ahmad, and H. A. Rahnamaye Aliabad, "Elastic constants of cubic crystals," *Computational Materials Science*, vol. 95, pp. 592–599, Dec. 2014.
[233] M. Müller, P. Erhart, and K. Albe, "Analytic bond-order potential for bcc and fcc iron—comparison with established embedded-atom method potentials," *J. Phys.: Condens. Matter*, vol. 19, no. 32, p. 326220, 2007.
[234] M. I. Mendelev, S. Han, D. J. Srolovitz, G. J. Ackland, D. Y. Sun, and M. Asta, "Development of new interatomic potentials appropriate for crystalline and liquid iron," *Philosophical Magazine*, vol. 83, no. 35, pp. 3977–3994, Dec. 2003.
[235] M. Hillert, "A solid-solution model for inhomogeneous systems," *Acta Metallurgica*, vol. 9, no. 6, pp. 525–535, Jun. 1961.
[236] J. Miettinen, "Calculation of solidification-related thermophysical properties for steels," *Metall and Materi Trans B*, vol. 28, no. 2, pp. 281–297, Apr. 1997.
[237] D. Raabe and M. Sachtleber, "Measurement of plastic strains by 3D image correlation photogrammetry at the grain scale," *edoc Server, Max-Planck-Society , MPI Düsseldorf*, p. 22.
[238] K. Carlsson, "Modeling of three dimensional microstructures including grain boundary mechanisms," Chalmers University of Technology, Gothenburg, Sweden 2013.
[239] W. Ludwig, S. Schmidt, E. M. Lauridsen, and H. F. Poulsen, "X-ray diffraction contrast tomography: a novel technique for three-dimensional grain mapping of polycrystals. I. Direct beam case," *Journal of Applied Crystallography*, vol. 41, no. 2, pp. 302–309, Apr. 2008.
[240] R. L. Klueh, P. J. Maziasz, and E. H. Lee, "Manganese as an austenite stabilizer in Fe□Cr□Mn□C steels," *Materials Science and Engineering: A*, vol. 102, no. 1, pp. 115–124, Jun. 1988.
[241] J. E. Guyer, D. Wheeler, and J. A. Warren, "FiPy: Partial Differential Equations with Python," *Computing in Science Engineering*, vol. 11, no. 3, pp. 6–15, May 2009.
[242] J.-O. Andersson, T. Helander, L. Höglund, P. Shi, and B. Sundman, "Thermo-Calc & DICTRA, computational tools for materials science," *Calphad*, vol. 26, no. 2, pp. 273–312, Jun. 2002.
[243] G. Sterner and L. Höglund, "Unpublished work."
[244] D. J. Eyre, "Unconditionally Gradient Stable Time Marching the Cahn-Hilliard Equation," *MRS Online Proceedings Library Archive*, vol. 529, ed 1998.
[245] Ł. Bolikowski, *Numerical solutions of Cahn-Hilliard equation on various domains: bolo1729/cahn-hilliard*. 2018.

Appendix

10.1 A1: Setup for phase-field modelling

In order to illustrate the effect of different thermodynamic descriptions on the simulation of microstructure evolution during ageing of binary Fe-Cr we numerically solve the Cahn-Hilliard equation (C-H) [36]. The C-H equation is a modified diffusion equation where, for the case of Fe-Cr, the flux of chromium is written as

$$J_{Cr} = -L_{CrCr}\nabla\frac{\delta G}{\delta x_{Cr}} \tag{1}$$

L_{CrCr} is a phenomenological parameter related to the motilities of Cr and Fe [44], x_{Cr} is the mole fraction of Cr and $\delta G / \delta x_{Cr}$ is the vibrational derivative of the Gibbs energy functional

$$G = \frac{1}{V_m}\int\left\{G_m(x_{Cr},T) + \frac{\varepsilon^2}{2}(\nabla x_{Cr})^2\right\}d\Omega \tag{2}$$

The integral in Eq. 2 is taken over the domain of interest, V_m is the molar volume, G_m is the molar Gibbs energy taken from the two descriptions. The second term on the right-hand side of Eq. 2 is the gradient energy contribution to the total Gibbs energy, and during minimization, this term is responsible for smoothening the composition profiles. The ε^2 is the gradient energy coefficient, here taken to be [11]:

$$\varepsilon^2 = \frac{\omega_{CrFe}\delta^2}{2} \tag{3}$$

ω_{CrFe} is the regular solution parameter and δ is the interaction distance. For the new description $\omega_{CrFe}^{New} = 28990 - 22.082\cdot T$ and for the description by Xiong et al. [12] $\omega_{CrFe}^{Xiong} = 24212 - 15.507\cdot T$. In this work, it is assumed that the L_{CrCr} is dependent on temperature but not on composition. This scheme can be used to solve FiPy PDE coupled to CALPHAD. However, this has not been the focus of this work instead of the 4% difference at 525°C has been used to estimate how it might alter the structure.

Equations 1-3 together with the continuity equation forms the C-H equation which can be solved using the finite volume PDE solver FiPy [241]. Thus the G_m and its derivatives are

updated each time-step with the help of a coupling between FiPy and ThermoCalc [242] using 2e.g. a Python interface [243].

To illustrate the effect on the structure the difference in interaction parameter from this optimization might have, Eyre's [244] linearly stabilized CH integration scheme is used to solve the CH equation in 2D in MATLAB [245]. A reference state is used for the comparison, in this case, there the system is not connected to CALPHAD. A simple double-well potential is used to minimizing the free energy that allows for complete phase separation.

Ref.

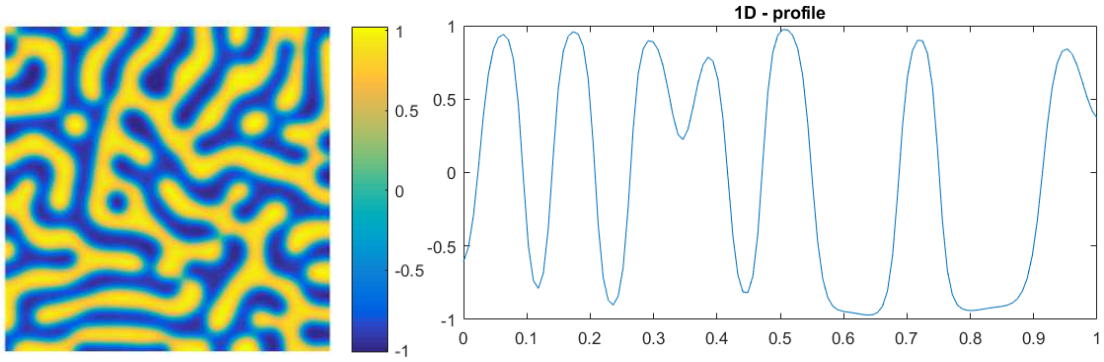

New

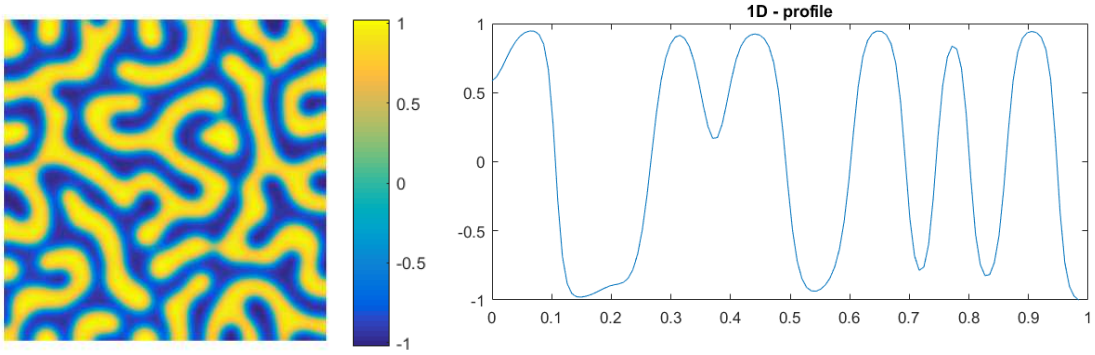

10.2 Tensile test of Fe-50Cr

Solution treatment: 1100°C 2h

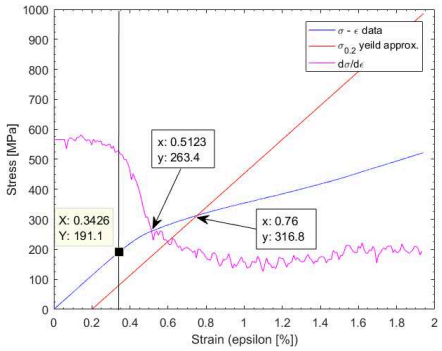

Strain rate: 0.25 mm/min, Peak force: ~2.5kN

Slow cooled to 600°C

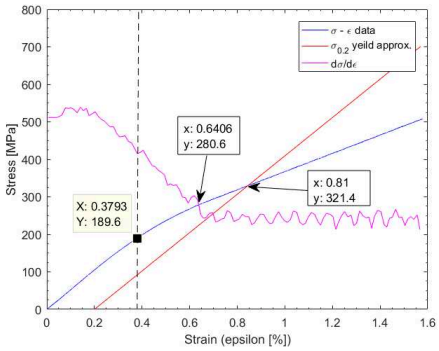

Strain rate: 0.25 mm/min, Peak force: ~2.5kN

500°C 1h

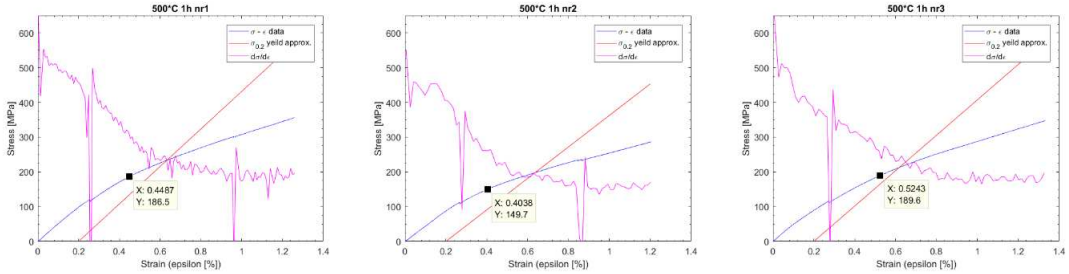

500°C 4h

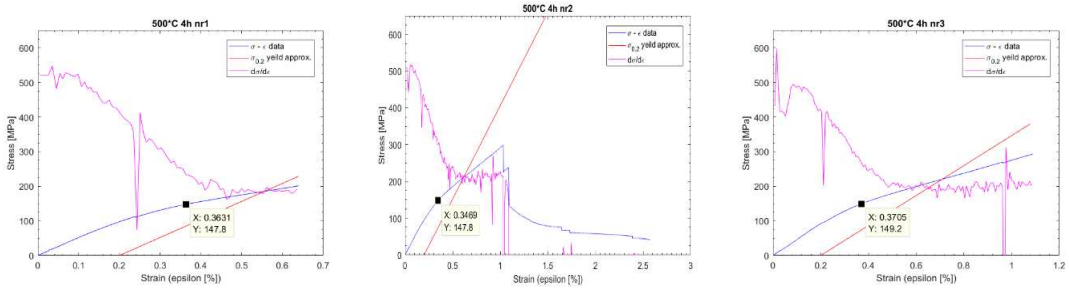

500°C 9h

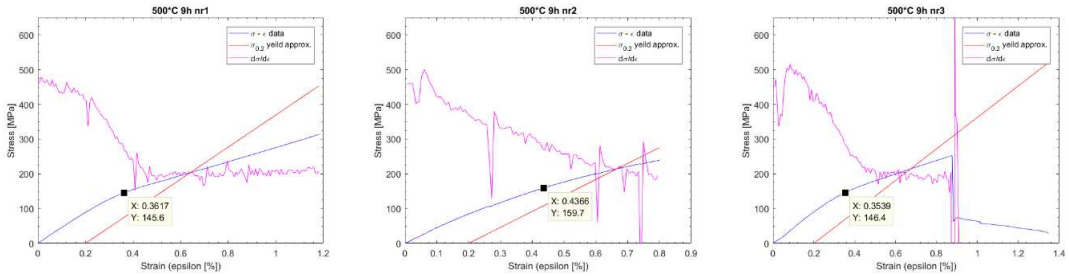

10.3 A2: APT tips 150 MPa

These data set were acquired with an evaporation rate of 0.30%, 20% pulse fraction with 200 kHz at 50K. The high quality (HQ) runs reached single detections ~88%, multiple detections ~12%, with a background noise estimate of 27ppm. Less fortunate (LF) tips (containing higher Ga^+ and CrN) with the same parameters achieved single detection ~78% and multiple ~22%, with a background noise of 39ppm. Two tips were acquired from each direction <101> and <111>. The less fortunate tips were prepared in the older Zeiss XB 1530 FIB, where the FIB gun at times was unstable during low voltage cleaning.

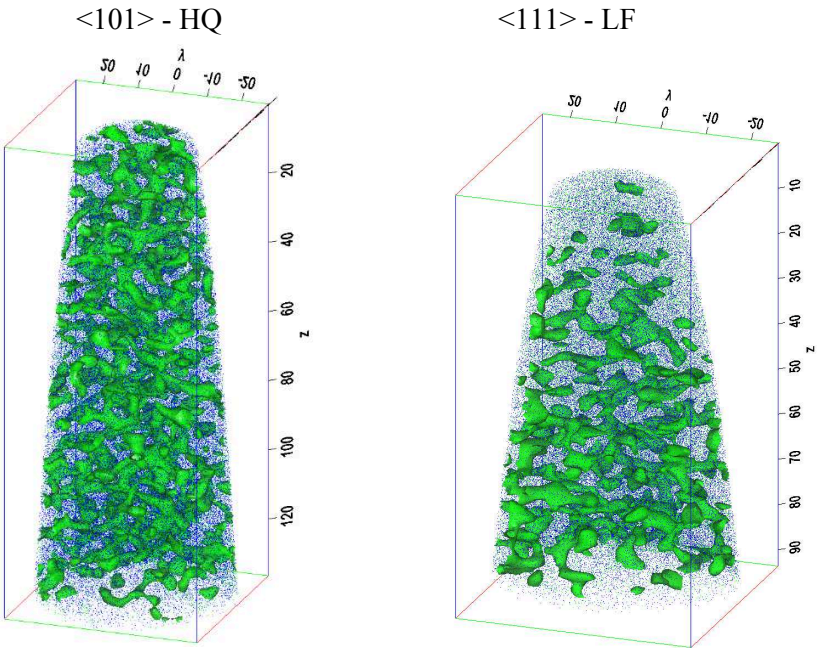

Figure 11-1. Reconstructions of samples stress-aged at 148MPa *iso*-surface at 50at.%-Cr

10.4 A3: APT reconstruction Fe-35Cr 235 MPa

The APT analysis was performed with the following parameters: evaporation rate of 0.30%, pulse fraction 20%, repetition rate 200 kHz and temperature at 50K. Fe atoms are displayed as blue and Cr atoms are displayed as green ~7% of the collected ions are displayed in the figures. The *iso* - surface is set to 50at.%-Cr with a sigma error of 0.10. For the <111> samples which were prepared in the older Zeiss XB 1530, the first 50nm of the tip needed to be discarded due to Ga^+ implantation as a result of an unstable and sometimes blanked FIB gun, which resulted in poor cleaning. In addition, after ~200nm analysis depth a Cr2N was found in the <111> sample, hence the abrupt change in morphology.

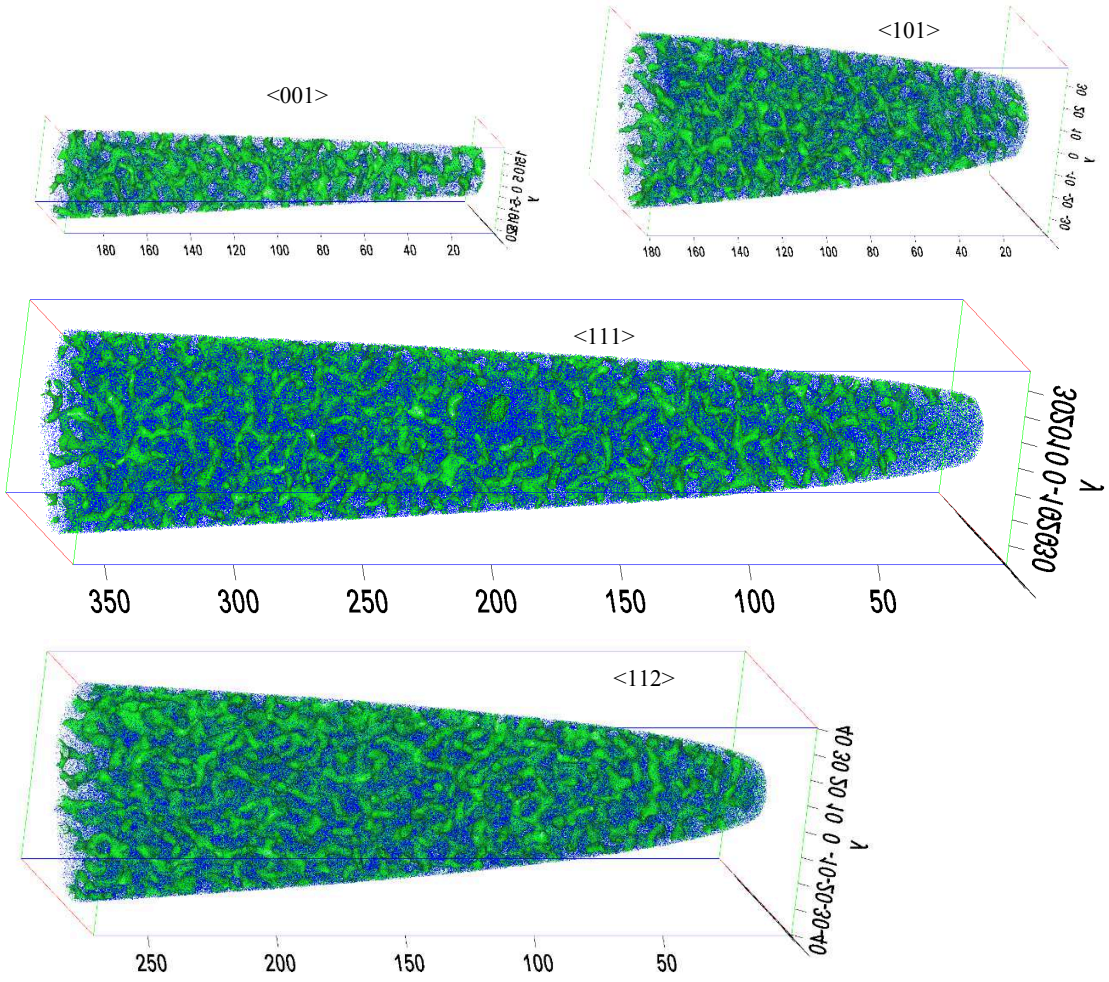

Figure 11-2. Orientation dependent APT reconstructions, *iso*-surface at 50at.%-Cr.